Conception, fabrication, et évaluation de modulateurs déportés pour les réseaux d'accès et radio sur fibre

Guilhem de Valicourt

ParisTech
INSTITUT DES SCIENCES ET TECHNOLOGIES
PARIS INSTITUTE OF TECHNOLOGY

TELECOM ParisTech

Doctorat ParisTech

T H È S E

pour obtenir le grade de docteur délivré par

Télécom ParisTech

Spécialité “Electronique et Communications”

présentée et soutenue publiquement par

Guilhem de VALICOURT

7 Octobre 2011

Conception, fabrication et évaluation de modulateurs déportés pour les réseaux d’accès et radio sur fibre

Directeur de thèse : **Cédric WARE**
Co-encadrement de la thèse : **Romain BRENOT**

Jury

M. Xavier Marie, Professeur, Département du génie physique, INSA de Toulouse	Président
M. Jean-Claude Simon, Professeur, CNRS FOTON, ENSSAT, Université de Rennes 1	Rapporteur
Mme Catherine Lepers, Professeur, Département Electronique et Physique, Télécom SudParis	Rapporteur
M. Joël Jacquet, Professeur, Supelec de Metz	Examinateur
M. Philippe Chanclou, Docteur Ingénieur de recherche, Orange Labs, France Telecom R&D	Examinateur
M. Didier ERASME, Professeur, COMELEC, Télécom ParisTech	Examinateur

T H È S E

Télécom ParisTech
Grande école de l’Institut Télécom – membre fondateur de ParisTech
46, rue Barrault – 75634 Paris Cedex 13 – Tél. + 33 (0)1 45 81 77 77 – www.telecom-paristech.fr

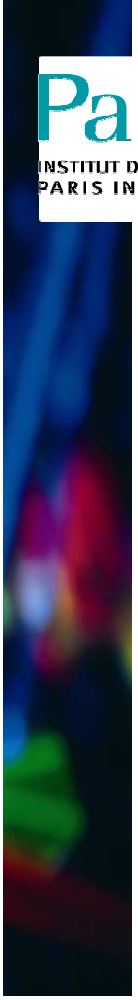

"This instrument can teach, it can illuminate; yes, and even it can inspire. But it can do so only to the extent that humans are determined to use it to those ends. Otherwise it's nothing but wires and lights in a box."

E. Murrow, 1958

Télécom ParisTech
Grande école de l'Institut Télécom – membre fondateur de ParisTech
46, rue Barrault – 75634 Paris Cedex 13 – Tél. + 33 (0)1 45 81 77 77 – www.telecom-paristech.fr

Table of contents

Acknowledgement

Il y a pas très longtemps
à quelques kilomètres de Paris,
Au fin fond du plateau de Saclay…
Commence notre histoire…

Au commencement …

Le 13 octobre 2008, en tant que jeune « Padawan », je fus investi d'une mission pour le bien de la science. Je ne comprenais pas encore les aboutissants et les finesses du sujet, malgré cela je fus choisi pour y participer. Je remercie donc F. Brillouet de m'avoir accepté dans son laboratoire, le III-V Lab, et fait confiance pour répondre aux besoins de cette étude.

Comme tout aventurier, je partais donc à la recherche du Graal photonique.

Une quête sans guidance est vouée à être éternelle. Je fus conseillé, aiguillé et guidé par un des grands philosophes de ce monde, Romain Brenot. Je te salue et te témoigne mon plus grand respect. Sans ta sagesse et tes conseils, rien n'aurait pu aboutir.

En parlant de maître spirituel, merci, à Cédric Ware, mon directeur de thèse. Nos échanges, nos débats et nos discussions m'ont permis d'aborder le sujet sous de nouveaux angles. Ta disponibilité m'a été d'une aide précieuse quand j'en avais besoin. Merci, de m'avoir donné l'occasion de transmettre mon savoir aux nouveaux scientifiques de demain, un jour je serai Jedi moi aussi !

Sur la route …

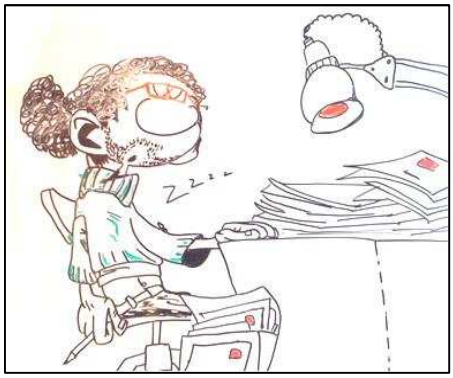

Lors de mon épopée, de nombreux compagnons de route me rejoignirent pour le meilleur et pour le pire.
Tout d'abord, mon fidèle ami du champ de bataille, Marco Lamponi. Avoir un compagnon d'armes est essentiel pour avancer tout en gardant le moral. On s'est battu, on a gagné des batailles, on en a perdu d'autres mais on a avant tout scellé notre amitié ! Merci d'avoir partagé ces trois ans avec moi. Le premier tome est écrit mais de nombreux

tomes restent encore à coucher sur le papier.

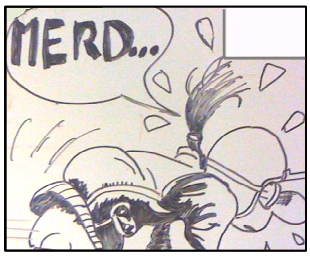

L'expérience et le savoir sont des bases fondamentales pour avancer et prennent parfois des apparences inattendues. Chevauchant son destrier à deux roues, une queue de cheval reposant fièrement sur ses épaules, j'ai eu le privilège de rencontrer un homme incarnant ces valeurs, Francis Poingt. Maître en plusieurs arts tels le dessin, la peinture, la cuisine ou encore la photolithographie, ton expérience m'a permis d'apprendre énormément et mon seul regret est que cet apprentissage se termine. Il me manque encore tant de chose à assimiler…

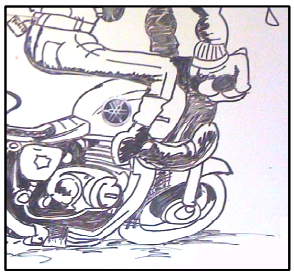

Une autre rencontre m'a amené à une nouvelle perception du monde. Ce fut celle avec Guang-Hua Duan. Il m'a appris à voir le monde comme un ensemble de modèles d'équations plus ou moins justes avec comme objectif le souci d'une reproduction parfaite de la réalité. Merci de m'avoir ouvert ton monde.

Je tiens bien sur à remercier tous les membres du labo III-V Lab. Toutes ces interactions, ces échanges et la bonne humeur constante de toute l'équipe ont contribué à un travail de qualité. Merci à vous tous : Alban Leliepre, Hoi Leung, Perrine Berger, Dalila Make, Frederic Van Dijk, Frederic Pommereau, Mickael Tran, Nadine Lagay et à tous ceux que j'oublie…

Cette quête m'a amené à voyager dans de nombreuses contrées lointaines où j'ai eu le privilège de rencontrer d'autres aventuriers scientifiques. Ce fut des collaborations et des échanges intenses! Je vous remercie pour votre accueil et votre recherche. Merci à Anthony Nkansah, David Wake, Nathan J. Gomes, Manuel Violas et Bernhard Schrenk.

Mais le voyage peut être parfois semé d'embûches… Je tiens à remercier Gautier Morel, Hubert de Ferron et Samuel Laulhau pour avoir complexifié la rédaction de ce manuscrit et de m'avoir appris à résister aux nombreuses tentations.

L'arrivée …

Les voies de la science sont parfois variées et improbables. Il faut souvent improviser, s'adapter et adopter de nouveaux rôles.

Charles Cayron, merci à toi de m'avoir impliqué dans le tournage d'un court-métrage de vulgarisation scientifique. Quelle ambiance et que de fou rire commun!

Je te tiens à remercier toute l'équipe de « Colorlife ». L'entreprenariat est souvent un autre visage de la science et de l'innovation. Merci de me l'avoir fait découvrir et merci pour m'avoir montré

qu'avec une équipe motivée tout est possible. Merci à vous : Oriol Bertran-Pardo, Corinne Olivier, François Guern, Yann Lopez, Mercedez Martinez Martin et Jean-Luc Beylat.

Le jour du jugement dernier arriva, je me présentais donc devant un jury impartial. Chers membres du Jury, Xavier Marie, Jean-Claude Simon, Catherine Lepers, Joël Jacquet, Philippe Chanclou et Didier Erasme, merci de m'avoir fait l'honneur d'accepter d'être membres du jury. Merci de vos corrections et de vos remarques avisées.

Souvent une motivation personnelle nous donne la rage au ventre, cette sensation qui nous pousse à nous surpasser. Jeune Padawan, je suis devenu roi grâce à ma femme de l'autre bout du monde. Nous avons, ensemble, surmonté toutes les difficultés et traversé le monde pour nous réunir. Mi corazoncito, gracias por haber dicho « Si ». Te amo!

Pour finir, cette aventure n'aurait jamais eu lieu sans le soutien et l'amour de mes chers parents et de mon petit frère. Merci, je vous aime ! Encore une fois, merci pour tout ce que vous avez fait pour moi.

Résumé

La télécommunication est un processus actif d'échange à distance d'informations qui implique le codage, la transmission et le décodage d'un message initial. Que l'on retienne une vision linéaire de la communication, par le biais d'une séquence simple émetteur-média-récepteur, ou une conception plus holistique, consacrant l'objectif d'élaboration d'un espace social de consensus, celle-ci n'est concevable que par l'intercession d'un média. Les supports télécommunicationnels peuvent être des ondes sonores, des impulsions électriques, ou de la lumière. L'évolution de ces vecteurs permet de transcender les distances.

L'évolution des réseaux, une révolution des usages

Ces outils de transmission évoluent. Le télégraphe, conçu en 1861, fut un des premiers moyens de communication sur de grandes distances. Les réseaux ont dû s'adapter à une demande grandissante. Le câble coaxial remplaça le câble de cuivre à partir des années 1950 puis la fibre optique fit son apparition dans les années 1980. Le message n'est plus alors transmis par des impulsions électriques mais optiques. Les données se propagent ainsi dans un tunnel de verre. En France, l'échelle de ce changement s'opère en millions d'utilisateurs. De 1022 bureaux de télégraphe en 1863, ce sont 44 000 foyers qui sont équipés de la fibre optique en 2010 selon l'ARCEP [1]. Par ailleurs, une large partie des 4,5 milliards d'euros que l'Etat français prévoit de consacrer au volet numérique du grand emprunt [2,3] permettra le développement de la fibre. France Telecom ambitionne, en outre, d'en faire bénéficier 15 millions de foyers d'ici à 2020.

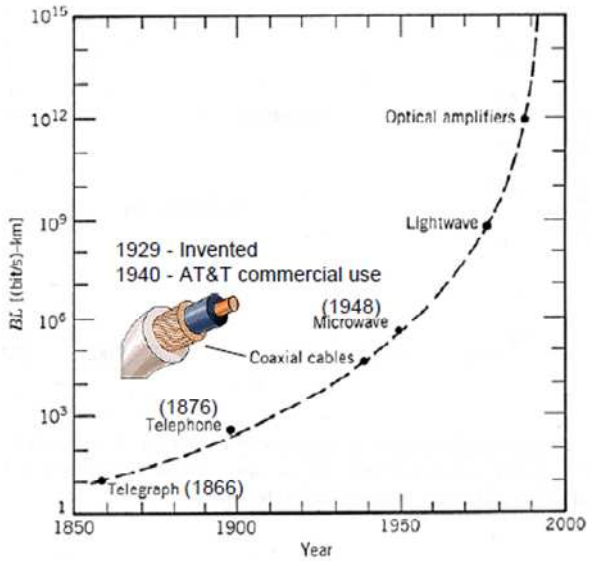

Figure a – Augmentation du produit débit-distance à travers le temps [4]

Le temps où des systèmes digitaux requérant des capacités de réseau croissantes seront installés partout, à la maison, au bureau, dans la rue, voire sur nous-mêmes n'est plus loin. Or, malgré l'actuel déploiement massif de la fibre optique, le potentiel de cette technologie reste sous exploité. En effet, dans les réseaux d'accès, tous les utilisateurs communiquent avec la même longueur d'onde. En d'autres termes, ils utilisent tous la même couleur. Les informations sont envoyées successivement dans le temps, limitant ainsi les débits. Cependant, l'utilisation de plusieurs longueurs d'onde permet depuis peu la transmission simultanée de données. Un

utilisateur doté d'une longueur d'onde propre aura donc un canal de communication qui lui sera entièrement dédié. Utilisée dans les réseaux très longue distance, la mise à disposition de cette technologie au grand public nécessite l'insertion dans le transcepteur d'une puce optique modulant les différentes longueurs d'onde. Plusieurs années de recherche ont permis l'élaboration d'un composant pouvant satisfaire ces ambitions technologiques : le RSOA (Reflective Semiconductor Optical Amplifier). Invisible, exploitant la fibre optique généralisée et disponible partout, le RSOA donnerait accès à des applications existantes et permettrait d'explorer, qui plus est, des domaines encore balbutiants.

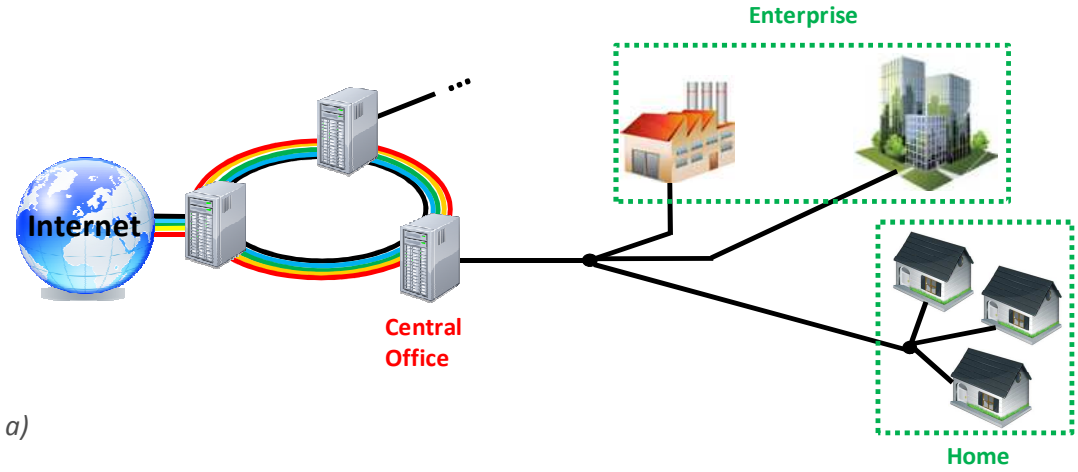

a)

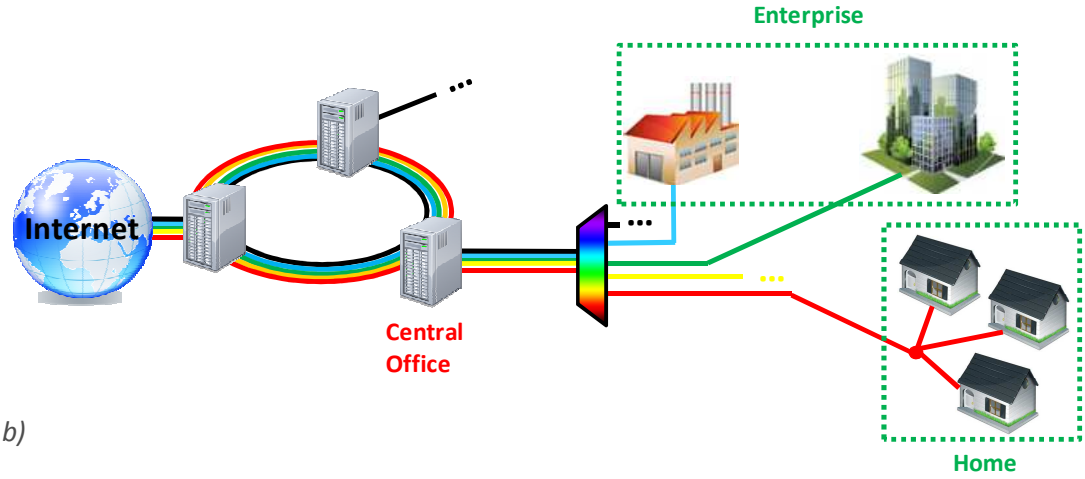

b)

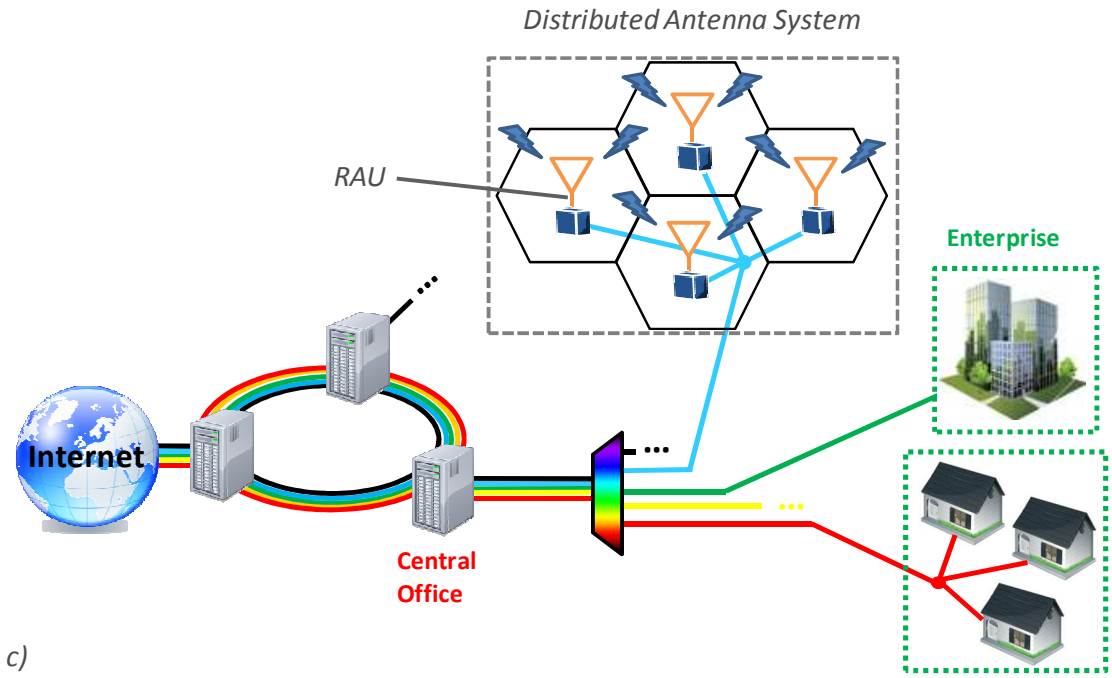

Figure b – Architecture de réseaux d'accès basé sur (a) une longueur d'onde unique (b) plusieurs longueurs d'onde et c) la convergence avec un réseau de type radio sur fibre

La mobilité aura été une nouvelle variante de notre époque. L'utilisateur veut pouvoir profiter, sur ces équipements mobiles, des même facilitées et de la même qualité de communication que sur un poste fixe. Dans ce contexte d'ubiquité permanente s'inscrit le projet FUTON qui accompagna cette étude durant ces trois ans. Le concept est simple : le déploiement de plusieurs antennes communicant avec tous objets de communications mobiles et reliées par fibre optique. Or, la réalisation de ce genre d'architecture est bien plus complexe notamment d'un point de vue source photonique. Le composant devra se plier aux nouvelles exigences de la radio-sur-fibre (RoF : transmission de signaux radio fréquence par fibre optique).

Dans le but de répondre à toutes ces conditions, différents objectifs furent définis pour l'évaluation et l'optimisation de ces composants optiques:

- Identification et compréhension des mécanismes physiques à l'intérieur du RSOA
- Conception, modélisation et fabrication de composants RSOA
- Caractérisations statiques et dynamiques de ces composants
- Identification des limites du composant et propositions de solution innovante pour les surmonter
- Développement de composants optimisés
- Evaluation des RSOAs pour les réseaux d'accès et de type RoF

De la Physique fondamentale à une conception concrète

Ce doctorat oscille entre de nombreux domaines des sciences. Les chapitres 1 et 2 abordent les bases fondamentales de la physique des matériaux semi-conducteurs et de la physique des lasers ainsi que quelques notions sur la conception de composants optoélectroniques.

Le chapitre 1 est dédié à une présentation des concepts de base nécessaire à la compréhension de cette thèse. Les différentes interactions entre la lumière et la matière sont explicitées ainsi que les procédés de recombinaison radiative et les différentes notions introduites par Einstein. La théorie et les principes particuliers liés à l'utilisation d'un composant SOA en réflexion sont décrits et comparés à des composants plus classiques tels que le laser Fabry-Perot et le SOA en transmission.

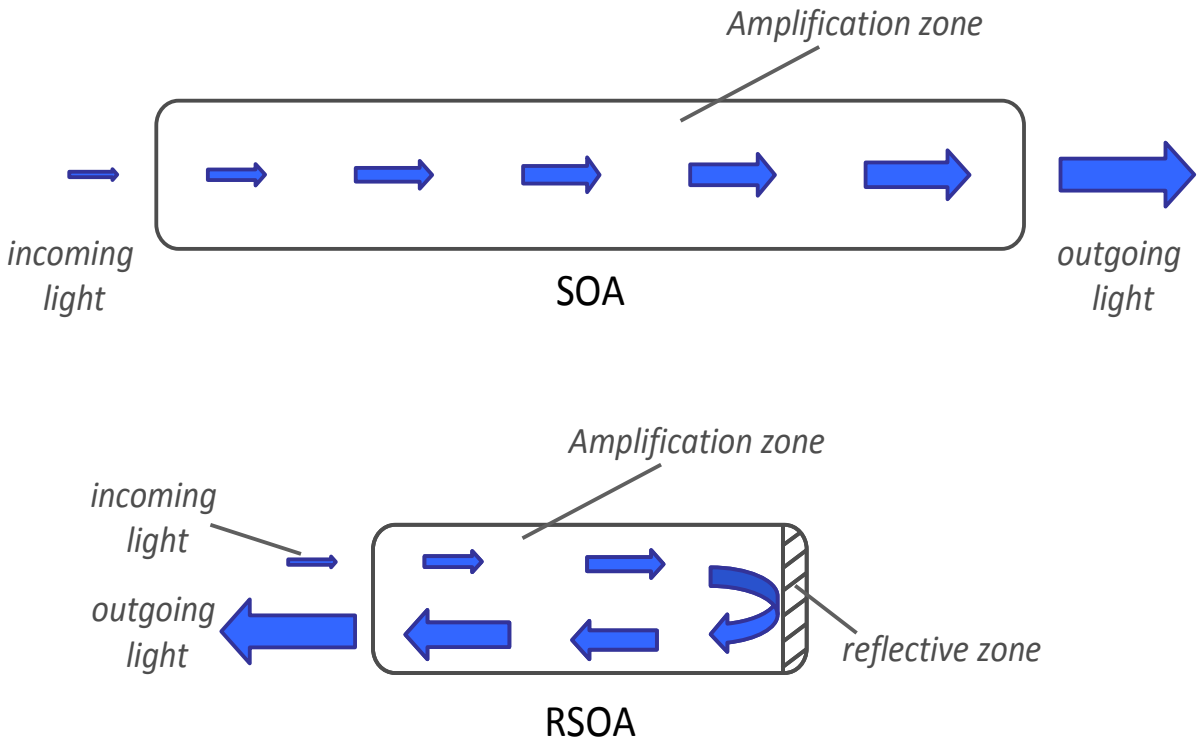

Figure c – Principe de fonctionnement d'un SOA et d'un RSOA

Nous abordons par la suite les propriétés intrinsèques des matériaux eux-mêmes. Le gain matériaux, dépendant de la densité de porteurs présente dans son milieu, en est extrait. Les bandes de conduction et de valence sont approximées par une fonction parabolique et leurs niveaux de remplissage obéissent à la statistique de Fermi-Dirac. Les propriétés directement liées à une structure spécifique constituée par un empilement de différentes couches telles que les hétéro-structures nous permettent de calculer le gain net. Celui-ci est inférieur au gain matériaux dû aux pertes dans la zone active mais aussi aux pertes dans les couches voisines.

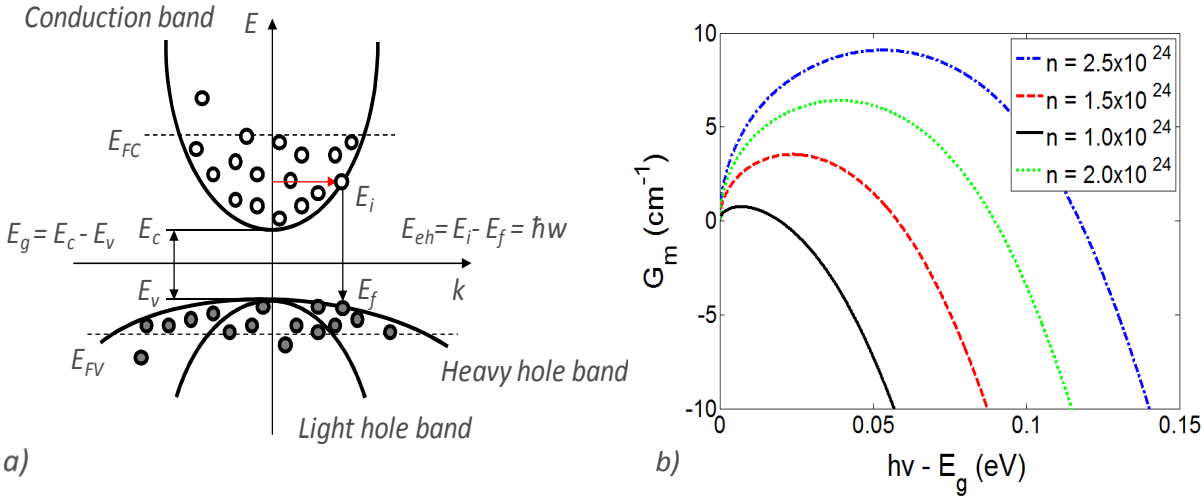

Figure d – (a) diagramme des bandes d'énergie d'un matériaux semi-conducteur à gap direct (b) Simulation du gain matériaux en fonction de l'énergie des photons incidents pour plusieurs densités de porteurs

Nous étendons cette étude à la considération de la propagation d'une onde dans ce milieu à gain ainsi que dans une cavité de résonateur optique (laser). Le gain optique peut finalement être calculé à partir de paramètres clefs tels que la réflectivité des facettes, le gain simple passage calculé à partir du gain net et de la longueur d'onde.

Ce chapitre 1 se conclue par une analyse préliminaire de la répartition spatiale de la densité des porteurs dans des composants de type SOA. Une répartition inhomogène est mise en évidence ainsi que son influence sur le gain total du composant.

Une fois ces concepts de base abordés, nous nous concentrerons sur la conception et la fabrication de ces composants photoniques.

L'épitaxie des différentes couches est décrite dans un premier temps. Même si cette étape ne fut pas réalisée lors de cette étude, la compréhension et l'analyse de celle-ci restent clef dans la conception de RSOA.

Le confinement optique est légèrement différent en fonction des polarisations, or il est primordial d'obtenir des composants insensibles à la polarisation pour les applications visées. Il est possible de compenser cette différence de confinement optique par une différence des gains matériaux comme nous l'indice la formule ci-dessous.

$$PDG = G_{int,TE} \times \left(1 - \frac{\Gamma_{TM} \times g_{mat,TM}}{\Gamma_{TE} \times g_{mat,TE}}\right)$$

Où G_{int} est le gain interne pour le mode optique TE, g_{mat} est le gain matériaux et Γ est le confinement optique.

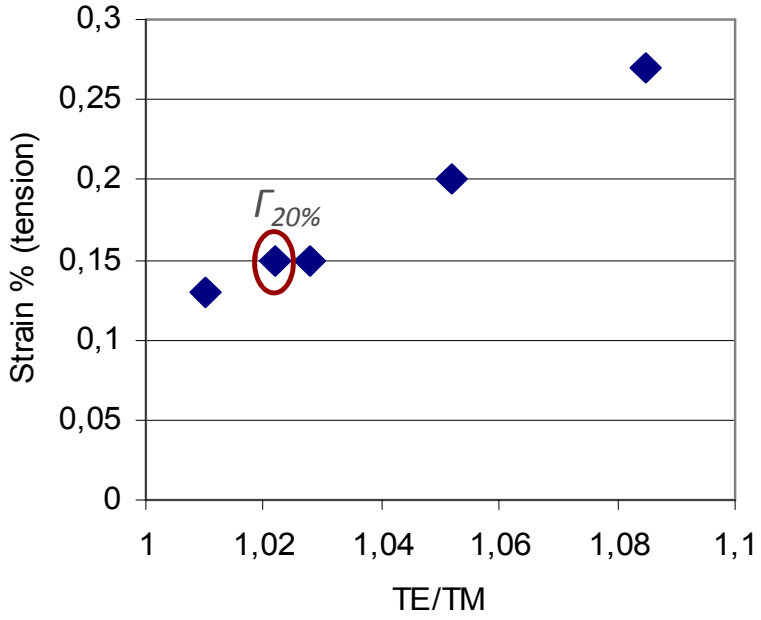

Figure e – Valeurs expérimentales des tensions appliquées au matériau en fonction du rapport des confinements optiques TE/TM

Par exemple pour un confinement optique de 20 %, un rapport des confinements de 1.02 est obtenu. Différents gains matériaux peuvent être obtenus par une dégénérescence des bandes d'énergie du matériau. Cette dégénérescence est elle-même obtenue par l'application d'une contrainte sur celui-ci. C'est ainsi que contrainte en tension de 0.15% est nécessaire pour l'obtention de composant indépendant à la polarisation ayant un rapport TE/TM de 1.02.

Une étude de la structure et de la conception est ensuite réalisée.

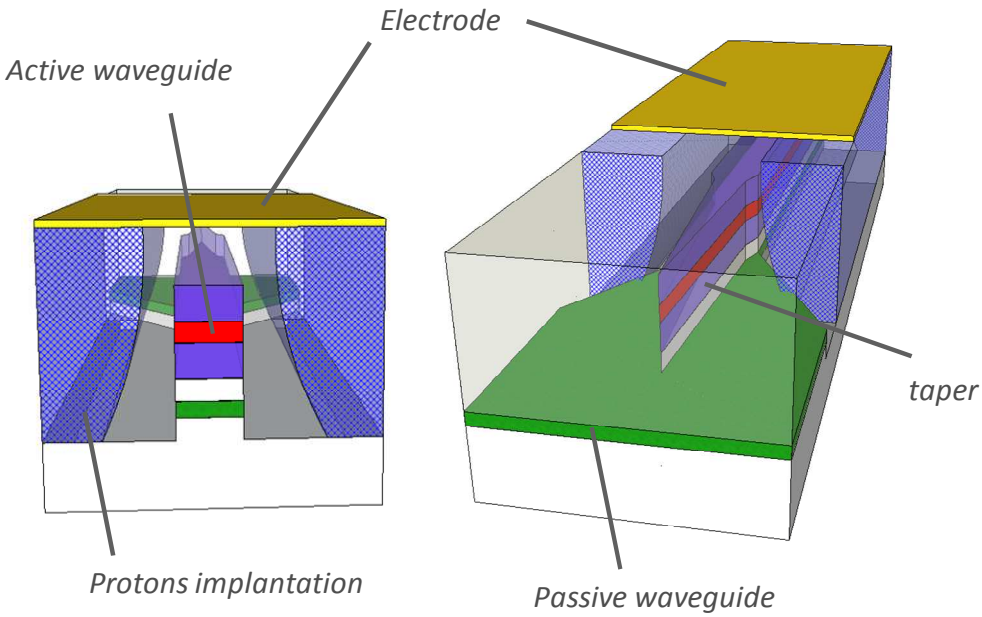

Figure f – Structure « ridge » enterré RSOA avec double « tapers » actif/passif

Une structure de type « ridge » enterrée sera utilisée pour la conception et fabrication de ces composants car permettant une injection électrique efficace ainsi qu'une bonne dissipation de la chaleur. Cette structure est analysée, décrite et caractérisée électriquement et optiquement. Notamment une caractérisation originale par mesures d'émission spontanée nous permet d'identifier facilement un courant de fuite dans la zone passive se traduisant par un pic d'émission autour de 1.17 μm.

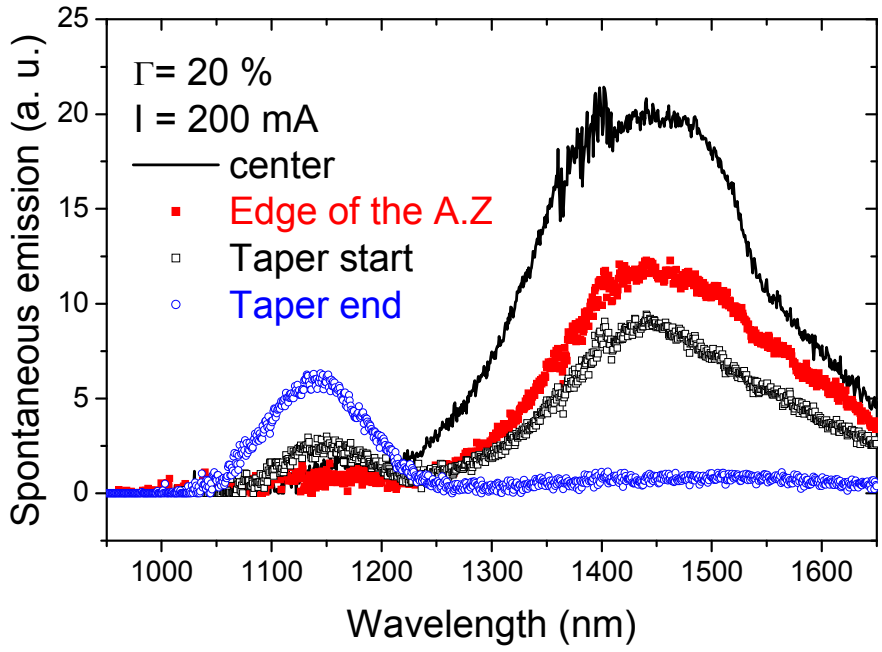

Figure g – Mesures d'émission spontanée le long d'un composant SOA ayant un confinement optique de Γ = 20%

La structure du RSOA comporte une zone active où la lumière est amplifiée et une zone passive servant à l'expansion du mode optique pour un couplage optimisé avec la fibre. Un « taper » est utilisé pour transférer le mode optique d'une zone à l'autre. Les problèmes technologiques liés à la réalisation de cette structure sont décrits tels qu'un courant de fuite élevé ou encore l'apparition d'une cavité parasite. Bien sur différentes solutions et différentes conceptions optimisées sont proposées par palier à ces limitations.

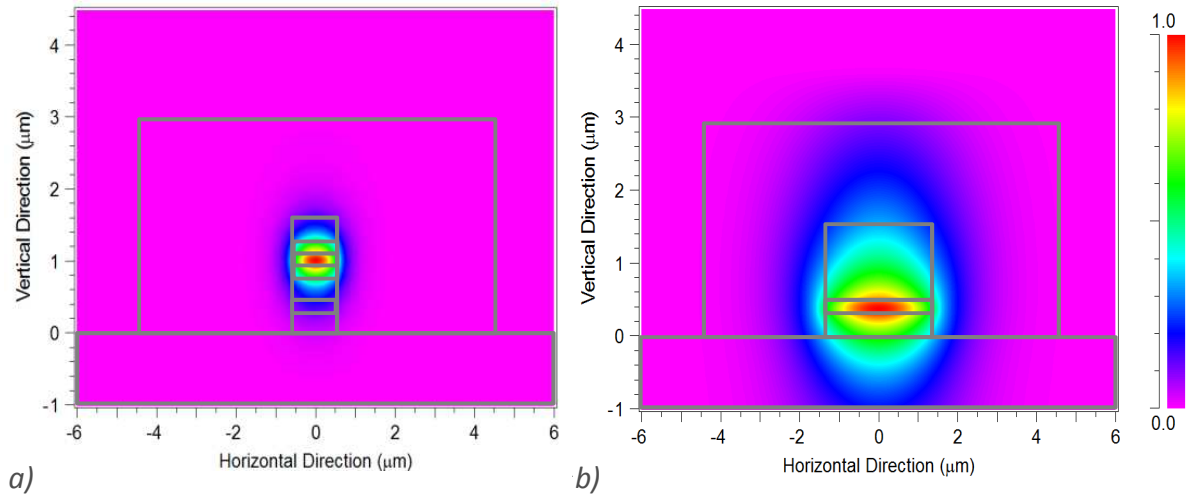

Figure h – Simulation des modes optiques à l'intérieur de la zone active (a) et de la zone passive (b)

Les différentes étapes de fabrication sont ensuite décrites. Le procédé est donc composé de huit étapes majeures :

1. Croissance épitaxiale de la structure verticale
2. Ecriture E-beam de la zone active
3. Gravure Plasma de la zone active
4. Gravure Plasma de la zone passive
5. Re-croissance épitaxiale (MOCVD) au dessus de la zone active
6. Dépôt métallique des contacts
7. Implantation ionique
8. Amincissement de la plaque et dépôt métallique en face

Chaque étape est détaillée et illustrée tout au long de ce chapitre. Une fois les composants procédés, ceux-ci sont montés sur des embases hautes fréquences, nous permettant de réaliser les caractérisations statiques et dynamiques.

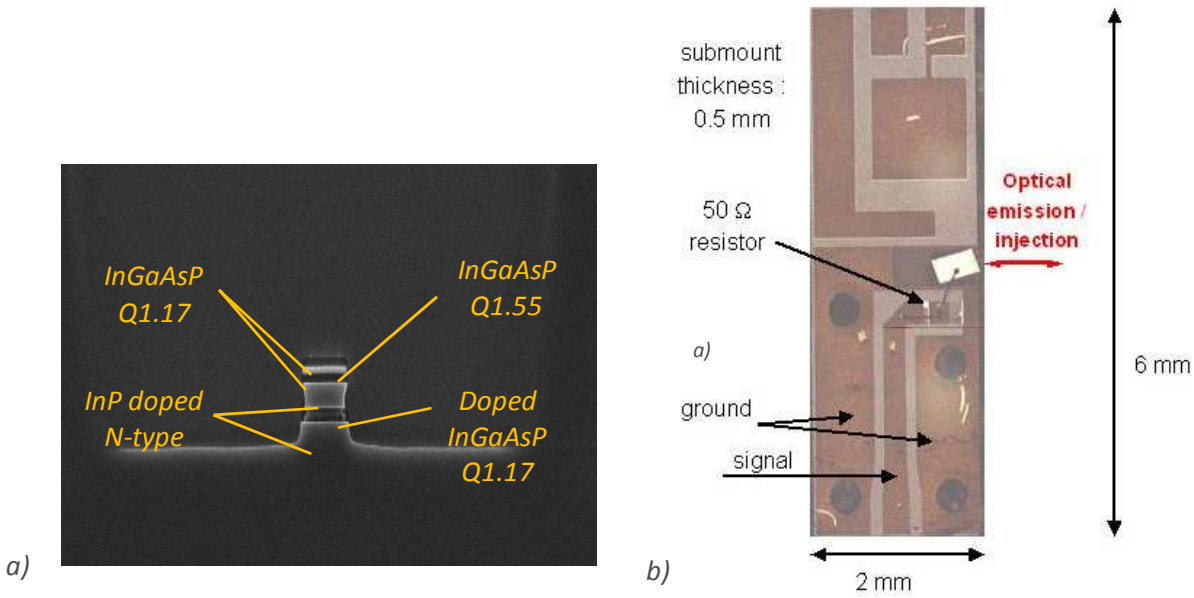

Figure i – Structure « ridge » enterré RSOA avec double « tapers » actif/passif

Pour finir, la maîtrise de la réflectivité des facettes dans ce composant est fondamentale. Une étude détaillée des différentes techniques pour obtenir soit une très forte réflectivité, soit une très faible réflectivité est présentée ainsi que l'impact de celles-ci sur les performances des composants, par exemple l'ondulation du gain. Une étude originale de la réflectivité en fonction de la taille du mode est ébauchée et complétée en Annexe de ce document.

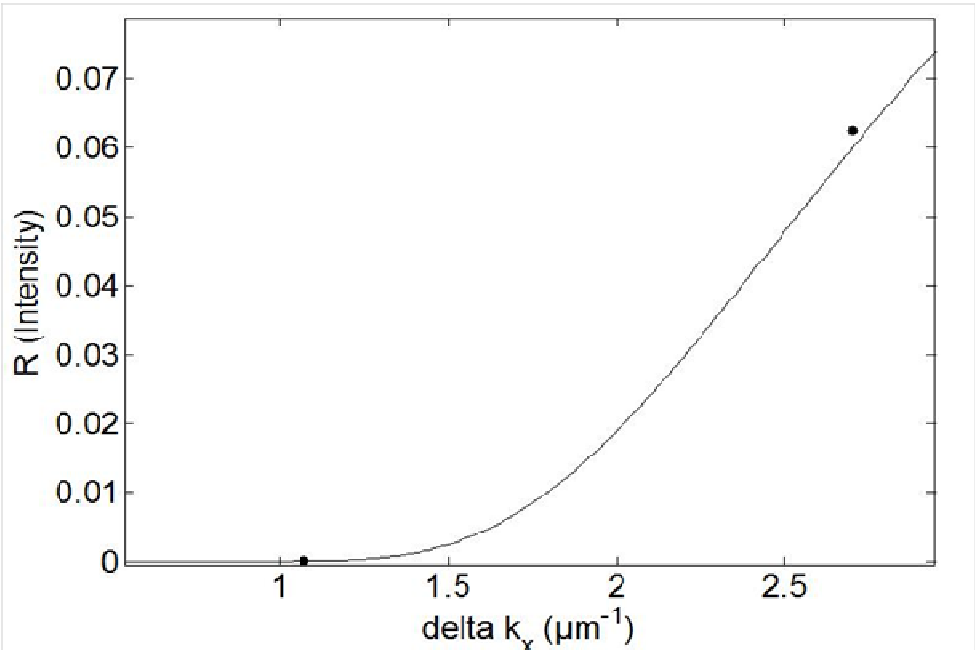

Figure j – Simulation et mesures expérimentales de la réflectivité d'un guide d'onde incliné à 7° en fonction de la variation du vecteur d'onde Δk_x

De l'analyse statique au comportement dynamique, de la modélisation à la caractérisation

Dans le chapitre 3, les différents mécanismes physiques contrôlant la densité de porteur dans le RSOA sont présentés. Le courant de polarisation, les mécanismes de recombinaison radiative et non-radiative ainsi que le phénomène de recombinaison spontanée contrôlent cette densité de porteur. L'équation régissant la densité de porteurs peut donc s'exprimer sous la forme:

$$\frac{dn(z,t)}{dt} = \frac{I(t)}{e.V} - (A.n(z,t) + B.n(z,t)^2 + C.n(z,t)^3) - v_g g_{net}.S(z,t)$$

Où n(z,t) est la densité de porteur, I(t) est le courant de polarisation, e est la charge élémentaire de l'électron, A B et C sont respectivement les coefficients Shockley-Read-Hall, d'émission spontanée et d'Auger, v_g est la vitesse de groupe et S(z,t) est la densité de photon.

Un modèle multi-section incluant deux ondes contra-propagatives caractérisant l'amplification du signal, la compression du gain et l'impact de l'ASE, fut développé. La propagation des ondes optiques est décrite par les équations suivantes:

$$P^+(z+\Delta z) = P^+(z)e^{g_{net}\Delta z}$$
$$P^-(z-\Delta z) = P^-(z)e^{g_{net}\Delta z}$$

Où g_{net} est le gain net.

Certaines approximations furent réalisées dans le but de réduire le temps de calcul de notre modèle. L'influence de l'ASE est un paramètre majeur dans la détermination des conditions à l'équilibre et devient encore plus dominant à faible puissance optique d'injection ou/et fort courant de polarisation. La densité de porteur et de photons furent modélisés le long de la structure RSOA.

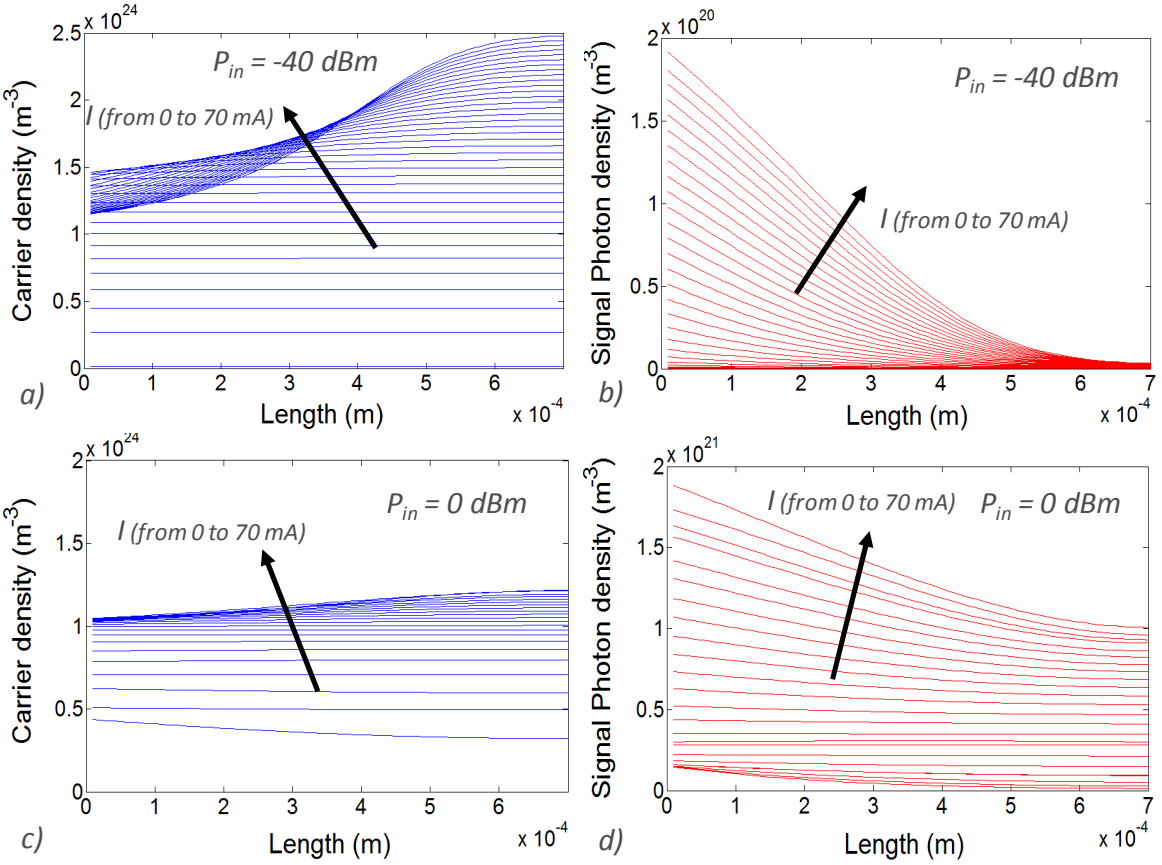

Figure k – Distribution spatiale de la densité de porteur et de photon dans les composants RSOA. (a) et (b) représentant les simulations pour P_{in} = -40 dBm ; (c) et (d) pour P_{in} = 0 dBm

Cette répartition des porteurs se répercute directement sur les performances statiques du composant. L'impact des différents paramètres ajustables lors de la conception et de la fabrication de ces composants sont étudiés. Deux confinements optiques de 20% et 80% sont comparés. La réduction du facteur de confinement optique engendre une réduction du phénomène de « spatial hole burning » comme simulé précédemment. En effet, moins d'émission spontanée est alors guidée dans la zone active réduisant la déplétion des porteurs et laissant ainsi les porteurs à disposition pour l'amplification du signal utile. Les composants ayant un confinement de 20% sont alors considérés car ayant un gain bien supérieur aux composants avec un confinement de 80%.

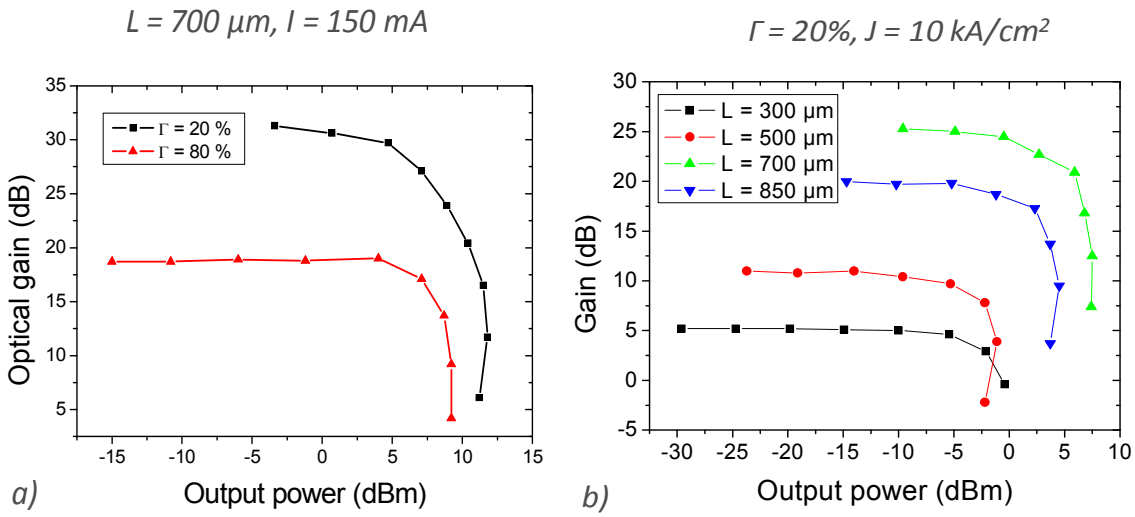

Figure l – (a) Saturation du gain optique en fonction de la puissance de sortie et (b) effet de la longueur de la zone active sur un composant RSOA avec un confinement optique de 20% optical confinement RSOA en fonction de la puissance de sortie

Se concentrant sur une valeur de confinement optique de 20%, nous étudions l'impact de la longueur de la zone active sur les performances statiques du composant. Une longueur de 700 µm est optimum pour un fort gain optique. En effet, deux effets sont alors en compétition l'augmentation du gain avec la longueur de propagation dans la zone active et les forts effets de saturations dans les composants très longs. L'effet de saturation des porteurs en fonction de la longueur de la zone active fut modélisé et confirmé par des mesures d'émissions spontanées.

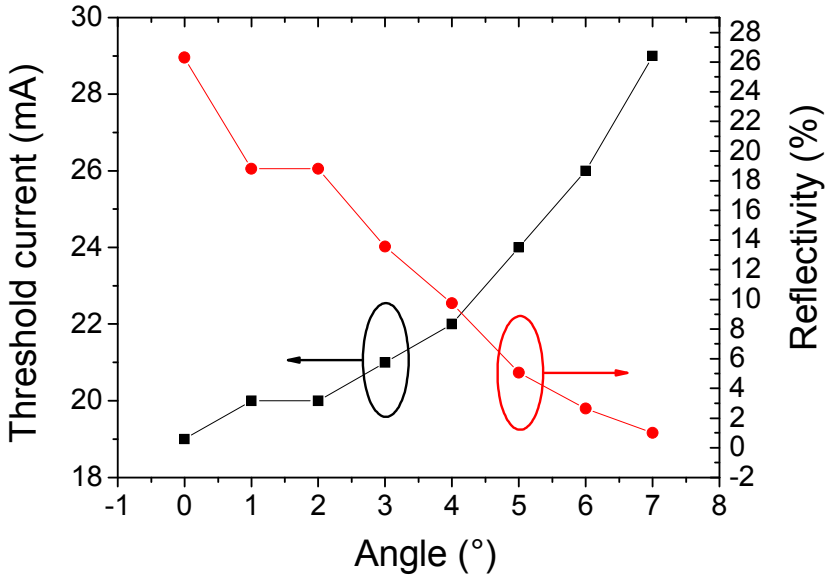

Figure m – Courant de seuil et réflectivitée pour plusieurs guides d'onde actif inclinés

Une dernière étude sur l'impact de la réflectivité des facettes est alors menée. Différents guides d'ondes ayant plusieurs angles d'inclinaison avec le plan de clivage sont réalisés. La mesure

du courant seuil nous permet de remonter à la réflectivité des facettes. Un angle important permet de réduire la réflectivité empêchant ainsi l'effet laser et réduisant l'ondulation du gain.
Ces différentes études nous permettent d'obtenir des composants RSOAs optimisés statiquement et présentant un fort gain de 30 dB et de forte puissance de saturation (7 dBm).

La dynamique des porteurs est ensuite étudiée dans le chapitre 4. La réponse du RSOA sous modulation électrique est alors comparée à celle d'un laser et présente une limitation due à l'absence de résonnance photon-électron. La modulation électro-optique de ce composant se comporte comme un filtre passe-bas avec une fréquence de coupure dépendante essentiellement du temps de vie des porteurs. La réduction de ce temps de vie des porteurs permet l'augmentation de la bande passante, il est donc nécessaire d'analyser et de comprendre ce paramètre dans le but de le réduire. Une première approximation du temps des porteurs est obtenue et se présente sous la forme :

$$\frac{1}{\tau_{eff}} = A + B.n + C.n^2 + \Gamma \times a \times S \times v_g$$

Où le gain différentiel est défini par $a = \frac{\partial g}{\partial N}$ et S est la densité total de photon incluant le signal et l'émission spontanée amplifiée.

Cette approximation nous montre que ce temps de vie dépend essentiellement des taux de recombinaison spontanée et non-radiative, ainsi que du taux de recombinaison stimulé. Ce paramètre sera donc inhomogène le long du composant et dépendra des conditions d'opération. Il est donc important de savoir quels mécanismes physiques régissent celui-ci et dans quelles conditions.

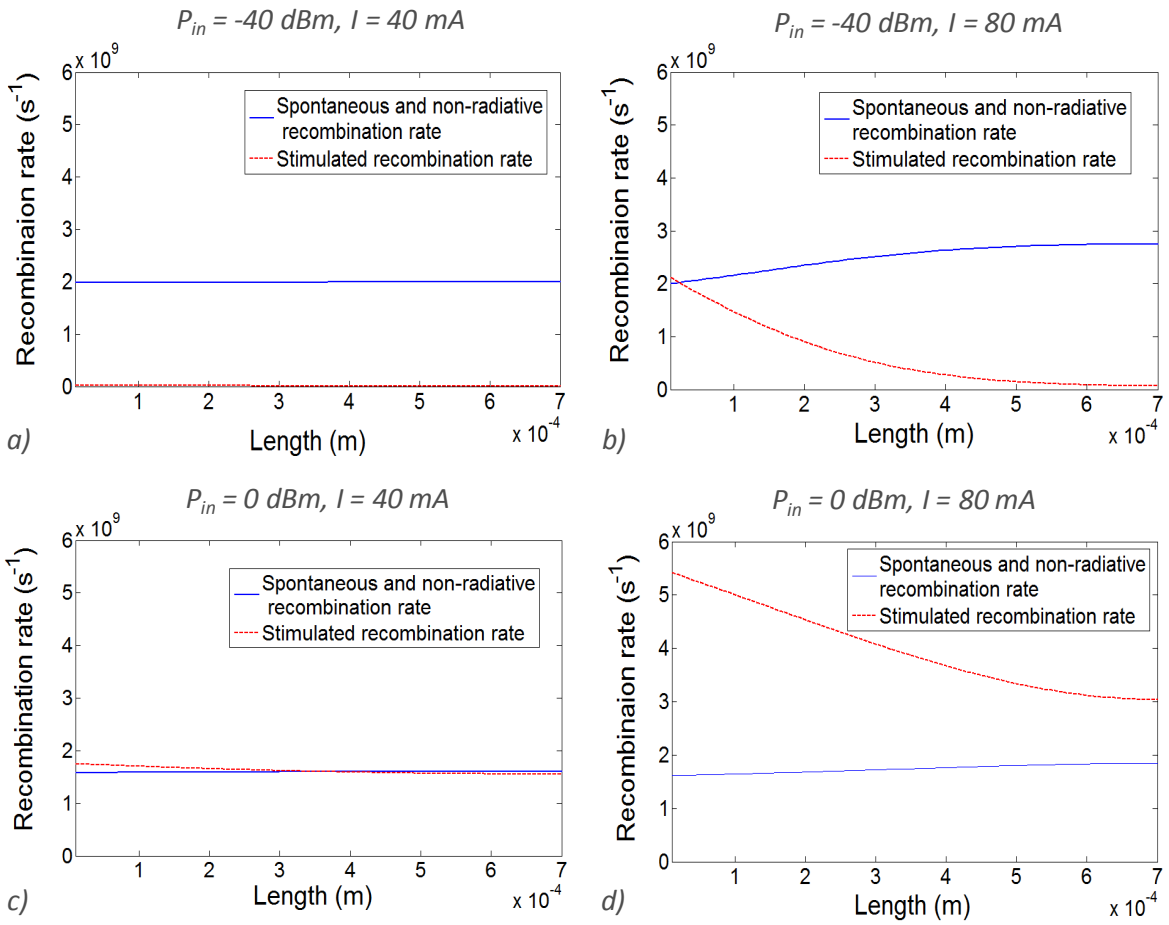

Figure n – Distribution spatiale du taux de recombinaison spontanée et non radiative comparé au taux d'émission stimulé dans des composants RSOA long de 700 µm pour différentes conditions d'opération. (a) P_{in} = -40 dBm et I = 40 mA, (b) P_{in} = -40 dBm et I = 40 mA, (c) P_{in} = 0 dBm et I = 40 mA et (d) P_{in} = 0 dBm et I = 80 mA

Le temps de vie est alors modélisé en fonction de la répartition spatiale ainsi que du courant de modélisation et de la puissance optique d'injection.

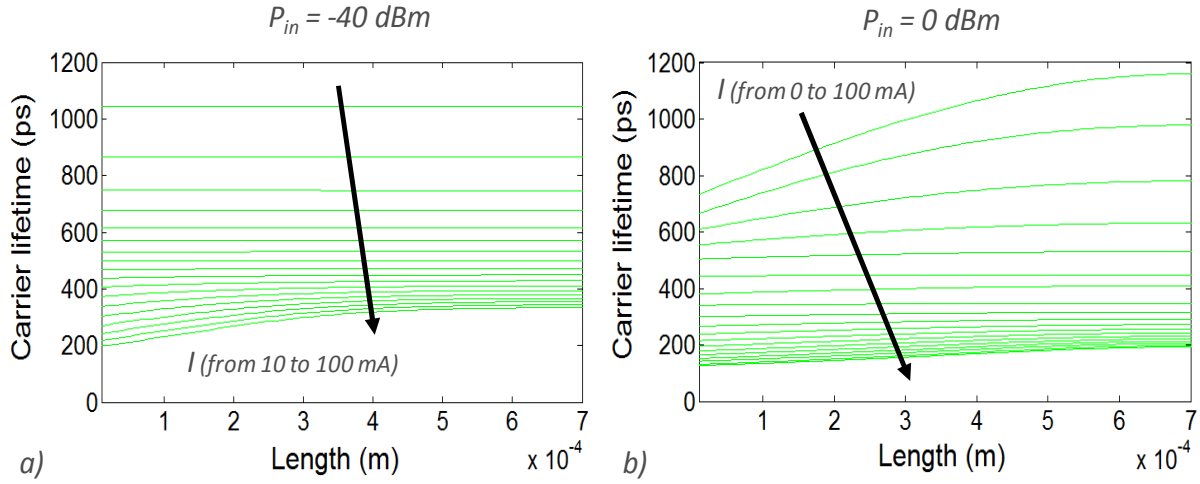

Figure o – Modélisation du temps de vie des porteurs le long d'un composant RSOA de 700 µm à (a) faible (P_{in} = -40 dBm) et (b) forte (P_{in} = 0 dBm) puissance optique d'injection

Ce temps de vie est alors relié au calcul de la bande passante de modulation. Les simulations sont comparées à des mesures de bande passante et présentent une bonne accordance sur plusieurs GHz. A partir des mesures et simulations de la réponse en modulation du RSOA, la bande passante à -3 dB peut être extraite et la mesure est comparée à la théorie. Pour ces simulations, deux méthodes sont adoptées. La première consiste à prendre un temps de vie des porteurs moyen sur toute la longueur du composant. La seconde consiste à prendre la valeur la plus faible correspondant à la valeur en entrée du RSOA où la déplétion des porteurs est la plus forte.

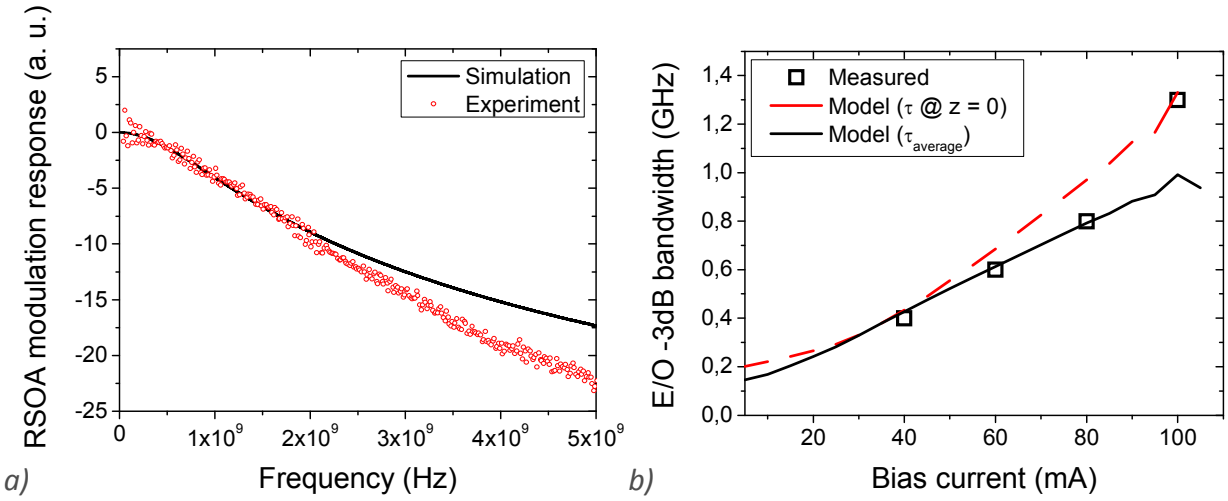

Figure p –(a) Bande passante Electro-optique du RSOA en function de la fréquence pour I = 80 mA (b) Bande passante de modulation à -3 dB en fonction du courant de polarisation pour une longueur de 700 µm de zone active

La première approche correspond aux valeurs obtenues par l'expérience sur une plage de 0 à 80 mA. Cependant à partir de 80 mA, la bande passante augmente plus rapidement. Ceci est dû aux conditions de forte saturation dans le composant et le temps de vie en sortie du composant semble plus approprié. Sous des régimes à forte saturation, des problèmes de convergence du modèle se posent. Cette analyse ne pourra pas être poussée au dessus de courants supérieur à 100mA..

Comme démontré dans le chapitre 3, de forts effets de saturation des porteurs sont obtenus pour des composants ayant une longue zone active. Nous avons donc décidé de tirer avantage de cette forte déplétion pour réduire le temps de vie des porteurs.

Une première comparaison est réalisée entre des RSOAs avec une zone active de 500 µm et de 850 µm. Des mesures d'émission spontanée nous permettent de confirmer les effets de saturation de la densité de porteur et sont validées par des mesures de spectre optique.

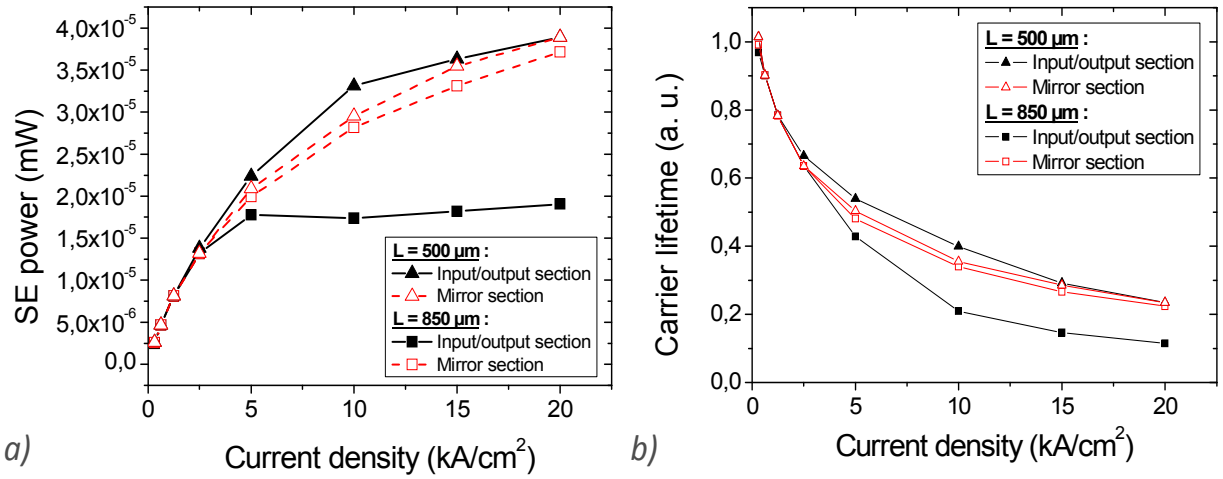

Figure q – (a) SE power and (b) effective carrier lifetime on both facets of 500µm and 850µm long RSOA as a function of the current density.

Des mesures de bande passante sont alors réalisées en fonction de la longueur et confirment la réduction du temps de vie des porteurs dans des composants plus long. Une bande passante de modulation à l'état de l'art est obtenue (au dessus de 3GHz).

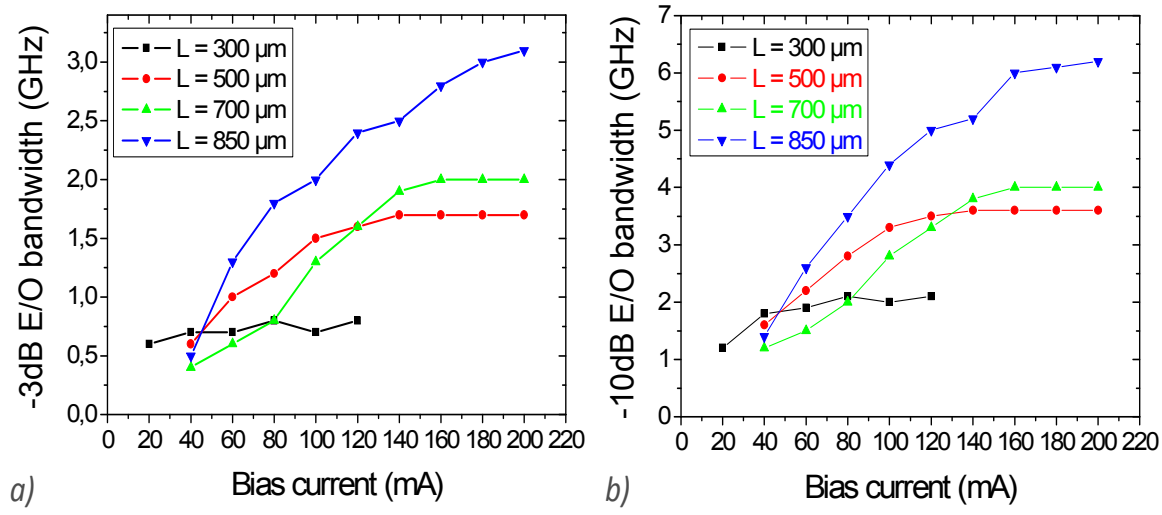

Figure r – Bande passante de modulation à (a) -3 dB et (b) -10 dB pour plusieurs longueurs de RSOA en fonction du courant injecté.

Comme nous l'avons démontré, le temps de vie des porteurs dépend fortement des conditions d'opération. En effet, les différents mécanismes régissant celui-ci deviennent plus ou moins prépondérants en fonction des différents points de fonctionnement. Nous analysons donc en premier les états d'une modulation digitale en ON-OFF-Keying à l'équilibre.

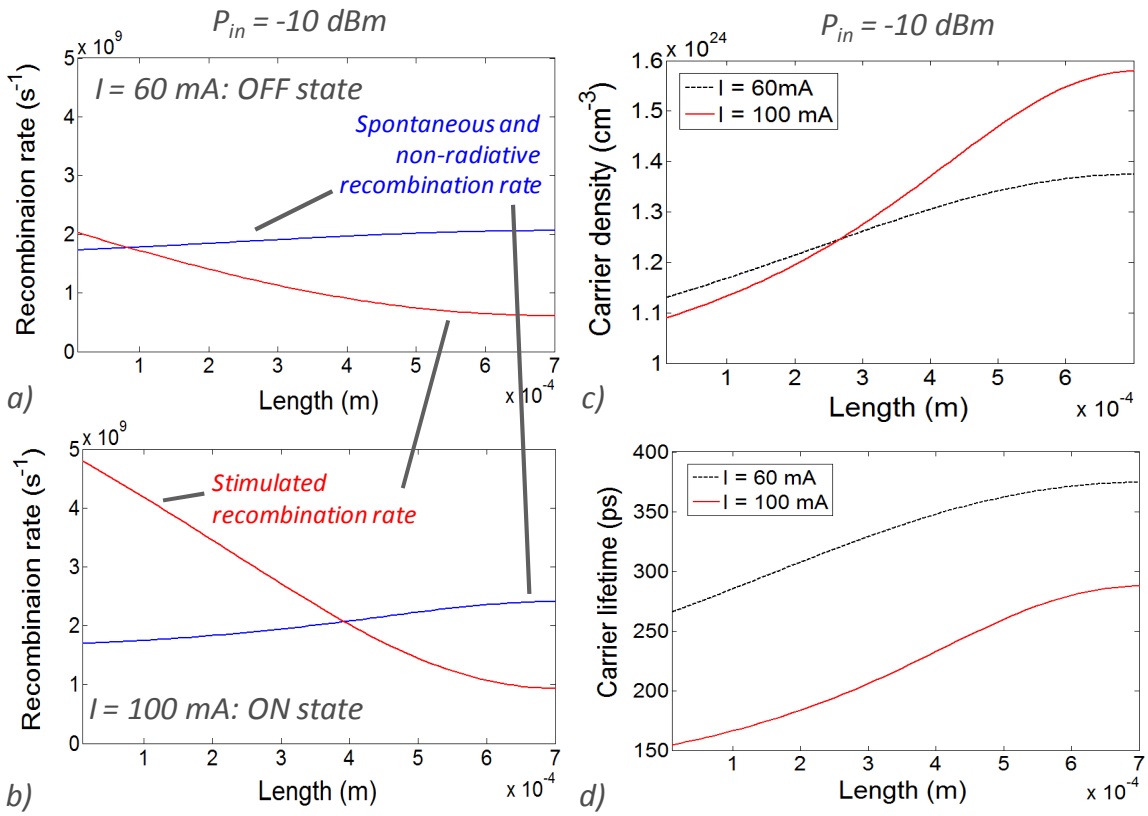

Figure s – Comparaison des mécanismes de recombinaison (a) à l'état "OFF" (b) à l'état "ON" et (c) représentation de la densité de porteurs , (d) du temps de vie des porteurs dans ces deux états. La puissance optique d'injection est de -10 dBm.

Les temps de descente et de montée sont ensuite analysés. Le temps de montée est plus rapide pour une densité de photons élevée. Une forte puissance optique d'injection ainsi qu'un courant de polarisation élevé seront donc bénéfique à l'accélération de celui-ci. L'analyse du temps de descente est plus compliquée. En effet, les mécanismes régissant ce temps de descente alternent en fonction du temps. On peut deux temps de descente différents. Ce phénomène fut décrit, analysé et confirmé par des mesures expérimentales.

L'influence de plusieurs paramètres tels que la longueur, la puissance optique d'injection et la vitesse de modulation est aussi analysée pour une modulation digitale.

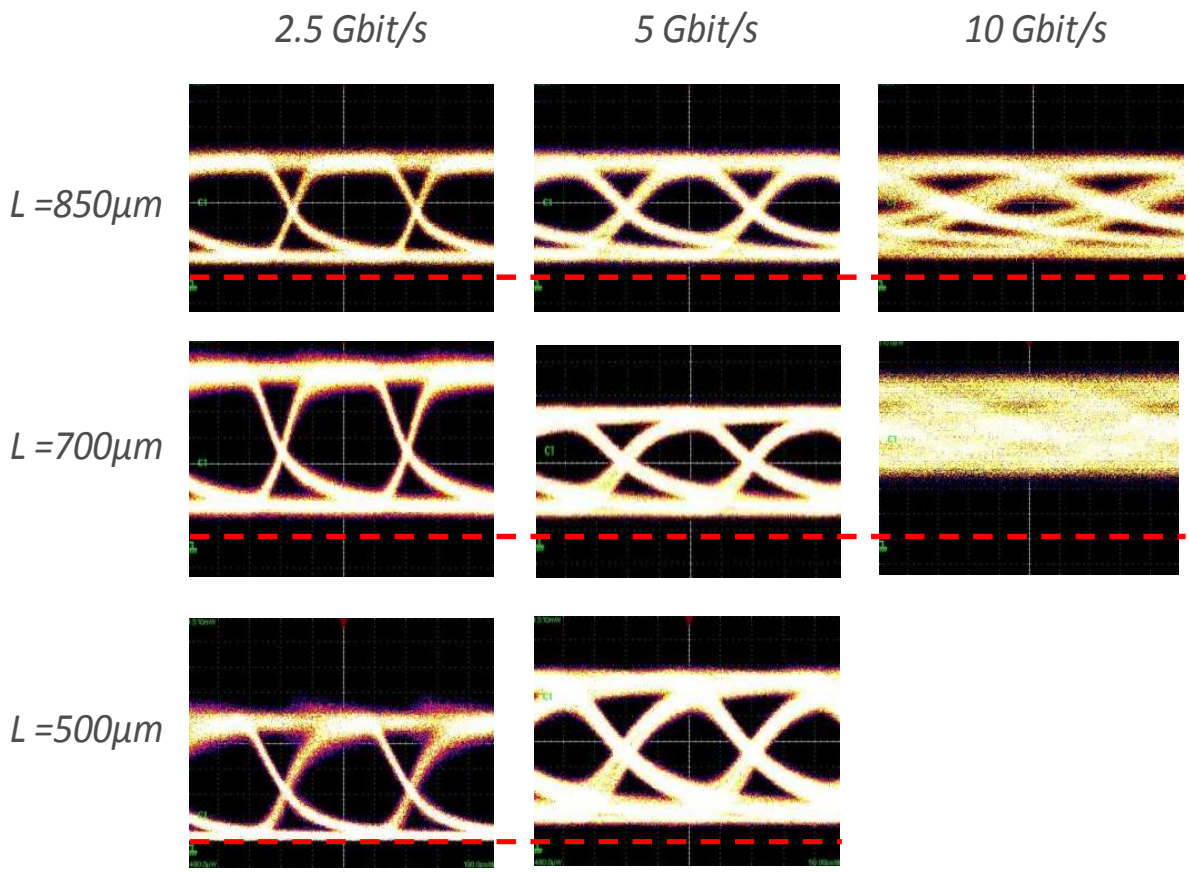

Figure t – Diagramme de l'œil à différent débit pour des RSOAs de longueur variable (500 à 850 µm). La puissance reçue est de l'émission spontanée amplifiée pure.

Finalement, un compromis entre l'optimisation statique et dynamique doit être considéré pour une implémentation système.

Un composant comprenant plusieurs sections pour une meilleure optimisation

L'utilisation de RSOA multi-électrode peut être avantageuse pour surmonter plusieurs limitations.

En effet, le gazouillis, dit « chirp » en anglais, dans ces composants représente une limitation majeure vers la montée en débit et la propagation sur de plus longues distance.
Tout d'abord une analyse théorique est proposée. Le facteur d'Henry peut s'écrire sa la forme:

$$\alpha_H = 2P\frac{\partial \Phi}{\partial P}$$

Où $\frac{\partial \Phi}{\partial P}$ est la variation de phase sur la variation de puissance optique.

Dans un composant à deux sections, une section est généralement soumise à une modulation de courant alors que la seconde reste sous une injection électrique constante. Ceci

nous amène à deux comportements différents en fonction de la section considérée. L'expression générale peut être adaptée en fonction la section observée. Si la section est sous courant de polarisation constant et reçoit une puissance optique modulée alors le facteur d'henry peut s'exprimer sous la forme :

$$\alpha_H = \alpha' \frac{dG/dP_{in}}{1 + dG/dP_{in}}$$

Où P_{in} est la puissance optique injectée dans le SOA.

Ors si la section est sous courant modulé et reçoit une puissance optique constante alors le facteur d'henry s'écrit :

$$\alpha_H = \frac{\alpha'}{\Gamma a \Delta NL.10log_{10}.e}\left(\frac{\partial G}{\partial N}\right)$$

Les définitions des différents paramètres sont présentées dans le chapitre 5.Ceci nous permet d'obtenir un gazouillis de signe opposé dans chacune des sections compensant ainsi le gazouillis total.
Cette analyse théorique fut complétée par une analyse expérimentale. L'impact de chaque section sur la déviation en fréquence et le taux d'extension est mesuré.

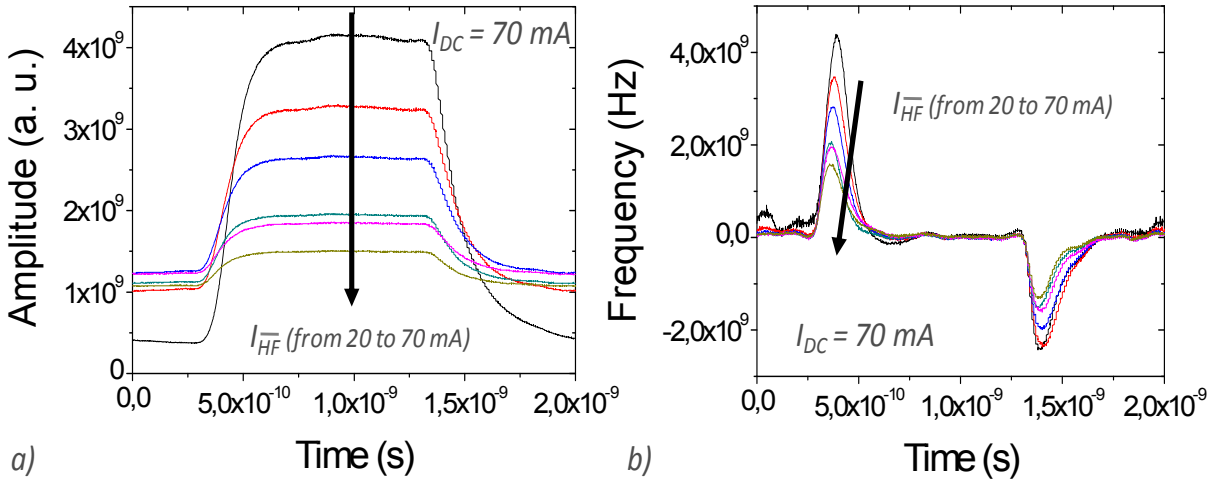

Figure u – Réponse en amplitude (a) et fréquence (b) pour un composant RSOA à 2 sections avec le courant de polarisation de l'électrode SOA1 comme variable.

Dans les RSOAs classiques, une réduction du gazouillis se traduit par une réduction du taux d'extension et un compromis doit être considéré.
L'utilisation de composants RSOA à deux électrodes nous permet d'obtenir un meilleur taux d'extension tout en maintenant une déviation en fréquence faible.

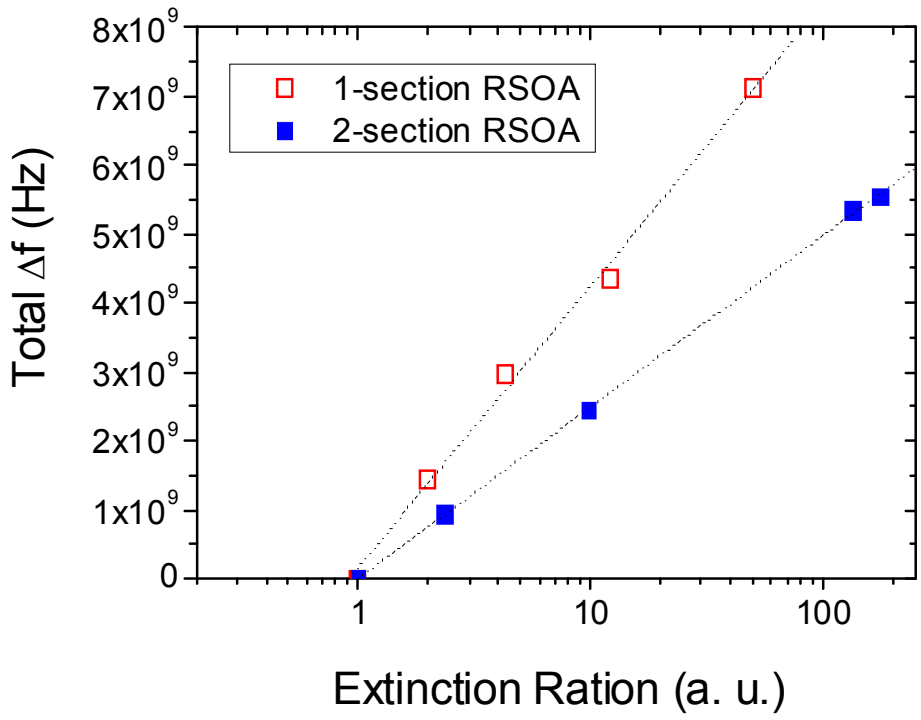

Figure v – Gazouillis total en fonction du taux d'extinction

Des simulations de la densité de porteur furent réalisées dans le but de déterminer une configuration optimum d'utilisation de ces composants. Une modulation de l'électrode avant avec un faible courant de polarisation ainsi qu'un courant de polarisation constant et fort sur l'électrode du côté miroir sont idéales pour la réduction du gazouillis.

Le gazouillis étant bien plus important dans les composants à fort confinement optique, une première étude avec les composants à 80% est réalisée. Pour une transmission sur 50 km à 2.5 Gbit/s, une amélioration de la sensibilité de 3 dB est obtenue.

Ces composants bi-électrode furent aussi évalués pour les réseaux de types radio sur fibre (RoF). En effet, il a été démontré que ces composants présentent un gain de liaison inférieur à celui des lasers directement modulé [5].

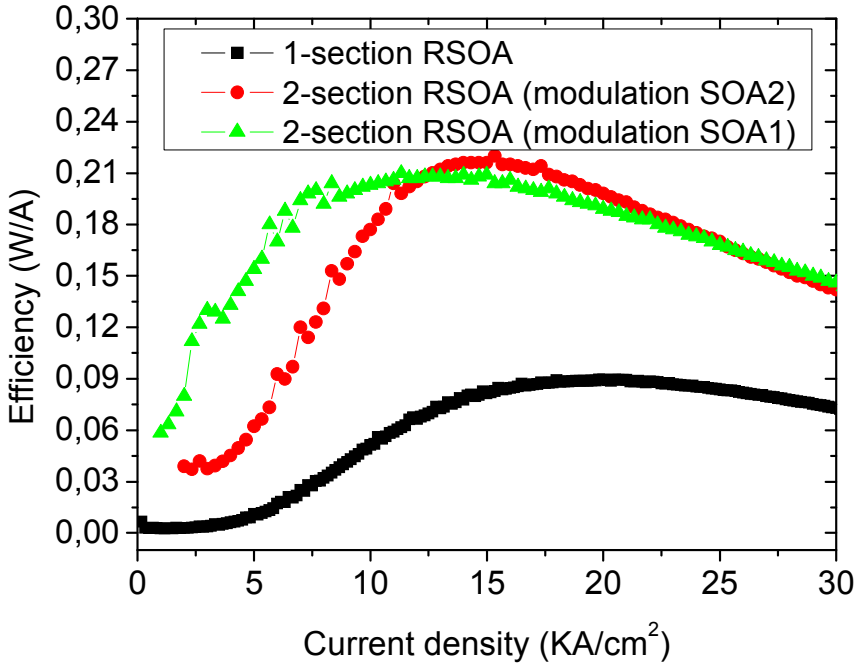

Figure w – Efficacité d'un RSOA à une et deux sections.

L'utilisation de ces composants à deux sections permet l'augmentation de l'efficacité interne du composant. Une efficacité interne de 0.09 W/A est mesurée pour les RSOAs à une section et une efficacité interne de 0.2 W/A pour les composants à deux sections. Le gain de liaison dépendant directement de cette efficacité, celui-ci est alors très fortement augmenté.

$$G_{hyp} = \frac{P_{PD}}{P_{signal}} = \left(\frac{R_{PD} \cdot {\eta_{PD}}^2}{R_{RSOA}} \times T_{RF\_RSOA} \times T_{RF\_PD} \times T_{opt}^2 \right) \times {\eta_{RSOA}}^2$$

Où η_{RSOA} est l'efficacité interne d composant.

Une analyse théorique est comparée aux valeurs expérimentales et une augmentation du gain de liaison de 10 dB est mesurée avec une modulation de l'électrode du côté miroir du composant bi-électrode.

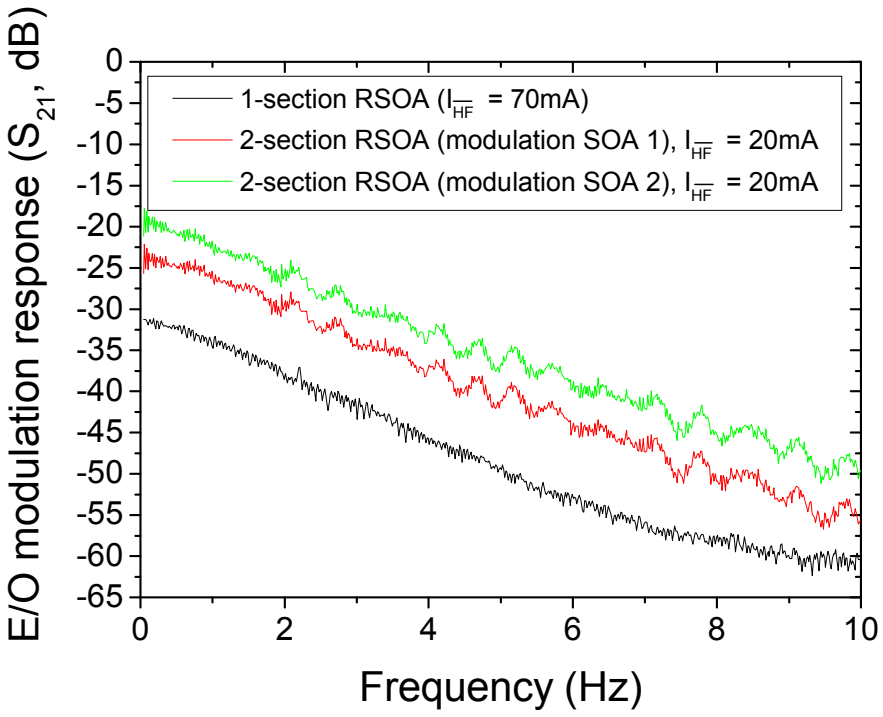

Figure x – Réponse en fréquence d'un RSOA sous modulation d'un signal électrique pour une et deux électrodes

Les RSOAs bi-électrode présentent donc un avantage pour les différentes raisons énoncées précédemment néanmoins une évaluation du composant dans un environnement système doit être faite pour confirmer ce fort potentiel.

De la puce aux systèmes

Le chapitre 6 est consacré à l'application des différents RSOAs optimisés dans différentes approches réseaux. Une nouvelle utilisation des RSOAs en tant que source indépendante à la longueur d'onde pour les réseaux d'accès et de type RoF a récemment donné un regain d'intérêt à la recherche sur ces composants.

Plusieurs approches sont possibles pour les réseaux d'accès. Dans ces travaux, nous nous concentrerons sur une alimentation du RSOA par une source laser externe.
En plaçant le laser au niveau du nœud de controle et en utilisant les composants optimisés (fort gain et forte puissance de saturation), nous avons démontré un budget optique de l'ordre de 36 dB et une transmission à 2.5 Gbit/s sur huit longueurs d'onde pour une distance de 45 km. Ce fort budget optique peut être notamment utilisé pour obtenir des connexions partagées notamment en utilisant le multiplexage temporel (TDM).

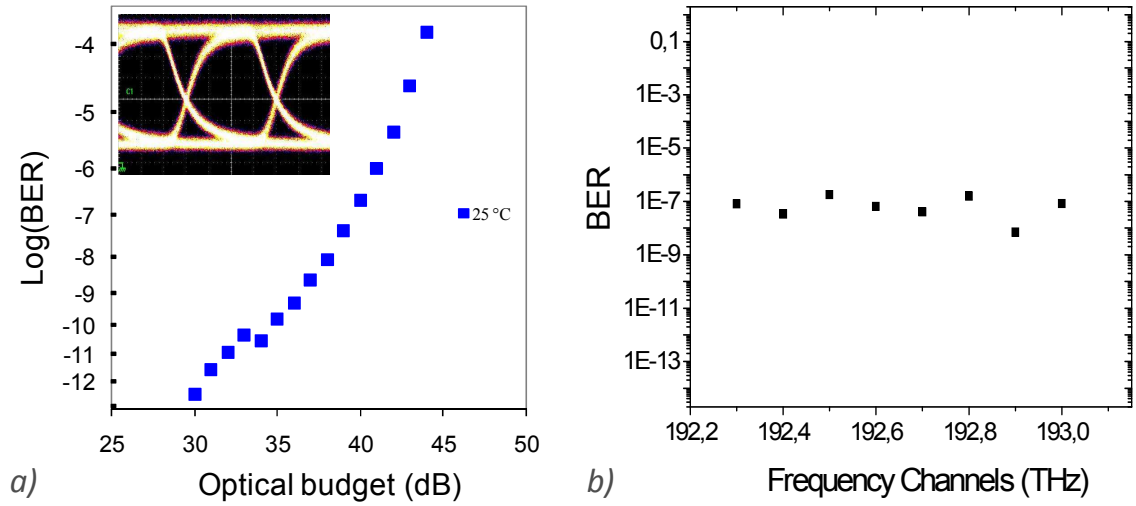

Figure y – (a) Taux d'erreur en fonction du budget optique. Inset: diagramme de l'œil à 2.5 Gbit/s pour un courant de 90 mA et une puissance optique de -10 dBm (b) taux d'erreur pour différentes longueurs d'onde pour un budget optique de 40 dB.

Dans une configuration similaire, l'utilisation de composants bi-électrode nous permet de réaliser la première transmission sur 100 km à 2.5 Gbit/s en dessous de la limite FEC (code correcteur d'erreur considérant un BER de 10^{-4}).

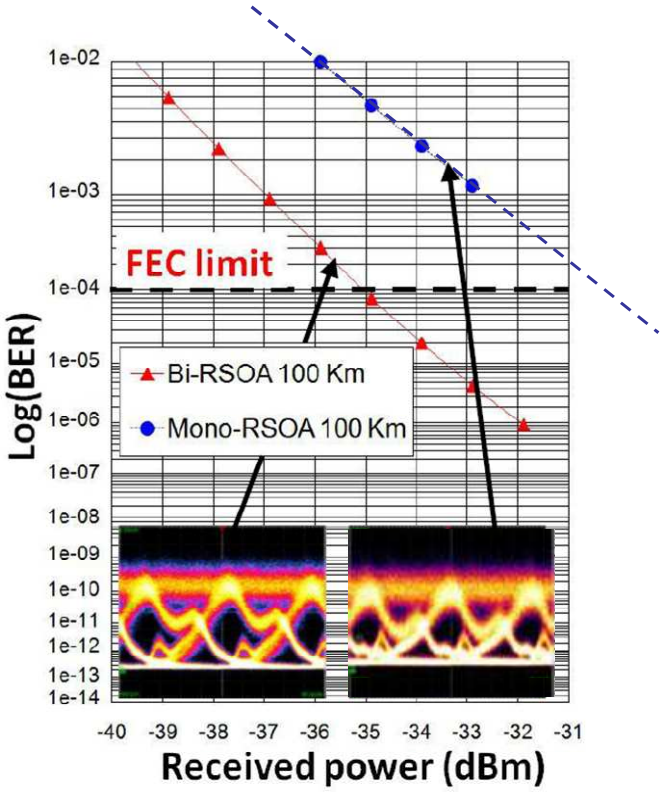

Figure z – Comparaison du taux d'erreur en fonction de la puissance reçue sur le récepteur pour un composant RSOA à 1 et 2 électrodes sur 100 km à 2.5 Gbit/s

Comme étudié dans le chapitre 4, les composants RSOAs ont une bande passante limitée due à l'absence de résonnance dans la cavité ainsi qu'un temps de vie des porteurs élevés. Une

modulation à 10 Gbit/s est néanmoins nécessaire pour envisager une l'évolution continue des systèmes à fibre optique et ceci bien sur à un moindre coût. La réduction du temps de vie des porteurs a permis d'obtenir la première modulation directe à 10 Gbit/s sans aucun traitement électronique (actif ou passif) et en dessous de la limite FEC. Cependant les distances restent encore limitées à quelques kilomètres.

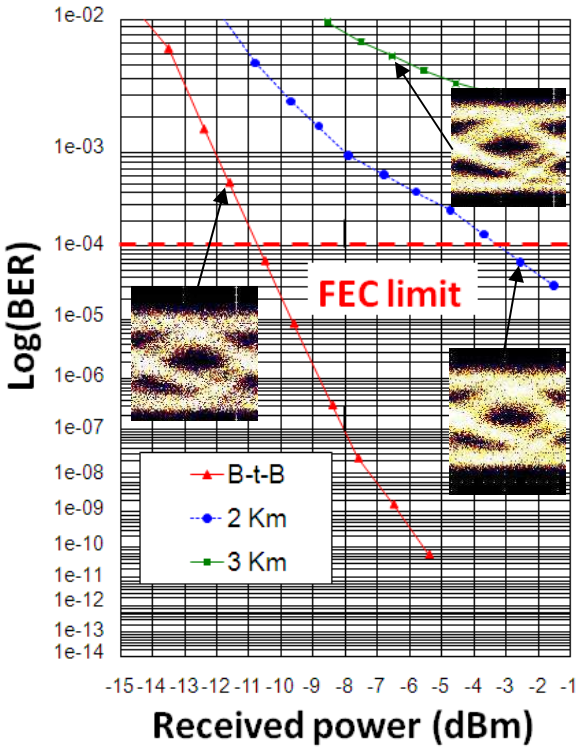

Figure α – Taux d'erreur en fonction de la puissance reçue pour une longueur de zone active de 850 µm modulé à 10 Gbit/s

Des émetteurs indépendant à la longueur d'onde sont aussi essentiels pour les réseaux de type RoF. Un fort gain de liaison, un faible bruit et de faibles non-linéarités furent démontrés pour ces nouveaux RSOAs confirmant leur compatibilité avec de genre de réseaux [6]. Une liaison de 20 km de fibre optique fut démontrée pour le transport de signaux radio et des valeurs EVM (error vector magnitude : taux d'erreur) en dessous de 4% confirme le bon comportement des composants.

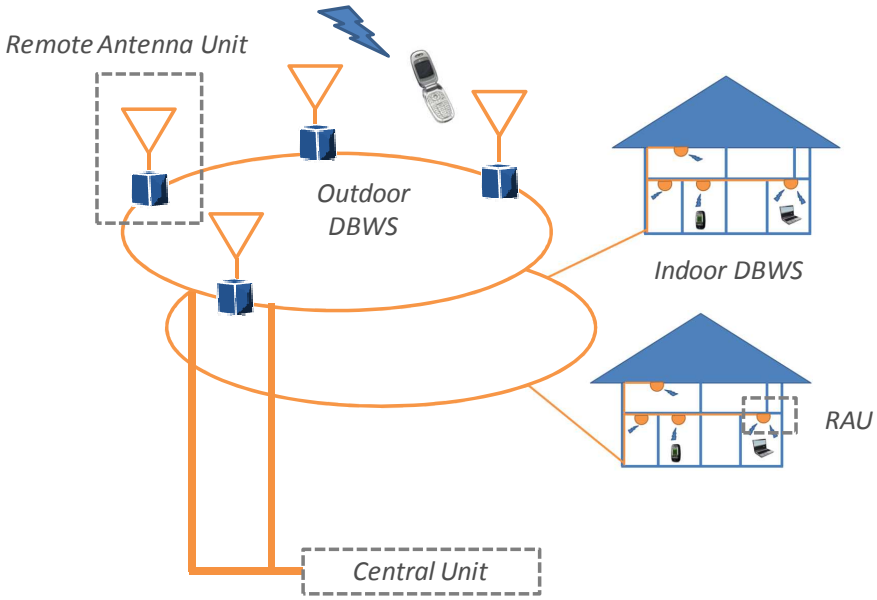

Figure β – Architecture pour les futures générations de systèmes distribuées sans fils en intérieur et en extérieur

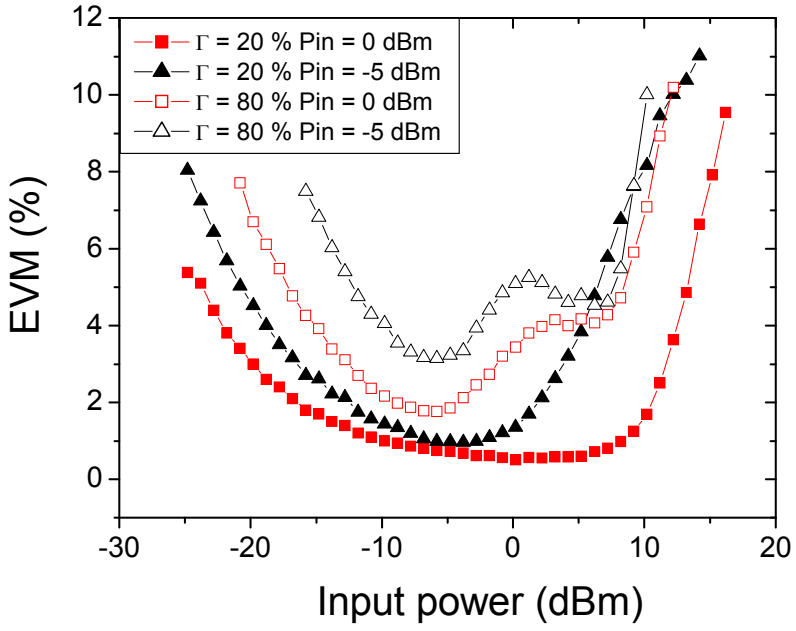

Figure γ – Valeurs EVM en fonction de la puissance électrique RF d'entrée dans une configuration en b-t-b

Une portée radio des antennes de l'ordre de 440m peut être calculée en fonction des performances systèmes de ces composants. Néanmoins le gain de liaison restent inférieur à ceux d'autres composants tel que les lasers directement modulés. Comme démontré au chapitre 5, l'utilisation de RSOA bi-électrode permet l'augmentation du gain de liaison induisant une portée radio calculée de plus de 470m.

Conclusion

La distance, le temps ou encore l'indisponibilité des moyens de communication ont souvent limité la capacité de l'homme à échanger, et aujourd'hui l'intensification de la demande de l'outil communicationnel ne faiblit pas. La coloration des fibres optiques ne répond pas seulement à une demande d'augmentation des débits mais permet en outre un changement complet des usages. Sans révolutionner la communication, elle amplifie les possibilités d'échange. A ce titre, les démonstrations d'images 3D, la vidéoconférence ou la réalité augmentée en devenir sont quelques exemples illustrant ce que pourraient être les futurs usages de l'industrie, de la santé ou des particuliers. Ces utilisations nécessitent à la fois immédiateté et omniprésence du support de l'information. Le RSOA satisfait entièrement à ces exigences.

Néanmoins les faibles performances de ce composant furent jusqu'à présent une des barrières majeures à son développement. Ces travaux de doctorat se focalisèrent donc sur l'optimisation de ces composants pour les différentes applications potentielles telles que les réseaux d'accès et la RoF.

Une analyse théorique, la modélisation, une conception optimisée et la caractérisation de plusieurs paramètres physiques nous a permis d'obtenir des performances statiques et dynamiques à l'état de l'art.

	2007 (Γ = 20%)	**2009** (Γ = 20%)	**2011** (Γ = 20%)
Gain (dB)	20	30	25
Saturation Power (dBm)	4	10	5
Optical Bandwidth (nm)	27	49	45
3-dB ASE bandwidth (GHz)	1.1	2	3
Polarization dependence (dB)	0.5	0.8	0.8
Noise Figure (dB)	10	8	8

Table a – Technical characteristics and evolution of RSOA during this work

Ces composants optimisés furent utilisés dans différents types de réseaux et montrent un potentiel réel en tant qu'émetteur indépendant à l longueur d'onde. De nouveaux records furent démontrés comme une transmission sur 100 km à 2.5 Gbit/s ou une transmission à 10 Gbit/s. Néanmoins les distances pour des débits élevés restent limitées et de nouveaux défis doivent être surmontés.

La course à l'augmentation du débit a commencé depuis plusieurs années. La fibre optique est d'ores et déjà le support de nombreux modes de télécommunications. Mais du fait de son

actuelle utilisation, elle est victime d'un manque cruel de disponibilité. Or, toute technologie au service de l'échange se doit de contourner cet écueil de latence. L'évolution des ces technologies FTTH reste mystérieuse. Une analyse technico-économique évaluant les différentes technologies et le compromis entre le coût et les performances systèmes déterminera le futur des réseaux d'accès. La seule certitude est l'accélération de l'outil communicationnel avec par exemple Google annonçant son projet de connections à 1 Gbit/s à Kansas city, Cisco prédisant le même débit pour les utilisateurs finaux (à la maison) d'ici 2016 ou encore les premiers réseaux déployés en Corée se basant sur la technologie RSOA.

Dès lors, l'instantanéité de l'échange anticipant l'actuelle demande pourrait bien devancer nos capacités à l'exploiter. Un portail coloré pour la créativité de l'homme s'ouvre sur un éventail infini de possibilités. La généralisation de la coloration des réseaux par une technologie pervasive telle que le RSOA servira la diffusion des informations partout et en tout lieux.

L'accélération de la communication donne l'illusion d'une bonne communication qui serait l'information pure réalisant la transparence entre émetteur et récepteur et réduisant, ainsi, les différences et annulant les différends. Cependant, comme l'exprimait le talentueux journaliste Edouard M. Murrow qui avait pleine conscience de la « couleur » des mots : *« Le plus récent ordinateur peut simplement compliquer, en terme de vitesse, le problème le plus ancien dans les relations entre les êtres humains, si bien qu'à la fin, le communicateur demeurera confronté au vieux problème de quoi dire et de la façon de le dire. »*

References

[1] Portail de l'Autorité de régulation des communications électroniques et des postes : http://www.arcep.fr

[2] Portail d'Orange : http://actu.orange.fr/high-tech/deploiement-fibre-optique-le-gouvernement-veut-mettre-les-bouchees-doubles_96151.html

[3] "L'Etat s'engage à fournir le très haut débit à tous", Marie Cécile Renault, Le Figaro, mardi 19 janvier 2010

[4] G. P. Agrawal, "Fiber-optic communication systems", Third Edition, John Wiley & Sons Inc., Chap. 1, 2002, pp. 2-4

[5] David Wake, Anthony Nkansah, Nathan J. Gomes, Guilhem de Valicourt, Romain Brenot, Manuel Violas, Zhansheng Liu, Filipe Ferreira and Silvia Pato, "A Comparison of Radio over Fiber Link Types for the Support of Wideband Radio Channels", Journal of Lightwave technology, Vol. 28, No. 16, March 2010, pp. 2416-2422

[6] G. de Valicourt, M. A. Violas, D. Wake, F. van Dijk, C. Ware, A. Enard, D. Maké, Zhansheng Liu, M. Lamponi, G. H. Duan and R. Brenot, "Radio over Fibre Access Network Architecture based on new optimized RSOA Devices with large modulation bandwidth and high linearity", Microwave Theory and Techniques, Vol. 58, No. 11, October 2010, pp 3248-3258

List of figures

List of Tables

List of abbreviations

AC: alternating current
AM: amplitude modulation
APD: Avalanche Photo-Diode
ASE: amplified spontaneous emission
AR: Anti reflective
AROME:
AZ: Active Zone
AWG: Arrayed Waveguide Grating

BER: Bit Error Rate
BL: Bit rate-distance product
BPON: Broadband PON
BtB: back-to-back

CAPEX: cost capital expenditures
CB: conduction band
CO: central office
CU: Central Unit
CW: continuous wave

DAS: distributed antenna system
DBWS: distributed broadband wireless system
DC: direct current
DFB: Distributed feed-back
DML: Directly modulated laser
DSF: dispersion-shifted fibre
DSL: Digital Subscriber Loop (or line)

EAM: electro-absorption modulator
ECL: external cavity laser
EDFA: Erbium Doped Fibre Amplifier
E/O: electro-optical
EPON: Ethernet PON
ER: extension ratio
EVM: Error Vector Magnitude

FEC: Forward Error Correction
FGL: external cavity fibre grating laser
FP: Fabry-Perot
FUTON: Fibre-Optic Networks for Distributed Extendible Heterogeneous Radio Architectures and Service Provisioning

GEPON: Gigabit Ethernet PON
GPON: Gigabit Passive Optical Network

HF: high frequency
HR: High reflective

IF: intermediate frequencies
IMD: intermodulation distortion point

LSHB: Longitudinal spatial hole burning

MZ: Mach Zehnder

NF: Noise floor
NGPON: Next Generation PON
NRZ: No Return to Zero

OB: optical budget
OC: optical circulator
OFDM: Orthogonal frequency-division multiplexing
ONU: Optical Network Unit

PD: Photodiode
PIC: Photonic Integrated Circuits
PON: Passive Opitcal Network
P2P: point-to-point
PRBS: Pseudo-Random Binary Sequence

RAU: remote access units
RBS: Rayleigh Back-Scattering
RF: radio frequency
RIN: Relative Intensity Noise
RN: remote node
R-o-F: Radio-over-Fibre
RoFnet: radio over fibre network
RSOA: Reflective SOA
RZ: Return to Zero

SCM: subcarrier multiplexing
SCH: separate confinement heterostructure
SE: spontaneous emission
SFDR: Spurious-Free Dynamic Range
SHB: Spatial Hole Burning
SM: single mode
SMF: single mode fibre
SOA: semiconductor amplifier
SPM: self-phase modulation
SSC: spot-size converter

TDM: Time-Division Multiplexing
TW-SOA: Travelling Wave SOA

VB: valence bands

WDM: Wavelength-Division Multiplexing

Introduction

This manuscript presents an overview of the achievements done during this PhD in the field of Reflective Semiconductor Optical Amplifiers. RSOAs promise to take a key role in the evolution of optical communication networks: despite the development of SOA devices having a sluggish start compared to that of fibre amplifiers, the recent progress in optical semiconductor fabrication techniques and device design has pushed the performance of RSOAs well beyond the state of the art. So RSOA looks like the perfect candidate for the next generation of colourless source in reflective Optical Network Units (ONU) which is the interface between the optical fibre and the customers.

This introductory chapter discusses the past history, the general context and the evolution of SOA and RSOA with the development of optical communication systems. The level of knowledge and development on this technology are described as well as the context of this study (Worldwide, inside III-V lab and related to the European project FUTON). This chapter attempts to provide a comprehensive introduction of RSOA design and applications focusing on specific issues related to current challenges.

Historical overview

In this section, we present a historical overview of the network evolution and the optical amplifiers. By being aware of the past/component evolutions, it helps to understand the present state-of-the-art and to prepare the future of optical communication.

Network evolution

Communication networks have evolved in order to fulfil the growing demand of our bandwidth-hungry world. First, the coaxial cable has replaced the copper cable since 1950 for long- and medium-range communication networks. The Bit rate-distance product (BL) is commonly used as figure of merit for communication systems, where the B is the bit rate (bit/sec) and L is the repeater spacing (km). In coaxial cable, the bandwidth was limited by frequency-dependent cable losses and the best microwave communication system available by 1970 had a BL product of ~100 (Mbit/s)-km.

A suitable medium for transmission needed to be available and optical fibres were selected as the best option to guide the light (since 1966) [1-2]. Then the fibre optic revolution started in 1980 when a fibre with only 4 dB/km attenuation was available. Such low attenuation ushered in optical fibre telecommunication. A radical change occurred, the information was transmitted using pulses of light. Thus further increase in the BL product was possible using this new transmission medium because the physical mechanisms of the frequency-dependent losses are different for copper and optical fibres. Another main challenge appeared: coherent optical sources had to be developed (the laser and SOA evolution is described below).

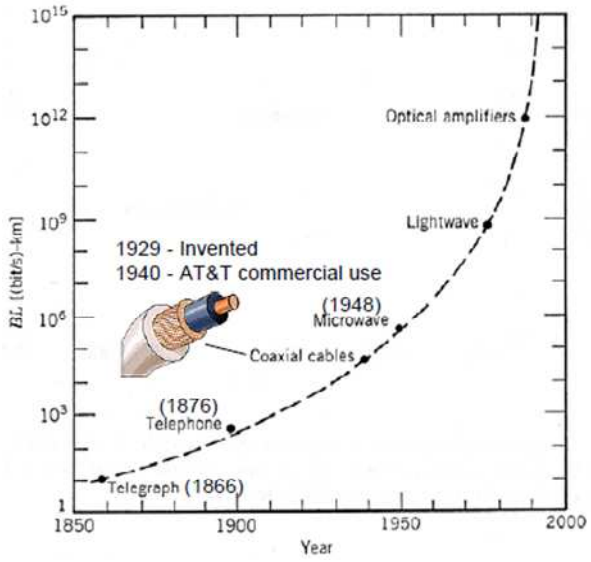

Figure 1 – Increase in Bit rate-distance product (BL) with time [3]

In order to reach appreciable distances of any fibre-optic communication systems optoelectronic repeaters were used at the beginning. The first fibre optical system enabled a data bit rate of 45 Mb/s over 10 km repeater spacing (compared with 1 km for coaxial systems). This first system was based on GaAs lasers with a wavelength emission at 0.8 μm. The fibre attenuation was a major issue and systems moved gradually towards the lowest-attenuation spectral window. The first shift was to the 1.3 μm wavelength. The losses and dispersion in optical fibres were reduced allowing a transmission at 1.7 Gb/s over 50 km repeater spacing (in 1987). But fibre losses were still the main drawback (~0.5dB/km). It was overcome by using optical systems based on 1.55 μm wavelength however large dispersion was obtained. The solution was to limit the laser spectrum to single mode (SM) and to use zero-dispersion-shifted fibre (DSF) [4]. Therefore by 1990, Lightwave systems had bit rate at 10 Gb/s using DSF and SM InGaAsP lasers. Electronic repeater spacing was about 60-70 km for signal regeneration and they were the main limitation for the overall system performances. The problem was solved with the 4th generation of optical systems with the advent of optical fibre amplification. Optical amplifiers were considered as a perfect alternative approach allowing the deployment of optically transparent network and overcoming the electronic bottleneck.

In 1985, the Erbium Doped Fibre Amplifier (EDFA) was invented by Dr. Randy Giles, Professor Emmanuel Desurvire, and Professor David Payne. This optical amplifier was the perfect candidate for online amplification. EDFAs had high gain, low insertion losses, low noise figure and negligible non-linearities [5]. In 1989, EDFAs increased the repeater spacing to 60-80 Km. By 1990, EDFAs became widespread in long-haul lightwave systems. The bit-rate was also increased by the introduction of a new technique: Wavelength-Division Multiplexing (WDM). The use of WDM revolutionized the system capacity since 1992 and in 1996, they were used in the Atlantic and Pacific fibre optic cables (5 Gbit/s was demonstrated over 11,300 Km by using actual submarine cables [6]). The backbone network evolution between Europe and North America is represented in Figure 2.

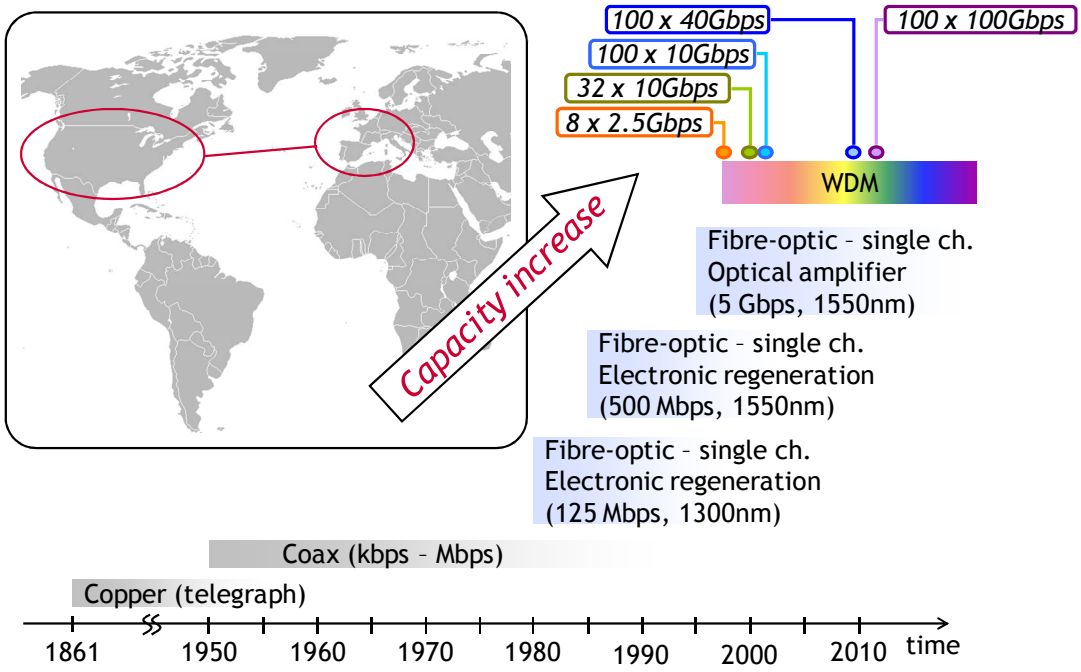

Figure 2 – Transatlantic Submarine systems evolution

While WDM techniques were mostly used in long-haul systems employing EDFA for online amplification, access networks were using more and more bandwidth. Access network includes the infrastructures used to connect the end users (Optical Network Unit - ONU) to one central office (CO). The CO is connected to the metropolitan or core network. The distance between the two network units is up to 20 km. The evolution of access network was very different from in the core network [7]. High bit-rate transmissions are a recent need. At the beginning, it provided a maximum bandwidth of 3 kHz (digitised at 64 kbit/s) for voice transmission and was based on copper cable. Today, a wide range of services need to be carried by our access network and new technologies are introduced which allow flexible and high bandwidth connection. The access network evolution is obvious in Europe with the rapid growth of xDSL technologies (DSL: Digital Subscriber Loop). They enable a broadband connection over a copper cable and allow maintaining the telephone service for that user. In 2000, the maximum bit rate was around 512 kbit/s while today it is around 12 Mbit/s. However since 2005, new applications as video-on-demand need even more bandwidth and the xDSL technologies have reached their limits. The introduction of broadband access network based on FTTx technology is necessary to answer to the recent explosive growth of the internet. Today, Internet service providers propose 100 Mbit/s using optical fibre. The experience from the core network evolution is a great benefit to access network. The use of WDM mature technology in access and metropolitan network should offer more scalability and flexibility for the next generation of optical access network.

However the cost mainly drives the deployment of access network and remains the principal issue. Cost effective migration is needed and the cost capital expenditures (CAPEX) per customer has to be reduced. ONU directly impacts on the CAPEX. New optical devices are needed in order to obtain high performances and low cost ONU. In this work, WDM passive optical network (PON) based on RSOA is studied. A complete analysis of the access network

evolution has been done where GPON (Gigabit Passive Optical Network), BPON (Broadband PON) and EPON (Ethernet PON) upgrading scenario are analysed [8-9].

Optical Amplifier (fibre amplifier and SOA)

The development of semiconductor materials allowed the fabrication of high performances devices such as lasers and optical amplifiers. The development of semiconductor amplifier (SOA) followed the development of laser diodes. SOAs have a gain medium as in laser devices but with the suppression of the resonance cavity. The stimulated emission concept itself was introduced by A. Einstein in 1917 (as detailed in Chapter 1). The feasibility of stimulated emission in semiconductor was demonstrated in 1961 [10-11] and in 1962, the first observation of lasing action in semiconductor materials was done by several research groups [12-13]. The first lasers were GaAs homojunction devices operating at low temperature and called Fabry-Perot laser because of the Fabry-Perot cavity (standard cavity with two mirrors which are separated by an amplifying medium). Heterostructure design was proposed in 1963 [14] and demonstrated in 1969 [15]. The arrival of heterostructure devices spurred the investigation on SOAs as they were first considered at the beginning as bad laser. In fact, high threshold current laser were attractive to amplify optical beam when they were operated under the lasing regime. Therefore, these first semiconductor optical amplifiers were called Fabry-Perot SOAs (FP-SOA) and have been deeply investigated [16-17]. In the 1970's, FP-SOA were not considered seriously as important candidate for optical telecommunication [18-19]. It was due to the low gain (operation below threshold current), high gain ripple and the instability during the amplification process due to the proximity to the threshold condition. In 1980's, important achievements on facet reflectivity were realized and new type of SOAs appeared. In 1982, J. C. Simon reported the first Travelling wave SOA (TW-SOA) where the facet reflectivity was around 10^{-3} [20]. The previous drawbacks of FP-SOA were overcome. The threshold current was extremely high and allowed 15 dB of gain, the instability was not anymore an issue at relatively high current (~80mA). Development of high quality anti-reflection coating were carried out and the first TW-SOA in InGaAsP system with facet reflectivity of 10^{-5} was realized in 1986 [21]. First SOAs were AlGaAs based operating in the 830 nm region [22] then InP/InGaAsP SOAs appeared in the late 1980's [23], centred in the 1.3 μm and 1.5 μm windows. In 1989, Polarization insensitive devices started to become a reality thanks to symmetrical waveguide structure specially designed for SOAs [24]. Prior to this, SOA structures used laser diode design (asymmetrical waveguide structure) leading to strongly polarisation sensitive gain.

After the invention of the EDFA, the research on SOA (more specifically on TW-SOA) was slowed down for application such as the in-line amplification which was the main application at this time. As described in the previous section, EDFAs were chosen as the preferred solution for online amplification in core networks.

New applications were investigated in order to take advantage of the important features of SOAs. These devices could be used as elements for all optical switches and optical crossconnects [25-26]. Highly non-linear phenomena also take place in SOAs and can be used for wavelength conversion and cross gain modulation [27-28]. Other applications were based on SOA as intensity/phase modulators [29-30], logic gate [31-32], clock recovery [33-34-35], dispersion compensator [36-37], format conversion from No Return to Zero (NRZ) to Return to Zero (RZ) [38] and so on...

The SOA is of smaller size, electrically pumped and can be potentially less expensive than the EDFA. It can also be integrated with semiconductor lasers, modulators, and so on. However, they have not been industrialized as much as EDFAs and this technology has been waiting for market needs.

RSOA device

The first idea of a Reflective SOA (RSOA) was proposed by N. A. Olsson in 1988 to reduce the polarization sensitivity via a double pass configuration using classic SOA [39]. This reflective configuration has been reused by several groups for this application [40]. In parallel, Optical communication with SOAs started in the 1990's [41] but two-port packaging was still required. The first integrated RSOA for optical communication appeared in 1996 [42] where the device was employed for upstream signal modulation at a bit rate of 100 Mbit/s. Then several experiments based on RSOAs for local access network were realized where the bit rate was increased to 155 Mbit/s [43]. New applications such as wavelength conversion based on cross gain modulation were also tested [44]. They were not commercially available RSOAs at this time and they were custom made devices.

In this thesis, we mainly focus on the wavelength upgrade scenario for WDM-PON systems. While current optical access networks use one single channel to transmit information, WDM systems use up to 32 channels increasing therefore the total transmitted information. RSOA is the perfect candidate because of its wide optical bandwidth, large gain, high modulation speed and low cost, therefore fulfilling most of the requirements. For instance, its large optical bandwidth makes it a colourless cost-effective modulator for WDM-PON. The same type of device can be used in different ONUs, which reduces the network cost. Moreover, the large gain provided by an RSOA can compensate link losses without using an extra amplifier, which simplifies the overall solution.

Therefore since 2000, RSOA devices saw a fast growing interest in upstream channels transmission based on reflective ONU for WDM-PON applications [45]. The first re-modulation scheme has been proposed in [46] where the downlink signal was transmitted at 2.5 Gbit/s and uplink data stream was re-modulated on the same wavelength via the RSOA at 900 Mbit/s. Then further investigations were realized and 1.25 Gbit/s re-modulation was demonstrated [47-48].

Today, several research groups work on these solutions such as III-V Lab [49], Universitat Politècnica de Catalunya (UPC) [50], Orange labs [51], ETRI [52], KAIST [53], IT [54] and various optical devices manufacturers proposed commercial RSOA devices as CIP [55], MEL [56] and Kamelian [57].

State of the art

In this section, we detail the state of the art at the beginning of this work. A first description of WDM technology and the devices required at the ONU are described. We present and compare the different remote modulators available today and then we focus on the RSOA performances from different actors and III-V lab.

WDM-PON technology

High-speed connectivity is needed for applications such as high definition television, video-on-demand and on-line gaming. Innovative devices are required to reach high data bit rates that can fill the future demand. Passive optical Network, active network and direct point-to-point (P2P) optical links are foreseen as promising technologies for broadband access. So far Time-Division Multiplexing (TDM) technique, employing two wavelength channels to serve multiple users for up- and downstream traffic, is being widely used in PON architecture. One wavelength is shared by several users. Figure 3-(a) represents a single-wavelength architecture using pure TDM techniques. Various scenarios enabling large bandwidth access have been studied, and WDM PON turns out to be an efficient solution. WDM enables one single fibre solution (as TDM PON) but providing one dedicated wavelength per enterprise for example. WDM-PON has been developed in parallel to GPON and GEPON (Gigabit Ethernet PON) technology but has not been standardized yet (however it is suggested in the frame of NGPON2: Next Generation PON). Smooth migration is required by operators from the current PON architecture to a WDM approach. The use of TDM and WDM in the same architecture is a promising solution and it is called as hybrid WDM/TDM PON (an experimental evaluation is done in chapter 6). Such architecture is presented in Figure 3-(b).

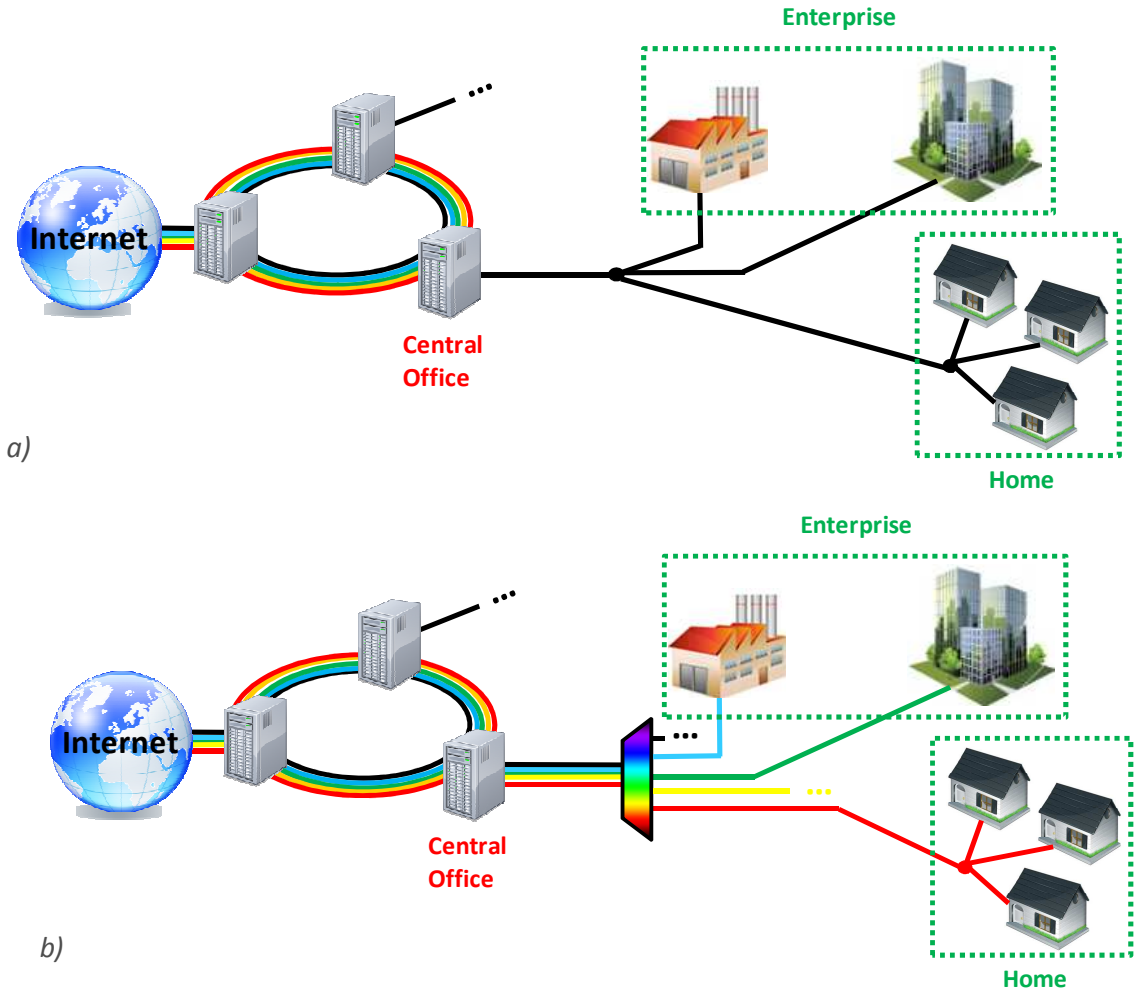

Figure 3 – (a) Single-wavelength vs (b) Multi-wavelength architecture

WDM PON market is a growing market even though there are no standards. Various telecom manufacturers and operators as LG-Nortel, Novera, Genexis, Korea Telecom, NTT and ETRI are interested in this solution but are still uncertain about the time to market. Korea was the early adopter and has started deploying this technology since 2005 reaching 100 Mbit/s to 1 Gbit/s per wavelength. However the cost of such a network is still an issue. In fact, given that high wavelength stability is needed, colourless and stable transceivers are key elements at the ONU.

An efficient solution for WDM-PON transmitters must meet some technical requirements. For example, the higher the power budget, the furthest from the subscriber the central can be, thus easing the deployment and the configuration of the global architecture for the telecom carrier. The electrical bandwidth is directly related to the information rate a device can generate: the higher the electrical bandwidth, the faster the WDM-PON is. The optical bandwidth refers to the number of wavelength channels a device can handle. Therefore, the higher the optical bandwidth, the more universal the device is. On the other hand, as any other electro-optical component, transmitters introduce a small degradation on the optical signal. Polarization dependence and noise figure refer to this degradation on the information. Thus, the lower these values, the better the performances are.

There are two main transmitter families: lasers (more specifically tunable lasers for colorless application) and reflective modulators. On the one hand, tunable lasers show great performances but are still very expensive and not ready for mass production. On the other hand, there are several types of remote modulator such as injection-locked Fabry-Perot lasers [58], reflective electro-absorption modulator (EAM) [59] and reflective EAM- SOA [60]. In order to develop large scale commercially available services, low cost and high performances solutions have to be investigated. Remote modulators for optical access network require high gain, high modulation bandwidth, low chirp, large optical bandwidth (minimum C-band, even larger for Coarse-WDM) and Polarization independence. A comparison of the different technology for reflective modulator devices is proposed in Table 1.

	High gain	Large modulation bandwidth	Low chirp	Wide optical bandwidth	Polarization independence
Injection-locked FP LD	*	*	***	**	*
REAM	*	***	***	**	***
REAM-SOA	**	***	**	**	**
RSOA	***	*	*	***	***

Table 1 – Comparison of reflective modulator devices

Reflective SOA (RSOA) is one candidate at moderate bit-rates filling most requirements. The chirp and the modulation bandwidth in RSOA devices are the major drawbacks. We have focused on these issues during this PhD.

RSOA technology

Some of the key technical requirements and characteristics presented above allow us to compare our competitors with ourselves from a technical point of view, as it can be seen in Table 2. Commercially available devices for WDM PON solutions present a gain between 20 and 25 dB, an electrical bandwidth between 1 and 1.5 GHz, an optical bandwidth between 30 and 40 nm and a polarization dependence around 1 dB. However the intrinsic characteristics of the device such as the optical confinement, the vertical structure or the waveguide design are not public. That is why we focus on RSOAs from III-V lab in order to understand the device evolution.

	CIP (model: CO)	**CIP** (model: 7S)	**Kamelian** (TO-CAN)	**ETRI** (MEL)
Gain (dB)	23	20	22	23
Saturation Power (dBm)	5	2	10	N/A
Optical Bandwidth (nm)	40	40	30	40
3-dB ASE bandwidth (GHz)	1.1	1.2	1.2	1.5
Polarization dependence (dB)	1	1.5	1	0.5
Noise Figure (dB)	7	7	7	N/A

Table 2 – Technical characteristics of RSOA products, from main competitors in 2011

In 2003, a RSOA device was used for the first time in Alcatel-lucent for this purpose by R. Brenot in order to perform a 2.5 Gbit/s modulation. Error free transmissions were limited to 8km of single mode fibre (SMF). RSOA with 45% of optical confinement and 500μm cavity length were used and it was the standard Alcatel-R&I SOA structure at this time. One year later, external cavity fibre grating laser (FGL) modules have been fabricated based on the same RSOA in the frame of the Coloratur project [61]. Also in 2004, T. Zami started to investigate the SOA behaviour under current modulation. Faster cross-gain modulation were obtained with 80% of optical confinement, therefore it was decided to use the same structure for direct modulation. From 1530 nm to 1540 nm, error free transmission at 2.5 Gbit/s was obtained over 48 km with penalty smaller than 4 dB. However the chirp impairment due to the deep modification of the carrier density under electrical modulation was the main limitation.

A first RSOA module with Γ = 45% was evaluated by Orange Labs [62]. The previous SOA structure with 80 % of optical confinement was re-used to realize high speed RSOA. High

reflective (HR) coating was deposed on one side of the device. However the device was not faster than RSOA with Γ = 45% and higher noise figure was measured. For the first time, two-electrode devices were realized and used for high modulation bandwidth [63] however the electro-optical (E/O) modulation bandwidth was not suitable for large signal transmission.

III-V lab decided to evaluate new RSOA structures such as the one with Γ = 20%. However the first idea was to use this structure without any HR coating. This thesis work started in this period where Γ = 20% and Γ = 80% RSOA showed similar modulation speed in digital transmission and two-electrode devices started to be used for increasing the modulation bandwidth. Chips with L = 500 μm were cleaved but no others lengths were studied. The effect of the facet reflectivity was not taken in account and not completely understood. A summary of all characteristics for the first generations of RSOA is presented in Table 3.

	2006 (Γ = 80% 1 section)	**2006** (Γ = 80% 2 section)	**2007** (Γ = 20% 1 section)
Gain (dB)	15	15	20
Saturation Power (dBm)	3	3	4
Optical Bandwidth (nm)	30	30	27
3-dB ASE bandwidth (GHz)	1	3.8 (I_1 = 80 mA & I_2 = 20 mA)	1.1
Polarization dependence (dB)	1	1	0.5
Noise Figure (dB)	13	13	10

Table 3 – Technical characteristics and evolution of RSOA in III-V lab

The FUTON project [64]

This work was part of the FUTON project. The motivations for FUTON were to impact the wireless and also the wireline communications by proposing this alternative architecture with the convergence of wired and wireless network.

Wireless communications services are becoming more important in our society as mobile devices penetration exceeds that of fixed devices in most developed countries. Many consumer devices such as Smartphone, laptop, PDA, Iphone enable us to establish a wireless personal network and bandwidth-hungry services are more and more used every day. Current 3G networks start to be saturated. As a consequence wireless systems require changes in the system architecture. 4G systems aim to solve this problem by providing a true broadband wireless access. Smaller radio cells are necessary in order to support more users at higher data bit rates. Due to the reduction of the radio cells, more and more antennas are needed to cover the same area. A

flexible optical architecture offers the possibility of efficient management of heterogeneous wireless systems using WDM technology. Converged network architecture for multiple optical services have been investigated by several companies such as in the "open Lambda initiative" project with Nokia Siemens Networks, Alcatel-Lucent, Vodafone and JDSU. Optical access and Radio-over-Fibre (R-o-F) networks tend to be mutualised to a single architecture as represented in Figure 4. In the FUTON (Fibre-Optic Networks for Distributed Extendible Heterogeneous Radio Architectures and Service Provisioning) concept, several remote access units (RAU) are connected via optical links. Such a network is called a distributed antenna system (DAS). More details on the FUTON architecture and performances are provided in Chapter 6.

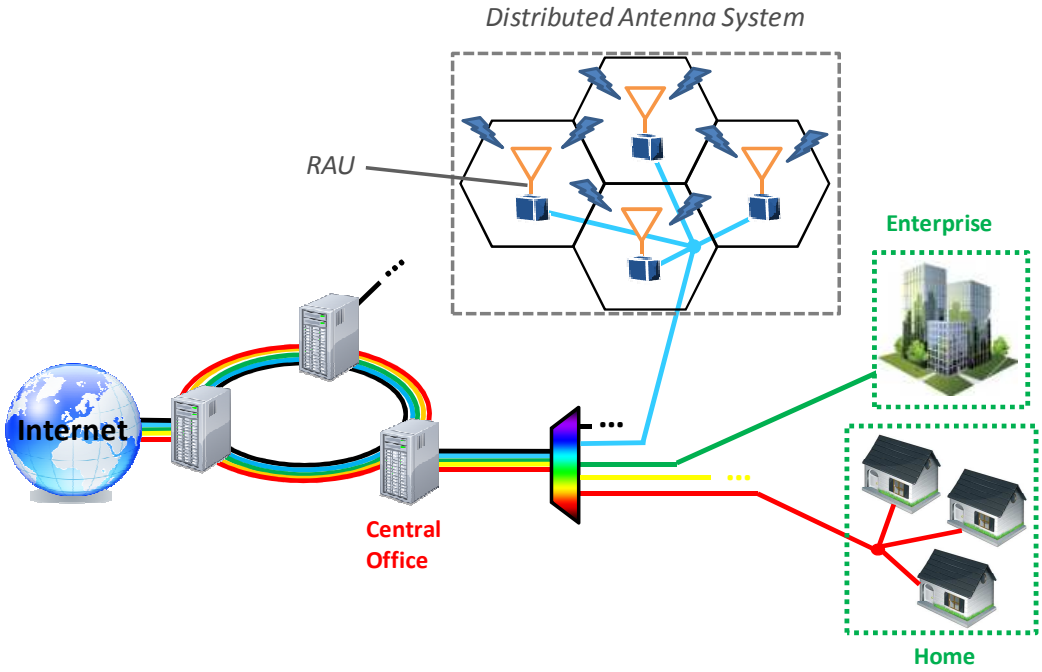

Figure 4 – Converged network architecture

For the same reasons as in optical access network, RSOA is an interesting device for WDM R-o-F network. It can be placed at the RAU for colourless operation and enables reconfigurable R-o-F Network Architecture. In 2007, important investigations have been realized in order to study the feasibility of such a RSOA-based network [65-66]. Then orthogonal frequency-division multiplexing (OFDM) signals have been widely used in wireless communication to extend transmission distance over fibre and air links. It was obvious that both technologies were going to meet. In 2008, a 10 Gbit/s transmission using Adaptively Modulated Optical OFDM for WDM-PON single fibre architecture was demonstrated with III-V lab devices [67]. However these devices were not optimized for R-o-F systems. The main idea is to find the universal device which can be used in ONU for fixed access network as well as in RAU for R-o-F network as both tend to be merged.

III-V lab was responsible for the development of high performances optical devices for R-o-F systems and meeting the FUTON requirements. New Directly Modulated Laser (DML) and RSOA devices were proposed and evaluated for this application.

Unsolved issues (PhD objectives)

This work was realized during a crucial period in the telecommunication industry. Ground-breaking innovations from the research need to address real customer issues and define the future of optical access network. Architecture based on single-fibre bidirectional link seems the most interesting and cost efficient approach. ONU becomes a key element for the network evolution. Transparent and flexible architecture based on WDM technology is necessary thus colourless ONU need to be available. High gain should be provided by the transmitter to reach the necessary optical budget and high modulation speed is needed. Bit rates up to 10 Gbit/s (per wavelength) are required to follow the evolution of the 10 Gbit/s GPON. RSOA could be the missing building block to reach this ideal network. However as detailed in Table 1, the modulation bandwidth and the chirp are still issues that need to be solved.

Converged network architecture starts to be a reality as wireless and wireline services become similar. A universal device is needed for digital transmission (as in optical access network) as well as for analogue transmission (as in R-o-F network). Even if the industrial exploitation drives the research, the fundamental physics inside the device needs to be further understood to overcome the device limitations. High performances RSOAs need to be investigated for WDM PON and R-o-F access technology. This thesis work is driven by all these fundamental issues. The main objective is the evaluation and optimization of RSOA devices for reflective optical network units. It consists of several action points:

- Identification and comprehension of the physical mechanisms inside RSOA
- Design, modelling and fabrication of RSOA devices
- Static and dynamic characterization of RSOA
- Identification of the limitations and proposition of alternative solutions
- Development of optimized RSOA
- Evaluation of RSOA devices in optical access and R-o-F network

Manuscript structure

This manuscript covers a wide range of topics, reflecting the diversity of objectives listed above, which the chapters deal with, roughly in order, from the lowest physical-level understanding to the industrial-level applications.

In chapter 1, the basic theory of SOA is investigated. The different interactions of light and matter are described. The operating principles of a RSOA are compared to a FP-laser and a classic SOA. The SOA/RSOA structure is presented. One major role of RSOA is the amplification of an optical signal. A complete study of the material characteristics is done based on the energy band theory and a simple model is proposed to evaluate the material gain. In relation to the vertical structure, the net gain is calculated taking into account the cladding layers losses, the optical confinement and the material gain. We finally calculate the optical gain considering the forward and backward propagation of the optical signal inside the active medium. Longitudinal spatial hole burning (LSHB) strongly affects the average optical gain. A first evaluation of the total gain in SOA devices including the LSHB (based on the Connelly model) is proposed. The influence of the optical confinement is described and leads to some design rules.

Chapter 2 describes the design and the fabrication of our RSOA. Two vertical structures are described considering the epitaxial layers (material composition, thickness and strain). The study was based on existing wafers (grown by III-V lab for SOA structure) with 80% and 20% of optical confinement. The buried ridge structure is detailed using both theoretical and experimental approach. The design is based on a double core structure with a spot-size converter (SSC). 2D optical Mode and the optical mode transfer between the active and passive layers are modelled in order to evaluate our design. A new design is proposed to increase the tolerance to the fabrication imperfections. During this thesis, several wafers have been processed with various RSOA designs (in the context of the FUTON and AROME project). The processing steps are detailed in this chapter to give the general fabrication recipe. Facet reflectivity strongly affects the device behaviour therefore a theoretical approach of the tilted and coated facet reflectivity is proposed.

In chapter 3, we focus on the device modelling and static characterization. Based on the theory developed in chapter 1, we develop a multi-section model in order to take in account the non-homogeneity of the carrier density. In this approach, we consider a forward and backward propagation as well as the amplified spontaneous emission (ASE) propagation. The carrier density is calculated in each section and it is based on the differential coupling equation between photons and electrons. The spatial carrier density distribution is completely different between the SOA and RSOA devices. The simulated optical gain is compared with the experimental data and shows a good agreement. The influence of RSOA parameters such as the optical confinement, the length and the facet reflectivity is described. Under the latter analysis, the performance of RSOA must be evaluated considering the trade-offs among the different parameters.

Dynamic analysis is then proposed in chapter 4. A first approximation of the modulation bandwidth is proposed. The SOA and RSOA modulation responses behave as a low-pass filter with a characteristic cut-off frequency. The carrier lifetime turns out to be a key parameter for high speed modulation and a decrease of its value appears to be required. The rates of recombination processes, such as stimulated, spontaneous and non-radiative recombination govern the carrier lifetime. They strongly depend on the position along the active zone and the operating conditions. Carrier lifetime reduction is demonstrated in order to increase the modulation bandwidth and confirms by spontaneous emission (SE) measurements. Finally, a simple dynamic model is proposed. Digital modulation is then studied from a theoretical and experimental point of view.

Chapter 5 investigates the use of multi-electrode RSOA. The theory of the linewidth enhancement factor is discussed and extended to multi-section devices. The multi-electrode design affects the carrier density profile under electrical modulation. We demonstrate that by modulating the input electrode of a two-section RSOA, the chirp can be reduced by taking advantage of the non-homogeneity of the carrier density distribution. Chirp reduction is theoretically and experimentally demonstrated using two-section devices. The total frequency deviation is measured and confirms the previous simulations. Error free transmissions are presented based on low chirp devices and compared to single-section RSOA. Two-section RSOA can be used to improve the link gain. Better internal efficiency is demonstrated. In collaboration

with the University of Kent, link gain measurements are performed. 2-section RSOA frequency response is measured at different bias currents and confirms link gain improvement.

Telecommunication networks based on RSOA are studied in chapter 6. High gain RSOA is used as colourless transmitter and WDM operations are performed. Laser seeding configuration at 2.5 Gbit/s is realized and error free transmission is obtained for 36 dB of optical budget over 45 km of SMF. Low chirp RSOAs enable a 100 km transmission at the same bit rate below the Forward Error Correction (FEC) limit. Direct 10 Gbit/s modulation is realized using high speed RSOA. Innovative R-o-F architecture as developed in the FUTON project is presented. The RSOA behaviour is evaluated by Spurious-Free Dynamic Range (SFDR) and Error Vector Magnitude (EVM) measurements. We demonstrated that RSOA is an ideal candidate for R-o-F applications. Radio range calculations are carried out based on link gain and noise measurements. Two-section RSOAs lead to larger radio range similar to DML performances.

Finally, we summarize the lessons learned in this manuscript and conclude on RSOA devices as colourless optical transmitters. Further investigations are recommended.

This work was realized at III-V lab, a joint Laboratory of "Alcatel Lucent Bell Labs", "Thales Research & Technology" and "CEA", in the context of the European FUTON project, and associated to Télécom ParisTech.

References

[1] K. C. Kao and G. A. Hockham, "Dielectric-fibre surface waveguides for optical frequencies", Proc. IEE, Vol. 113, No. 7, July 1966, pp. 1151-1158

[2] A. Werts, "Propagation de la lumiere coherente dans les fibres optiques", L'Onde Electrique, Vol. 46, 1966, pp. 967-980

[3] G. P. Agrawal, "Fiber-optic communication systems", Third Edition, John Wiley & Sons Inc., Chap. 1, 2002, pp. 2-4

[4] N. Zakhleniuk, "EE730: Optical components II", lecture notes, University of Essex, part A, 2007-2008, pp. 6-7

[5] G. P. Agrawal, "Fiber-optic communication systems", Third Edition, John Wiley & Sons Inc., Chap. 6, 2002, pp. 250-260

[6] T. Otani, K. Goto, H. Abe, M. Tanaka, H. Yamamoto, and H. Wakabayashi, "5.3 Gbit/s 11300 km data transmission using actual submarine cables and repeaters", Electron. Lett., Vol. 31, No. 5, 1995, pp. 380-381

[7] Wes Carter, "The access network - evolution from separate simple services to a fully flexible environment", Martel europe ltd, white paper, 2001, pp. 1-20

[8] Fabienne Saliou, "Etudes des solutions d'accès optique exploitant une extension de portée", PhD Thesis, École Nationale Supérieure des Télécommunications, Chap. 1, 2010, pp. 23-76

[9] Cristina Arellano Pinilla, "Investigation of Reflective Optical Network Units for Bidirectional Passive Optical Access Networks", PhD Thesis, Universitat Politecnica de Catalunya, Chap. 2, 2007, pp 18-23

[10] N. G. Basov, O. N. Krokhin and Yu. M. Popov, "Production of negative-temperature states in p–n junctions of degenerate semiconductors", Sov. Phys. JETP, Vol. 13, 1961, pp. 1320-1321

[11] M. G. A. Bernard and G. Duraffourg, "Laser Conditions in Semiconductors", Phys. Status Solidi, Vol. 1, No. 7, 1961, pp. 699-703

[12] R. N. Hall, G. E. Fenner, J. D. Kingsley, T. J. Soltys, and R. O. Carlson, "Coherent Light Emission From GaAs Junctions", Phys. Rev. Lett., Vol. 9, No. 9, 1962, pp. 366-368

[13] M. I. Nathan, W. P. Dumke, G. Burns, F. H. Dill, Jr., and G. Lasher, "Stimulated Emission of Radiation from GaAs p-n Junctions", Appl. Phys. Lett., Vol. 1, No. 3, 1962, pp. 62-64

[14] H. Kroemer, ""A Proposed Class of Heterojunction Injection Lasers", Proc. IEEE, Vol. 51, 1963, pp 1782-1783

[15] H. Kressel and H. Nelson, "Close-confinement gallium arsenide P-N junction lasers with reduced optical loss at room temperature", RCA Rev., Vol. 30, 1969, pp. 106-113

[16] P. G. Kryukov and V. S. Letokhov, "Propagation of a light pulse in a resonantly amplifying (absorbing) medium", Sov. Phy. Uspekhi, Vol. 12, March 1970, pp. 641-672

[17] Lee W. Casperson, "Threshold charasteristics of mirrorless lasers", J. Appl. Phy., Vol. 48, Jan. 1977, pp. 256-262

[18] G. Zeidler and D. Schicetanz, "Use of laser amplifiers in glass fibre communication systems", Radio and Electronic Engineer, Vol. 43, No. 11, 1973, pp. 675-682

[19] S. D. Personick, "Applications for quantum amplifier in simple digital optical communication systems", Bell Syst. Tech. J., Vol. 52, No. 1, 1973, pp. 117-133

[20] J. C. Simon, "Polarisation characteristics of a travelling-wave-type semiconductor laser amplifier", Electron. Lett., Vol. 18, No. 11, May 1982, pp. 438-439

[21] T. Saitoh and T. Mukai, "A low noise 1.5 μm GaInAsP traveling-wave optical amplifier with high saturation output power", in ISLC, Paper PD-5, 1986, Kanazawa, Japan

[22] Y. Yamamoto, "Charasteristics of AlGaAs Fabry-Perot cavity type laser amplifiers", J. Quantum Electron., Vol. 16, No. 10, 1980, pp. 1047-1052

[23] J. C. Simon, "GaInAsP semiconductor laser amplifiers for single-mode fibre communications", J. Lightwave Technol.,Vol. LT-5, No. 9, 1987, pp 1286-1295

[24] N. A. Olsson, R. F. Kazarinov, W. A. Nordland, C. H. Henry, M. G. Oberg, H. G. White, P. A. Garbinski and A. Savage, "Polarization-independent optical amplifier with buried facets", Electron. Lett., Vol. 25, No. 16, 1989, pp. 1048-1049

[25] D. M. Atkin and M. J. Adams, "Optical switching in the twin-guide travelling-wave laser amplifier", IEE proc.-J, Vol. 140, Oct. 1993, pp. 296-300

[26] T. Kirihara, M. Ogawa, H. Inoue, H. Kodera and K. Ishida, "Lossless and low-crosstalk characteristics in an InP-based 4x4 optical switch with integrated single-stage optical amplifiers", Photonics technology letters, Vol. 6, No. 2, Feb. 1994, pp. 218-221

[27] I. Valiente, J. C. Simon and M. Le ligne, "Theoretical analysis of semiconductor optical amplifier wavelength shifter", Electron. Lett., Vol. 29, No. 5, Mar. 1993, pp. 502-503

[28] T. Durhuus, B. Mikkelsen, C. Joergensen, S. L. Danielse and K. E. Stubkjaer, "All-optical wavelength conversion by semiconductor optical amplifiers", J. Lightwave Technol., Vol. 14, No. 6, Jun. 1996, pp. 942-954

[29] L. Gillner, "Modulation properties of a near travelling-wave semiconductor laser amplifier", IEE Proc.-J, Vol. 139, No. 5, Oct. 1992, pp. 331-338

[30] A. C. Labrujere, C. A. M. Steenbergen and C. J. van der Laan, "Phase modulation and optical switching by semiconductor laser amplifier", in Techn. Dig. of OFC, paper ThC4, 1991, pp. 138-141

[31] R. Schnabel, W. Pieper, R. Ludwig, and H. G. Weber, "All optical AND gate using femtosecond non-linear gain dynamics in semiconductor optical amplifiers", in proc. ECOC'93, Sept. 1993, pp. 133-136, Montreux, Switzerland

[32] C. Joergensen, T. Durhuss, C. Braagaard, B. Mikkelsen, and K. E. Stubkjaer, "4 Gb/s Optical wavelength conversion using semiconductor optical amplifiers", Photonics technology letters, Vol. 5, No. 6, June 1993, pp. 657-660

[33] S. Kawanishi, H. Takara, M. Saruwatari and T. Kitoh, "Ultrahigh-speed phaselocked-loop-type clock recovery circuit using a travelling-wave laser diode amplifier as a 50 GHz phase detector", Electron. Lett., Vol. 29, No. 19, Sep. 1993, pp. 1714-1716

[34] C. Ware and D. Erasme, "30 GHz sub-clock recovery using an opto-electronic phase-locked loop based on four-wave mixing in a semiconductor optical amplifier", in proc. CLEO/Europe, 17 june 2005, pp. 487

[35] J. Leuthold, R. Bonk, P. Vorreau, S. Sygletos, D. Hillerkuss, W. Freude, G. Zarris, D. Simeonidou, C. Kouloumentas, M. Spyropoulou, I. Tomkos, F. Parmigiani, P. Petropoulos, D.J. Richardson, R. Weerasuriya, S. Ibrahim, A.D. Ellis, C. Meuer, D. Bimberg, R. Morais, P. Monteiro, S. Ben Ezra, S. Tsadka,"An all-optical grooming switch with regenerative capabilities", in proc. ICTON, 2009, pp. 1-4, Azores, Portugal

[36] A. H. Gnauck, R. M Jopson and R. M. Derosier, "10 –Gb/s 360-km transmission over dispersive fiber using midsystem spectral inversion", Photonics technology letters, Vol. 5, No. 6, June 1993, pp. 663-666

[37] P. Y. Cortès, M. Chbat, S. Artigaud, J. L. Beylat, J. Chesnoy, "Below 0.3 dB polarisation penalty in 10 Gbit/s directly modulated DFB signal over 160 Km using Mid-Span Spectral Inversion in a semiconductor optical amplifier", in proc. ECOC'95, Sept. 1995, pp. 267-270, Brussels, Belgium

[38] L. Noel, X. Shan and A. D. Ellis, "Four WDM channel NRZ to RZ format conversion using a single semiconductor laser amplifier", Electron. Lett., Vol. 31, No. 4, Feb. 1995, pp. 277-278

[39] N. A. Olsson, "Polarisation-independent configuration optical amplifier", Electron. Lett., Vol. 24, No. 17, Aug. 1988, pp. 1075-1076

[40] L. F. Tiemeijer, G. N. van den Hoven, P. J. A. Thijs, T. van Dongen, J. J. M. Binsma, E. J. Jansen, and A. J. M. Verboven, "High-Gain 13 10-nm Reflective Semiconductor Optical Amplifiers with Low-Gain Uncertainty", Photonics technology letters, Vol. 9, No. 1, Jan. 1997, pp. 37-39

[41] U. Koren, B. I. Miller, M. G. Young, T. L. Koch, R. M. Jopson, A.H. Gnauck, J. D. Evankow, and M. Chien, "High frequency modulation of strained layer multiple quantum well optical amplifiers", Electron. Lett., vol. 27, No. 1, 1991, pp. 62-64

[42] M. Feuer, J. Wiesenfeld, J. Perino, C. Burrus, G. Raybon, S. Shunk, N. Dutta, "Single-port laser-amplifier modulators for local access", Photonics technology letters, Vol.8, No.9, Sept. 1996, pp.1175-1177

[43] N. Buldawoo, S. Mottet, F. Le Gall, D. Sigonge, D. Meichenin, S. Chelles, "A Semiconductor Laser Amplifier-Reflector for the future FTTH Applications", in Proc. ECOC'97, Sept. 1997, pp. 196-199, Edinburgh, UK

[44] P. S. André, A. J. Teixeira, J. L. Pinto and J. F. Rocha, "Performance Analysis of Wavelength Conversion Based on Cross-Gain Modulation in Reflective Semiconductor Optical Amplifiers", in proc. IMOC, 2001, pp. 119-122, Belém, Brazil

[45] P. Healey, P. Townsend, C. Ford, L. Johnston, P. Townley, I. Lealman, L. Rivers, S. Perrin, R. Moore, "Spectral slicing WDM-PON using wavelength-seeded reflective SOAs", Electron. Lett., Vol. 37, No. 19, pp. 1181-1182, Sep. 2001.

[46] J.J. Koponen, M.J. Söderlund, "A duplex WDM passive optical network with 1:16 power split using reflective SOA remodulator at ONU", in proc. OFC'04, MF 99, March 2004, Los Angeles, USA

[47] J. Prat, C. Arellano, V. Polo, C. Bock, "Optical network unit based on a bidirectional reflective semiconductor optical amplifier for fiber-to-the-home networks", Photonics technology letters, Vol.17, No.1, January 2005, pp.250-252

[48] P. J. Urban, M. M. de Laat, E. J. Klein, A. M. J. Koonen, G. D. Khoe, H. de Waardt, "1.25 Gbit/s Bidirectional Link in an Access Network Employing a Reconfigurable Optical Add/Drop Multiplexer and a Reflective Semiconductor Optical Amplifier", in proc. ICTON 2008, We.B4.5, 2008, pp. 166-169, Athens, Greece

[49] G. De Valicourt, D. Maké, J. Landreau, M. Lamponi, G.H. Duan, P. Chanclou and R. Brenot, "New RSOA Devices for Extended Reach and High Capacity Hybrid TDM/WDM -PON Networks", in Proc. ECOC'09, P9.5.2, 2009, Vienna, Austria

[50] C. Arellano, C. Bock, K-D. Langer and Josep Prat , "RSOA-based Optical Network Units for WDM-PON", in proc. OFC'06, OTuC1, March 2006, Anaheim, USA

[51] F. Payoux, P. Chanclou, T. Soret, N. Genay and R Brenot, "Demonstration of a RSOA-based Wavelength Remodulation Scheme in 1.25 Gbit/s Bidirectional Hybrid WDM-TDM PON", in proc. OFC'06, OTuC4, March 2006, Anaheim, USA

[52] Wooram Lee, Mahn Yong Park, Seung Hyun Cho, Jihyun Lee, Chulyoung Kim, Geon Jeong, and Byoung Whi Kim, "Bidirectional WDM-PON Based on Gain-Saturated Reflective Semiconductor Optical Amplifiers", Photonics technology letters, Vol.17, No.11, Nov. 2005, pp.2460-2462

[53] K. Y. Cho, Y. Takushima, and Y. C. Chung, "Enhanced Operating Range of WDM PON Implemented by Using Uncooled RSOAs", Photonics technology letters, Vol.20, No.18, Sept. 2008, pp.1536-1538

[54] Zhansheng Liu, Mojtaba Sadeghi, Guilhem de Valicourt and Romain Brenot, Manuel Violas, "Experimental Validation of a Reflective Semiconductor Optical Amplifier Model used as a Modulator in Radio over Fiber Systems", Photonics technology letters, Vol.23, No.9, 2011, pp.576-578

[55] http://www.ciphotonics.com/products/soa/soa-r-c-co-fca/

[56] http://www.mels.co.kr/product/GWPON-OLT-GBIC.html?idx=16

[57] http://www.kamelian.com/products.html

[58] Wai Hung, Chun-Kit Chan, Lian-Kuan Chen, and Frank Tong, "An Optical Network Unit for WDM Access Networks With Downstream DPSK and Upstream Remodulated OOK Data Using Injection-Locked FP Laser", Photonics technology letters, Vol. 15, No. 10, 2003, pp 1476-1478

[59] B. Pezeshki, D. Thomas, and J. S. Harris, "Optimization of Modulation Ratio and Insertion Loss in Reflective Electroabsorption Modulators," Appl. Phys. Letters, Vol. 57, No. 15, 1990, pp 1491-1493

[60] A. Garreau, J. Decobert, C. Kazmierski, M.-C Cuisin, J.-G Provost, H. Sillard, F. Blache, D. Carpentier, J. Landreau, P. Chanclou, "10Gbit/s Amplified Reflective Electroabsorption Modulator for Colourless Access Networks," in proc. IPRM, 2006, pp.168-170, Princeton, USA

[61] A. Leroy, H. Helmers, B. ThCdrez, S. Hubert, P. Peloso, S. Kerboeuf, G.-H. Duan, J. Jacquet, W. Heck, L. Lablonde and M. Boitel, "Low-cost wavelength stabilised plug and play lasers for WDM systems in future local networks", Electron. Lett., Vol. 37, No. 16, Aug. 2001, pp. 1012-1013

[62] F. Payoux, P. Chanclou, M. Moignard, R. Brenot, "Gigabit optical access using WDM PON based on spectrum slicing and reflective SOA", in Proc. ECOC'05, We3.3.5, 25-29 Sept. 2005, Glasgow, UK

[63] R. Brenot et al, "High modulation bandwidth reflective SOA for optical access networks", in Proc. ECOC, Sept. 2007, pp. 1-2, Berlin, Germany

[64] http://www.ict-futon.eu/

[65] M.C.R. Medeiros, R. Avo, P. Laurencio, N.S. Correia, A. Barradas, H.J.A. da Silva, I. Darwazeh, J.E. Mitchell, P.M.N. Monteiro, "Radio over fiber access network architecture employing reflective semiconductor optical amplifiers", in proc. ICTON-MW, Dec. 2007, Sa2.1, Rome, Italy

[66] Yong-Yuk Won, Hyuk-Choon Kwon, and Sang-Kook Han, "1.25-Gb/s Wavelength-Division Multiplexed Single-Wavelength Colorless Radio-on-Fiber Systems Using Reflective Semiconductor Optical Amplifier", J. Lightwave Technol., Vol. 25, No. 11, November 2007, pp. 3472-3478

[67] T. Duong, N. Genay, P. Chanclou, B. Charbonnier, A. Pizzinat, R. Brenot, "Experimental demonstration of 10 Gbit/s upstream transmission by remote modulation of 1 GHz RSOA using Adaptively Modulated Optical OFDM for WDM-PON single fiber architecture", in Proc. ECOC, Th.3.F.1, 2008, Brussels, Belgium

Chapter 1. Fundamentals of Semiconductor Optical Amplifier

Semiconductor optical amplifier (SOA), and more specifically Reflective SOA, becomes an important device for the next generation of optical access network. The aim of this chapter is to describe the basic theory on SOA devices which should lead to some design rules and that will be applied to Reflective SOA.

Semiconductor optical amplifier is very similar to semiconductor laser as they use a similar gain medium. Optical gain is provided by stimulated emission. The principle of this phenomenon, the differentiation between laser, SOA and RSOA, and the basic structure used to produce these devices are described in section 1.1. Since SOA and RSOA are electrically pumped in order to produce gain, it is necessary to understand the gain mechanism and how it is usually approximated. Section 1.2 describes the material properties of a semiconductor layer and the total gain of a waveguide structure (including cladding and internal losses).

Light travels through the structure and the optical amplification depends on the propagation on the light wave (forward and backward). In SOAs, unlike lasers, the cavity resonance must be suppressed. Therefore, facet reflectivity is also a crucial design parameter. Its maximum acceptable value must be determined, as a function of the gain, in order to remain below the oscillation threshold. Based on Maxwell's equations, we analyze the wave propagation theory and deduce the amplification factor in section 1.3 depending on the facet reflectivity.

The effect of the non-homogenous carrier density on the gain properties is also described in this section 1.3.3.

1.1 Basic concepts

In this section, the fundamental properties and the main concepts of SOA are introduced in a simple way. It starts from the simplest case with the interaction between the light and atoms. After this general introduction, the different SOA types are described and the typical structure is presented. All concepts are introductory concepts and will be discussed in the following sections and chapters.

1.1.1 Interaction between light and atoms

To understand the different mechanisms involved in a SOA, we should first focus on light emission and absorption. Figure 1-1 represents different interactions between light and atoms.

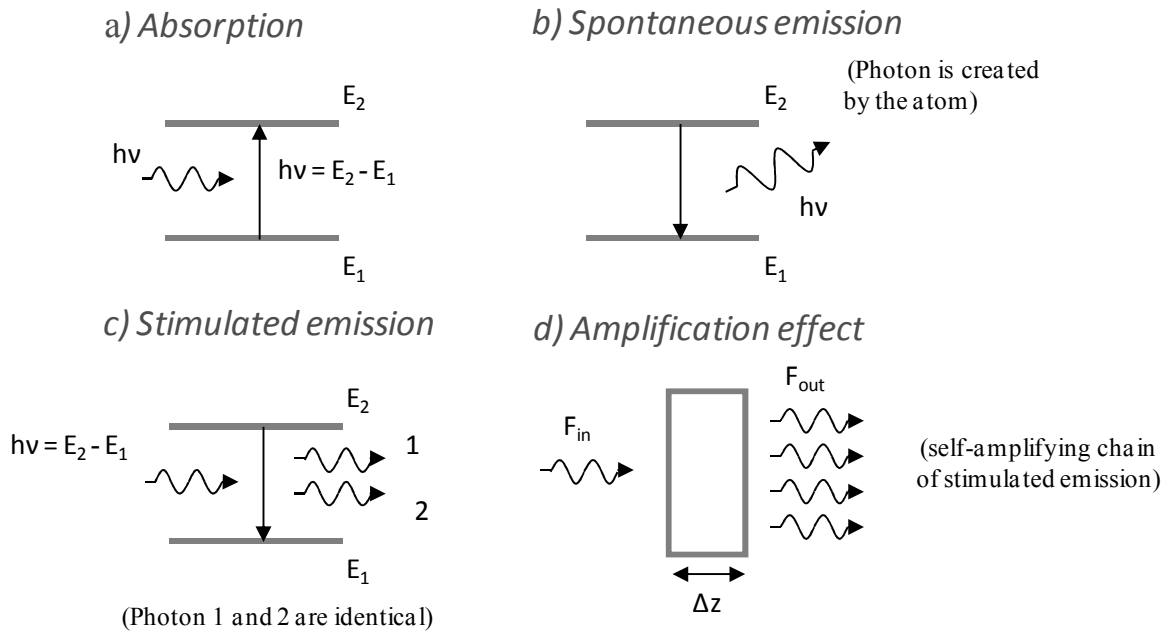

Figure 1-1 – Basics of interaction of light with atoms: (a) absorption, (b) spontaneous emission, (c) stimulated emission and (d) principles of amplification mechanism [1]

Let us consider a simple atom with two energy levels. A photon with an energy corresponding to the transition between level 1 and 2 may be absorbed by an electron, which is promoted to the higher energy level. This is the mechanism of absorption and the energy absorbed by the electron is equal to the photon energy:

$$E_{upper} - E_{lower} = h\nu = h\frac{c}{\lambda} \qquad 1\text{-}1$$

Where E, h, c and λ are the energy level, Planck's constant, the speed of light in vacuum and the wavelength respectively.

In the case of a semiconductor, absorption is possible only if the energy of the photon exceeds the band gap energy (Figure 1-1-(a)). In fact, an electron cannot be excited into the forbidden band and the minimum energy is defined by the absorption condition:

$$E_{photon} \geq E_g \qquad 1\text{-}2$$

If an atom or molecule lies in an energy state that is higher than the lowest, or ground level state, it can spontaneously drop to a lower level with the emission of a photon (with random phase and direction) as shown by the spontaneous emission schematic (Figure 1-1-(b)). The energy of the radiated photon is equal to the difference between the upper and lower energy states as described by equation (1-1) and the atom decays from level 2 to level 1. Radiative emission, as spontaneous emission, is one of the possible ways for the atom to decay. Non-radiative recombination processes are also possible. In this case, the energy difference between E_2

– E_1 is not dissipated by a radiation, but through other forms of energy (kinetic or internal energy). The non-radiative recombination processes will be described in Chapter 3 while analyzing the RSOA static behaviour.

Alternatively, considering the atom in an excited state, the atom may be stimulated by the incoming photon to return to the lower state and simultaneously emits a photon at that same transition energy (Figure 1-1-(c)). The two photons are in phase, with the same wavelength and direction of propagation. An exact replica or "twin" of the incoming photon is created. The mechanism that has been described above corresponds to the stimulated emission and forms the basis of optical amplifier operation (Figure 1-1-(d)).

In the case of a semiconductor, we consider energy bands instead of simple energy levels. Nevertheless, the mechanisms of stimulated emission are identical. The gain properties are directly related to the processes of spontaneous and stimulated emission. As a consequence, it is crucial to quantify this process. Let's introduce the quantity N_i which represents the number of atoms per unit of volume that at a given time (t) occupy a given energy level i and which is called the population of level i. Furthermore, the rate of decay of the level 2 due to the spontaneous emission is proportional to the population of level 2. We obtain [2]:

$$\left(\frac{dN_2}{dt}\right)_{spt} = -AN_2$$

1-3

Where A is the Einstein coefficient.

A similar approach can be used to determine the rate of decay of the level 2 due to the stimulated emission.

$$\left(\frac{dN_2}{dt}\right)_{st} = -B_{21}P(\upsilon)N_2$$

1-4

Where B_{21} is the stimulated emission parameter that quantifies the decay of the level 2 to the level 1 and $P(\upsilon)$ is the photon flux (incident radiation energy density at frequency υ).

The absorption can be modelled as:

$$\left(\frac{dN_2}{dt}\right)_{a} = +B_{12}P(\upsilon)N_1$$

1-5

At the beginning of the XX^e century, the stimulated emission was unknown. However the spontaneous emission and the absorption were already discovered. The equilibrium equation was written as:

$$\frac{dN_2}{dt} = -AN_2 + B_{12}P(\upsilon)N_1$$

1-6

Where A is the spontaneous rate and B_{12} is the absorption rate.

These notations were used by A. Einstein where "rate" means the probability per second and per atom. At the steady state condition, the previous equation becomes:

$$\frac{N_2}{N_1} = \frac{B_{12}}{A}\, P(\upsilon)$$

1-7

From this equation, it is possible to demonstrate, based on Planck's law, that the rate $\frac{N_2}{N_1}$ is in contradiction with the Boltzmann statistic. In 1917, Einstein introduced the stimulated emission in order to solve this apparent contradiction. Therefore the equilibrium equation became:

$$\boxed{\frac{dN_2}{dt} = -AN_2 + B_{12}P(\upsilon)N_1 - B_{21}P(\upsilon)N_2}$$

1-8

From here can be derived the so called Einstein relation. A complete analysis can be found in [3]. The amplification effect is shown in Figure 1-1-(d). A plane wave with a photon flux of $P(\upsilon)$ is traveling through a material (along the z direction). We introduce the absorption cross-section σ_{12} and the stimulated emission cross-section σ_{21}. The cross-section corresponds to a hypothetical area measure around the atom, it quantifies the likelihood of transition events and depends on the transition characteristics. Einstein showed from the equation (1-8) that $\sigma_{12} = \sigma_{21}$ therefore we can posit:

$$\boxed{\frac{dP}{dz} = \sigma_{21}(N_2 - N_1)P}$$

1-9

At thermal equilibrium, the level populations are described by the Boltzmann statistics:

$$\frac{N_2}{N_1} = e^{(-\frac{E_2 - E_1}{kT})}$$

1-10

Where k is the Boltzmann constant and T is the absolute temperature.

Let's consider non-degenerate levels of energy for more simplicity. At thermal equilibrium and according to equation (1-10), we obtain $N_2 < N_1$, therefore the material acts as an absorber ($\frac{dP}{dz} < 0$). As a consequence, population inversion is needed ($N_2 > N_1$) in order to obtain a positive gain ($\frac{dP}{dz} > 0$). A material in which population inversion occurs is called active medium and acts as an optical amplifier. The analysis of a propagating wave inside an active medium is presented in section 1.1.1.

1.1.2 SOA-RSOA-FP description

A Semiconductor Optical Amplifier (SOA) is a gain medium based on the stimulated emission. The purpose of optical amplifiers is to increase the power of the incoming signal, as depicted in Figure 1-2. The input signal or light is amplified along the amplification zone. The amplification takes place in the active zone only if an external current supply is provided. As mentioned previously, the optical gain is associated to the stimulated emission process, which requires the recombination of electron-hole pairs. Without electrical injection, the SOA would absorb the incoming photons (as described by equation (1-9) and (1-10)).

RSOA is a particular scheme of SOA. RSOA stands indeed for Reflective SOA. We insert a mirror at the output of the device in order to reflect back the light into the amplification zone. Therefore the input and output of the device are at the same facet and the device can be more compact because of the forward and backward amplifications. SOA and RSOA devices are represented in the following picture:

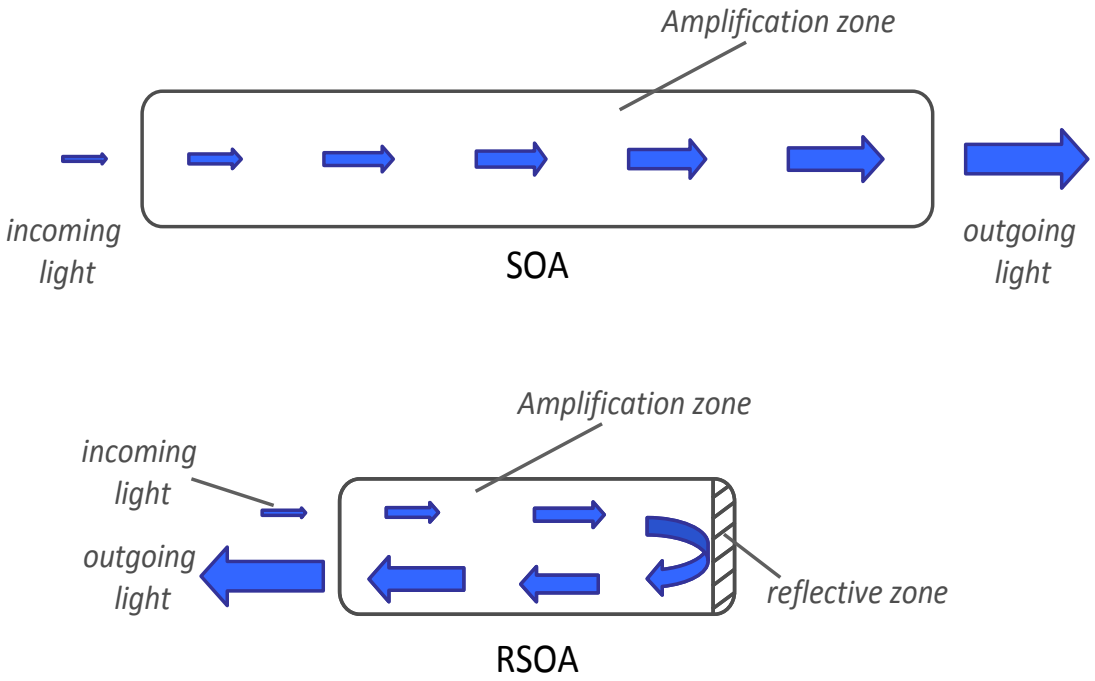

Figure 1-2 – SOA and RSOA operating principle

A Fabry-Perot laser (FP laser) consists of a gain medium surrounded by two mirrors. It is similar to a SOA except it includes reflecting facets in both ends. This configuration creates multiple reflections inside the cavity and produces the laser effect. No input light is needed and a semi-transparent mirror is placed at the output facet in order to enable the light emission.

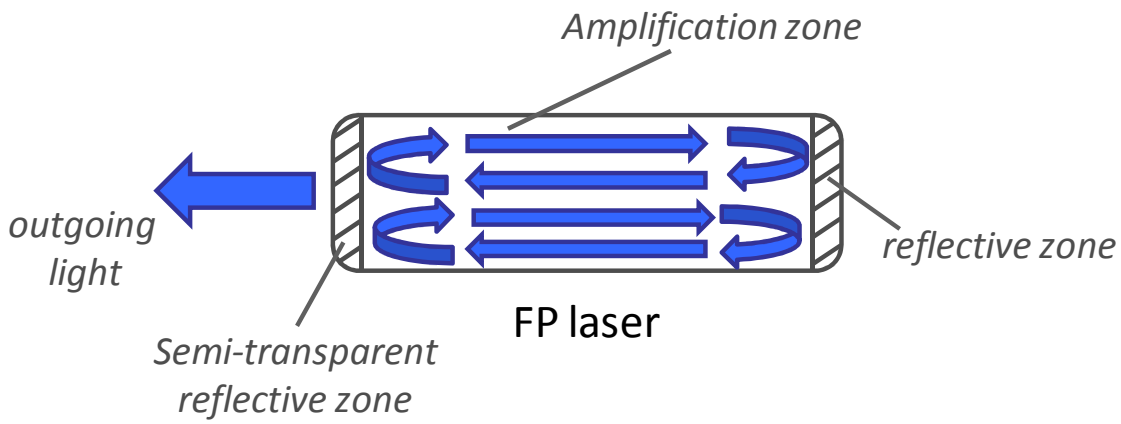

Figure 1-3 – FP laser operating principle

SOA devices can operate in these three configurations:

- TW-SOA (Travelling Wave SOA) using ultra-low reflective end facets
- FP-SOA where the reflections at the end facets are significant
- R-SOA where one facet is highly reflective and the other one has low reflectivity

Facet reflectivity is one of the key parameters in SOAs to form TW devices, optical cavities, or to redirect light to other directions. SOA components need a careful control on reflection from its end mirrors. Losses due to the facet reflectivity are a key parameter for mode selection. Depending on what we need, we can either minimize or maximize them. The influence on the design and the performances will be respectively described in chapter 2 and chapter 3.

1.1.3 Separate Confinement Heterostructure

In order to understand a separate confinement heterostructure (SCH), we should first analyze a simple heterostructure design. A heterostructure consists of a narrow bandgap active region (E_{g1}) sandwiched between wider bandgap barriers (E_{g2}) as we see in the Figure 1-4. If the active region is thin enough ($d \sim \lambda$), we obtain a quantization effect and we finally get a quantum well (QW). In bulk SOA structure, the central region is wide enough in order to get rid of the quantization effect ($d >> \lambda$).

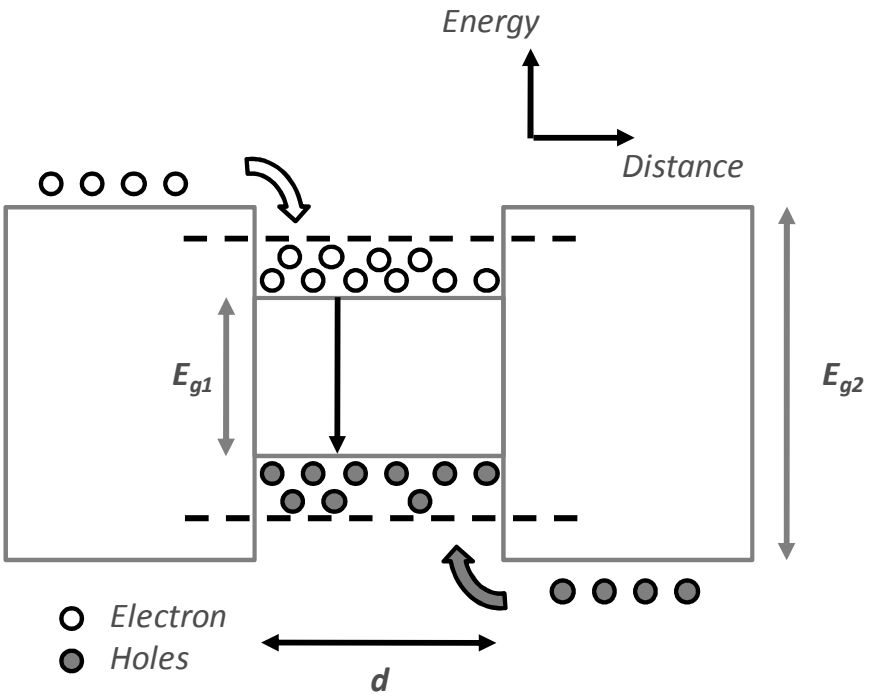

Figure 1-4 – Energy band diagram profile in a bulk heterostructure

We inject carriers (electrons in white and holes in grey) into the active region where they are confined thanks to potential barriers (bandgap discontinuity). The unpumped regions have wide bandgap and are transparent at the amplified wavelength. InGaAsP material is used for the SOA and RSOA active zone which is a III-V semiconductor with a narrow bandgap material. Narrow bandgap semiconductors are employed because their small energy gap means that their interband optical transitions produce emission in the mid-infrared. Interband structures show advantages over intersubband structures, in which it is difficult to establish sufficient electronic confinement for efficient operation, and generally have high threshold current densities. The main drawbacks of interband devices operating in the mid-infrared are the non-radiative loss by Auger recombination and intervalence band absorption. More details about the electronic confinement can be found in [4].

A good approximation for direct bandgap material is that bandgap and refractive index are inversely proportional. The refractive index step confines the optical mode in a controllable fashion. In fact, light is confined in high index region by total internal reflections. The allowed modes are obtained from the solution of Maxwell's wave-equation for electromagnetic wave which should satisfy the necessary boundary conditions. The refractive index profile and the simplest wave-shape are shown on the Figure 1-5. In SOA/RSOA design, it is important to know the amount of optical power confined to the central part of the waveguide. This is defined by the optical confinement factor Γ, which is defined as:

$$\Gamma = \frac{\text{Mode power in the active layer}}{\text{Total mode power}} = \frac{\int_{-d/2}^{+d/2} |E(x)|^2 dx}{\int_{-\infty}^{+\infty} |E(x)|^2 dx} \qquad (1\text{-}11)$$

It is usual to compute modal fields based on numerical solutions in order to calculate the optical confinement (as done in chapter 2).

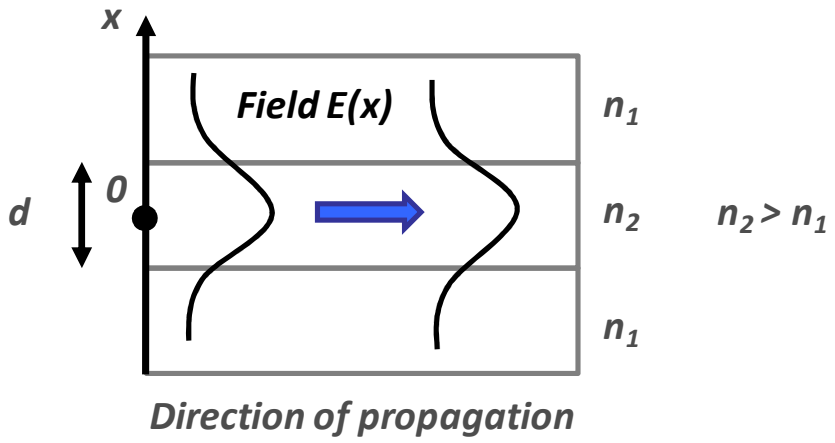

Figure 1-5 – Optical confinement in a bulk heterostructure

In the case of lasers, amplifiers and photodetectors, the electronic and optical confinements allow the engineering of the necessary wavelength for generation/detection of the radiation. Reduction of the active volume enables high optical gain at low injection current. A simple heterostructure is limited by a trade-off between the current density threshold and the optical confinement. The more we reduce d, the more J (density of current) will be small. But if d is too small, we lose the optical mode confinement. To solve these problems, we use a "SCH" in order to control independently the electronic and optical confinement. A "SCH" leads to more complex structures which allow separate confinement of carriers (d) and optical field (W) as represented in Figure 1-6. It is called double heterostructure.

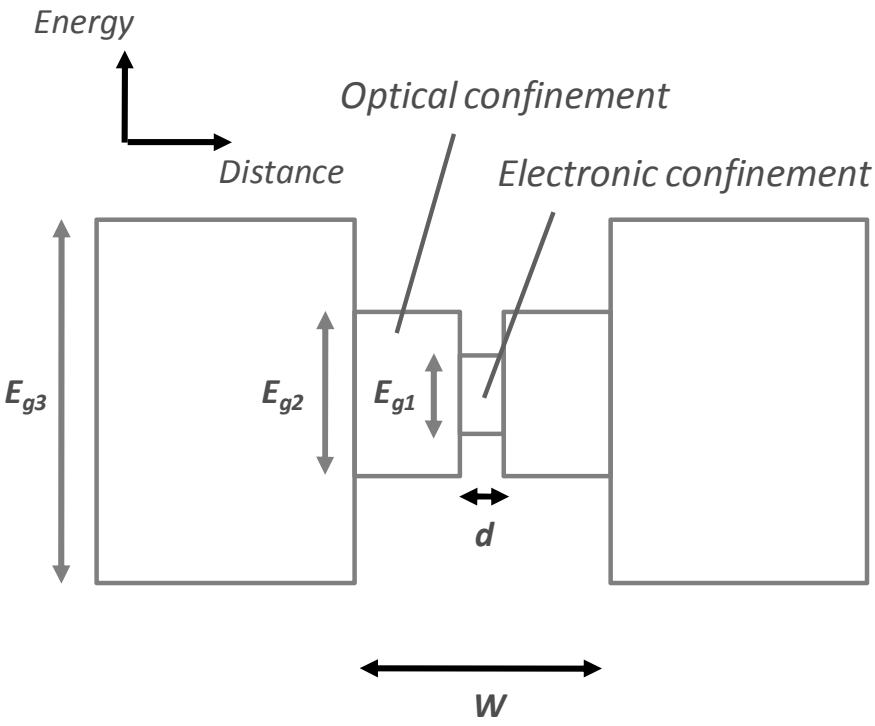

Figure 1-6 – Separate Confinement Heterostructure (SCH)

The double heterostructure consists of three different types of layers. The two central types of layers (E_{g1} and E_{g2}) lead to high Δn (Refractive index variation). A significant index step between the W region (E_{g2}) and the outside (E_{g3}) allows a good optical confinement in this region. Larger step in the refractive index allows tighter confinement. Naturally, electrons are looking for the lower energy level and hole for the higher one. That is why injected carriers are confined in the d region. This structure allows separating the electronic and optical confinement. All parameters such as the current density and the optical confinement can be separately optimized. We can choose a small d so a low current density threshold while keeping a good confinement factor [5]. SCH structure leads to some designs rules. The composition and thickness of these layers are detailed in chapter 2. The control of the optical confinement is critical in order to achieve high performances devices.

1.2 Material properties

Section 1.1.1 discusses radiative recombination mechanisms in direct gap semiconductors. As we mentioned, absorption, spontaneous and stimulated emissions are optical processes associated with radiative recombination. Calculation of the material gain depending on the recombination rates is presented and useful approximations are described in section 1.2.1. The gain approximation is then used for the model presented in chapter 3. Non-radiative recombination processes (which do not produce an emitted photon) will be discussed in chapter 3 as well as its impact on the RSOA dynamic (Chapter 4).

1.2.1 Material gain derivation

Let us consider idealized medium with a single propagation direction. A wave propagates in the z-direction, therefore from Maxwell's equation and considering the definition of the signal power P of the electro-magnetic wave, it can be demonstrated that [6]:

$$P(z) = P_0 \exp(2k_0 n'' z) \quad 1\text{-}12$$

Where P_0 is the initial power of the electro-magnetic wave, k_0 is the wave vector, n'' is the imaginary part of the refractive index and z is the direction of propagation.

Thus, it follows from the above expression for the power of electromagnetic wave in a medium with complex refractive index that the imaginary part of the refractive index n'' is directly related responsible for gain (or absorption g = -α) of the wave. The gain can be defined as:

$$g = -\alpha = 2k_0 n'' \quad 1\text{-}13$$

Where α is the absorption coefficient.

So we obtain the general definition of the gain:

$$\boxed{g = -\alpha = \frac{1}{P(z)} \frac{dP(z)}{dz}} \quad 1\text{-}14$$

The intensity is related with the overall photon density S(z) by:

$$P(z) = \hbar \omega v_g S_{eff} S(z) \quad 1\text{-}15$$

Where $S_{eff} = \frac{A}{\Gamma}$, v_g is the light group velocity and ω is the photon's angular frequency.

We are switching from the spatial-propagation model to a rate-equation model, and suppose that S(t) varies as given in (1-16), as it would in the case of a pulse propagation. So using the relation $z = v_g.t$ and $dz = v_g.dt$, we get:

$$\boxed{g = -\alpha = \frac{1}{v_g S(t)} \frac{dS(t)}{dt}} \quad 1\text{-}16$$

It is necessary to calculate the net rate $\frac{dS(t)}{dt}$ at which the photons appear (or disappear) in a unit volume of the semiconductor due to interaction with electrons. From a quantum-mechanical point of view, this rate is precisely the transition rate of electrons between the initial (i) and the final (f) states due to the interaction with an electro-magnetic wave.

The total net transition rate is called R_{nt} and we obtain $g = \frac{R_{nt}}{v_g S}$. This rate is obtained per unit volume of material and is given by the sum over all wave vectors k and k' where the wave vectors are those for the electron quantum states in the valence band (VB) and conduction band (CB).

$$R_{nt} = \frac{1}{V}\sum_{kk'}\left[W_{kk'}f(k)[1-f(k')] - W_{kk'}f(k')[1-f(k)]\right] = \frac{1}{V}\sum_{kk'}\left[W_{kk'}[f(k)-f(k')]\right]$$

1-17

Where we have used that $W_{kk'} = W_{k'k}$, V is the volume of the active zone and f(k) is the Fermi function of electron. $W_{kk'}$ is given by the Fermi's Golden Rule and it is equal to [7]:

$$W_{kk'} = \frac{2\pi}{\hbar}G^2(\omega)S\delta_{kk'}\left|M_{if}^T\right|^2\delta\left[E_f(k') - E_i(k) + \hbar\omega\right]$$

1-18

Where G(ω) is a constant which depends on the material parameters, ħ is the reduced Planck's constant, delta-symbol $\delta_{kk'}$ is null except when k=k', E_f and E_i are the energies at the initial (i) and the final (f) states and the matrix element M_{if}^T is a coefficient which depends on the light polarization.

The last term in the above expression represents the energy conservation for the electron transitions. We have to substitute $W_{kk'}$ in the expression of R_{nt} and to sum over k and k'. We notice that in order to carry out the summation over k, we transform equation (1-17) into an integral over the energy E. We obtain the final expression for R_{nt}:

$$R_{nt} = \frac{2\pi}{\hbar}G^2(\omega)S\left|M_{if}^T\right|^2\rho_r(E_{eh}-E_g)[f_c(E_e)-f_v(E_h)]$$

1-19

Where $E_{eh} = \hbar\omega$, ρ_r is the reduced density of states, E_e and E_h are fixed values because the conservation of both energy and momentum fixes the i and f states.

General expression for the material gain in bulk semiconductor, which will be noted g_m, is obtained by substitution of the net photon emission rate R_{nt} into the relation $g = R_{nt}/v_g S$. This yields:

$$g_m(\hbar\omega) = g_{3Dmax}(\hbar\omega)[f_c(E_e)-f_v(E_h)]$$

1-20

Where $g_{3Dmax}(\hbar\omega) = \frac{G_{3D}}{E_{eh}}\left|M_{if}^T\right|^2\rho_r\left(E_{eh}-E_g\right)$ and $G_{3D} = 2\pi\omega G^2(\omega) = \frac{\pi\hbar e^2}{n_r\varepsilon_0 c_0 m_0^2}$, here n_r is the index of refraction, c_0 is the speed of light in vacuum, m_0 is the free electron mass and ε_0 is vacuum permittivity.

In bulk materials, the reduced density of states is:

$$\rho_r\left(\hbar\omega - E_g\right) = \frac{1}{2\pi^2}\left(\frac{2m_r}{\hbar^2}\right)^{3/2}\sqrt{\hbar\omega - E_g}$$

1-21

The reduced density of states is calculated in exactly the same way as usual band density of states, except that instead of the electron (hole) effective mass one has to use the reduced effective mass: $\frac{1}{m_r} = \frac{1}{m_c} + \frac{1}{m_{dh}}$ where m_c is the electron effective mass in the CB and m_{dh} is the electron effective mass in the VB. The occupation probability of an electron (hole) with energy E_e (E_h) in the VB (CB) is given by the Fermi-Dirac statistic [8]:

$$f_{c,v}(E_{e,h}) = \frac{1}{1 + \exp(\frac{E_{e,h} - E_{F_c,F_v}}{k_B T})}$$

1-22

Where E_{F_c} and E_{F_v} are respectively the Fermi energy in the conduction and valence band, k_B is Boltzmann's constant and T is the absolute temperature.

We use a new coefficient C in order to simplify the expression of the gain where all material constants and factors with weak dependence on the photon energy are included:

$$\boxed{g_m(\hbar\omega) = C_{3D} \times (\hbar\omega - E_g)^{1/2} \times [f_c(E_e) - f_v(E_h)]}$$

1-23

We notice that the transparency condition detailed in equation (1-2) is confirmed ($\hbar\omega - E_g > 0$). The frequency dependence of the gain is determined by the density of states and the Fermi distribution functions, since $E_{e,h}$ depends on $\hbar\omega$ as well.

The optical gain formula is very convenient to analyse the key properties of the active medium. The square root imposes the condition: $\hbar\omega > E_g$ (which is implicit in the fact that we pick states in the conduction and valence bands) and amplification takes place if the gain is positive so:

$E_e - E_{F_c} \leq E_h - E_{F_v}$

$\Leftrightarrow E_e - E_h \leq E_{F_c} - E_{F_v}$

These conditions have been found in 1961 by Bernard and Duraffourg [9] and are given by:

$$\boxed{E_g < \hbar\omega = E_e - E_h \leq E_{F_c} - E_{F_v}}$$

1-24

The minimal value of the right hand side is called the transparency condition: $E_{F_c} - E_{F_v} = E_g$. At this condition $g_m(\hbar\omega) = 0$ and the material just becomes transparent at $\hbar\omega = E_g$, i.e. there are neither absorption nor gain. In order to achieve $E_g < E_{F_c} - E_{F_v}$ (positive gain), it is necessary to supply an excess of electrons and holes to the medium via electrical pumping (since the Fermi energy levels depend on the electron density). We estimated the Fermi energy level by using Nilsson approximation [10]:

$$E_{F_c} = \left\{ \ln\left(\frac{n}{n_c}\right) + \left(\frac{n}{n_c}\right)\left[64 + 0.05524 \times \left(\frac{n}{n_c}\right) \times \left(64 + \sqrt{\frac{n}{n_c}}\right)\right]^{-\frac{1}{4}} \right\} \times kT$$

$$E_{F_c} = \left\{ \ln\left(\frac{n}{n_v}\right) + \left(\frac{n}{n_v}\right)\left[64 + 0.05524 \times \left(\frac{n}{n_v}\right) \times \left(64 + \sqrt{\frac{n}{n_v}}\right)\right]^{-\frac{1}{4}} \right\} \times kT$$

1-25

Where n_c and n_v are constants: $n_c = 2\left(\frac{m_c kT}{2\pi\hbar^2}\right)^{3/2}$, $n_v = 2\left(\frac{m_{dh} kT}{2\pi\hbar^2}\right)^{3/2}$ and $m_{dh} = \left(m_{lh}{}^{3/2} + mhh3223\right.$.

The energy band structure can be simplified using parabolic shape with one single CB and two VBs as shown in Figure 1-7.

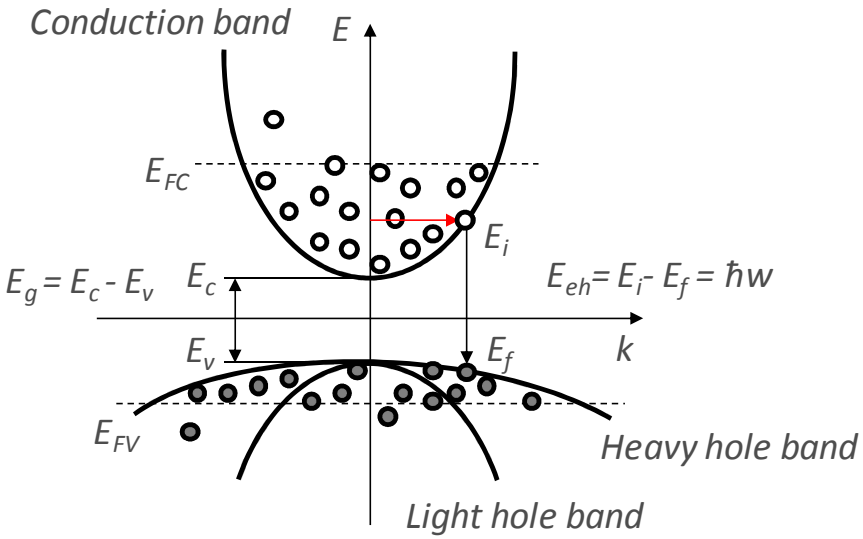

Figure 1-7 – Schematic energy band structure for direct bandgap semiconductor depending on the momentum (k)

Based on the parabolic approximation, the electron energy in the CB or VB can be written as:

$$E_e = E_c + \frac{\hbar^2 k^2}{2m_c}$$

$$E_h = E_V - \frac{\hbar^2 k^2}{2m_{dh}}$$

1-26

Considering a transition between the CB (energy E_e) and the VB (energy E_h) and having the same momentum vector, we obtained:

$$E_e - E_h = h\nu = E_g + \frac{\hbar^2 k^2}{2m_c} + \frac{\hbar^2 k^2}{2m_{dh}} = E_g + \frac{\hbar^2 k^2}{2m_r}$$

1-27

Then we obtain equation (1-28) when substituting (1-26) in (1-27):

$$E_e = E_c + \left(h\nu - E_g\right)\frac{m_{dh}}{m_c + m_{dh}} = E_c + \left(h\nu - E_g\right)\frac{m_r}{m_c}$$

$$E_h = E_V - \left(h\nu - E_g\right)\frac{m_c}{m_c + m_{dh}} = E_V - \left(h\nu - E_g\right)\frac{m_r}{m_{dh}}$$

1-28

We can demonstrate that equation (1-23) becomes [11]:

$$g_m(\hbar\omega) = \frac{{c_0}^2}{4\sqrt{2}\pi^{3/2} n_r^2 \nu^2 \tau_{rad}} \left[\frac{2m_{dh}m_c}{\hbar(m_c + m_{dh})}\right]^{3/2} [f_c(E_e) - f_v(E_h)] \sqrt{\nu - \frac{E_g}{h}}$$

1-29

The material gain is numerically calculated using the following parameters:

Symbol	Parameter	value	unit
c_0	Speed of light in vacuum	3.10^8	m/s
n_r	Refractive index	3.3	----
τ	Radiative recombination lifetime	900	ps
k_B	Boltzmann's constant	$1.38x10^{-23}$	J/K
T	Temperature	300	K
m_0	Electron rest mass	$9.11x10^{-31}$	Kg
m_c	Electron effective mass in the CB	$m_0x0.045$	Kg
m_{hh}	Electron effective mass in the VB	$m_0x0.46$	Kg
m_{lh}	Electron effective mass in the VB	$m_0x0.056$	Kg
E_g	Band gap Energy	$0.8x1.6x10^{-19}$	J
h	Planck constant	$6.63x10^{-34}$	J/s

Table 1-1 – SOA material parameters used for material gain calculation

Plot of g_m spectra is represented in Figure 1-8. The carrier density is the input parameter and the material gain is plotted against the difference between the photon and the band gap energy. All models are done using Matlab V7.9.

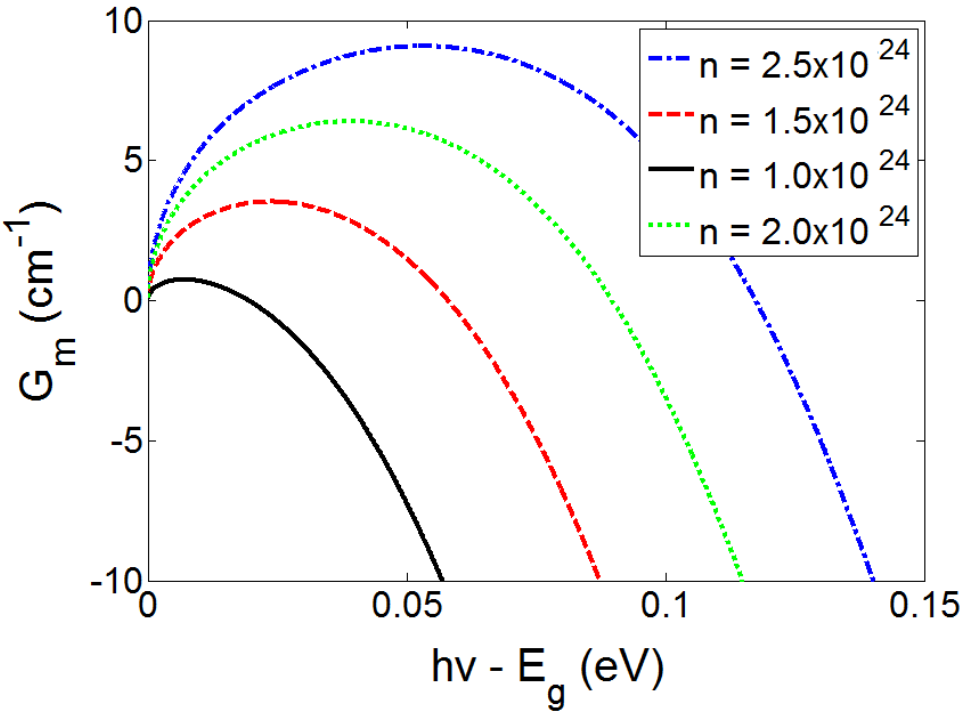

Figure 1-8 – Simulated material gain depending on the photon energy

1.2.2 Useful material gain approximation and net gain approach

The optical gain dependence on the photon energy and the carrier density is quite complex. However it can be approximated using simple expressions as:

$$\boxed{g_m(\lambda, n) = a(n - n_0) - a_2(\lambda - \lambda_p)^2} \quad \text{1-30}$$

Where $\lambda_p = \lambda_0 - b_2(n - n_0)$.

Numerical simulations were carried out and are represented in Figure 1-9.We assume typical values for the fitting parameters:

Symbol	Parameter	value	unit
a	Differential gain	6.10^{-20}	m^2
a_2	Constant related to the spectral width of the gain spectrum	$0.15x10^{19}$	$m^{-1}.m^{-2}$
b_2	Fitting parameter	$2.7x10^{-32}$	$m.m^3$
n_0	Carrier density at transparency	$1x10^{24}$	m^{-3}
λ_0	Operating wavelength	1550	nm

Table 1-2 – SOA fitting parameters for material gain approximation

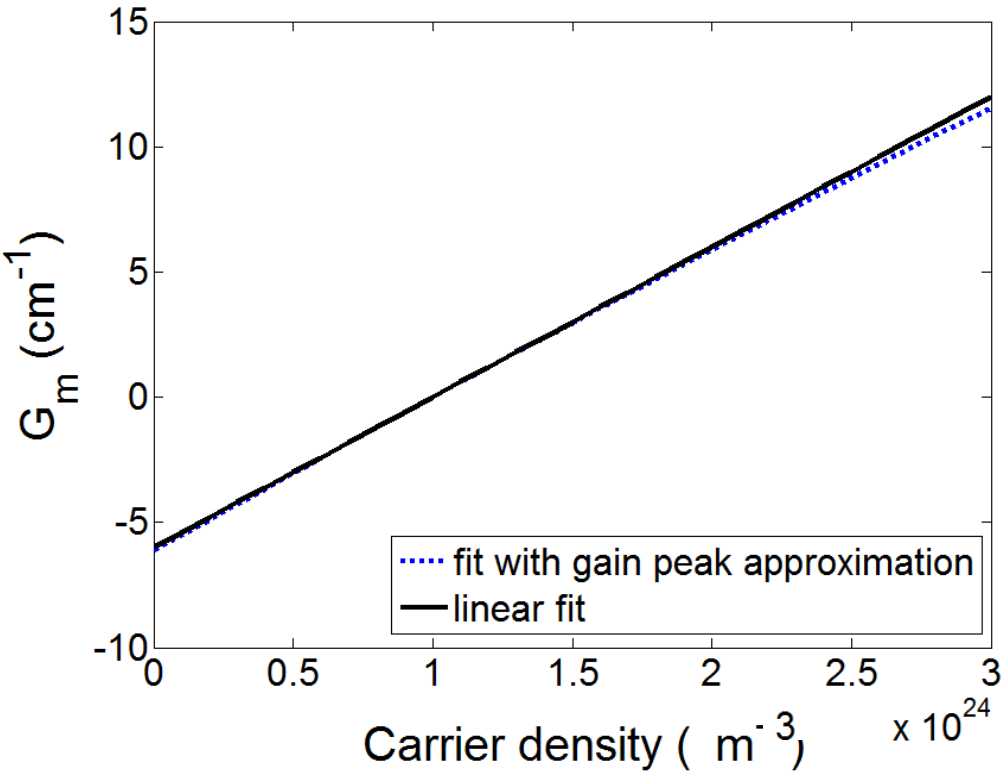

Figure 1-9 – Peak gain coefficient for bulk InGaAsP material at 1550 nm

The peak gain is approximately linear in a wide range of carrier density values. Thus a linear function is used when small computation time is required and moderate accuracy is acceptable.

$$g_m(\lambda, n) = a(n - n_0) \qquad 1\text{-}31$$

We already saw, in section 1.1.3, that the use of the separate heterostructure is important in order to optimize the electronic and the optical confinement. The optical field overlaps the active medium but also the parts around it. The amplification takes place in the active region. Only part of the optical field, confined in this region, takes part in the stimulated emission therefore the

optical gain (g) in equation (1-14) is not only equal to the material gain. Considering the material gain g_m, the modal gain is given by:

$$g_{mod} = \Gamma . g_m$$

1-32

We can define the waveguide modal attenuation coefficient α_i which characterizes the internal losses. These losses decrease the overall modal gain and the net mode gain can be defined by:

$$g_{net} = g_{mod} - \alpha_i = \Gamma . g_m - \alpha_i$$

1-33

The internal losses can be decomposed into two different losses (α_a, α_c). The modal loss in the active region is defined by $\Gamma.\alpha_a$ and the modal loss in the cladding region is defined by $(1-\Gamma).\alpha_c$. Thus, the total internal modal loss can be written as:

$$\alpha_i = \Gamma \alpha_a + (1 - \Gamma)\alpha_c$$

1-34

Figure 1-10 shows the different regions with the corresponding losses.

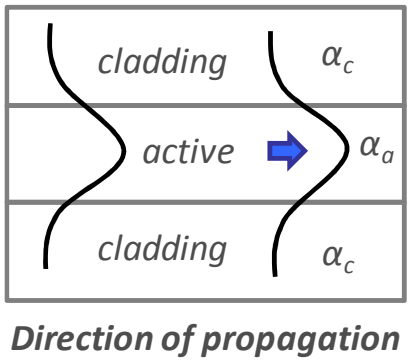

Figure 1-10 – Optical confinement taking into account the different losses

From equation (1-33) and (1-34), we get:

$$\boxed{g_{net} = \Gamma . g_m - \alpha_i = \Gamma . g_m - \Gamma \alpha_a - (1 - \Gamma)\alpha_c}$$

1-35

1.3 Theoretical approach of the optical amplification

The wave propagation in a gain medium is studied in this section by considering a complex refractive index. The solutions are then applied to an optical resonator (section 1.3.2) and the impact of the facet reflectivity on the optical gain is deduced. Finally, a preliminary analysis of the carrier density spatial distribution will be presented and the overall gain modelled (the carrier density spatial distribution will be used in Chapter 3 and 4 in order to analyse the static and dynamic performance of a RSOA device). The optical confinement strongly affects the carrier

density distribution and its analysis leads to some design characteristics that will be discussed in chapter 2.

1.3.1 Wave equation in a medium with gain or/and losses

We consider the propagation of an electromagnetic wave in a linear medium that can introduce gain or loss as represented in Figure 1-10. The refractive index (n) is complex and can be written as: n = n'+ i.n". n' is responsible for the refraction of light (real part of the refractive index) and n" is the imaginary part of the refractive index. The gain is equal to $g = 2k_0 n''$ ($g > 0$: amplification (gain) and $g < 0$: absorption (loss)). Based on Maxwell's equations, the propagation equation can be written as (known as Helmholtz's equation):

$$\nabla^2 E + \omega^2 \frac{n^2}{c_0^2} E = 0$$

1-36

The general solutions are linear combinations of $exp[i(\beta z - \omega t)]$. Each of which satisfy equation (1-36) and it becomes [12]:

$$E(z,t) = E_0 exp[i(\beta z - \omega t)]$$

1-37

Here E(z, t) is the electric field, which depends on the position z and time t. β, z and ω are the propagation constant, the propagation direction and the angular frequency respectively.

This solution can be written as:

$$E(z,t) = E_0 exp[i(\beta z - \omega t)] = E_0 e^{i\beta z} e^{-i\omega t} = F(z) e^{-i\omega t}$$

1-38

Then the propagation equation becomes:

$$\frac{\partial^2 F(z)}{\partial z^2} e^{-i\omega t} + \omega^2 \frac{n^2}{c_0^2} F(z) e^{-i\omega t} = 0$$

1-39

We can define $\beta = k_0.n$ and $k_0 = \omega / c_0$ so $\beta = (\omega / c_0).n$, where n = n'+ i.n" is the complex refractive index. Therefore equation (1-39) becomes:

$$\frac{\partial^2 F(z)}{\partial z^2} + \beta^2 F(z) = 0$$

1-40

The general solution for this equation is given by:

$$F(z) = A^+ . e^{-\beta i z} \equiv F^+(z)$$

1-41

Similarly, we get the solution for a backward wave:

$$F(z) = A^- . e^{\beta i z} \equiv F^-(z)$$

1-42

These results can be substituted in equation (1-38) and we can summarize:

For wave propagating forward,
$E^+(z,t) = F^+(z)e^{i\omega t}$ and $F^+(z) = A^+.e^{-\beta iz}$

For wave propagating backward,
$E^-(z,t) = F^-(z)e^{i\omega t}$ and $F^-(z) = A^-.e^{\beta iz}$

1-43

1.3.2 Amplification factor (Small-signal internal gain)

The light wave of amplitude F_{in} strikes the active medium at z = 0. Part of this wave will be reflected ($r.F_{in}$), and part ($t.F_{in}$) will be transmitted into the medium. Using $F^{\pm}(z)$ defined in section 1.3.1, transmitted field propagates forward along +z axis, strikes the second interface at z = L, part of this field is reflected back ($r.F^+(L)$), and part is transmitted out of the medium ($t.F^+(L)$). The reflected field at z = L propagates backward along – z direction, strikes again the first interface at z = 0. Part of this field is reflected ($r.F^-(0)$), part is transmitted out ($t.F^-(0)$). Reflected part propagates along + z direction, and so on. All different phenomena are represented in Figure 1-11.

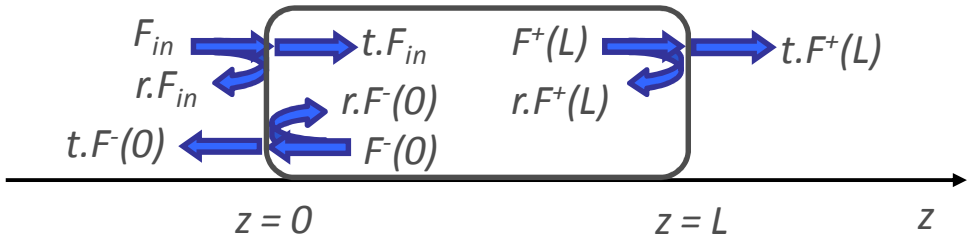

Figure 1-11 – Cavity field round trip

It is necessary to find the cavity transmission coefficient. In case of SOA or RSOA, it is defined as the intrinsic gain which is the ratio of the input signal power at the input facet to the signal power at the output facet:

$$G = \frac{|F_{out}|^2}{|F_{in}|^2}$$

1-44

F_{out} is equal to $tF^+(L)$ (for a SOA) or $tF^-(0)$ (for a RSOA). Considering the definition of $F^{\pm}(z)$, we obtain:

$$\begin{cases} F^+(0) = A^+;\ F^+(L) = A^+.e^{-i\beta L} \\ F^-(0) = A^-;\ F^-(L) = A^-.e^{i\beta L} \end{cases}$$

1-45

Considering the different round trip inside the cavity,

$$\begin{cases} F^+(0) = A^+ = t.F_{in} + r.F^-(0) \\ F^-(L) = A^-.e^{\beta iL} = r.F^+(L) \end{cases}$$

1-46

Therefore,

$$\begin{cases} A^+ = \frac{t}{1-r^2.e^{-2i\beta L}} \times F_{in} \\ A^- = \frac{r.t.e^{-2i\beta L}}{1-r^2.e^{-2i\beta L}} \times F_{in} \end{cases}$$

The output field can be calculated as:

$$F_{out} = t.F^+(L) = \frac{t^2 e^{-\beta iL}}{1-r^2.e^{-2i\beta L}} \times F_{in}$$

1-47

The gain G becomes:

$$G = \left| \frac{t^2 e^{-\beta iL}}{1-r^2.e^{-2i\beta L}} \right|^2 = t^4.\frac{e^{-\beta iL}}{1-r^2.e^{-2i\beta L}} \times \frac{e^{\beta^* iL}}{1-r^2.e^{2i\beta^* L}}$$
$$= \frac{t^4.e^{-i(\beta-\beta^*)L}}{1-r^2(e^{-2i\beta L}+e^{2i\beta^* L})+r^4(e^{-2i(\beta-\beta^*)L})}$$

1-48

Considering that the wave number can be written as:

$$\beta = k_0 n' + i\frac{g}{2}$$

1-49

Then the intrinsic gain can be written as:

$$G = \frac{t^4 e^{gL}}{1-2r^2 e^{gL}\cos(2k_0 n'L)+r^4 e^{2gL}} = \frac{t^4 e^{gL}}{(1-r^2 e^{gL})^2+4r^2 e^{gL}\sin^2(k_0 n'L)}$$

1-50

We introduce some new notations:

$r^2 = R$, the power reflectivity
$t^2 = 1 - r^2$ so $t^4 = (1-R)^2$

This gives the final formula for G (small-signal internal gain which means that the signal has negligible influence on the SOA gain coefficient):

$$G(\lambda_0) = \frac{(1-R)^2 e^{gL}}{(1-Re^{gL})^2+4Re^{gL}\sin^2(k_0 n'L)}$$

1-51

Where $k_0 = \frac{2\pi}{\lambda_0}$.

We had made the implicit assumption that both facets had the same reflectivity; if not ($R_1 \neq R_2 \neq R$), then the internal gain of a FP SOA becomes:

$$\boxed{G(\lambda_0) = \frac{(1-R_1)(1-R_2)e^{gL}}{(1-\sqrt{R_1R_2}e^{gL})^2 + 4\sqrt{R_1R_2}e^{gL}\sin^2(k_0n'L)}}$$

1-52

The internal gain depends on the wavelength $\lambda_0$which means that at some specific values of λ_0, $G(\lambda_0)$ is maximum. This happens when the denominator is minimal and takes place if $\sin^2(k_0n'L) = 0$ so $k_0 = \frac{\pi}{n'L}M$ where M is an integer. The wavelength at G_{max} is $\frac{\lambda}{2}M = L$ where $\lambda = \frac{\lambda_0}{n'}$ and λ_0 is the wavelength in the vacuum. The $\sin^2$ factor is equal to one at the anti-resonance frequencies.

If $R_1 = R_2 = 0$, we obtain a perfect TW SOA then:

$$\boxed{G_{TW} = G_S = e^{gL}}$$

1-53

Where G_S is the single-pass amplifier gain.

Therefore the optical power increases exponentially with the length of the device.

$$\boxed{P(z) = P_{in}e^{gz}}$$

1-54

The single pass gain is generally a very rough approximation. The carrier density is non-homogeneous along the SOA thus the gain must be carefully integrated. The spatial distribution of the carrier density in SOA device is presented in the next section.

1.3.3 Effect of non-homogeneous carrier density distribution

The carrier density is affected by the photon density, both from the amplified signal and the spontaneous emission. As described in Figure 1-1-(b), the spontaneous emission is created inside the active zone producing extra noise during the amplification. The spatial distribution of the carrier density is then strongly affected by this process. The spontaneous emission is produced all along (every z) the device. A part of the emitted photons are guided and amplified. It is called the Amplified Spontaneous emission (ASE). The main noise contribution is attributed to the ASE noise [13]. A model developed in [14] by M. J. Connelly is used to determine the influence of the optical confinement on the optical gain. Multi-section model for a bulk SOA enables us to take in account the non-homogeneous carrier density distribution. The model uses a determinist approach and neglects the interaction between the ASE noise and the signal. It is used as a preliminary approach. Then our own model will be developed in Chapter 3 in order to study in details the influence of the different recombination mechanisms. The optical gain depending on the optical confinement is represented in Figure 1-12.

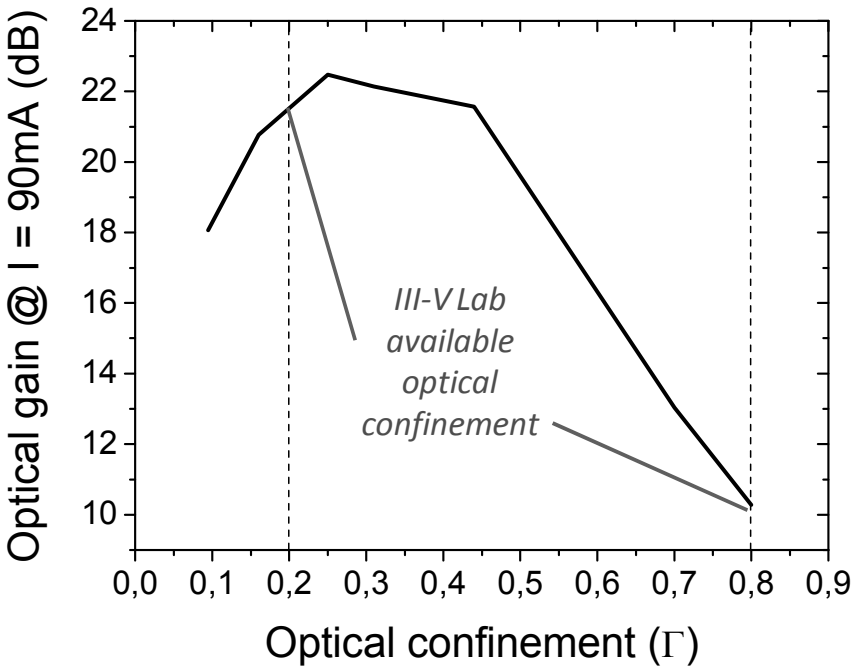

Figure 1-12 – Calculated optical gain depending on optical confinement in 700 µm long SOA at 1550 nm and P_{in} = -40 dBm (based on the Connelly's model)

During this work, two optical confinements have been studied (Γ = 20% and Γ = 80%). Simulations based on the Connelly's model [14] and our vertical structures (detailed in chapter 2) are carried out for both optical confinements and represented in Figure 1-13. At low input optical power, the signal power is neglected and the ASE is considered as dominant. The carrier density has a symmetrical shape with a peak at the centre of the SOA. In fact, the forward and backward travelling ASE signals are respectively maximum at the output and input facet. By decreasing the optical confinement from 80 % to 20%, we reduce the carrier depletion due to less guided ASE.

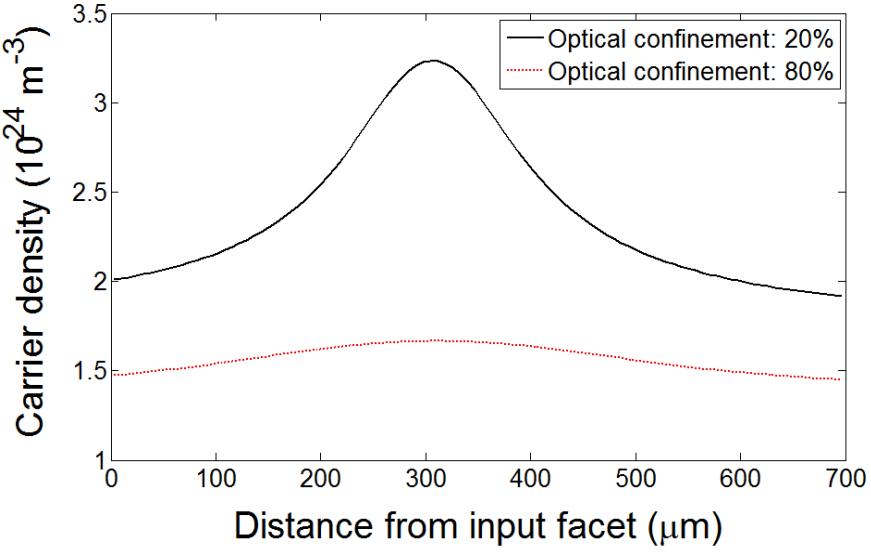

Figure 1-13 – Simulations of the carrier density spatial distribution based on the Connelly's model

At high optical confinement, the travelling ASE consumes all carriers and leads to a weak signal amplification. This carrier depletion along the SOA is called the Longitudinal Spatial Hole Burning (LSHB) and has been observed in SOA devices [15].

The LSHB induces a gain reduction. The impact of the optical confinement has been investigated in [16] and shows that low confinement devices are not saturated by the ASE. Therefore a trade-off must be considered between the necessary optical confinement for the signal amplification and the LSHB reduction.

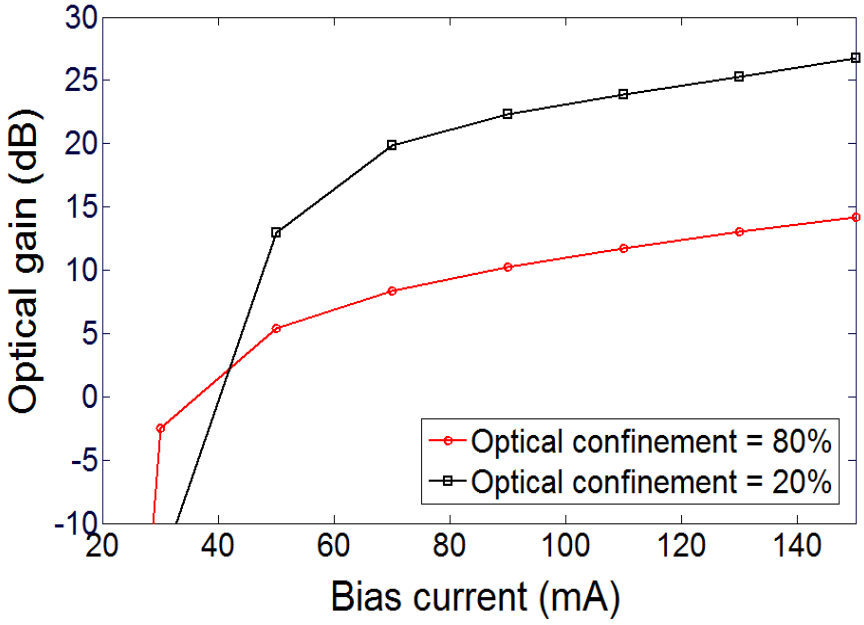

Figure 1-14 – Simulated optical gain in 700 µm long SOA at 1550 nm based on the Connelly's model. Input signal power = - 40 dBm

Figure 1-14 represents the simulated optical gain at 1550 nm for two values of the optical confinement (again Connelly's model [14] is used). At low optical confinement (20%), the gain is higher (by 12 dB at 90 mA) than high optical confinement (80%). In RSOA, this effect is even stronger because of the compactness of the device and should be taken into account when designing high performances structures.

1.4 Conclusions

This chapter discusses several aspects related to the SOA theory. An introduction about the radiative recombination processes was done and the different notions introduced by Einstein were described. The basic types of SOA structures as FP-SOA, TW-SOA and R-SOA have been presented and an introduction to optimized vertical structure as SCH was done. Low current density threshold while keeping a good optical confinement can be obtained and will be used to design SOA and RSOA in Chapter 2.

The problem of a radiation interacting with matter in a bulk semiconductor (whose physical dimensions are much larger than the Broglie wavelength of the electrons) is then detailed

and leads to the calculation of the material gain. The conduction and valence bands are approximated by parabolas and the occupation level obeys the Fermi-Dirac statistics. Calculations of the absorption and gain coefficient are detailed and the necessary condition for the positive gain is explained (Bernard and Duraffourg condition).

From a practical point of view, an approximation of the material gain was proposed based on two important physical parameters: the differential gain (a) and the transparency carrier density (n_0). The carrier lifetime has not been considered yet and will be detailed in chapter 4. The net gain of SCH is smaller than the material gain. It is because of the cladding and active zone losses. The optical confinement affects the optical mode spatial distribution and needs to be considered in our design (Chapter 2). A classic approach was used to provide an intuitive representation of the light-matter interaction. The real part of the refractive index directly acts on the field phase. The imaginary part of the refractive index interacts with the amplitude of the field (responsible for the gain). This approach allows the determination of the refractive index depending on the wavelength. The quantum mechanics approach was not described in this chapter but more details can be found in [17]. The classic approach provides a useful background to determine the light-matter interaction inside an optical resonator.

Section 1.3.2 explores the relevant features of such a cavity with gain medium. We calculated the optical gain depending on the facet reflectivity, the single pass gain (calculated from the net gain in section 1.2.2) and the wavelength. This expression confirms the importance of the facet reflectivity in the device behaviour and completes the introduction done in section 1.1.2.

Finally, an analysis of the spatial carrier distribution was proposed and shows the influence of the non-homogeneous carrier density profile on the overall gain. It will be completed in Chapter 3 where all recombination rates are detailed.

References

[1] N. Zakhleniuk, "EE721: Optical components I", lecture notes, University of Essex, part A, 2007-2008, pp. 25-27
[2] O. Svelto, "Principles of lasers", Plenum Press, 4th edition, pp 2-7
[3] G. H. Duan, "COM 341: FON Physique des Lasers", lecture notes, Ecole National Supérieure des Télécommunications, Chap. 2, 2006-2007, pp 11-17
[4] A. Yariv, "Optical electronics in modern communications", California Institute of technology, 1997
[5] J.Verdeyen, "Laser Electronics", University of Illinois,1994
[6] N. Zakhleniuk, "EE721: Optical components I", lecture notes, University of Essex, part B, 2007-2008, pp. 13-15
[7] N. Zakhleniuk, "EE721: Optical components I", lecture notes, University of Essex, part B, 2007-2008, pp. 17-18
[8] A. Yariv, Opt. Electron. New Yok: HWR International, 1985
[9] M. G. A. Bernard and G. Duraffourg, "Laser conditions in semiconductors," Phys. Status Solidi, Vol. 1, 1961, pp. 699-703
[10] N.G Nilsson, "empirical approximations for the Fermi energy of a semiconductor with parabolic bands", Appl. Phys. Lett., Vol. 33, No. 7, 1978, pp. 653-654
[11] M. Connelly, "Semiconductor Optical Amplifiers", Boston, MA: Kluwer Academic, Ch. 4. 2002, pp. 44-51
[12] C. Ware, "Récuperation d'horloge par boucle à verrouillage de phase utilisant le mélange à quatre ondes dans un amplicateur optique à semi-conducteurs". PhD Thesis, École Nationale Supérieure des Télécommunications, Appendix C, 2003, pp. 115-116
[13] M. Shtaif, B. Tromborg, G. Eisenstein, "Noise Spectra of Semiconductor Optical Amplifiers: Relation Between Semiclassical and Quantum Descriptions", J. Quantum Electron., Vol. 34, No. 5, 1998, pp. 869-878.
[14] M. J. Connelly, "Wideband Semiconductor Optical Amplifier Steady-State Numerical Model ", J. Quantum Electron., Vol 37, No. 3, March 2001, pp. 439-447
[15] J. L. Pleumeekers, M.-A. Dupertuis, T. Hessler, P. E. Selbmann, S. Haacke, and B. Deveaud, "Longitudinal Spatial Hole Burning and Associated Nonlinear Gain in Gain-Clamped Semiconductor Optical Amplifiers", J. Quantum Electron., Vol. 34, No. 5, May 1998, pp. 879 - 886
[16] R. Brenot et al., "Experimental study of the impact of optical confinement on saturation effects in SOA", in proc. OFC 2005, OME50, March 2005, Anaheim, CA
[17] G. H. Duan, "COM 341: FON Physique des Lasers", Lecture notes, Ecole National Supérieure des Télécommunications, Chap. 3, 2006-2007, pp 36-49

Chapter 2. Conception and fabrication of SOA and RSOA

The physical mechanisms involved in the optical amplification have been detailed in Chapter 1. The material gain strongly depends on the active zone medium, as the probability of radiative recombination should be high enough to ensure large gain at low current injection.

More precisely the semiconductor material should be based on the optimisation of many physical parameters, notably the differential gain (a) and the transparency carrier density (n_0). The net gain depends on the vertical structure and the design of the device (Active and cladding layers). The optical confinement directly impacts the carrier density distribution (section 1.3.3) and consequently the overall gain. It has been demonstrated that the facet reflectivity affects the amplification factor and needs to be carefully controlled. Therefore the structural design, the growth of the active zone and the facet reflectivity are key parameters in order to obtain high-performance SOA and RSOA.

The desirable properties of a practical SOA and RSOA are: a high gain, a large optical and modulation bandwidth, a low polarisation sensitivity, a high saturation output power, a low noise level, and good linearity.

Alcatel-Lucent extensively investigated the field of SOA during more than 20 years but new design rules are required for RSOA used as optical transmitter (direct electrical modulation). In fact, RSOA optimisation requires many experimental investigations and careful interpretations. In addition to the aforementioned gain and carrier density, other parameters, such as optical confinement, length and facet reflectivity, influence the linearity and modulation bandwidth in significant ways, for which intuitive guesses are far from being reliable.

In this chapter, we underline the main design rules related to SOAs and their equivalence for RSOA design. The growth of the vertical layers and the chosen structure are detailed in section 2.2.1. Then the fabrication and processing are discussed. In order to go from the wafers to the final device, cleaving, mounting, bounding and facet coating are needed. Each step is detailed in section 2.2. The static and dynamic evaluations are done respectively in chapter 3 and 4.

2.1 Design Outline

Structural designs of SOA and RSOA are detailed in this section. The composition, thickness and refractive index of the several layers are described for two different designs (commonly used in III-V lab). Quaternary (InGaAsP) alloy is grown. The active zone has a bandgap energy of 0.8 eV in order to amplify the 1.55 μm wavelength. The issues due to the lattice being mismatched (strained active zone) in order to obtain polarization independent devices are discussed. The advantages and defects of the Buried Ridge Structure (BRS) design used for our devices are explained in section 2.1.2. The optical confinement is modelled in the active and passive layers. To evaluate the SOA tapering zone geometry, the optical mode propagation is also calculated.

2.1.1 SOA wafers growth

The development of semiconductor photonic devices such as lasers, amplifiers and photodetectors, has been enabled by advanced epitaxial growth techniques: liquid phase epitaxy (LPE) [1], vapor-phase epitaxy (VPE) [2], metal organic chemical vapour deposition (MOCVD) [3] and molecular beam epitaxy (MBE) [4]. In III-V lab, SOA wafers are grown using MBE: thermionic emission allows the atoms from a material cell to escape and to be assembled on the substrate in ultra-high vacuum. Several layers with different compositions and dopings can be grown. In order to obtain high quality interfaces between the different grown layers, it is necessary to match the various lattice constants. A lattice mismatch induces poor quality interface and related defects inducing non-radiative recombination. However, strained layers based on lattice mismatch can be grown in particular cases as described below.

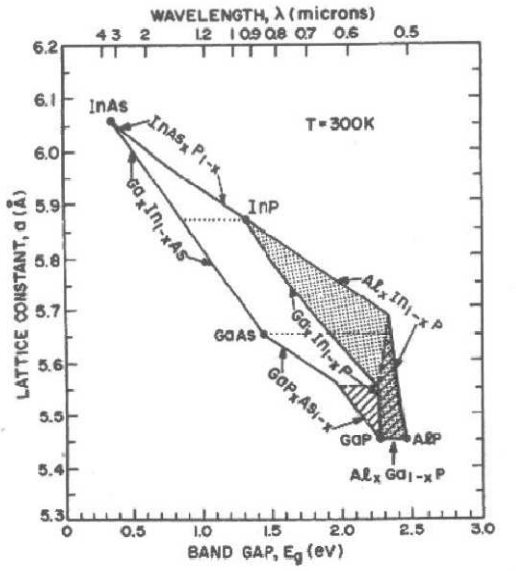

Figure 2-1 – Band gap and lattice constants of several ternary and quaternary compounds formed from the binary compounds [5].

The active regions of the SOA developed in this project are bulk structures based on InGaAsP. This section describes the advantages and limitations of the vertical structure. The refraction index values and the doping density for the various materials are reported in Table 2-1.

Material	Bandgap Wavelength (µm)	Doping Density (cm^{-3})	Refractive Index
InP	0.9	N $1x10^{18}$	3.16
InP	0.9	P $7x10^{17}$	3.165
InP	0.9	Undoped	3.17
InGaAsP (Q1.55)	1.6	Undoped	3.54
InGaAsP (Q1.17)	1.17	Undoped	3.33
InGaAsP (Q1.17)	1.17	N $1x10^{18}$	3.32

Table 2-1– Bandgap wavelength and refractive index for various materials and doping

The refractive index of all layers takes into account the injection of carriers into the semiconductor material. A carrier density of 2.10^{18} cm^{-3} is considered. It is important to note that the passive layer (InGaAsP Q1.17) is n-type doped in order to keep high electron mobility when the carriers need to pass through this layer.

During this thesis, two vertical structures have been studied. The vertical structure includes an active and passive layer. The active zone of the RSOA was grown using molecular beam epitaxy (MBE), consisting of InGaAsP Q1.55. In order to achieve low optical confinement, extra InGaAsP layers are used and based on low refractive index (n = 3.33). The passive layer is used to attract the optical mode when propagating through the tapering region. More details on the Spot-size converter design are presented in section 2.1.3.

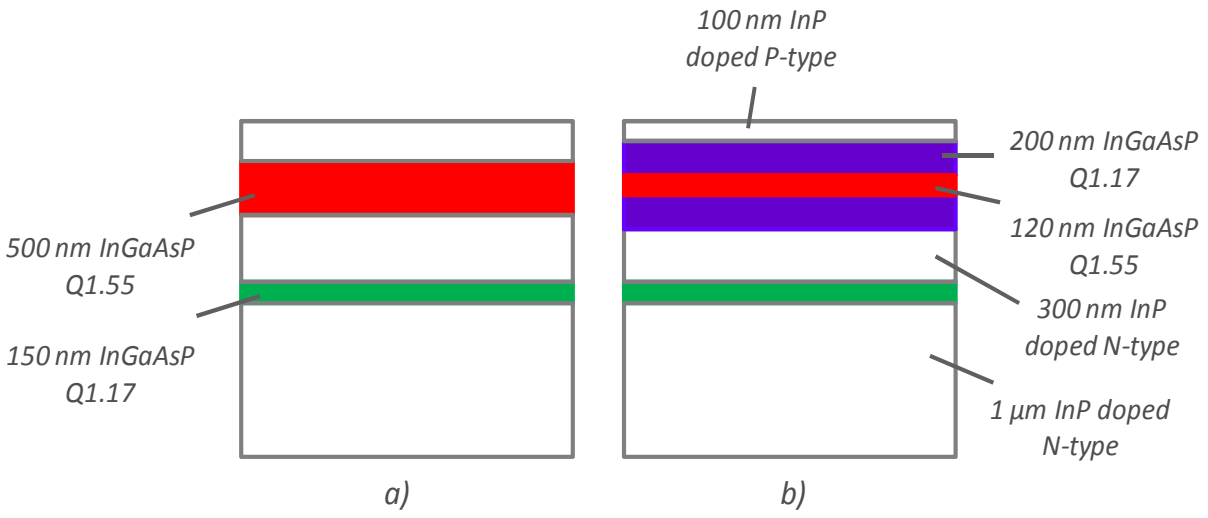

Figure 2-2 – Layer structure of the InGaAsP-based bulk SOA (a) for 80% and (b) for 20% optical confinement

In order to achieve the polarisation independence required for practical uses of SOAs, TE and TM eigenmodes are considered separately. Figure 2-3 shows the calculated TE and TM

optical confinements (left scale) as a function of the active region thickness, which is surrounded by 200 nm of separate confinement heterostructure (SCH) [6]. As expected, optical confinement increases as a function of active region thickness, since these high refractive index regions concentrate the optical field within the active material. The advantages of such a structure (SCH) have been detailed in section 1.3.3. It is important to obtain an accurate control of the optical confinement because it is directly related to the net gain as developed in equation (1-35).

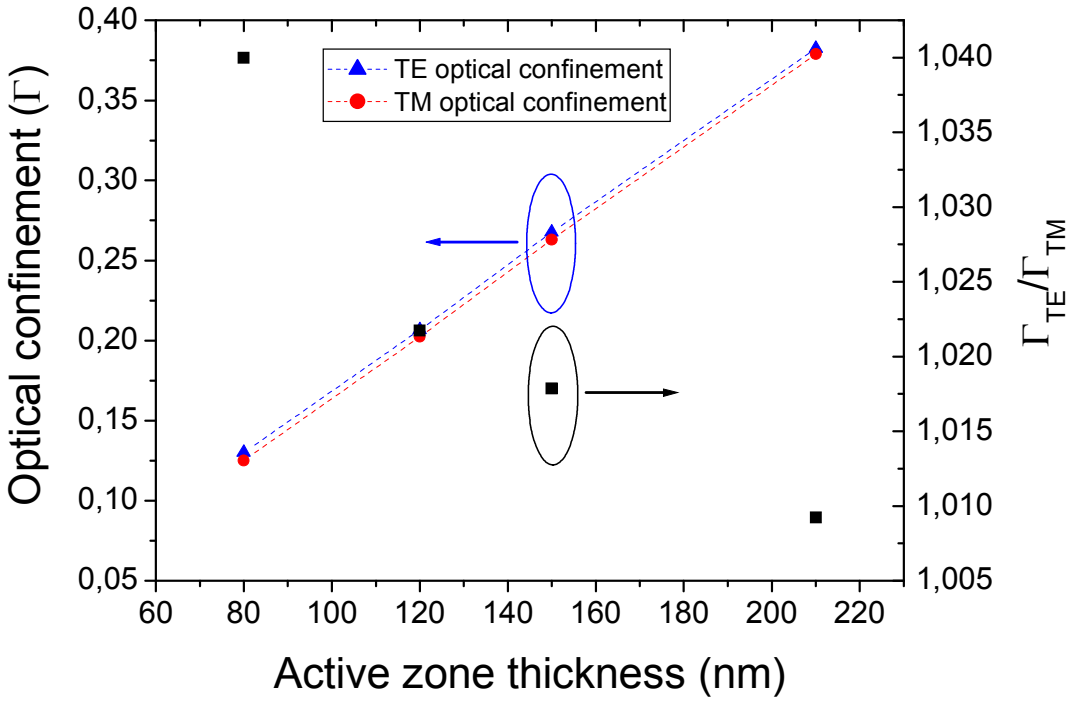

Figure 2-3 – Calculated TE/TM confinement ratios and TE confinements as a function of the active region thickness

Indeed the TM and TE optical confinement are slightly different. Therefore different material gains are required to compensate for this difference and to obtain low polarisation sensitivity devices. The $\Gamma_{TE}/\ \Gamma_{TM}$ ratio is plotted on the right scale as a function of the active region thickness. The polarization dependence is usually expressed as:

$$PDG = G_{int,TE} \times \left(1 - \frac{\Gamma_{TM} \times g_{mat,TM}}{\Gamma_{TE} \times g_{mat,TE}}\right) \quad 2\text{-}1$$

Where G_{int} is the internal gain for TE mode, g_{mat} is the material gain and Γ is the optical confinement.

The difference between Γ_{TE} and Γ_{TM} can be compensated by means of different values for $g_{mat\ TM}$ and $g_{mat\ TE}$. In our structure, Γ_{TE} is higher than Γ_{TM} therefore we need a higher $g_{mat\ TM}$ than $g_{mat\ TE}$ in order to obtain a polarization insensitive gain. Material gains can be varied by properly choosing the material strain in the active region [7]. The strain in this device structure is tensile and the optical transition is therefore mainly between the conduction band and the light-hole

band. Usually, in lattice matched structures, the TM material gain has similar values compared to the TE material gain. As represented in Figure 2-4, the tensile bulk region favours the transition between the conduction band and the light-hole band and consequently increases the TM material gain. More details on strained layers can be found in [8,9].

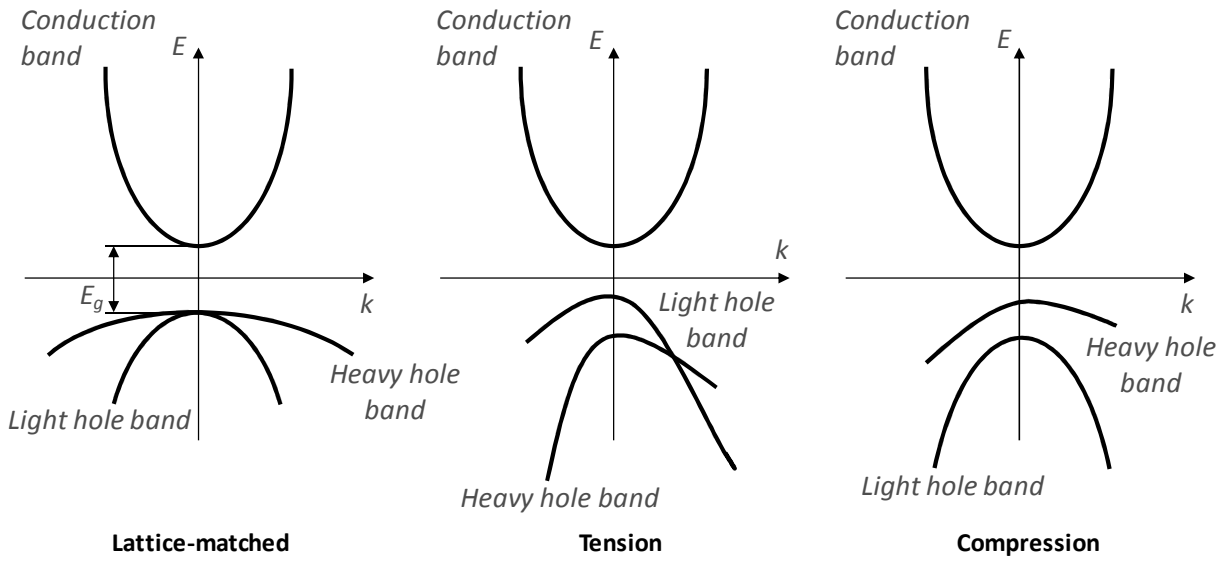

Figure 2-4 – Schematic energy band structure for a direct bandgap semiconductor for lattice matched (left), tensile (centre) and strained (right) structures. Tensile structures favour transitions to the light-hole band, increasing the TM gain.

Figure 2-5 reports the experimental strain values giving rise to polarization insensitive gain versus TE/TM confinement ratios as computed. In order to obtain Γ=20%, the SOA structure needs a 120 nm active zone thickness which leads to a TE/TM confinement ratio of 1.022 (Figure 2-3). In order to compensate for this ratio, a tensile strain of - 0.15 % is required for the InGaAsP material (Figure 2-5). A linear dependence between calculated confinement ratios and needed strain is apparent.

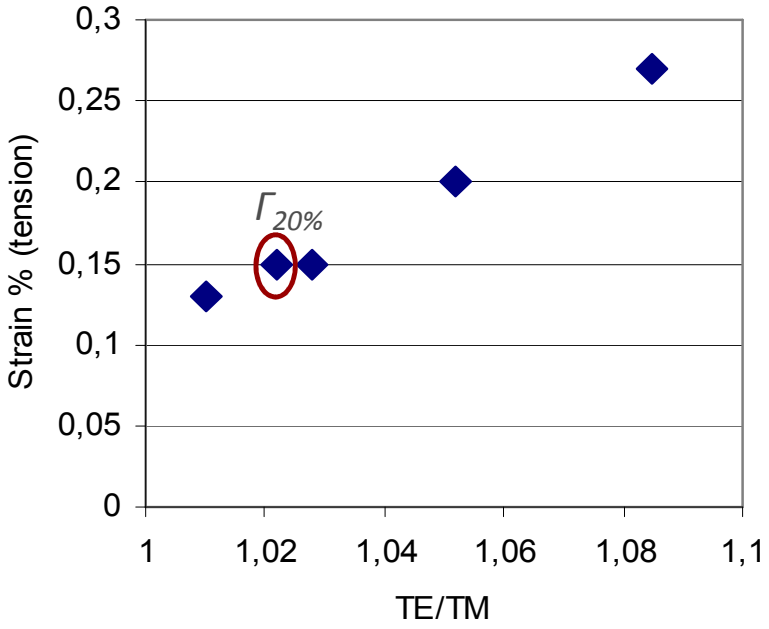

Figure 2-5 – Experimental strain values vs TE/TM confinement ratios

2.1.2 Buried Ridge structure

As the semiconductor lasers, early amplifiers were based on GaAs/AlGaAs or InGaAsP/InP material. They used a junction lasers with a stripe geometry contact to improve mode control as in [10-11]. An insulating $Si0_2$ layer was used and etched in order to define high-resistance zones so that the top metallic contact meets the p+ layer only in the stripe cross-sectional area. Ion implantation is an alternative solution in order to induce high-resistance implanted zones.

Ridge waveguide type structure can be designed to improve the overlap between the optical mode propagation and the gain [12] as well as to increase the modulation bandwidth [13]. Low noise amplifiers can be obtained using strongly index guided designs [14].

However a buried ridge structure (BRS) is used to provide efficient current injection into the active region and good thermal dissipation. Figure 2-6 shows the transverse section of a BRS with ion implantation under electrical current injection. It is also more convenient from a technological point of view to use this structure in order to fabricate efficient spot-size converter as discussed later. An overview and comparison of all different amplifier structures are presented in [15].

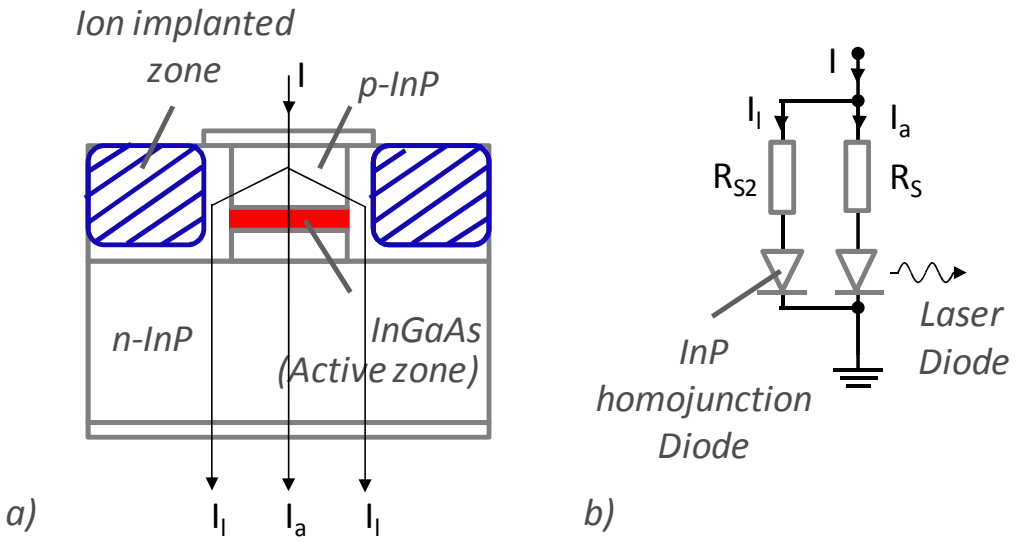

Figure 2-6 – (a) Buried Ridge structure with ion implanted and (b) equivalent electrical circuit

A tapering zone is used to transfer the optical mode from the active zone to the passive zone and acts as a spot size converter (SSC). Figure 2-7 represents a cross-section in the tapering zone under current injection and the top view of the overall structure. A double core structure was chosen with active and passive waveguide integration by means of a taper. It can be considered as a SSC in order to optimize the mode transfer between the active and passive region, as well as the output mode for the coupling. The integration of a mode size expander, based on tapered waveguide, leads to an improvement of the practical performances such as low-coupling losses and large positional alignment tolerances. These improvements lead to reduced packaging costs using passive alignment between the RSOA and optical fibre.

More details about the spot size converter are presented in the next section.

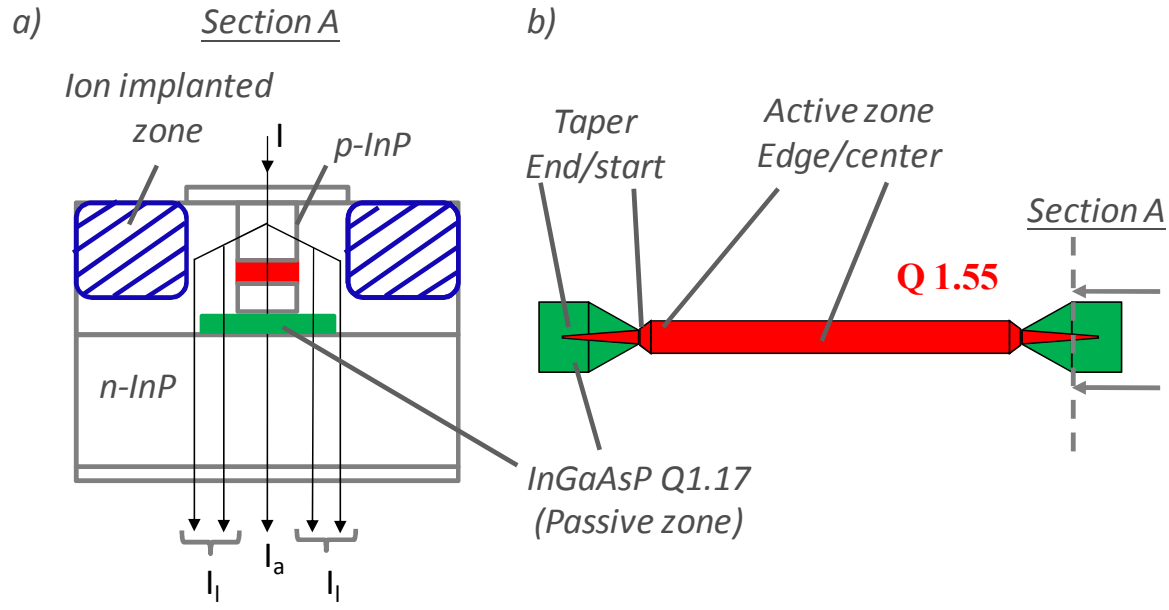

Figure 2-7 – Schematic BRS SOA structure (a) sectional view and (b) top view considering the tapering region

The total injected current (I) into the BRS structure partially goes into the active zone (I_a). The difference between both currents is called the leakage current (I_l) [16]:

$$I = I_l + I_a \qquad 2\text{-}2$$

The flow of current from the p-InP to the n-InP follows several paths. The first one is through the heterojunction which is the active zone and the second consists of an InP homojunction (leakage path). The turn-on voltage of the homojunction is larger than the heterojunction turn-on voltage, because of the larger band-gap. However at high injected current, the homojunction leakage may exceed the current inside the heterojunction and leads to a lower optical gain. Therefore it is crucial to optimize the current confinement for SOA and RSOA fabrication. Both junctions can be represented with an equivalent electrical circuit consisting of a resistance and a diode (Figure 2-6). A complete study of the leakage current is detailed in [17]. Figure 2-8 represents the Intensity-Voltage (I-V) measurement and the equivalent electrical circuit for the developed BRS SOA. The InP homojunction turns on at a higher voltage (E_g = 1.38 eV) that the heterojunction (active zone, E_g = 0.8 eV).

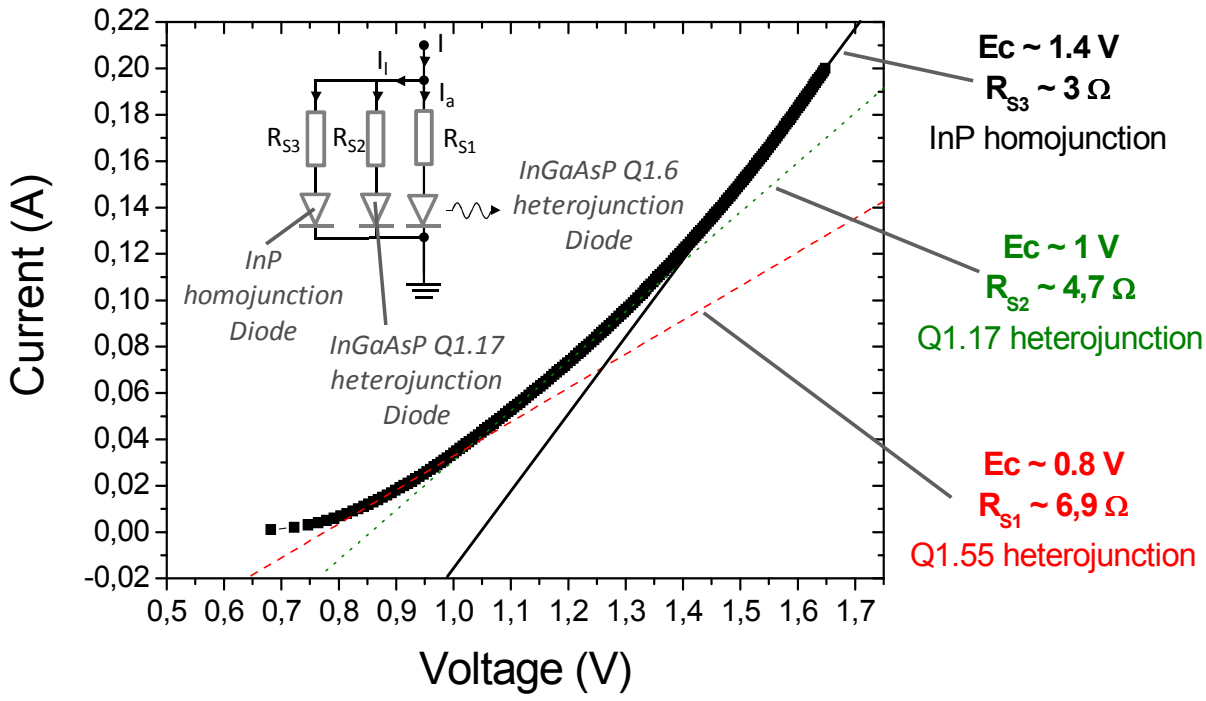

Figure 2-8 – I-V characteristics and equivalent electrical circuit of a BRS SOA with Γ = 20%

However we observe that the second turn-on voltage is around 1V which corresponds to the heterojunction based on InGaAsP (passive layer). Therefore the leakage current due to the tapering region is higher than the one due to the InP homojunction.

It can be easily confirmed by Spontaneous Emission (SE) measurements along the device. Figure 2-9 represents SE measurements along the active stripe. At higher current (I = 200 mA), SE emission confirms the effect of the passive layers (InGaAsP) with a peak wavelength at 1.17

μm. In comparison, the emission wavelength in the active zone is centred around 1.55 μm (InGaAs). The influence of the taper can be reduced by the fabrication of completely passive tapers (no injection of electrical current in this region so no leakage current from the taper). Further work is underway to realize more complex structure using a butt-joint process (passive tapers).

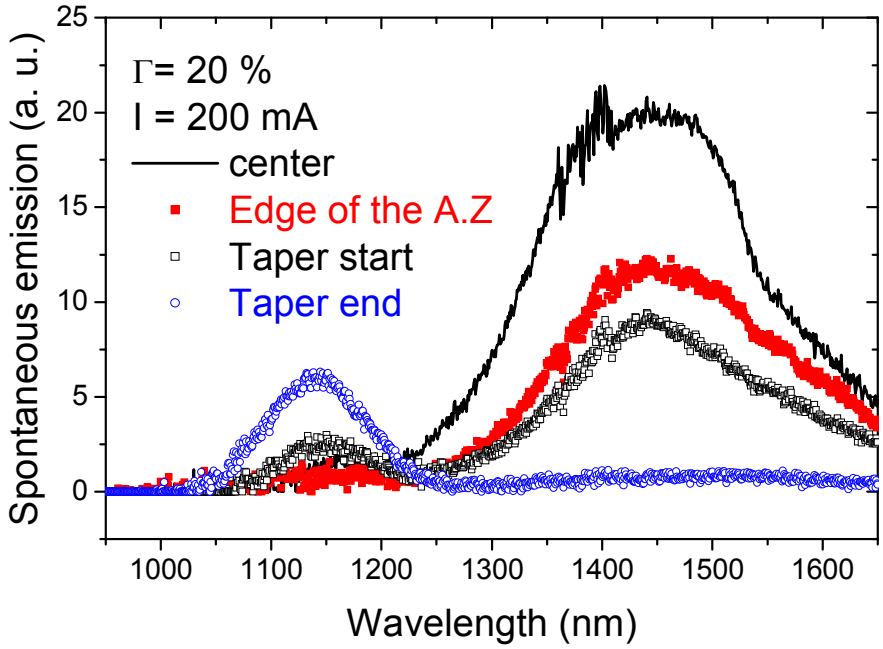

Figure 2-9 –SE measurements along the SOA active stripe with Γ = 20%

2.1.3 Optical mode confinement and transfer

Different confinements have been designed to achieve a high (Γ~80%) or small (Γ~20%) optical confinement. As we demonstrated in chapter 1, the optical confinement strongly affects the spatial distribution of the carrier density and consequently the optical gain. Therefore the optical confinement control is of prime interest for the design of high performance SOA and RSOA.

SSC is used to increase the output optical mode size and reduce the beam divergence. The reduction of the coupling losses is due to a lower divergence. This effect is already well known and has been extensively studied [18-19].

2.1.3.1 SSC design

Confinement layers of InGaAsP with a lower refractive index are used to ensure lower confinement as shown in Figure 2-10. The p- and n- InP regions are respectively above and below the active zone. Stationary solutions of modal distribution are computed from both structures using BeamPROP software. The vertical structure (material thickness and refractive index) are the same as presented in section 2.1.1. A BRS structure is used in both cases.

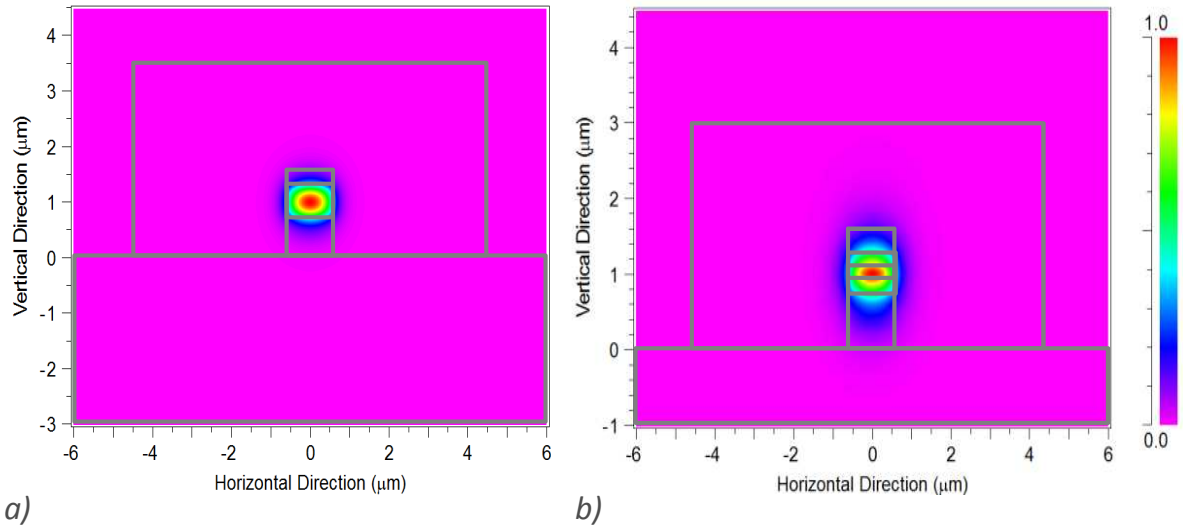

Figure 2-10 – Optical mode profile for BRS with (a) high and (b) low optical confinement

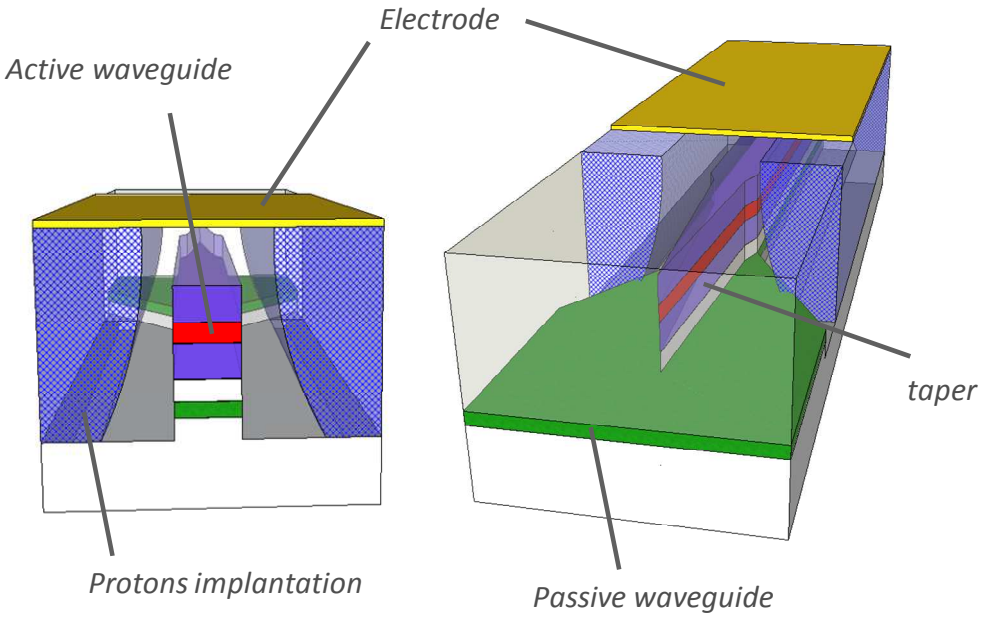

Figure 2-11 - Spot size converter in RSOA design via double active/passive waveguide

Figure 2-11 represents both facets of the RSOA structure. The active and passive tapers have been optimized to increase the coupling efficiency between both layers and to increase the optical mode size (thus to reduce the divergence of the output beam). Spot size converter structure allows optical mode expansion. 2D calculations have been carried out for the design of the structure. The modes in the passive and active zones for the SOA with 20% of optical confinement are represented in Figure 2-12. Optical mode simulations lead to horizontal mode width values of 4.5µm and 1.7µm respectively after and before the SSC. We also verified experimentally and demonstrated theoretically that mode expansion leads to the reduction of the tilted facet reflectivity. The full theory, as well as the characterization of this effect, are detailed in

Appendix I. This effect is very interesting in order to have more tolerant anti-reflection (AR) coating as detailed in section 2.2.3.1.

We performed the far field measurement of the SOAs, as shown in Figure 2-13-(a) with SSC and in Figure 2-13-(b) without SSC. We observe small divergence values with SSC due to a large optical mode and high divergence in the case of a small optical mode without SSC. The 3-dB divergence angles ($\Delta\alpha_{3dB}$) in both horizontal and vertical directions as well as the values of the mode size Δx and those of the wave variation vector (Δk_x), expressed as a function of the full width at half maximum (FWHM) of the divergence, are shown in the Table 2-2. When Δk_x increases, the optical mode size decreases (high divergence) and when Δk_x decreases, the optical mode becomes larger and the divergence decreases (tending toward an infinitely large optical mode, that is, a plane wave, for a zero divergence). Depending on the vertical ($\varphi = 90°$) or horizontal axis ($\varphi = 180°$), minor differences occur. We have thus obtained coupling losses between 2 and 3 dB.

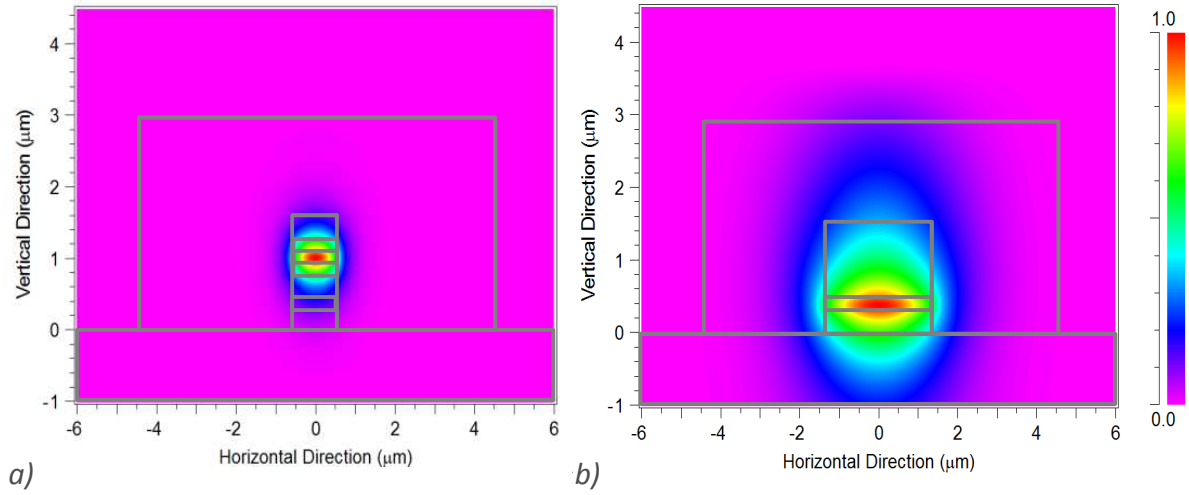

Figure 2-12 – Simulated field intensity inside the active (a) and passive (b) layers

	SSC-SOA, $\varphi = 90°$	SSC-SOA, $\varphi = 180°$	SOA , $\varphi = 90°$	SOA, $\varphi = 180°$
$\Delta\alpha_{3dB}$ (degrees)	15.17°	19°	44.7°	45.1°
Δk_x (μm^{-1})	0.91	1.14	2.69	2.71
Δx (µm)	4.31	3.44	1.46	1.45

Table 2-2- SOA optical mode parameters

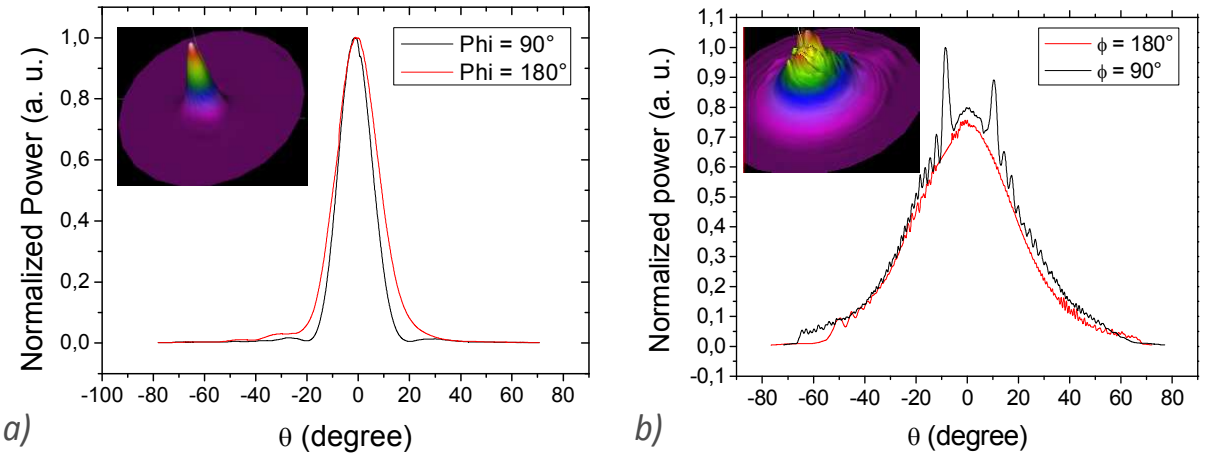

Figure 2-13 - Far-field measurements on SOA chip (a) with SSC and (b) without SSC

The geometry of the double core tapers was designed for SOA devices in order to determine the best parameters for an efficient transition between both optical modes [6]. Simulations of the optical mode propagation have been performed and confirm a coupling ratio of ~95 % in the tapered structure between active and passive regions. Results of the mode transfer and the geometry of the final SSC structure are represented in Figure 2-14.

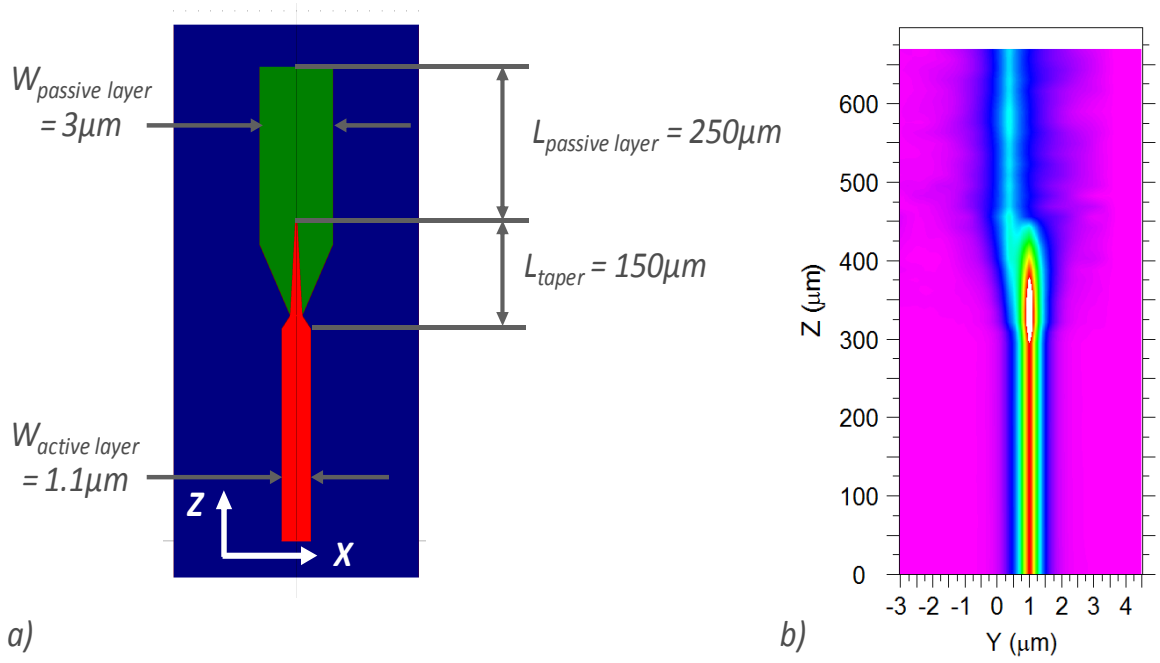

Figure 2-14 - Mode transfer simulation of Active/passive waveguide RSOA: top-view of the tapered region (a) and mode intensity simulation along the tapers (X-cut, b)

The ideal situation depicted before, where the active and the passive guides are perfectly centred, is rarely obtained, since during the SOA realization process the accuracy in positioning photomasks can be estimated to be within 0.5 µm. It is therefore important to evaluate the optical propagation in case of misalignment between the guides. Previous studies show that the propagation is qualitatively unaffected even in case of a large shift (0.5µm) [6]. In particular, the

optical field is still guided in the passive section and no perturbation in the intensity profile is observed at the device exit. However larger shifts and/or large taper ends can lead to internal reflection and make SOA and RSOA unsuitable for signal amplification. This case is discussed in section 2.1.3.2. The tolerance of the coupling ratio depending on the misalignment and the tapers thickness are discussed in appendix III.

Figure 2-15 shows SEM picture of the tapers before the over growth. The processing details are described in section 2.2.1.

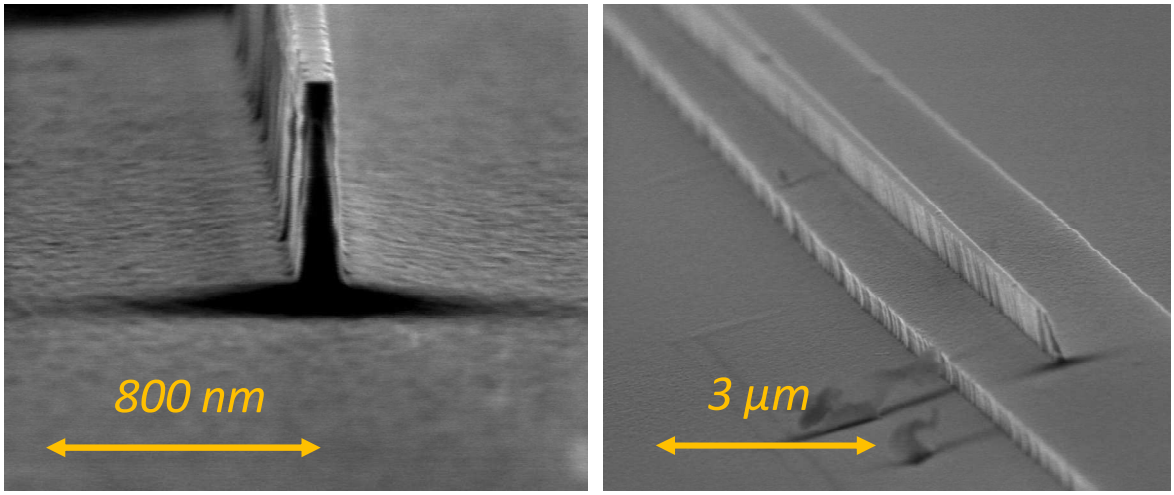

Figure 2-15 – SEM picture of the double core structure using active and passive tapers

2.1.3.2 Spot Size Converter issues

The perfect situation simulated above is almost impossible to obtain. During this work, several wafers have been processed and various conditions were found necessary in order to obtain high performances devices. The design of SSC has been detailed and a coupling ratio of ~95 % between active and passive layers was obtained, according to simulations. However, larger taper ends (> 0.2 µm), a misalignment between both regions and an incomplete etching strongly affect this coupling ratio. Figure 2-16 represents a sectional view of the SSC at the end of the active taper. In this SEM picture, all defects are presented.

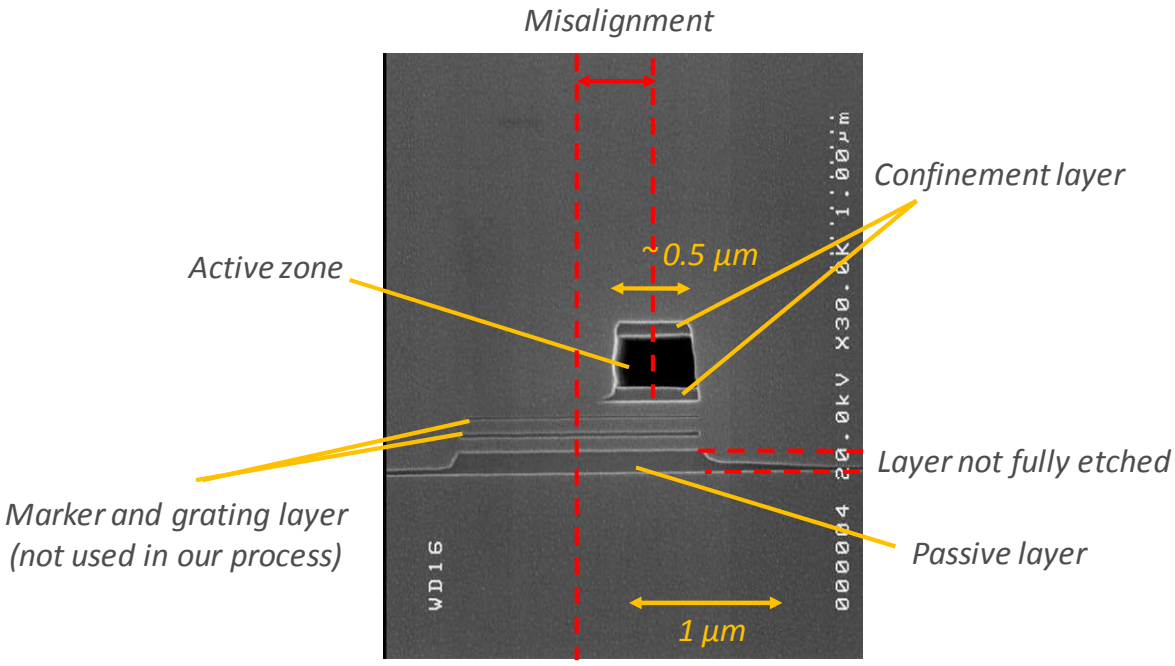

Figure 2-16 – SEM picture of the tapers transition between the active and passive layer after re-growth

As a result, the optical mode is not fully transferred to the passive layer therefore reflections occur at the interface between the active region and the InP material (re-growth region). Then an internal cavity appears between the facet and the active zone end. Figure 2-17 describes this phenomenon. Due to these internal oscillations, the gain is modulated and the variation of theses oscillations is slower than a classic gain ripple. We propose an alternative design in order to obtain more tolerant SOA and RSOA structures. The idea is to design a long taper up to the facet. In this case even if the optical mode is not fully transferred, the reflection can be suppressed thanks to the AR facet coating.

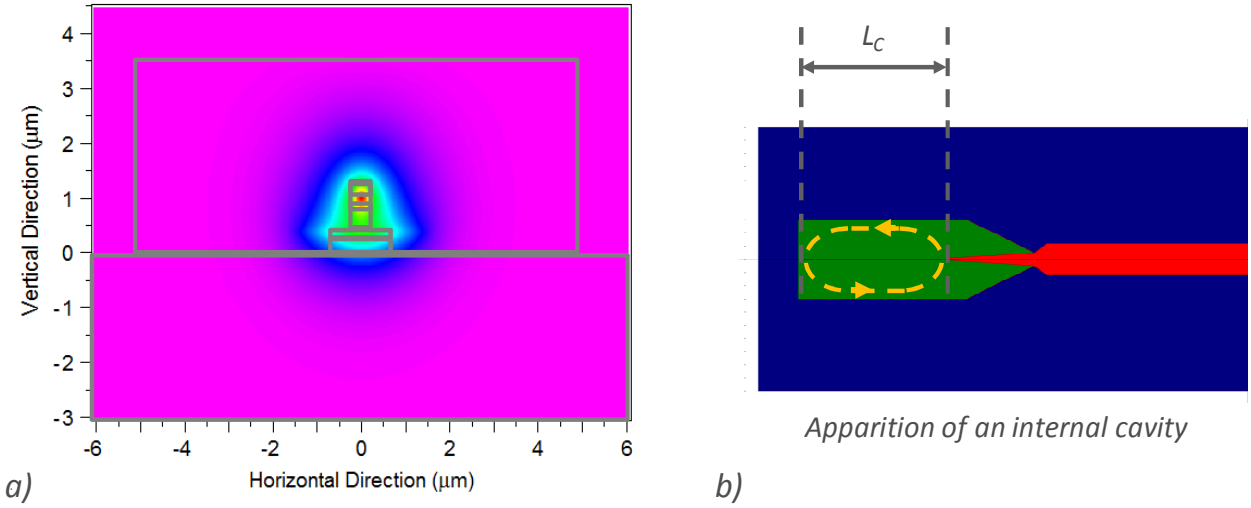

Figure 2-17 – (a) Optical model profile and (b) cavity representation in unoptimised SSC structure

The proposed design and a comparison between the two structures (with optimized and not optimized tapers) are present in Figure 2-18. The gain ripple is clearly reduced using new SSC design. Slowly varying envelop is also observed in classic SSC RSOA due to the presence of the internal cavity.

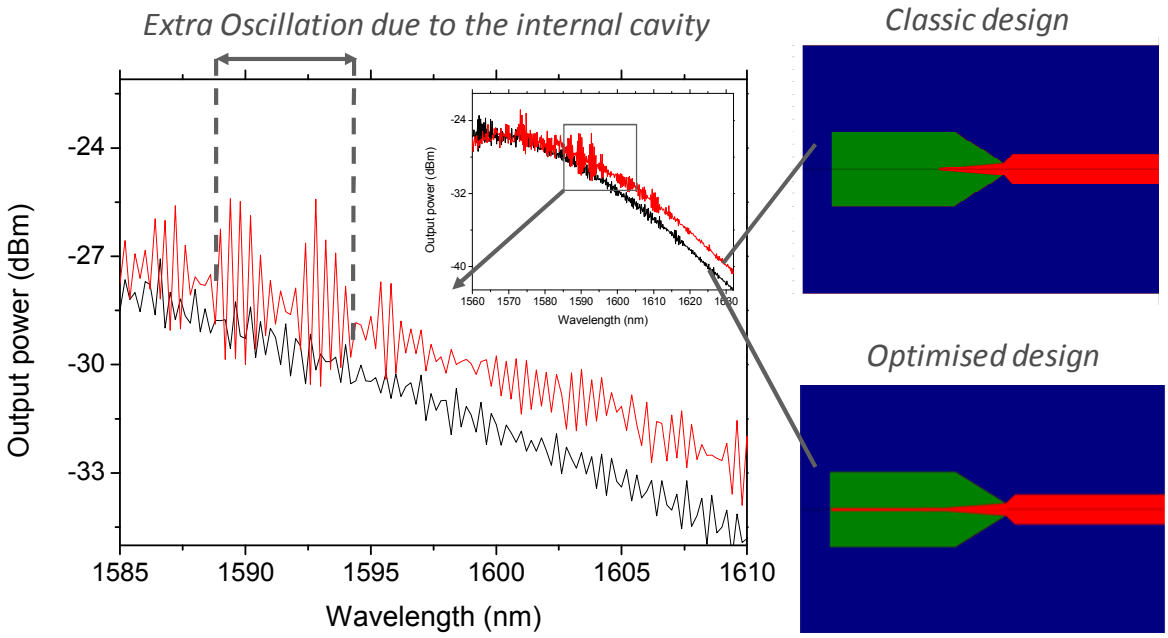

Figure 2-18 – Optical spectrum and schematic representation of classic and optimized SSC structure

2.2 Device processing

The SOA and RSOA structures presented above are built up using several processing stages. Material can be added by deposition or removed by etching. In both cases, the patterning of the wafer is done by photolithography, or with electronic-beam lithography. The necessary steps in order to obtain the final SOA and RSOA structures (Figure 2-11) are presented in section 2.2.1. The cleaving, mounting and facet coating is then described in section 2.2.2 and 2.2.3.

2.2.1 SOA and RSOA processing steps

Although technical processes are difficult to patent, they are nearly impossible to copy without knowing the recipe. Technological processes require deep knowledge and high expertise to be correctly conducted. The process has been developed in III-V Lab during the last 20 years. It is a legacy from the SOA and RSOA research. The SOA process is composed of 8 main steps:

9. Epitaxial growth of vertical structures
10. E-beam writing of the active zone
11. Plasma Etching of the active zone

12. Plasma Etching of the passive zone
13. Epitaxial overgrowth (MOCVD) over the active zone
14. Ohmic contact metal deposition and baking
15. Ion implantation
16. Wafer thinning and Back-metal deposition

We control the process after each step using microscope and profilometer. In situ measurements are performed during the etching process.

Figure 2-19 - Clean room facilities in III-V Lab

The epitaxial growth of the vertical structures has been detailed in section 2.1.1 (Step 1). The second step (E-beam writing of the active zone) is presented in Figure 2-20. In the SOA structure, Plasma Enhanced Chemical Vapour Deposition (PECVD) is used to deposit silicon dioxide (SiO_2), whose function is to pattern the active zone before the plasma etching. In this technique, plasma is used to dissociate gases, the atoms of which form a solid layer on the surface of the substrate (chemical reactions are involved in the process). The necessary energy for the chemical reaction is introduced by heated gas or plasma and not by heating the whole reaction chamber. E-beam lithography is used to define the active zone region. Then metal deposition (Ti) is performed using sputtering techniques. Sputtering involves mounting the substrate in a vacuum chamber, containing the target material to be deposited. In the Ion Beam Sputter Deposition (IBSD), the target is bombarded by an ion beam, causing atoms to be ejected, which coats the surface of the substrate. The metal pattern is then defined by lift-off technique. Photolithography, E-beam lithography, etching and lift-off techniques are detailed in Appendix II.

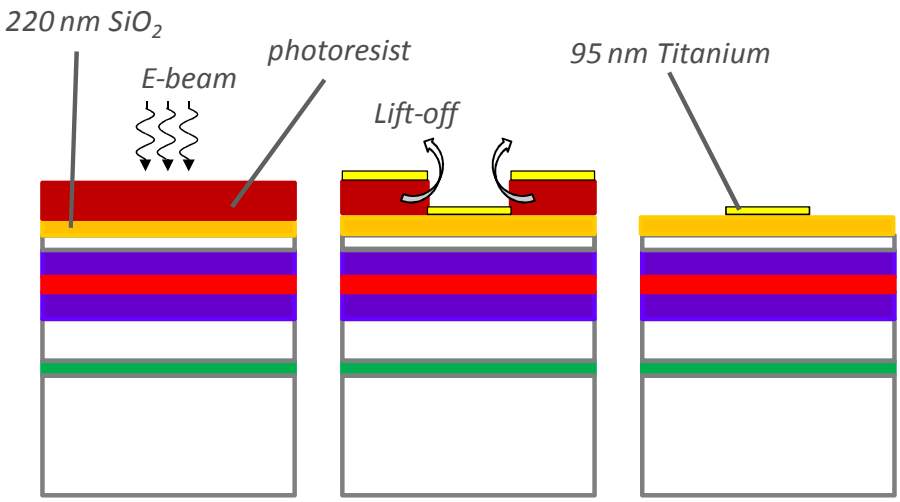

Figure 2-20 - E-beam writing of the active zone

The third step of the process is represented in Figure 2-21. The silicon dioxide is etched using Reactive Ion Etching (RIE), and the ridge is defined using CH_4/H_2 RIE. The etch finishes below the active region, in the n-type InP layer above the passive layer. In order to control the depth of this dry etching, in situ control is performed using reflectometry technique (Figure 2-22). More details about the reflectometry are presented in Appendix II. A marker layer is used in order to stop the etching process.

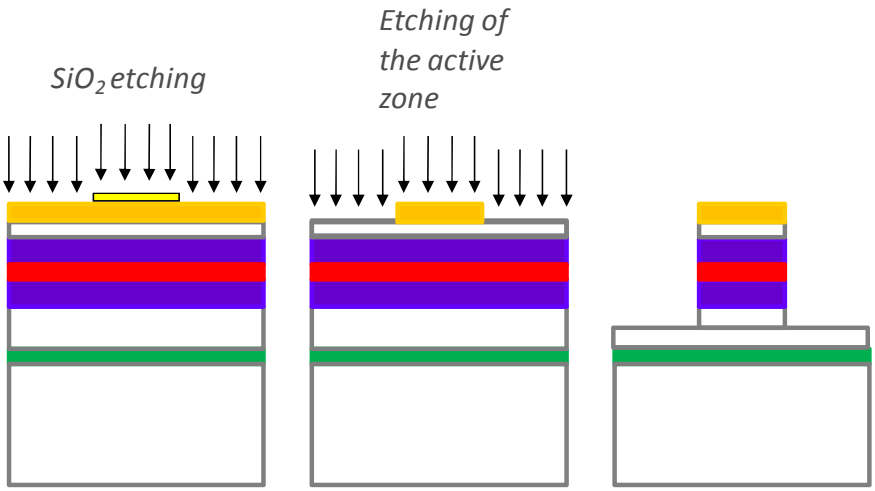

Figure 2-21 – Plasma etching of the active zone

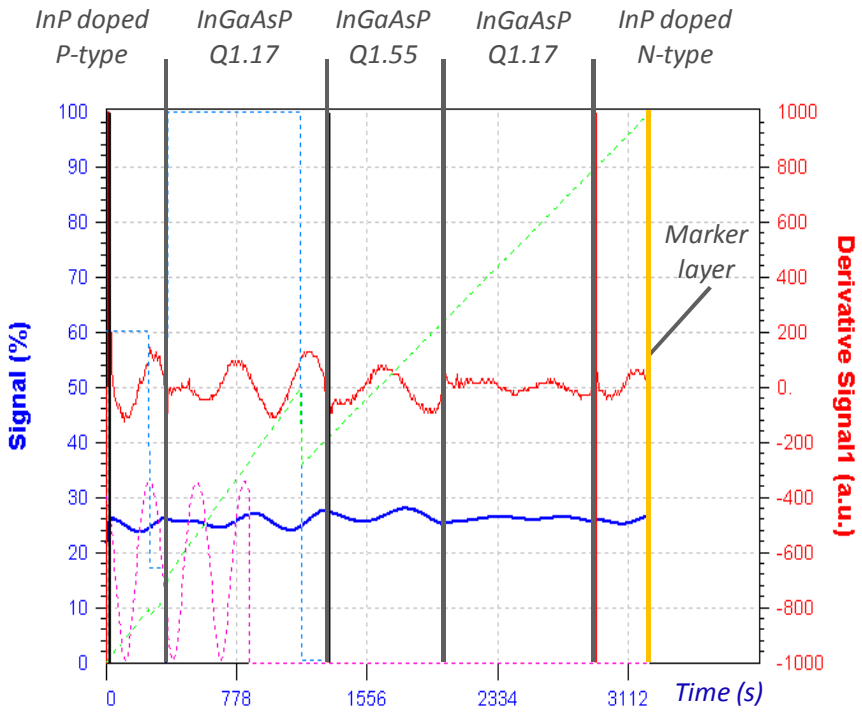

Figure 2-22 – Reflectometry control of the active zone etching

The passive zone is defined using photolithography and is etched by CH_4/H_2 RIE. The etch is stopped in the buffer layer (n-type InP). The different stages are represented in Figure 2-23.

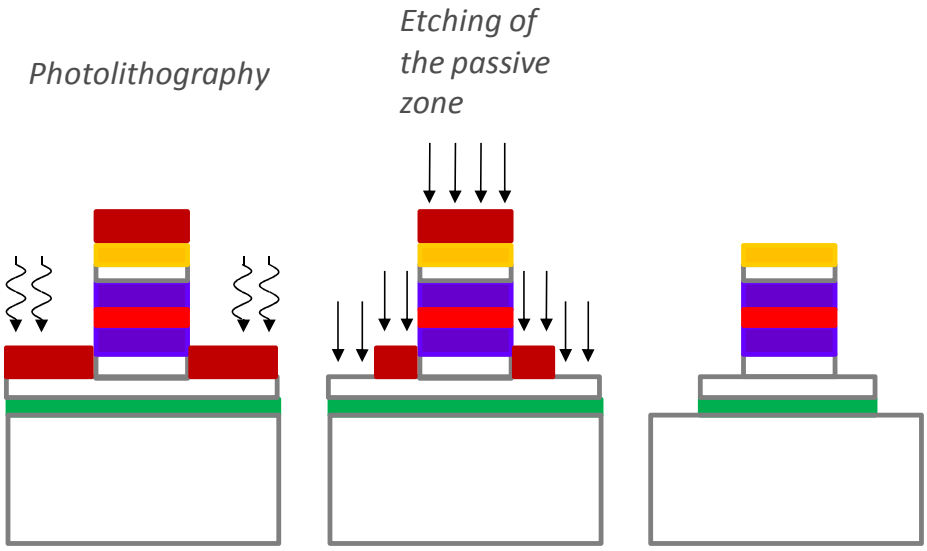

Figure 2-23 – Plasma etching of the passive zone

The epitaxial re-growth over the passive and active layer is done using the MOCVD technique (step 13). The doping profile of the re-growth requires a precise optimization. In order to increase the amplification of a SOA at a given current, it is important to reduce the losses

encountered by the optical mode. The overlap between optical eigenmode and p-doped layer is large in the taper section because of mode expansion. A low p-doped layer is used at the bottom of the epitaxial re-growth. Then higher doping profile for top InP layers are realized. In fact, p-doped layers induce efficient electrical current injection. Therefore a trade-off between the losses and the electrical injection efficiency has to be found. Highly doped GaInAs layer is used at the top of the structure in order to obtain high quality contact.

Ohmic contact deposition (P-type contact) is then realized (step 14). Photolithography is used to define the contact region. The metal deposition technique employed for processing the SOA contact is evaporation. Three layers of Ti, Pt and Au are deposed respectively with 50, 100 and 250 nm thickness. After the lift-off, an annealing at 420°C is done allowing the diffusion of the titanium into the contact layer (InGaAs) to reduce the contact resistance. Platinum is used as a barrier layer to prevent from the diffusion of gold.

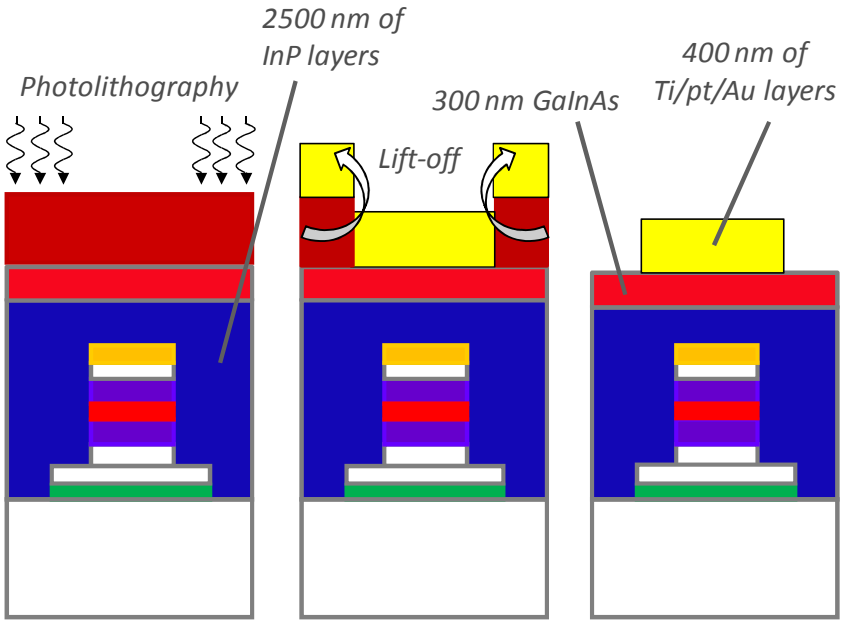

Figure 2-24 – Ohmic contact deposition

Ion implantation is outsourced (step15). The ion implantation step is represented in Figure 2-25 and a SEM picture is presented in Figure 2-26.

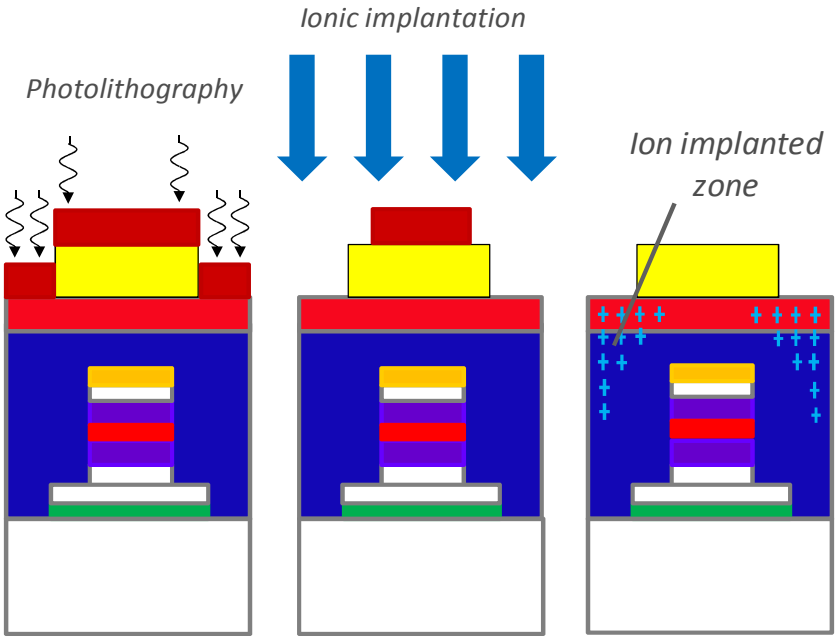

Figure 2-25 – Ion implantation step

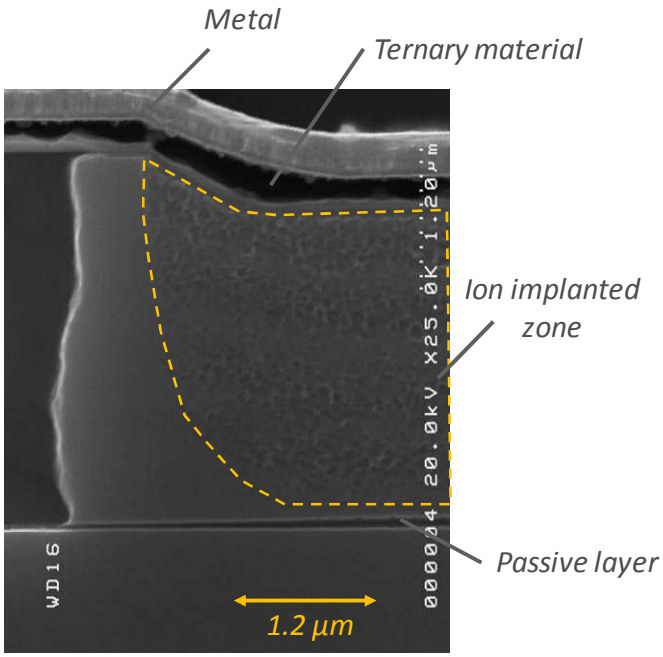

Figure 2-26 – SEM picture of the Ion implanted zone

The ternary material used for the over growth is removed using wet etching. Wafer thinning and back metal deposition is then realized to finalize the SOA structure.

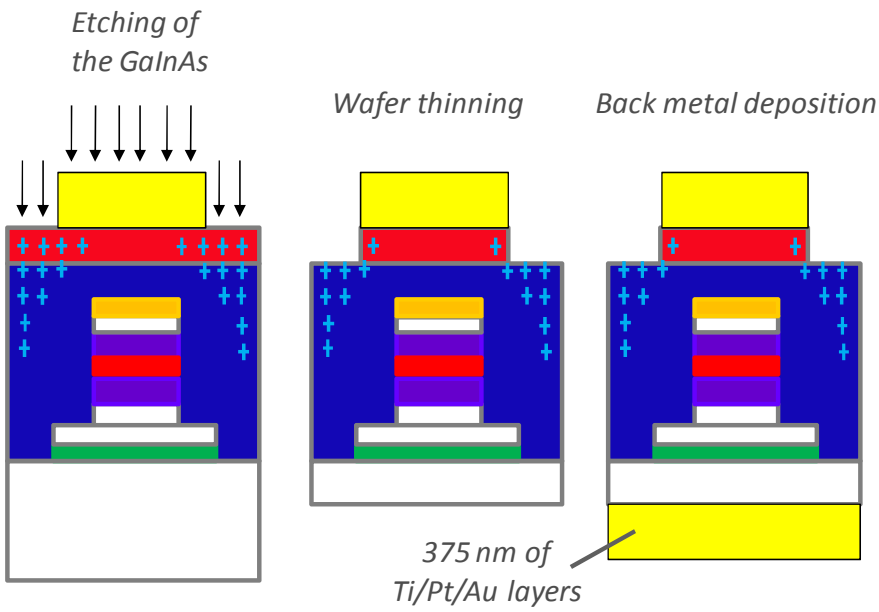

Figure 2-27 – Etching, wafer thinning and back metal deposition

A schematic diagram of the complete structure is shown in Figure 2-27 and a SEM picture of the BRS SOA with low optical confinement is presented in Figure 2-28.

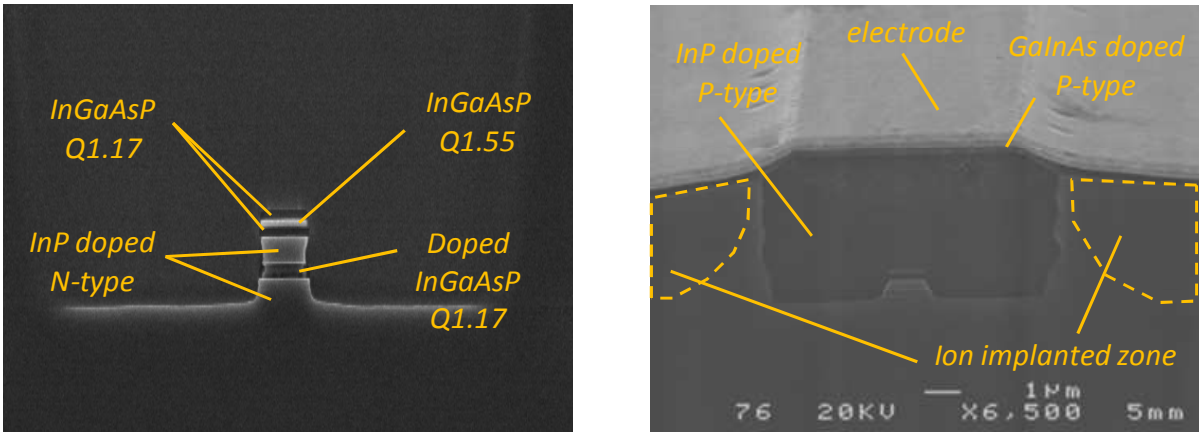

Figure 2-28 – SEM picture of buried ridge SOA structure with low optical confinement

2.2.2 Cleaving, bonding and mounting

The devices are scribed and cleaved manually, to define cavities with various lengths (from 300 µm to a few mm typically). The scriber tool uses a diamond tip in order to realize deep initiation marks (~25µm). The devices are cleaved along the crystalline axis which leads to low surface roughness. The devices are mounted p-side up for a more convenient fibre coupling. As shown in Figure 2-29, the RSOA chip is mounted on an AlN submount by AuSn soldering for a better thermal management. The electrode of the chip (also called pad) is connected to one track using one gold bond wire. A probe can be connected to the track to perform static and dynamic measurements. The gold bond wire is 25 µm wide and the gold ball on the pad is around 60 and

80 µm. The p-type pad (titanium-platinum-gold layer) is connected to the BRS where the p-type region of the wafer is located. The electrical injection is localised to the active zone thanks to the ion implantation. The n-type pad is connected at the bottom of the BRS, where the n-type region of the wafer is located.

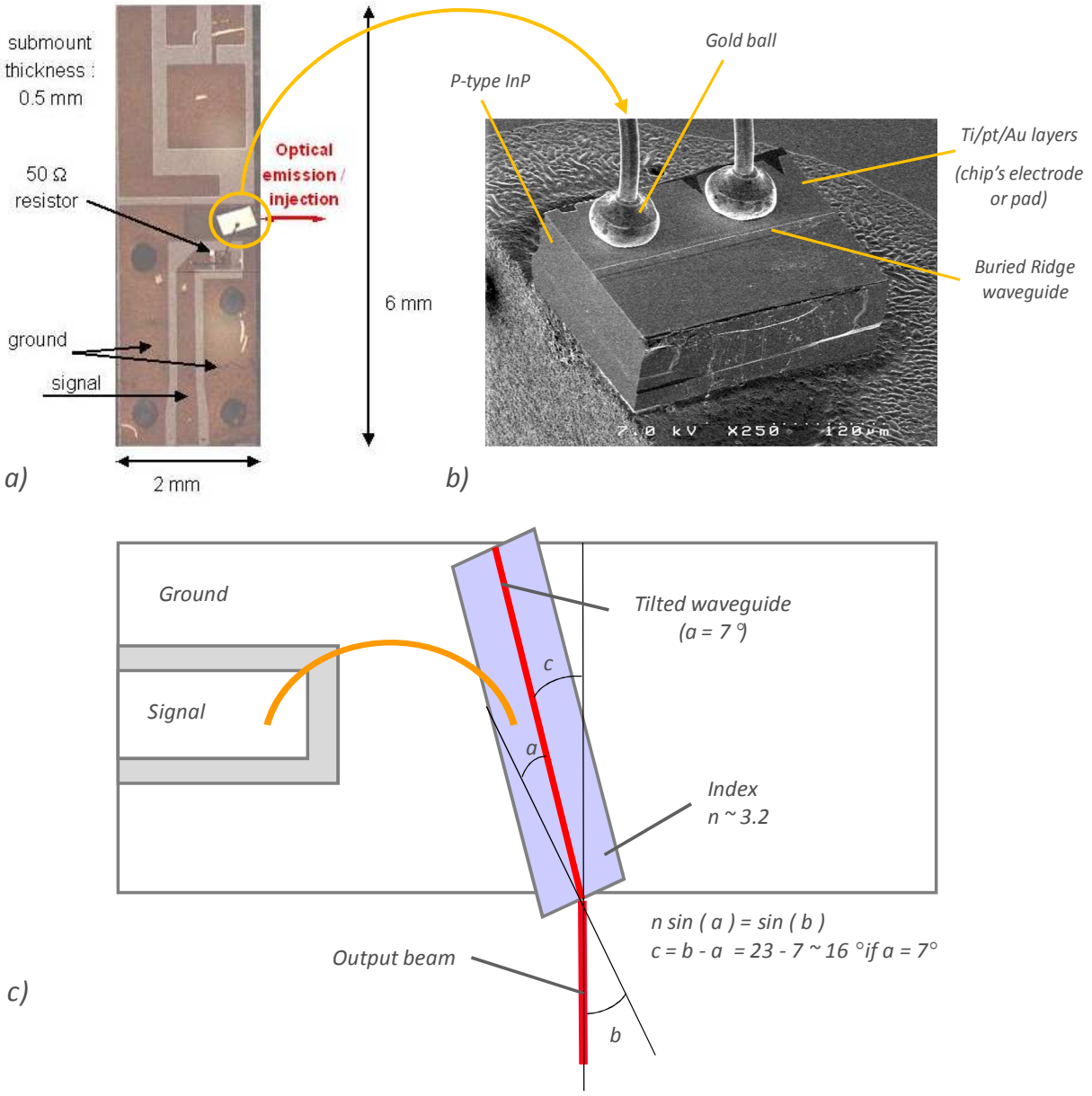

Figure 2-29 – (a) Photography, (b) SEM picture and (c) schematic representation of RSOA device mounted on AlN submount and wire-bonded

In order to obtain RSOA devices, AR (HR) coatings are deposited on the angled front (rear) facet. Due to a tilted waveguide, the chip needs to be angled for efficient coupling into the optical fibre.

2.2.3 Facet reflectivity

Components such as SOAs and RSOAs require a careful control of reflection coefficients from its facets. Low reflectivity and high reflectivity are key characteristics in the development of high performance RSOA devices.

2.2.3.1 Low facet reflectivity

2.2.3.1.1 Anti-reflection coating

The reflection control can be done through several ways. The reflectivity at the interface between two dielectric materials can be calculated for normal incidence as:

$$R = \left(\frac{n_2 - n_1}{n_2 + n_1}\right)^2 \qquad 2\text{-}3$$

Where n_1 and n_2 are the refractive index of the materials

A cleaved facet displays a reflectivity of typically 30 % considering a semiconductor-air interface and an effective index of the guided mode close to 3.2. Such a large reflectivity leads to laser oscillation. First, facet coating is used to achieve low facet reflectivity [20, 21]. Multi-layers deposition is required to ensure low facet reflectivity over a wide wavelength range. However to achieve reproducible values of the facet reflectivity, a precise control of the thickness and refractive index of the deposited layers is required. We use one dielectric layer of TiO_2 and one layer of SiO_2. The thickness and the refractive index are measured by ellipsometry after the coating process. The TiO_2 layer has a refractive index around $n_{TiO2} = 2.25$ and a thickness around 130 nm. The SiO_2 layer has a refractive index around $n_{SiO2} = 1.45$ and a thickness around 210 nm. Both parameters (refractive index and thickness) depend on the deposition process. Taking into account the accuracy of the deposition process and its control, facet reflectivity as low as 0.1 % can be guaranteed. However, since our devices exhibit small signal gains up to 30 dB, a reflectivity of 0.1 % is too large for ensuring moderate gain ripple. The gain ripple is defined as the maximum difference in power gain between the resonant and non-resonant gains. From equation (1-52), the gain ripple is given by [22]:

$$\boxed{G_{ripple} = \left[\frac{1 + \sqrt{R_1 R_2} \times G_S}{1 - \sqrt{R_1 R_2} \times G_S}\right]^2} \qquad 2\text{-}4$$

Where R_1 and R_2 are the facet reflectivity and G_S is the single pass gain as defined in equation (1-53).

We assume the reflectivity is the same for both facets therefore we obtain: $R = \sqrt{R_1 R_2}$. Considering the gain ripple in dB, the previous equation becomes:

$$\left(G_{ripple}\right)_{dB} = 20 \times log_{10}\left[\frac{1 + R \times G_S}{1 - R \times G_S}\right] = \frac{20}{\ln(10)} \times [\ln(1 + R \times G_S) - \ln(1 - R \times G_S)]$$

2-5

This expression can be expanded to the second order as:

$$\left(G_{ripple}\right)_{dB} = \frac{20}{\ln(10)} \times \left[RG_S - \frac{RG_S{}^2}{2} + RG_S + \frac{RG_S{}^2}{2}\right]_{dB} = \frac{40}{\ln(10)} \times [RG_S]_{dB}$$

2-6

Gain ripple lower than 1 dB is required for colourless operation. Curves of $\left(G_{ripple}\right)_{dB}$ versus R are shown in Figure 2-30 with G_S as parameter.

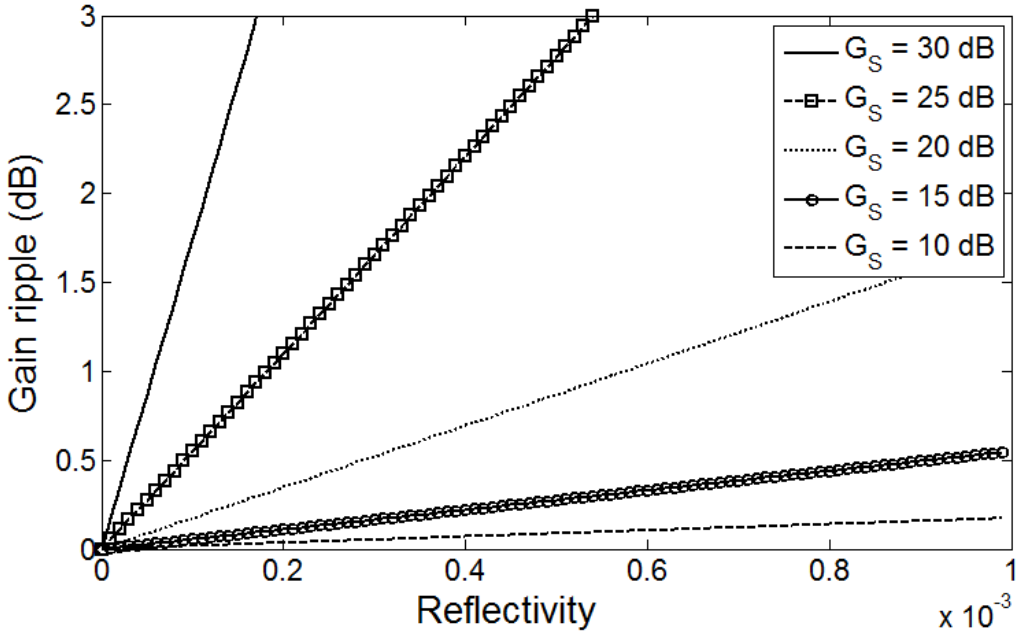

Figure 2-30 – Gain Ripple depending on the facet reflectivity with single pass gain as parameter

For example, to obtain a gain ripple less than 1 dB with a single-pass gain of 25 dB, the facet reflectivity need to be lower than $R < 1.8.10^{-4}$. As a result, most research groups also tilt the waveguide with respect to the crystalline axis [23], usually with an adequate facet coating [24, 25]. Let us study more in detail the tilt impact on the facet reflectivity.

2.2.3.1.2 Tilted waveguide

In 1989, D. Marcuse developed a model in order to calculate the reflection loss from tilted end mirror. Here this model is used as a first approach to describe the influence of tilted waveguide on the facet reflectivity. A width parameter characterized the fundamental TE mode (distribution of the field strength). In angled facet SOAs and RSOAs, the TE mode width for the power (w_{full}) can be approximated by [26-27]:

$$W_{full} = \frac{w}{2}\left(9.2063 \times 10^{-3} + \frac{1.7265}{\sqrt{V}} + \frac{0.38399}{V^3} - \frac{9.1691 \times 10^{-3}}{V^5}\right)$$

2-7

Where $V = \frac{\pi w}{\lambda_0}\sqrt{n_1^2 - n_2^2}$, w is the waveguide width, n_1 and n_2 are the refractive index of the active region and the cladding region respectively.

We assume a Gaussian distribution of the optical field therefore the reflectivity of the tilted facet is given by:

$$R_{ang}(\theta) = R_f(\theta)e^{-\left(\frac{2\pi n_2 W_{full}\theta}{\lambda_0}\right)^2}$$

2-8

Where θ is the angle between the beam direction and the normal to the end facet (Figure 2-29); R_f is the Fresnel reflectivity of a TE plane wave at the angled facet.

$$R_f(\theta) = \frac{n_1 cos\theta - n_{air}\sqrt{1 - \frac{n_1^2}{{n_{air}}^2}sin^2\theta}}{n_1 cos\theta + n_{air}\sqrt{1 - \frac{n_1^2}{{n_{air}}^2}sin^2\theta}}$$

2-9

TM plane wave has a similar reflectivity. The reflectivity decreases as the angle increases. However the coupling losses become higher at large tilted angle due to the far-field asymmetry. The reflectivity also decreases as the waveguide width increases. Figure 2-31 represents the effective reflectivity of SOA tilted waveguide with and without SSC. The refractive indices are extracted from Table 2-1.

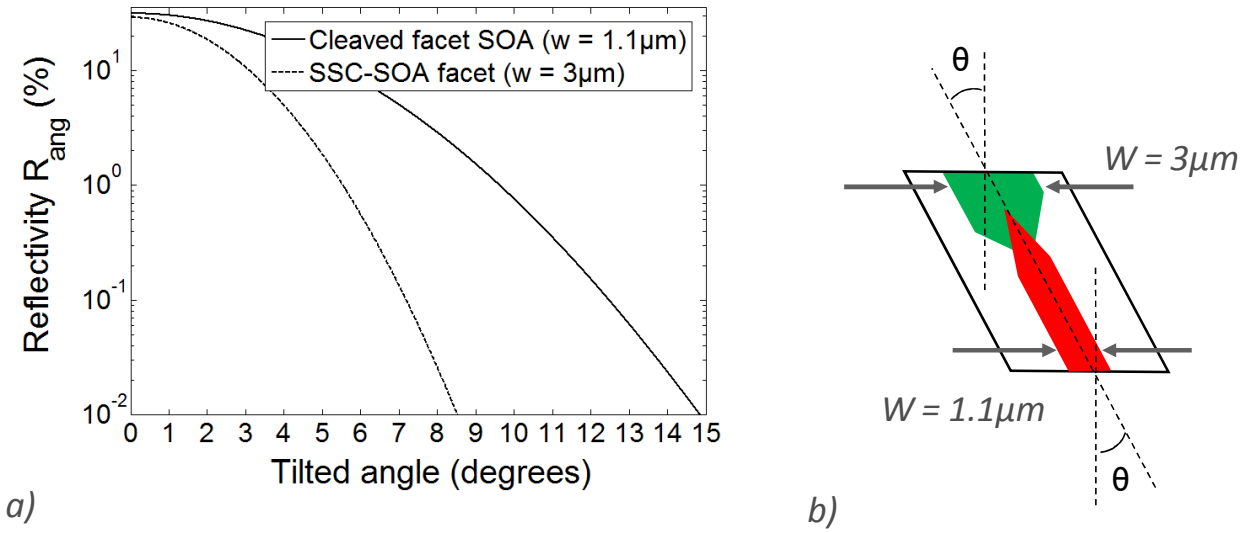

Figure 2-31– Effective reflectivity of angled facet SOA devices

However this model does not consider the optical field as an infinite sum of plane wave. In the k space, the optical mode size strongly affects the distribution of the k vector and needs to be included in the effective reflectivity. Section 2.2.3.3 discusses the modal reflectivity of a tilted facet and the entire calculation is described in Appendix I.

2.2.3.1.3 Window facet structure

The introduction of a window region leads to the reduction of the facet reflectivity [28, 29, 30]. It consists of a transparent region between the active region and the facet. Inside this region, free space propagation is obtained therefore the part of the light coupled back into the active waveguide is a small fraction of the total reflected light. In fact, the optical mode is broadened in the free space region before and after reflection as represented in Figure 2-32. The material used for the window region has larger band gap in order to avoid photon absorption, however intrinsic material absorption is present and induces losses. The effect of the window region on the facet reflectivity has been modelled [31] but is not described here.

However the use of a window region increases the coupling losses as the light is diffracted from the end of the active region. In our structure, we use a passive waveguide to continuously guide the optical signal to overcome this limit. The mode expansion reduces the effective facet reflectivity as described in section 2.2.3.3.

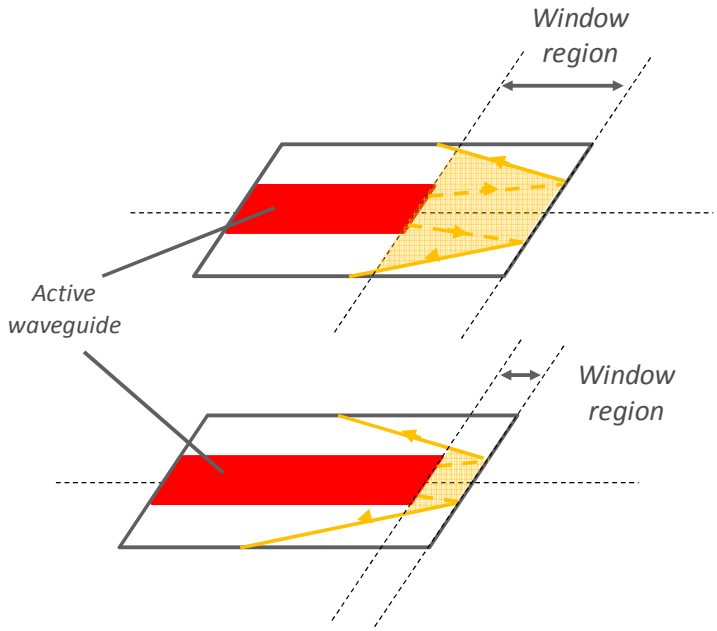

Figure 2-32 – RSOA with window region schematic representation with different window length

2.2.3.1.4 Multi-layer coating on tilted waveguide RSOA

A multi-layers AR coating model has been developed in [20]. The reflectivity of the tilted facet at 7° has been measured and simulated (see Figure 2-33). An effective reflectivity of $5x10^{-4}$ for polarization S (TE mode) and $3x10^{-4}$ for polarization P (TM mode) is measured at 1550 nm. S and P are the polarization states of the incident light.

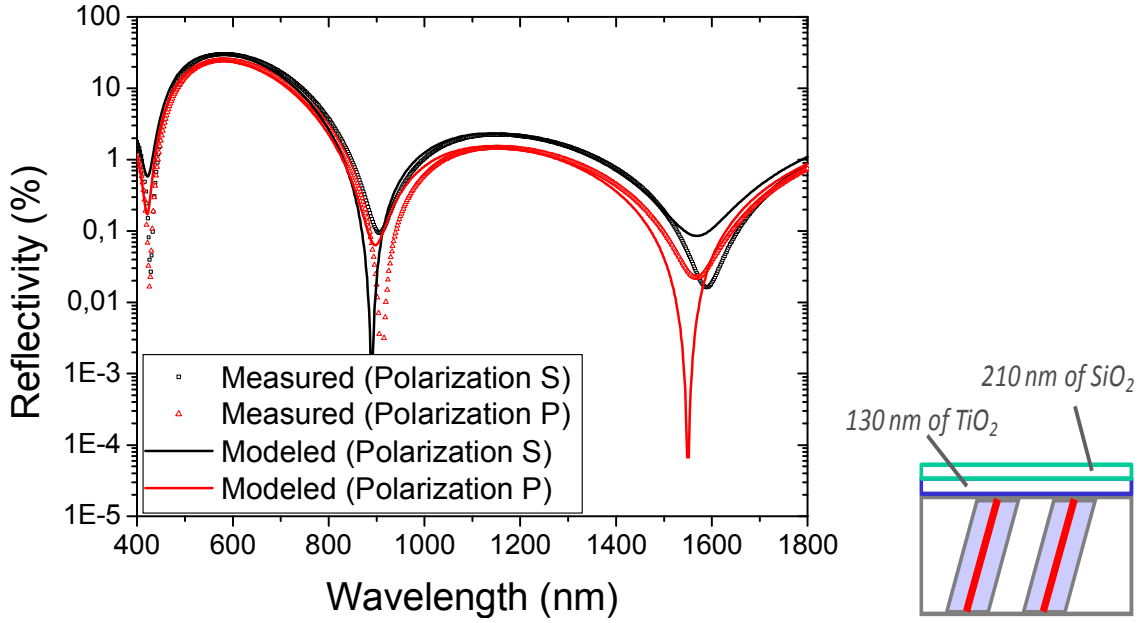

Figure 2-33 – Anti-reflective facet coating reflectivity depending on the wavelength at 7° angle

The measurements clearly show that the reflectivity of a tilted and coated facet cannot be efficiently reduced. However in this model and in the measurements, we assume a plane wave which is not relevant in our study. As a waveguide structure is used, it is important to calculate the effective reflectivity which leads to couple back the light into the active waveguide. Because not all the reflected light is coupled back to the waveguide, a lower reflectivity can be obtained. The optical re-injection effect is discussed in section 2.2.3.3.

2.2.3.2 High-reflectivity facet

HR coating is done by deposition of dielectric layers as SiO_2 and TiO_2. The reflectivity modelling can be done using the transmission matrix method for a multilayer dielectric structure. This method was developed in [32] and consists to represent several layers by a 2×2 matrix Q_n, which is:

$$Q_n = D_n P_n {D_n}^{-1} \qquad 2\text{-}10$$

Where D_n and P_n are the transmission and propagation matrices of n^{th} layer, respectively.

The definitions of the matrices are as follows:

$$D_n = \begin{bmatrix} 1 & 1 \\ n_n \cos(\theta_n) & -n_n \cos(\theta_n) \end{bmatrix}_S \; or \begin{bmatrix} \cos(\theta_n) & \cos(\theta_n) \\ n_n & -n_n \end{bmatrix}_P$$

$$P_n = \begin{bmatrix} e^{i\varphi_n} & 0 \\ 0 & e^{-i\varphi_n} \end{bmatrix} \qquad 2\text{-}11$$

Where n_n, θ_n, and φ_n are the refractive index, the incident angle, and the phase shift of the n^{th} layer.

The phase shift is given by:

$$\varphi_n = \left(\frac{\omega}{c_0}\right) d_n n_n \cos(\theta_n)$$

2-12

Where ω, c_0, and d_n are the angular frequency of light, the speed of light in a vacuum and the thickness of the n^{th} layer respectively.

Hence, the whole structure can be represented by a single matrix, which is a product of matrices in sequence of each layer. The product of the matrices is sandwiched by the inverse transmission matrix of air and the transmission matrix of the substrate.

$$\begin{bmatrix} M_{11} & M_{12} \\ M_{21} & M_{22} \end{bmatrix} = {D_0}^{-1}\left[D_1 P_1 {D_1}^{-1} \times D_2 P_2 {D_2}^{-1} \ldots D_n P_n {D_n}^{-1}\right] D_s$$

2-13

By using the 2×2 matrix method, the reflectance and transmittance of monochromatic plane waves through a multilayer dielectric structure can be obtained. The reflection and transmission coefficients are defined as:

$$r = \frac{M_{21}}{M_{11}}$$

$$t = \frac{1}{M_{11}}$$

2-14

Note that these expressions are complex and hence also give the phase shift of the reflected or transmitted light. So for instance the reflectivity can be written:

$$r = |r| e^{-i\Phi}$$

2-15

where Φ is the phase shift on reflection.

The power reflectivity and transmittance is given by:

$$R = |r|^2$$

$$T = |t|^2$$

2-16

The reflectivity of the coating is calculated using the Matlab model developed in [33].The refractive index and the thickness respectively are 2.288 (252.12 nm) for TiO_2 layers and 1.468 (166.38 nm) for SiO_2 layers. The reflectivity spectrum presents a rectangular central peak with

maximum reflectance at N = 10. However the side–lobes are quite prominent (The dependence of the refractive indices on the wavelength for the different layers is not taken into account).

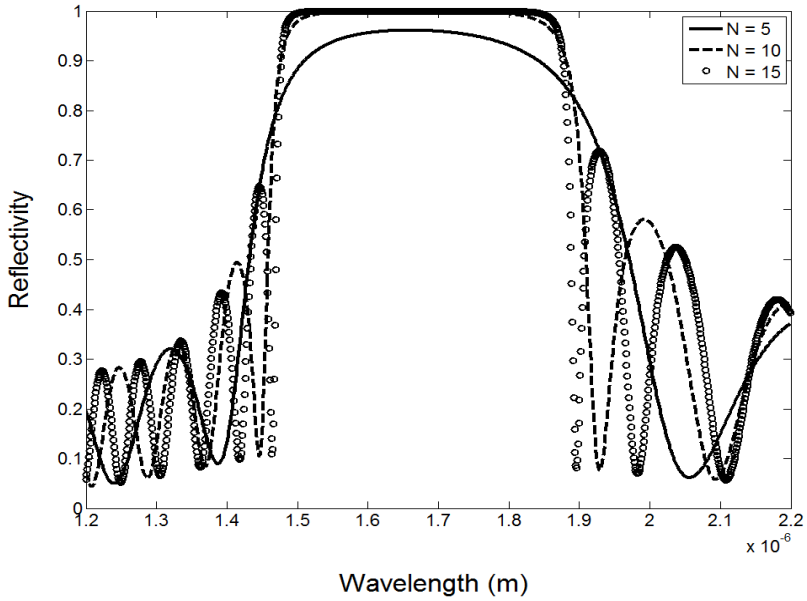

Figure 2-34 – HR SOA facet reflectivity depending on the wavelength

In practice, adding too many layers causes a compression of the different layers, which modifies the thickness and the refractive index. It also leads to impurities and defects apparition, therefore the reflectivity decreases. Consequently, a low number of layers are usually used. In III-V lab, four pairs of layers are used which is closely equivalent to the N = 5 in Figure 2-2-34 and give a reflectivity of 96.1%. Tilted waveguides are used to reduce the reflectivity of the output facet (as described previously) and also affect the HR coating profile. The simulation of a tilted HR SOA facet at 7° is presented in Figure 2-36 (for N = 4).

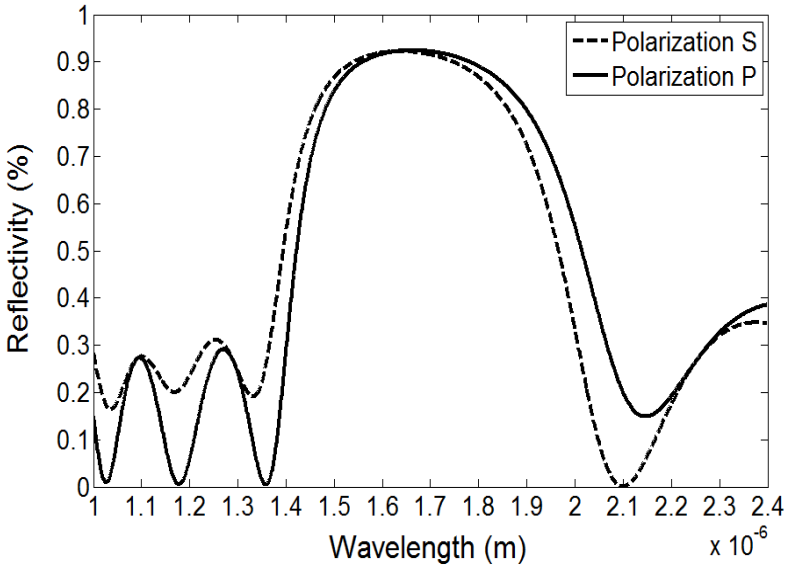

Figure 2-35 – Tilted HR SOA facet reflectivity at 7° depending on the wavelength (N = 4)

The reflectivity decreases to 89.5% for the P polarization and 90.4% for the S polarization. It is weakly affected by the tilt. The HR facet reflectivity has been measured and corresponds to 94.27% - 95.3%, respectively for P and S polarization. However the total reflectivity of the SOA also depends on the optical mode size. In fact, the light coupled back into the active waveguide experiences a different reflectivity compared to the plane-wave approximation.

2.2.3.3 RSOA optical feedback

When the optical mode becomes larger, the divergence decreases (in fact, an infinitely large optical mode can be considered as a plane wave).

In a waveguide, plane waves reflected back and forth between the two interfaces of the middle layer are one possible representation of guided modes. The light propagation is characterized by an angle of incidence which should be smaller than a critical angle ($a_{critical}$) in order to be guided. The critical angle depends on the material refractive index, which may vary depending on the light wavelength. Therefore injected light should have a minimum angle when it is launched into the waveguide in order to be guided.

The same idea is considered here where the injected light is reflected from a tilted facet. If a plane wave is assumed (large optical mode), the reflected light is not guided due to an incompatible angles ($a_{reflected} > a_{critical}$). In the case of a small optical mode, a high divergence is observed which means a large amount of wave vectors with different angles, so some of them have smaller angle than the critical angle and a part of the reflected light is guided back into the slab waveguide. A schematic representation is proposed in Figure 2-36.

Thus in a tilted waveguide, the optical mode size strongly affects the reflectivity. Then the reflectivity can be reduced using a larger optical mode. This effect also depends on the polarization of the optical mode.

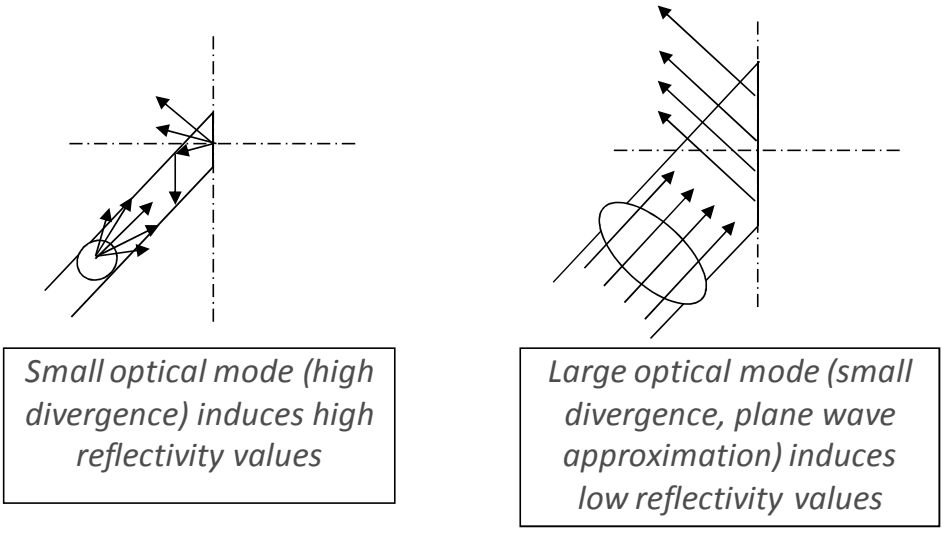

Figure 2-36 – Schematic representations of optical modes divergence and its effects on the reflectivity

The effective facet reflectivity of an SOA depending on the optical mode size has been studied both theoretically and experimentally [34]. A theoretical model is proposed which is based on the electric field formalism. In case of a small optical mode, an average divergence of $\Delta\alpha_{3\mathrm{dB}}$ = 44.9° (which corresponds to Δk_x = 2.7 μm^{-1}) is measured (see Table 2-2), which gives a reflectivity of 6.25%. The simulated reflectivity is 6% (for TE mode) for the same average divergence. The difference can be due to some approximations in our model such as the Gaussian distribution of the beam but also to the limited precision of the experimental measurement (the reflectivity should be higher due to the facet roughness).

For low divergence values ($\Delta\alpha_{3db}$ = 17°), a smaller reflectivity is obtained from the experiment: R = 0.013%. Simulated reflectivity of 0.0025 % is observed for Δk_x = 1.07 μm^{-1} (which corresponds to $\Delta\alpha_{3db}$ = 17°). Such a difference can be explained due to the internal reflectivity produced by the tapers which means that even when applying an anti-reflection coating, it is not possible to decrease the reflectivity below 10^{-4}. So the low theoretical values of the reflectivity, when large optical modes are considered, can never be reached. All simulated and experimental results are presented in Figure 2-37. Because no fitting parameters are used in this model, the fit in this figure is significant even though we only use two data points.

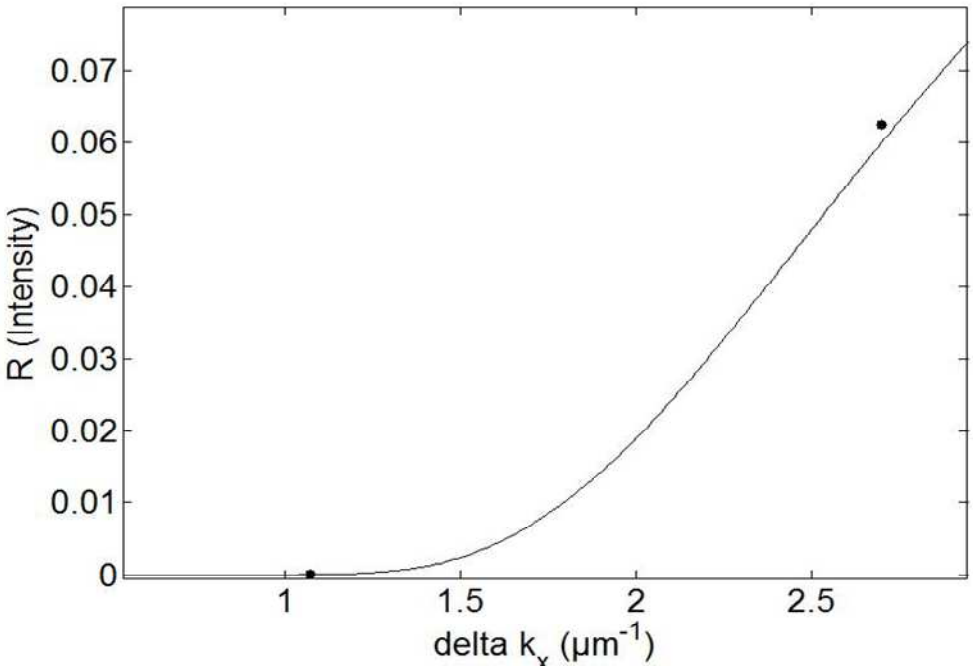

Figure 2-37 – Simulated and experimental reflectivity of 7° tilted waveguide as a function of Δk_x

1-D analysis has been made based on electric field theory which matches with experimental measurements. The optical mode size clearly affects the facet reflectivity based on plane-wave decomposition techniques and Fresnel's law. More details are presented in the Appendix I. SSC-SOAs should be used in order to minimize the gain ripple since these have a lower reflectivity. The impact of the facet reflectivity on the device performances is further studied in chapter 3 as well as the effective reflectivity taking in account the backward coupled optical wave into the active zone.

2.3 Conclusions

In this chapter, we presented the design and processing of RSOA devices. The growth of two different vertical structures is first detailed. Quaternary alloys (InGaAsP) are used for the active and passive layers as well as for the SCH layers. Then InP materials are grown with various doping profiles and thicknesses. The thickness, material composition, doping density and refractive index of the several layers are detailed in section 2.1.1. The active zone thickness enables us to control the optical confinement. However the TM and TE optical confinement are slightly different and induce polarisation dependent devices. Different values for $g_{mat\ TM}$ and $g_{mat\ TE}$ are used to compensate for this effect and achieved using tensile strain bulk material for the active zone. BRS is then described. The impact of the different heterojunctions and homojunction is experimentally evaluated based on I-V and SE measurements. A leakage current is observed in the tapering region.

The design of an efficient SSC is then discussed. Stationary solutions of modal distributions in the active and passive layers are calculated. The coupling ratio between both solutions is also computed depending of the SSC geometry. Efficient coupling is obtained for an ideal situation. The mode expansion is observed and confirmed by far-field measurements. Issues related to not perfect SSC are discussed. A new SSC design is proposed and clearly reduces the gain ripple.

The SOA and RSOA processing steps are described in section 2.2.1. The different deposition and etching techniques as well as the ion implantation are presented. SEM pictures show the structure at different building stages. Bounding and cleaving are described in section 2.2.2. The facet reflectivity is one of the main parameter in order to realize high performances RSOAs. Indeed a low gain ripple is required for RSOA practical use (colourless operation). Then low reflectivity facet is obtained by combining AR coating, tilting waveguide and large optical output mode. These techniques are first described separately. The effective reflectivity of an angled facet SOA devices is calculated using Marcuse's model. The simulations confirm that a tilted waveguide is needed to reduce the input facet reflectivity. High reflectivity is obtained by HR coating (deposition of dielectric layers as SiO_2 and TiO_2). The mirror reflectivity is first computed based on the transmission matrix method for a multilayer dielectric structure.

However the effective input and mirror reflectivity need to be calculated considering the optical mode size. Section 2.2.3.3 presents an original approach based on the electric field formalism. Simulated and experimental reflectivity of a 7° tilted waveguide as a function of Δk_x are presented and more details can be found in Appendix I.

2.4 References

[1] H. Nelson, "Epitaxial Growth from the Liquid State and Its Application to the Fabrication of Tunnel and Laser Diodes", RCA Rev. 24, 1963, pp. 603

[2] W. F. Finch and E. W. Mehal, "Preparation of $GaAs_xP_{1-x}$ by Vapor Phase Reaction", J. Electrochem Soc., Vol. 111, Issue 7, 1964, pp. 814-817

[3] R. D. Dupuis, "AlGaAs-GaAs lasers grown by metalorganic chemical vapor deposition", J. Crystal Growth, Vol. 55, Issue 1, 1981, pp. 213-222

[4] A. Y. Cho, "Film Deposition by Molecular-Beam Techniques", J. Vac. Sci. Technol., Vol. 8, No. 5, 1971, pp. s31-s38

[5] T. H. Maiman, "Stimulated Optical Radiation in Ruby", Nature 187, 1960, pp. 493-494

[6] "SOA Design Rules", Technical Note, Alcatel-lucent, 2002

[7] J.Y. Emery, "Control of the low tensile strained bulk SCH based 1.55µm SOA", Technical Note, Alcatel-lucent, 1999

[8] G. P. Agrawal, "Semiconductor lasers : Past, Present, and future", AIP Series on Theoretical and Applied Optics, AIP Press, chap. 1, New York, 1995 , pp. 15-18

[9] Joachim Piprek, "Semiconductor optoelectronic devices: Introduction to Physics and simulation", Academic Press, chap 2, 2003, pp27-32

[10] J. C. Dyment, "Hermite-Gaussian Mode Patterns in GaAs Junction Lasers", Appl. Phys. Lett., Vol. 10, No. 3, 1967, pp. 84-86

[11] B. Schwartz, M. W. Focht, N. K. Dutta, R. J. Nelson and P. Besomi, "Stripe geometry InP/InGaAsP lasers fabricated with deuteron bombardment", Trans. Electron Devices, Vol. 31, No. 6, 1984, pp. 841-843

[12] W. T. Tsang and R. A. Logan, "A new high-power, narrow-beam transverse-mode stabilized semiconductor laser at 1.5 µm: the heteroepitaxial ridge-overgrown laser", Appl. Phys. Lett., Vol. 45, No. 10, 1984, pp. 1025-1028

[13] R. S. Tucker, "High-Speed Modulation of Semiconductor Lasers", Trans. Electron Devices, Vol. 32, No. 12, 1985, pp. 2572 - 2584

[14] T. Tsukada, "GaAs/$Ga_{1-x}Al_xAs$ buried-heterostructure injection lasers", J. Appl. Phys., Vol. 45, No. 11, 1974, pp. 4899-4906

[15] N. K. Dutta and Q. Wang, "Semiconductor Optical Amplifiers", World Scientific Publishing, Chap. 4, 2006, pp. 96-98

[16] N. K. Dutta and Q. Wang, "Semiconductor Optical Amplifiers", World Scientific Publishing, Chap. 4, 2006, pp. 100-101

[17] N. K. Dutta, D. P. Wilt and R. J. Nelson, "Analysis of Leakage Currents in 1.3-µm InGaAsP Real-Index-Guided Lasers", J. Lightwave Technol., Vol. LT-2, No. 3, 1984, pp. 201-208

[18] P. Doussiere, P. Garabedian, V. Colson, O. Legouezigou, F. Leblond, J. L. Lafragette, M. Monnot, and B. Fernier, "Polarization insensitive semiconductor optical amplifier with buried laterally tapered active waveguide", in Optical Amplifiers and Their Applications, Vol. 17 of OSA Technical Digest Series, FA2, 1992

[19] N. Yoshimoto, T. Ito, K. Magari, Y. Kawaguchi, K. Kishi, Y. Kondo, Y. Kadota, O. Mitomi, Y. Yoshikuni, Y. Hasumi, Y. Tohmori, and O. Nakajima, "Four-channel polarization-insensitive SOA gate array integrated with butt-jointed spot-size converters", Electron. Lett., Vol. 33, No. 24, 1997, pp. 2045-2046

[20]T. Saitoh, T. Mukai, and O. Mikami, "Theoretical analysis and fabrication of antireflection coatings for laser-diode facets", J. Lightwave Technol., Vol. 3, No. 2, 1985, pp. 288-293

[21] G. P. Agrawal, N. A. Olson, and N. K. Dutta, "Effect of fiber-far-end reflections on intensity and phase noise in InGaAsP semiconductor laser", Appl. Phys. Lett., Vol. 45, No. 6, Sept. 1984, pp. 597-599

[22] M. J. Connelly, "Semiconductor Optical Amplifiers", Boston, MA: Kluwer Academic, Chap. 2, 2002, pp. 15-17

[23] C. E. Zah, J. S. Oinski, C. Caneau, S. G. Menocal, L. A. Reith, J. Salzman, F. K. Shokoohi, and T. P. Lee, "Fabrication and performance of 1.5 μm GaInAsP travelling-wave laser amplifiers with angled facets", Electron. Lett., Vol.23, No. 19, 1987, pp. 990-992

[24] G. De Valicourt, D. Maké, J. Landreau, M. Lamponi, G.H. Duan, P. Chanclou and R. Brenot, « New RSOA Devices for Extended Reach and High Capacity Hybrid TDM/WDM -PON Networks », in Proc. ECOC'09, P9.5.2, 2009

[25] C. E. Zah, C. Caneau, F. K. Shokoohi, S. G. Menocal, F. Favire, L. A. Reith, and T. P. Lee, "1.3 μm GaInAsP near-travelling-wave laser amplifiers made by combination of angled facets and antireflection coatings", Electron. Lett., vol. 24, No. 20, 1988, pp. 1275-1276

[26] D. Marcuse, "Reflection loss of laser mode from tilted end mirror", J. Lightwave Technol., Vol. 7, No. 2, 1989, pp. 336-339

[27] M. J. Connelly, "Semiconductor Optical Amplifiers", Boston, MA: Kluwer Academic, Ch. 3, 2002, pp. 28-30

[28] N. A. Olsson, R. F. Kazarinov, W. A. Nordland,C. H. Henry, M. G. Oberg, H. G. White, P. A. Garbinski and A. Savage, "Polarisation-independent optical amplifier with buried facets", Electron. Lett., Vol. 25, No. 16, 1989, pp. 1048-1049

[29] I. Cha, M. Kitamura, H. Honmou and I. Mito, "1.5 μm band travelling-wave semiconductor optical amplifier with window facet structure", Electron. Lett., Vol. 25, No. 18, 1989, pp. 1241-1242

[30] M. Connelly, "Semiconductor Optical Amplifiers", Boston, MA: Kluwer Academic, Ch. 3, 2002, pp. 30-31

[31] J. R. Kim, J. S. Lee, S. Park, M. W. Park, J. S. Yu, S. D. Lee, A. G. Choo, T. I. Kim, and Y. H. Lee, "Spot-Size Converter Integrated Polarization Insensitive Semiconductor Optical Amplifiers", IEEE Photonics technology letters, Vol. 11, No. 8, Aug. 1999, pp. 967-969

[32] C.J. Herpburn & M.P. Vaughan, "Bragg reflectivity modeling", Technical Note, University of Essex, 2002

[33] G. de Valicourt, C. Porzi, M. Guina, and N.Balkan, "Dilute Nitride Vertical-Cavity Gate for All-optical Logic at 1.3μm", IET optoelectronic, Vol. 4, No. 5, 2010, pp 201-209

[34] G. de Valicourt, G. H. Duan, C. Ware, M. Lamponi and R. Brenot, "Experimental and theoretical investigation of Mode Size Effects on Tilted Facet Reflectivity", IET optoelectronics, Vol. 5, No. 4, 2011, pp. 175-180

Chapter 3. Static model and characterization of RSOA devices

In a laser, the net gain is clamped above threshold, which usually leads to small and almost constant carrier densities. On the contrary, in a SOA, carrier density strongly depends on the current and on the position along the active stripe [1]. Besides, it is not possible to consider only photons having the wavelength of the amplified signal. The characteristics of most SOAs are mainly governed by the photons of the Amplified Spontaneous Emission (ASE), which propagate in both directions and cover a wide spectral range. Carrier density is therefore governed by ASE and signal photon density.

Finally, since photon density is not homogeneous along the SOA, carrier density also depends on the position. This Lateral Spatial Hole Burning (LSHB) is also present in many lasers, but it results from the coupling between carriers and a single photon population. These saturation effects strongly influence the performances of SOAs [2], and they have not been modelled accurately yet. In RSOA, this effect is even stronger as the signal propagates forward and backward into the active zone.

For the static performances, steady-state models have been proposed [3] and show good agreement with experiments but using extracted SOA/RSOA parameters. Besides, none of these models has been validated for small and large confinement factors. SOA/RSOA models can be space-resolved numerically, which take into account facet reflectivity as well as forward and backward propagating signals [4-5] or simplified analytical model [6-7].

Up to now, RSOA fundamental parameters have not been studied extensively. The optical confinement, length and facet reflectivity strongly affect the carrier density distribution and consequently the static performances. Thus, these parameters have to be considered in order to realize optimized devices. A specific and simple model has to be developed in order to find an optimum configuration. Furthermore, this model will be used to understand the slow dynamic of RSOA compared to Directly Modulated Lasers.

In this chapter, we underline the physical phenomenon under the carrier's rate equation and we propose a simple multi-section model approach to give a first evaluation of the RSOA static parameters. The radiative and non-radiative recombination mechanisms are described and applied to RSOA structures. Approximations are done in order to keep the model as simple as possible. The model allows a preliminary analysis of the carrier density and the photon density distribution. The impact of this inhomogeneous distribution is discussed. Several RSOA have been fabricated with various values of optical confinement, length and facet reflectivity in order to evaluate experimentally the impact of these parameters. The experimental data are compared to the proposed model. The results lead to some design rules for high static performances RSOA.

However, dynamic modelling requires additional approximations and a dedicated study as it is demonstrated in chapter 4.

3.1 Interaction between Photon and electron

In this section, we detail the physics involved in SOAs and RSOAs. We first propose a theoretical approach in order to understand the entire physical phenomenon in section 3.1.1. A multi-section approach is chosen to model the device behaviour under static conditions. The aim of this section is not to propose a complex model but to underline and understand the different mechanisms in RSOA devices.

3.1.1 Carrier density rate equation

Gain in a semiconductor material results from current injection into the PIN structure. The relationship between the current *I* and the carrier density (n) is given by the rate-equation. The number of electrons (holes) supplied to the active zone per unit of time is:

$$\left(\frac{dN}{dt}\right)_{supply} = \frac{I}{e} \qquad 3\text{-}1$$

Where e is the electron charge.

The number of carrier supplied per unit time per unit volume is:

$$\left(\frac{dn}{dt}\right)_{supply} = \frac{I}{eV} \qquad 3\text{-}2$$

Where $n = \frac{N}{V}$ and V is the active zone volume.

The electrical injection based on the active zone dimensions is represented in Figure 3-1.

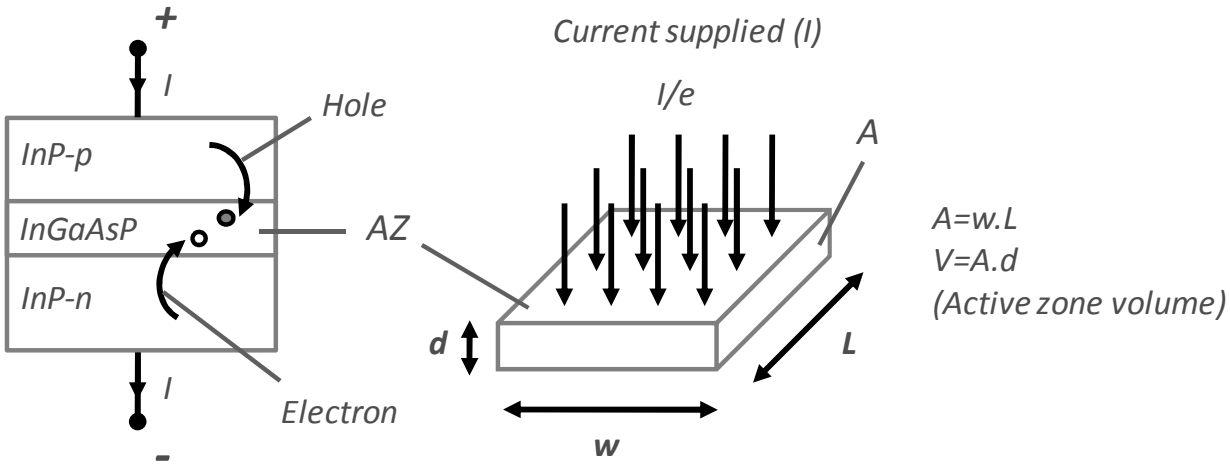

Figure 3-1 – Current injection in semiconductor materials

As we introduced in equation (1-8), the rate-equation should include the stimulated emission as well as the spontaneous and absorption rate. $R(n)$ is the rate of carrier recombination including the spontaneous emission. Electrons can recombine radiatively and non-radiatively therefore $R(n)$ can be written as:

$$R(n) = R_{rad}(n) + R_{non-rad}(n)$$

3-3

When an electron from the CB recombines with a VB hole and this process leads to the emission of a photon, it is called the radiative recombination. The rate of radiative recombination is:

$$R_{rad}(n) = B.n^2$$

3-4

This term corresponds to the spontaneous emission recombination. Non-radiative processes deplete the carrier density population in the CB then fewer carriers remain available for the stimulated emission and the generated amount of light is limited. The three main non-radiative recombination mechanisms in semiconductor are:

- The linear recombination due to the transfer of the electron energy to the thermal energy (in the form of phonons). This mechanism is called the Shockley-Read-Hall (SHR) recombination. The rate of SRH recombination is:

$$R_{SRH} = A.n$$

3-5

- The Auger recombination due to the transfer of the energy from high-energy electron/hole to the low-energy electron/hole with subsequent energy transfer to the crystal lattice. The rate of the Auger transitions is:

$$R_{Aug} = C.n^3$$

3-6

- Another non-radiative recombination process is the carrier leakage, where carriers leak across the SOA heterojunctions. The leakage rate depends on the drift or the diffusion of the carriers therefore is given by [8]:

$R_{leak} = D_{leak}.n^{3.5}$ for diffusion and $R_{leak} = D_{leak}.n^{5.5}$ for drift

3-7

The dominant leakage current is usually due to carrier drift. Therefore the total recombination rate is given by:

$$R(n) = R_{rad}(n) + R_{non-rad}(n) = A.n + B.n^2 + C.n^3 + D_{leak}.n^{5.5}$$

3-8

The carrier leakage is usually neglected. So the rate-equation states that the resulting change of the carrier density in the active zone is equal to the difference between the carrier supplied by

electrical injection and the carrier's recombination. The rate-equation without considering the stimulated emission is:

$$\frac{dn}{dt} = \frac{I}{e.V} - R(n) = \frac{I}{e.V} - (A.n + B.n^2 + C.n^3)$$

3-9

Amplification results from stimulated recombination of the electrons and holes due to the presence of photons. We demonstrated in section 1.2.1 that the material gain can be written as $g = \frac{1}{v_g S(t)} \frac{dS(t)}{dt}$ then $\frac{dS(t)}{dt} = g v_g S(t)$ where v_g is the light group velocity, $\frac{dS(t)}{dt}$ is the rate of the photon generation and $S(t)$ is the photon density (equation 1-16). Since the generation photons' rate corresponds to the electron (holes) disappearance therefore the stimulated recombination rate is:

$$\left(\frac{dn}{dt}\right)_{stimulated} = -\frac{dS}{dt} = -g v_g S$$

3-10

The interaction between photons and electrons inside the active region depends on the position and the time. Therefore the carrier density at z and t is governed by the final rate-equation. We neglect carrier diffusion in order to simplify the carrier density rate-equation. This assumption is valid as long as the amplifier length L is much longer than the diffusion length, which is typically on the order of microns. We also assume that the carrier density is independent of the lateral dimensions.

$$\boxed{\frac{dn(z,t)}{dt} = \frac{I(t)}{e.V} - (A.n(z,t) + B.n(z,t)^2 + C.n(z,t)^3) - v_g g_{net}.S(z,t)}$$

3-11

Where $n(z,t)$ is the carrier density, $I(t)$ is the applied bias current and $S(z,t)$ is the photon density including the light velocity group.

The first term of this equation represents the addition of carriers into the active region through electrical injection as described previously. Amplification of the signal induces carrier depletion as described by the last term of the equation (3-11). Section 1.2.1 detailed the role of stimulated emission in relation to the material gain. The absorption is included in the net gain approximation when considering the internal losses (section 1.2.2). At the steady-state condition, the carrier density converges over time to a constant value. Simulations based on the equation (3-11) are represented in Figure 3-2 at various initial carrier densities. A 700 μm cavity long device is considered. We use ode23s Matlab solver to calculate the carrier density evolution over the time. This is a first approximation (one section model) as the final carrier density should depend on z as well, given that we take into account input light, which is amplified along z.

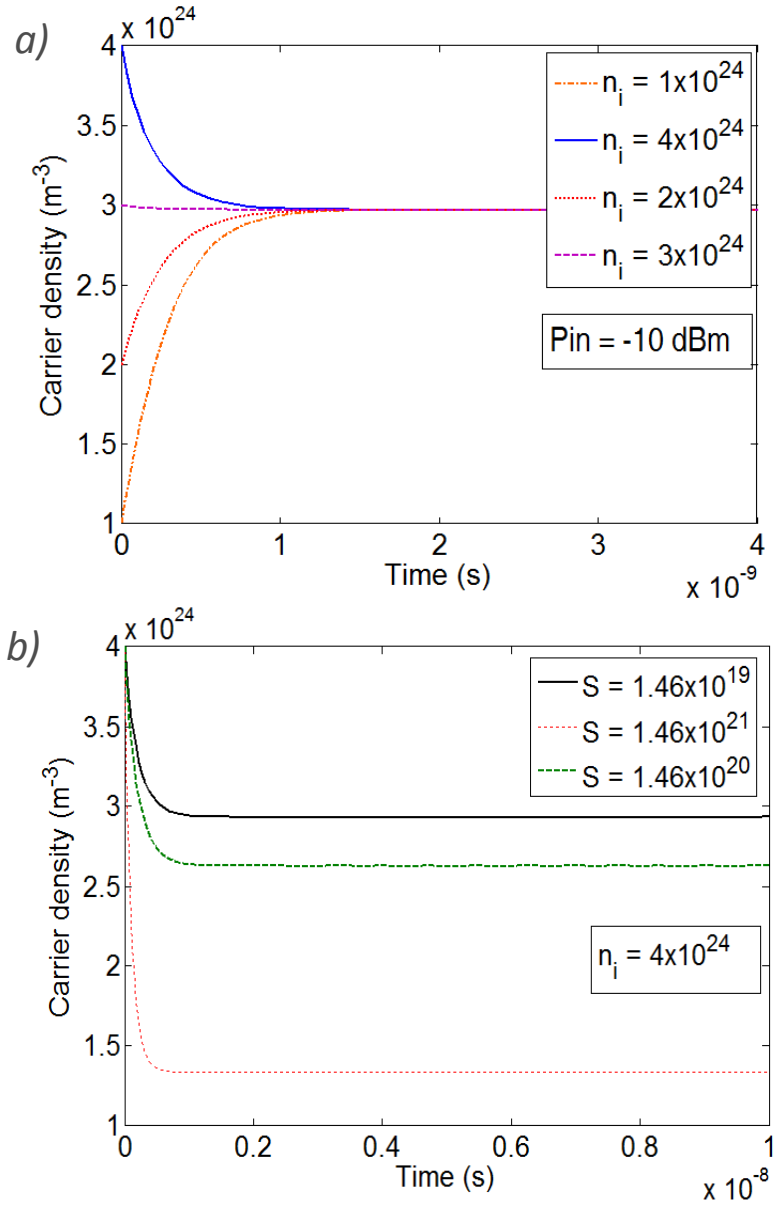

Figure 3-2 – Carrier density convergence (a) with initial carrier density as parameter (b) with input photon density as parameter based on Matlab Simulation

At the steady state, the carrier density level depends on the input photon density as represented in Figure 3-2-(b) however the initial value does not affect this convergence (Figure 3-2-(a)). It can be noticed that the convergence time depends on the input carrier density and input photon density. These two parameters strongly affect the dynamic of the device. More details are presented in Chapter 4. In this previous simulation, a single-section device is considered. Signal photon density is amplified along z and produces a non-homogeneous carrier distribution. The wave propagation in a gain medium was solved in the section 1.3.1 by considering a complex refractive index. Then an optical resonator was considered (section 1.3.2). Single pass gain was calculated as $G_{TW} = G_S = e^{gL}$. In SOAs or RSOAs, the signal is split up as two travelling waves whose amplitudes vary in a complex way in the forward and backward directions as described in 1.3.1. The z direction is assumed to lay along the SOA axis with its origin at the input facet. We consider a double propagation direction model in order to keep it

closer to a real-life case. The signal propagation is numerically calculated by using a multi-section model as described in the next section.

3.1.2 Multi-section model

A time domain model for reflective semiconductor optical amplifiers (RSOAs) was developed based on the carrier rate and wave propagation equations. In this model, the non linear gain saturation and the amplified spontaneous emission have been included. Previous works have addressed the non linear compression gain [9] and the amplified spontaneous emission [10]. Recently, they have been considered and implemented together in a current injected RSOA modulator model [11]. In our model we have also included both. This approach follows the same analytical formalism as Connelly's static model [12].

To make the model suitable for static analysis some assumptions have been made and simplifications have been introduced. Since, as a modulator, the RSOA is mainly illuminated by a CW optical source, the material gain is assumed to vary linearly with the carrier density but with no wavelength dependence. Amplified spontaneous emission power noise is assumed to be a white noise, with an equivalent optical noise bandwidth. When the current is modulated in a RSOA, the carrier density and the photon density are varying with time and position. This is caused by the optical wave propagation and the carrier/photon interaction. The carrier density variation is introduced in the model by dividing the total device length into smaller sections. For each section the carrier density is assumed to remain constant along the longitudinal direction. The equations are linking the driving current, the carrier density and the photon density. Figure 3-3 represents the model elementary section. It includes ports representing the input and output photon density (forward and backward), input and output amplified spontaneous emission (forward and backward), the input electrical current injection and carrier density. We do not consider the phase shift of the signal.

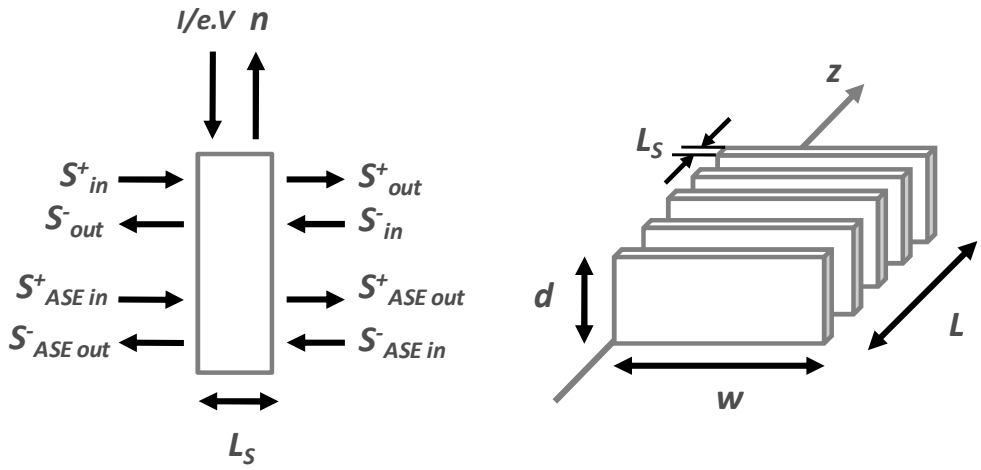

Figure 3-3 – RSOA elementary representation for numerical modelling

The forward and backward propagating optical fields (excluding spontaneous emission) are described by the relation between the input optical power and output optical power which for one section is given by equation (1-54).

$$P^{+}(z+\Delta z) = P^{+}(z)e^{g_{net}\Delta z}$$
$$P^{-}(z-\Delta z) = P^{-}(z)e^{g_{net}\Delta z}$$

3-12

Where g_{net} is the net gain defined by equation (1-35).

The material gain is usually approximated by a linear function of the carrier density, given by equation (1-31). In general the material gain also depends on the photon density S. For high photon density, the gain saturates and this phenomenon is described by the gain compression factor. Then, the material gain equation becomes:

$$g_S = \frac{g_m}{1+\varepsilon.S}$$

3-13

Where ε is the gain saturation parameter.

The boundary conditions for the device input and output facets, are given by equation (1-45).

$$P^{+}(0) = (1-R_1)P_{in} + R_1P^{-}(0)$$
$$P^{-}(L) = R_2P^{+}(L)$$

3-14

Where R_1 and R_2 are power reflection coefficients.

The amplified spontaneous emission is the main noise source in an RSOA and determines the RSOA static and dynamic performances under low input optical power. For high stimulated emission output power the spontaneous emission drops significantly and its impact on the device performances is less significant. For a section of length Δz the ASE power spectral density generated within that section is given by the following equation:

$$P_{ASE} = \eta_{Sp}(G_S(z)-1)h\nu B_0$$

3-15

Where G_s is the single pass gain of one section and η_{sp} is the spontaneous emission factor.

The spontaneous emission factor can be approximated by [13]:

$$\eta_{Sp} = \frac{n}{n-n_0}$$

3-16

In our model we have assumed a constant noise power spectral density over an optical bandwidth B_o. The bandwidth B_o is estimated at $5x10^{12}$ Hz as detailed in [11]. The implementation of the ASE noise travelling wave follows a procedure similar to the optical signal travelling wave. The spontaneous emission output power for the forward and backward noise signals has two

contributions: the amplified input noise and the generated spontaneous emission component within the section. The relations for the input/output noise are:

$$\mathrm{P_{ASE}}^{+}(\mathrm{z}+\Delta\mathrm{z}) = \eta_{Sp}(G_S(\mathrm{z})-1)\mathrm{h}\nu\mathrm{B}_0 + G_S(\mathrm{z})\mathrm{P_{ASE}}^{+}(\mathrm{z})$$
$$\mathrm{P_{ASE}}^{-}(\mathrm{z}-\Delta\mathrm{z}) = \eta_{Sp}(G_S(\mathrm{z})-1)\mathrm{h}\nu\mathrm{B}_0 + G_S(\mathrm{z})\mathrm{P_{ASE}}^{-}(\mathrm{z})$$

3-17

Therefore the final rate equation of carrier density at z and t is given by:

$$\boxed{\frac{dn(z,t)}{dt} = \frac{I(t)}{e.V} - (A.n(z,t) + B.n(z,t)^2 + C.n(z,t)^3) - v_g.g_{net}.S(z,t) - v_g.g_{net}.S_{ASE}(z,t)}$$

3-18

The signal photon density S(z,t) includes the forward and backward signal power. The photon density generated by the ASE $S_{ASE}(z,t)$ also includes the ASE propagating in both directions. It was demonstrated in section 1.2.1 that the signal power is related to the photon density S(z) by:

$$P_{total}(z) = \hbar\omega v_g S_{eff} S(z)$$

3-19

Therefore,

$$\boxed{S(z) = \frac{P^+(z) + P^-(z)}{\hbar\omega v_g S_{eff}}}$$

3-20

3.1.3 Numerical calculation and input parameters for the steady-state model

Parameter values are extracted from the literature. The physical dimensions correspond to the fabrication process detailed in Chapter 2. All input parameters are summarized in Table 3-1.

Symbol	Parameter	value	unit
L	Active region length	700	μm
L_S	Section length	10	μm
d	Active region thickness	120	nm
Γ	Optical confinement factor	0.2	----
a	Differential gain	$4x10^{-20}$	m^{-2}
a_2	Approximation parameters for material gain	$0.15x10^{19}$	$m^{-1}.m^{-2}$
b_2	Approximation parameters for material gain	$2.7x10^{-32}$	$m.m^3$
ε	Gain saturation parameter	$1.1x10^{-22}$	m^3
A	non-radiative recombination coefficient	$3.5x10^8$	s^{-1}
B	Bimolecular radiative recombination coefficient	$5.6x10^{-16}$	$m^3.s^{-1}$
C	Auger recombination coefficient	$3x10^{-41}$	$m^6.s^{-1}$
α_a	Attenuation coefficient in the active zone	25	cm^{-1}
α_c	Attenuation coefficient in the cladding zone	15	cm^{-1}

Table 3-1 – RSOA physical dimension and input parameters

We also assume 3 dB of coupling losses. Most of parameters are extracted from [11] and were obtained using ADS algorithm optimization based on fitting measurements with our devices (measurements done by Instituto de Telecomunicações).

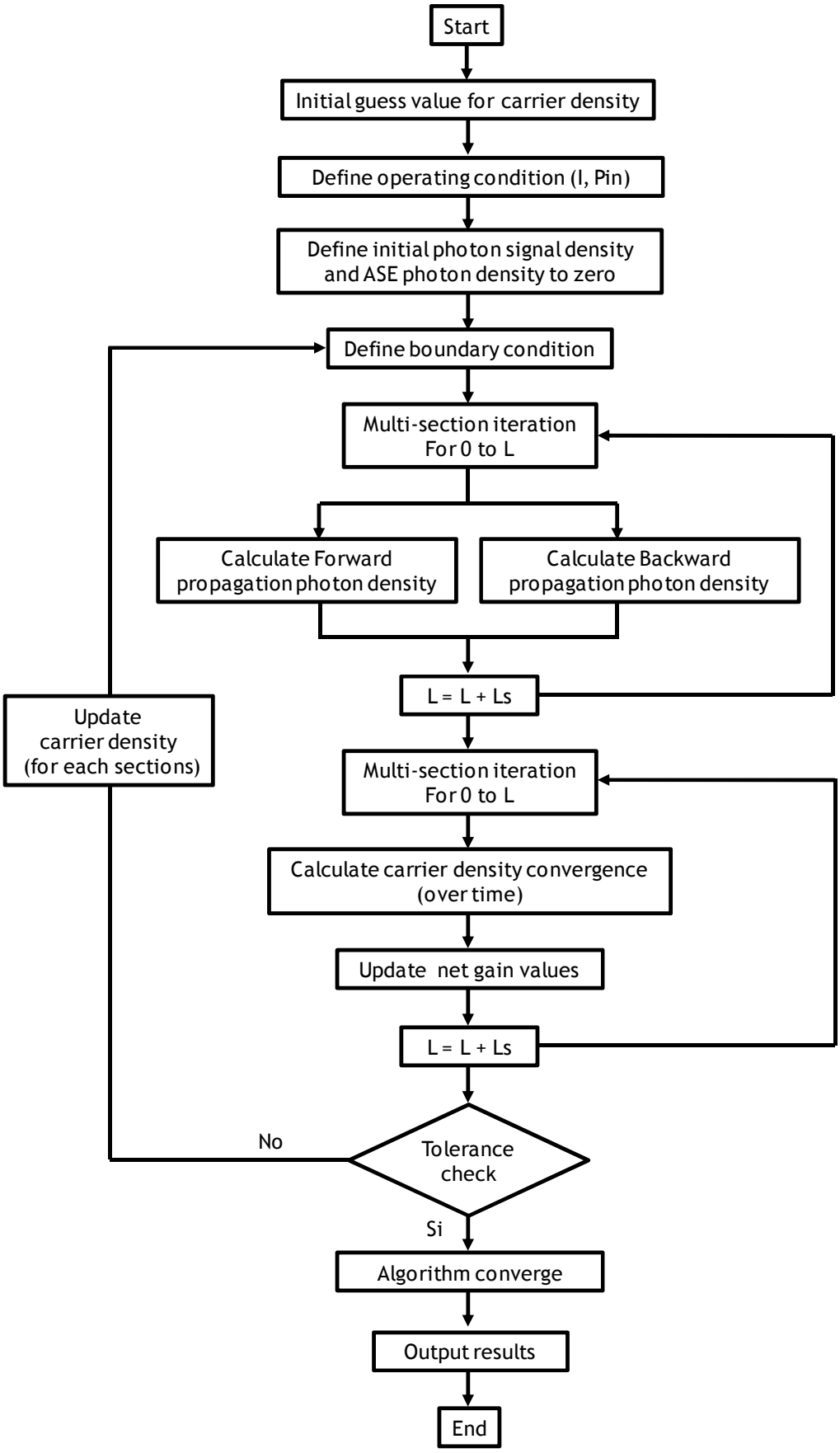

Figure 3-4 – Flow chart of SOA and RSOA numerical model

The principle of our model (flow chart) is detailed in Figure 3-4. An initial guess value is used for the carrier density to calculate the forward and backward signals and the ASE propagation photon density along the device. Our model uses Matlab solver functions to implement the model equations (section 3.1.1). Equations that include differentials can also be implemented by this program. Then using the Matlab solver, the carrier density rate equation is solved in each section. If equation (3-14) is not verified, the program starts the iteration again based on the previous carrier density profile. The carrier density profile is updated to a lower or higher value depending on the sign of the boundary condition until the convergence is obtained. A tolerance level needs to be defined and depends on the required accuracy. This algorithm is done for each bias current. Then the carrier density, photon density and optical gain are extracted into an output file to analyze the results.

This study was not focused on modelling. Good convergence and stability is limited to some particular operating conditions and more advanced models can be found in [14-15]. The gain variations with the bias current (Experimental and modelled) are compared in Figure 3-5. The experimental values were not used to fit the parameters and show that the model predicts measured values.

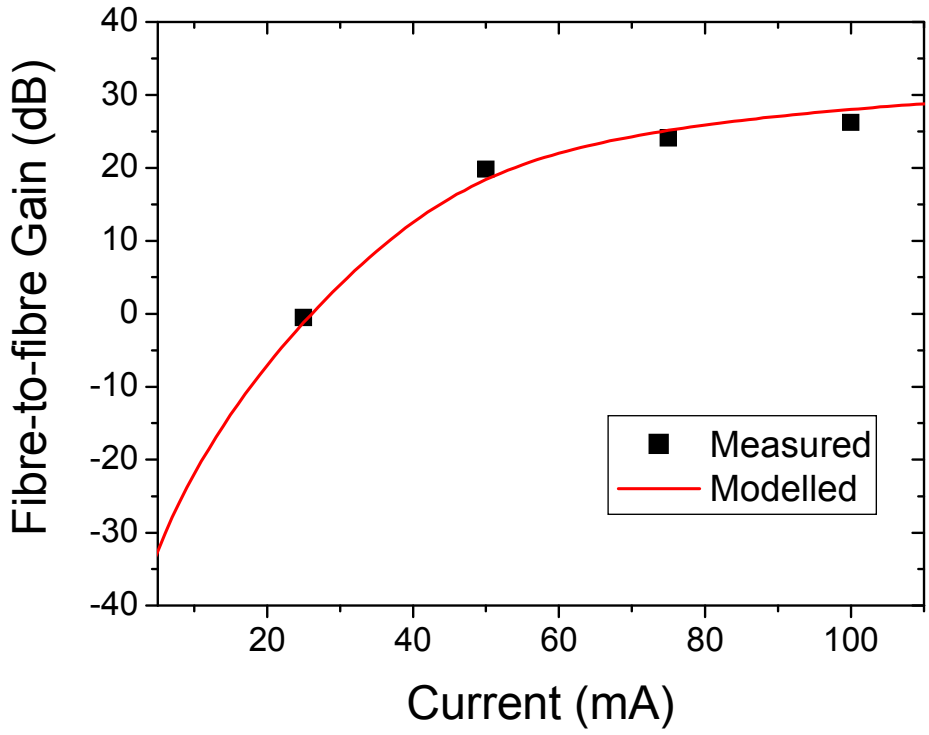

Figure 3-5 – Fibre-to-fibre gain for RSOA versus bias current

3.1.4 Carrier and photon density in SOA and RSOA devices

At first, the spatial distribution of the carrier and photon density has been studied in an SOA. A bell-shaped curve for the carrier density is obtained at low input injection (Figure 3-6-(a)). In this case, the carrier density profile is mainly due to the ASE propagation which is symmetrical for both directions. Therefore high ASE power is obtained at the input and output

facets and depletes the carrier in these regions. The signal photon density grows along the propagation axis and starts to become significant after 800 µm (Figure 3-6-(b)).

At high input power, the carrier density becomes asymmetrical and the peak is shifted to the input facet (Figure 3-6-(c)). This phenomenon can be explained by the signal propagation dominance. Signal photon density starts to grow significantly at 200 µm but saturates at the output facet of the device due to the strong carrier depletion (Figure 3-6-(d)).

In both cases, carrier consumption and saturation effects become more important at high input electrical injection.

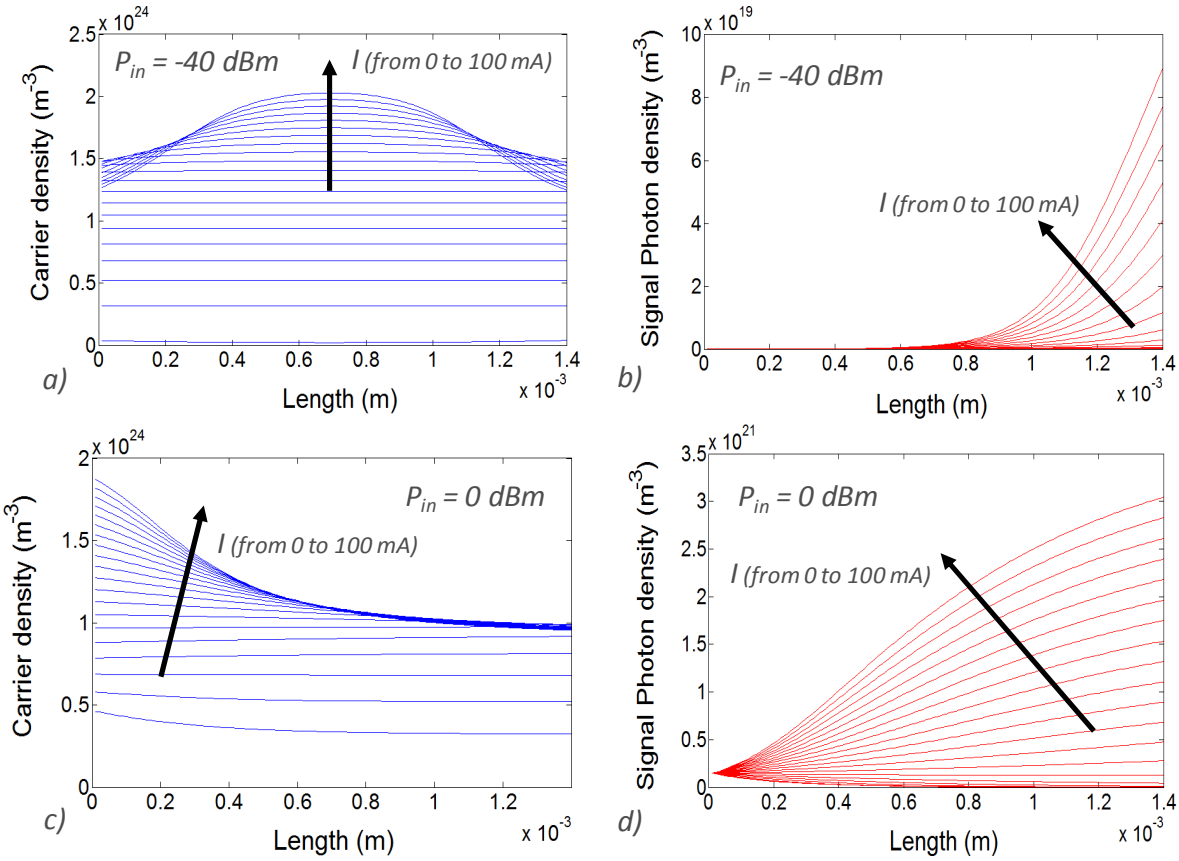

Figure 3-6 – Carrier and photon density spatial distribution in SOA device. (a) and (b) represents the simulation for P_{in} = -40 dBm ; (c) and (d) for 0 dBm

The second model consists of RSOA devices with half the length. In this case, the carrier density profile is represented in Figure 3-7 as well as the total photon density. The algorithm is the same but the input parameters are changed such as the second facet's reflectivity. At low input injection (P_{in} = -40 dBm), the carrier density profile is in this case not symmetrical due to the high reflection of the second facet. Stronger depletion than in SOA occurs from the ASE and the signal double propagation (reflective behaviour of the device). Also at P_{in} = -40 dBm, the ASE power dominates the signal power which explains that the RSOA device saturates more at high input electrical current. Thus the total photon density is higher than in an SOA device because more ASE is produced.

At high input optical power, the behaviour of the reflective device becomes completely different as compared to a classic SOA. In fact, the carrier density in an RSOA is flattened due to

the forward and backward propagations of the signal inside the device. The saturation effect occurs all along the RSOA and the signal photon density is smaller than in the SOA due to the overall depletion. At the mirror and input facets, the signal photon density becomes larger with the injected current as it has been more amplified during the forward and backward propagations.

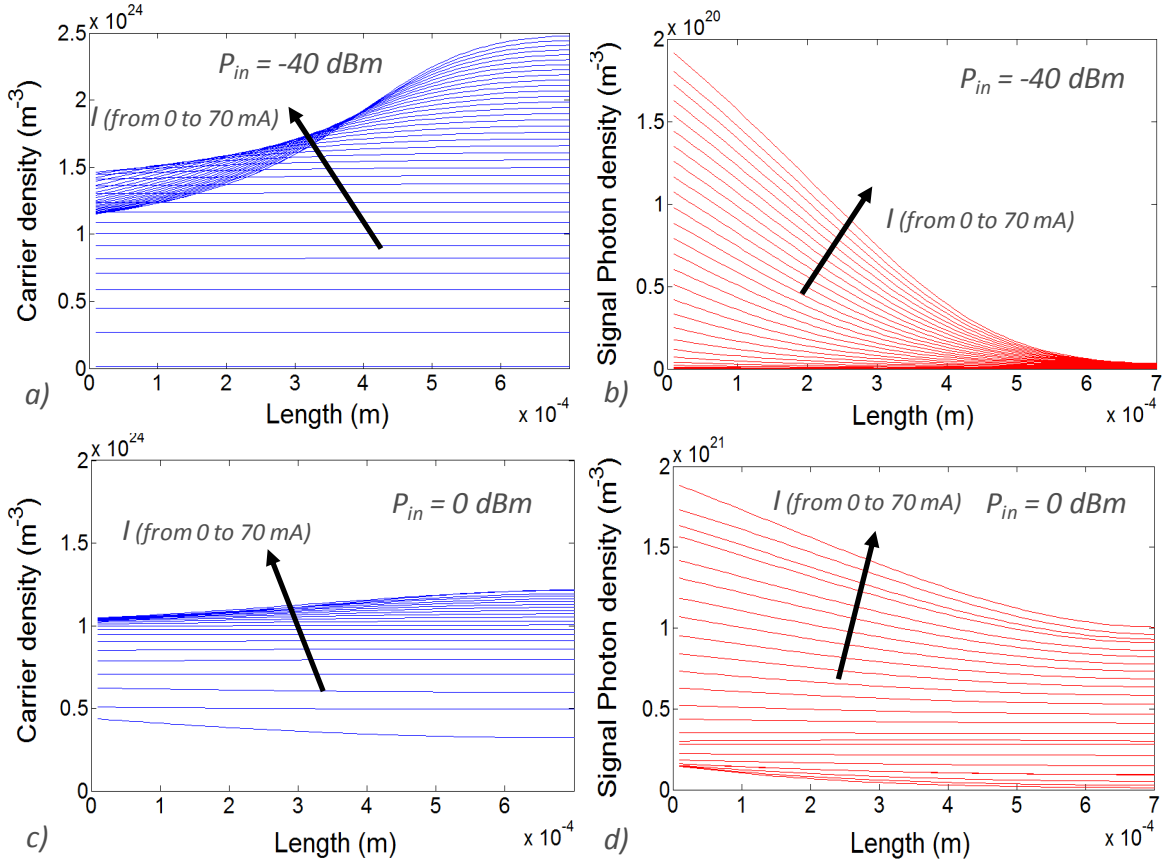

Figure 3-7 – Carrier and photon density spatial distribution in RSOA device. (a) and (b) represents the simulation from P_{in} = -40 dBm ; (c) and (d) for 0 dBm

From this preliminary analysis, a general conclusion can be deduced. RSOAs are more ASE-dominated than SOAs. Therefore RSOAs should saturate faster than classic SOAs. The overall photon density inside a RSOA is larger than in a classic SOA, reducing the material gain available for signal amplification. However the forward and backward signal amplifications could compensate for this effect. Large photon density should also affect the E/O bandwidth and is studied in chapter 4. All these effects are stronger at high input electrical injection and high input optical power. However they have not been modelled due to numerical convergence issues and will be studied experimentally.

3.2 Static devices characteristics

In this section, the main static characteristics are detailed and related to the design optimization. An optical fibre is used to couple the light into the device. In the active region, the incoming light encounters a single pass gain G_s. We define the input/output facet reflectivity as R_1 and the mirror facet as R_2. The facet R_1 has to be anti-reflection coated to prevent the RSOA

from lasing. The only straightforward design rule is the influence of the coupling efficiency: it has to be increased as much as possible. In order to assess the influence of L, R and Γ, various RSOAs have been fabricated. As discussed in sections 2.1.3 and 2.2.3.3 in chapter 2, SSC is used to increase the output optical mode size, to decrease the reflectivity and to increase the coupling efficiency (lower divergence). Two different optical confinements are studied (Γ = 20% and Γ = 80%) and various lengths are cleaved.

3.2.1 Experimental characterization set-up

In the absence of LSHB, the single pass gain can be deduced from the optical confinement Γ of the mode, the material gain g_m and the chip length L, as described in section 1.3.2. It is necessary to find the cavity transmission coefficient which strongly depends on the facet reflectivity (equation (1-52)). The RSOA intrinsic gain (ratio of the input signal power at the input facet to the signal power at the output facet) differs from the SOA one because the output and input facet are the same. Therefore we can write from equation (1-44):

$$G = \frac{|F_{out}|^2}{|F_{in}|^2} = \frac{|t.F^-(0)|^2}{|F_{in}|^2}$$

3-21

We adapt our earlier model (section 1.3.2), redefining the gain as in (3-21)

$$\boxed{G(\lambda_0) = \frac{R_2(1-R_1)^2 e^{2gL}}{(1-\sqrt{R_1R_2}e^{gL})^2 + 4\sqrt{R_1R_2}e^{gL}\sin^2(k_0 n' L)}}$$

3-22

If $R_2 = 0$, the light is not reflected back into the gain medium and the output power is zero. However it is useful to consider $R_1 = 0$, this means no reflection occurs at the input/output facet of the device. Then the previous equation becomes:

$$\boxed{G_S = R_2 e^{2gL}}$$

3-23

However, this expression is in general a very rough approximation, and the gain must be carefully integrated along the chip (as detailed in section 3.1.2). The optical confinement (Γ), the length (L) and the reflectivity (R) affect the single pass gain. The ASE power which is responsible for the LSHB changes depending on these parameters. The effect on non-homogenous carrier density distribution is similar in SOA (section 1.3.3). The device behaviour is counter-intuitive for reasons that are far from being obvious, not to mention the influence of the various parameters on the electrical bandwidth and dynamic characteristics (chapter 4). RSOA optimisation requires many experimental investigations and careful interpretations.

Therefore, optical gain measurements depending on the input current and optical power were realized. Figure 3-8 shows the experimental setup which is used to perform static measurements. The required wavelength controlled by an external cavity laser is launched into the RSOA through an optical circulator (OC). A combined power meter and attenuator is used to control the input power to the RSOA. An optical spectrum analyser and a power meter are used

in order to determine the static performances of the device, such as optical gain, gain peak, bandwidth and ripple, noise figure and output saturation power.

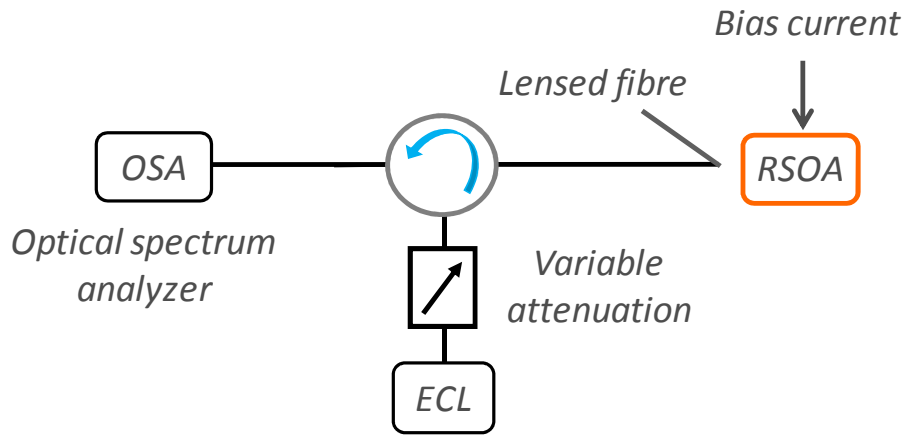

Figure 3-8 – Static experimental setup

The impacts of these several parameters (Γ, L and R) are experimentally studied in the next sections.

3.2.2 Influence of the optical confinement

As described in section 2.1.1, two vertical structures were grown. The optical gain for the optical confinements of Γ~20% and Γ~80% are compared depending on the input electrical current and optical power in Figure 3-9. The gain increases with the bias current as modelled in section 3.1.3 and starts to saturate at high electrical injection. Increasing the input power, the gain drops quickly due to the saturation effect. That is, the increase of optical input power at a constant current consumes many carriers for the stimulated emission therefore decreases the carrier density and increases the saturation effect. This transition corresponds to the frontier between the linear and the saturated regime. In this regime, the noise factor increases due to gain saturation.

The low confinement factor (Γ~20%) devices show higher gain than the high confinement factor (Γ~80%) devices. This result is counter-intuitive as the net gain should increase with higher optical confinement as defined in equation (1-35) and therefore the single pass gain as in equation (3-24). Because of the reflective behaviour of the device, RSOAs are more ASE-dominated than SOAs (as described in section 3.1.4) and high Γ means more ASE and more saturation. Thus a low confinement factor induces lower spontaneous emission power by reducing the effect of the ASE inside the device [2]. As the RSOA is less saturated, the single pass gain is also increasing with the reduced confinement factor (because the LSHB is reduced).We demonstrated in section 3.1.4 that RSOA devices have a non-uniform carrier density along the active zone. This interpretation can be confirmed by the simulations of the carrier density spatial distribution and SE measurements. This longitudinal spatial hole burning effect can be reduced by using lower optical confinement (Γ~20%).

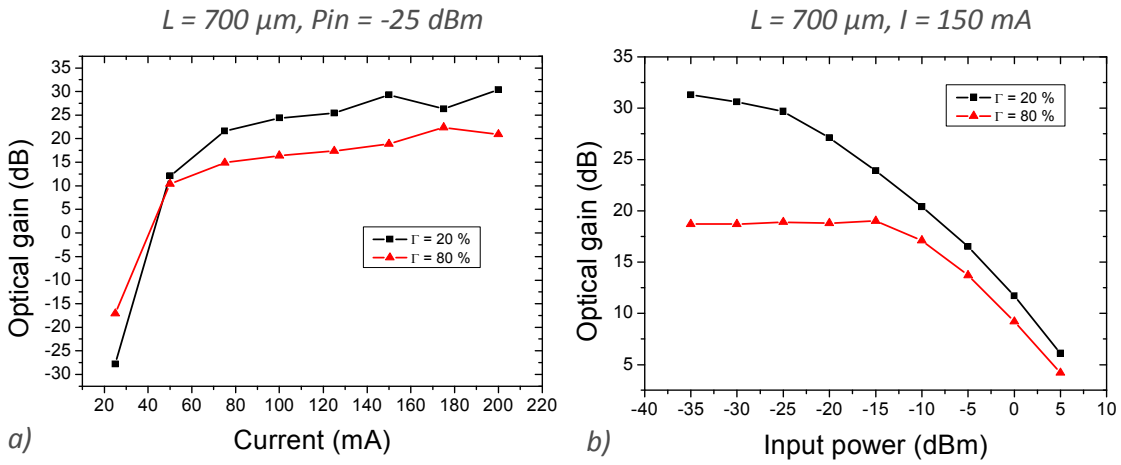

Figure 3-9 – Confinement effect on 700 µm long RSOA depending on the current (a) and the input power (b)

A common and useful figure of merit is the dependence of the optical gain on the output power. From this curve, we obtained the saturation power (P_{sat}) when the gain drops by 3 dB. Figure 3-10-(a) shows the optical gain versus the output power. The noise factor is reduced at low optical confinement and confirms the reduction of the guided ASE (Figure 3-10-(b)).

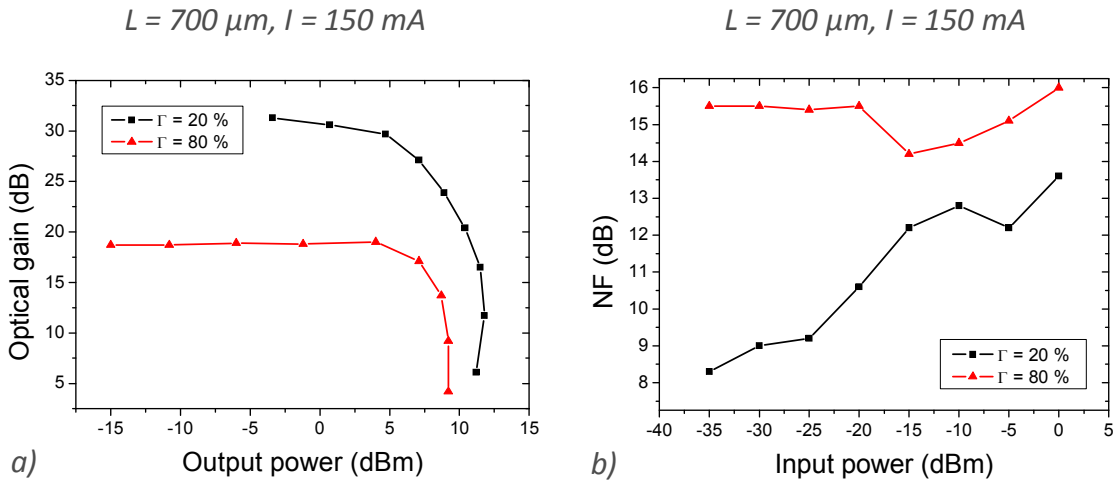

Figure 3-10 – (a) Saturation of the optical gain depending on the output power and (b) Noise factor depending on the input power

The saturation output powers obtained from Figure 3-10 are summarized in Table 3-2. Most of SOA devices show saturation power around 10 dBm and optimized SOA can reach 20 dBm [16]. However optimizing for maximum saturation power induces low gain (<15 dB) and large energy consumption (I > 500mA). In RSOA devices, high gain is obtained as well as reasonable saturation power. Saturation power of 7.5 and 7 dBm are observed for 700 µm active zone length and respectively for Γ = 80 % and Γ = 20 %.

	Γ = 20 %	Γ = 80 %
L = 700 µm	7 dBm	7.5 dBm

Table 3-2 – Saturation output power depending on the optical confinement

3.2.3 Saturation effect in long RSOA

Two optical confinement values have been studied and the best is found to be around 20%. It was the consequence of the LSHB reduction inside the active material which leads to an overall higher gain. However as described in equation (1-53), the length (L) also affects the single pass gain (G_s). Again two effects are in competition inside the active zone: the exponential growth of G_s with the length and the non-homogenous carrier density distribution (which leads to strong saturation effect). Therefore a trade-off needs to be found in order to balance these two effects.

By increasing the length, the forward and backward amplifications are also increased up to an optimum point. Devices that are too long induce high saturation and reduce the optical gain. Figure 3-11-(a) shows the optical gain versus the current density in different RSOA cavity lengths. The current density (J) is more relevant from a device point of view in order to compare similar operating conditions however the intensity (I) is more relevant from a system point of view in order to compare the power consumption of these devices (Figure 3-11- (b)).

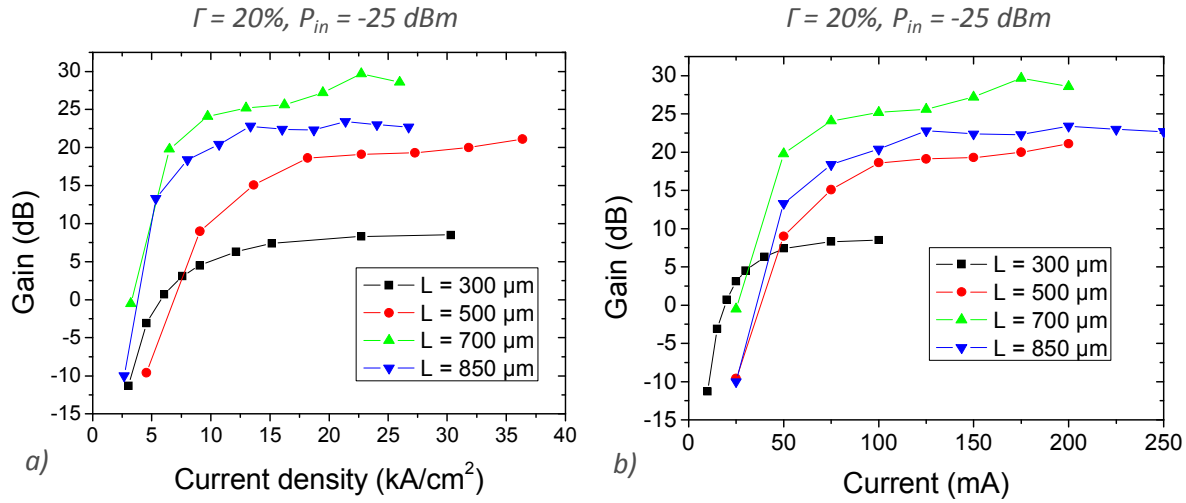

Figure 3-11 – Length effect on 20% optical confinement RSOA depending on the current density (a) and the output power (b)

At first, the increase of the cavity length induces higher optical gain (from 300 µm to 700µm) however when it reaches 850 µm, the gain drops back. Therefore a maximum gain is obtained for 700 µm long devices.

The optical gain versus the output power is presented in Figure 3-12-(a) and (b) respectively at the current density J = 10 kA/cm² and J = 20 kA/cm². The same phenomenon is

observed as in Figure 3-11. We can notice that increasing the gain leads to higher saturation power (in opposition to the observations in section 3.2.2). It can be explained by the fact that we are at a constant current density therefore the electrical bias current increases with the length of the device leading to an improvement of the saturation power. We can notice that at J = 20 kA/cm^2, all devices are under the saturated regime.

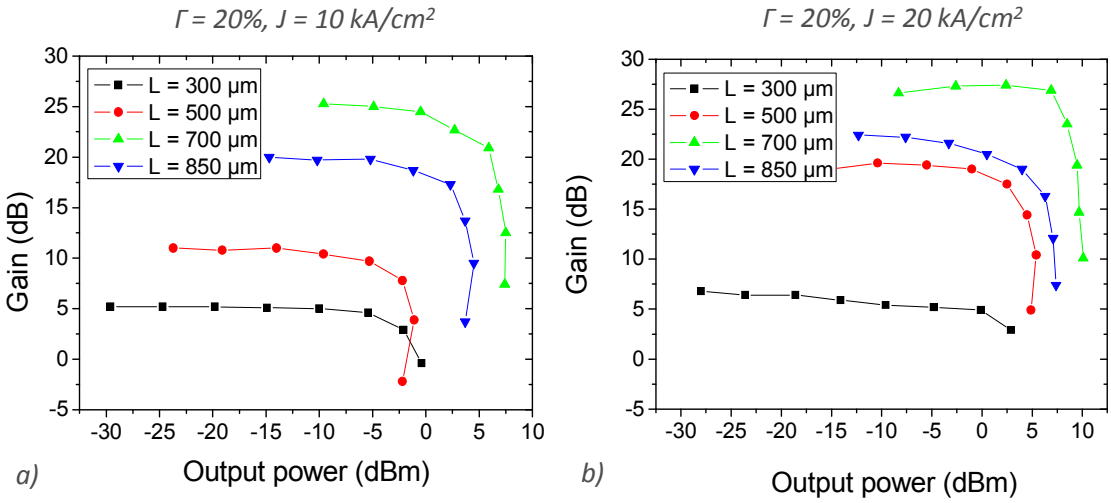

Figure 3-12 – Length effect on 20% optical confinement RSOA depending on the output power (a) for J = 10 kA/cm^2 and (b) for J = 20 kA/cm^2

For one specific optical confinement (Γ = 20%), an optimal length can be found in order to obtain the best static performances (high optical gain). At first, the optical gain increases linearly with the length. In fact, the forward and backward amplifications control the single pass gain. The impact of the length on the carrier distribution is studied in Figure 3-13. Figure 3-13-(a) represents the SE measurement set-up where an optical fibre is placed along the active zone at the input/output, centre and mirror region. Based on the previous model analysis, the carrier spatial distribution for several RSOA lengths is presented in Figure 3-13-(b). Then SE measurements as a function of the injected current are shown in Figure 3-13-(c). SE measurements are performed in 700 µm long RSOA in order to confirm the presence of the saturation effect.

At low input bias current, no difference is observed (Figure 3-13-(c)) due to the flat carrier density as simulated in Figure 3-7. The saturation effect starts to appear above 50 mA when the carrier density spatial distribution becomes non-homogeneous. Low SE power is collected at the input region due to the saturation effect which means low carrier density in the region. However the mirror region emits more SE power due to the high carrier density value. This demonstrates the presence of a strong saturation effect in the device.

At 300 µm, a flat carrier density profile is simulated (Figure 3-13-(b)). The increase of the length leads to some main observations. In longer RSOAs, the depletion becomes stronger which induces a lower overall carrier density and a larger absolute difference in the carrier density between input and mirror facet.

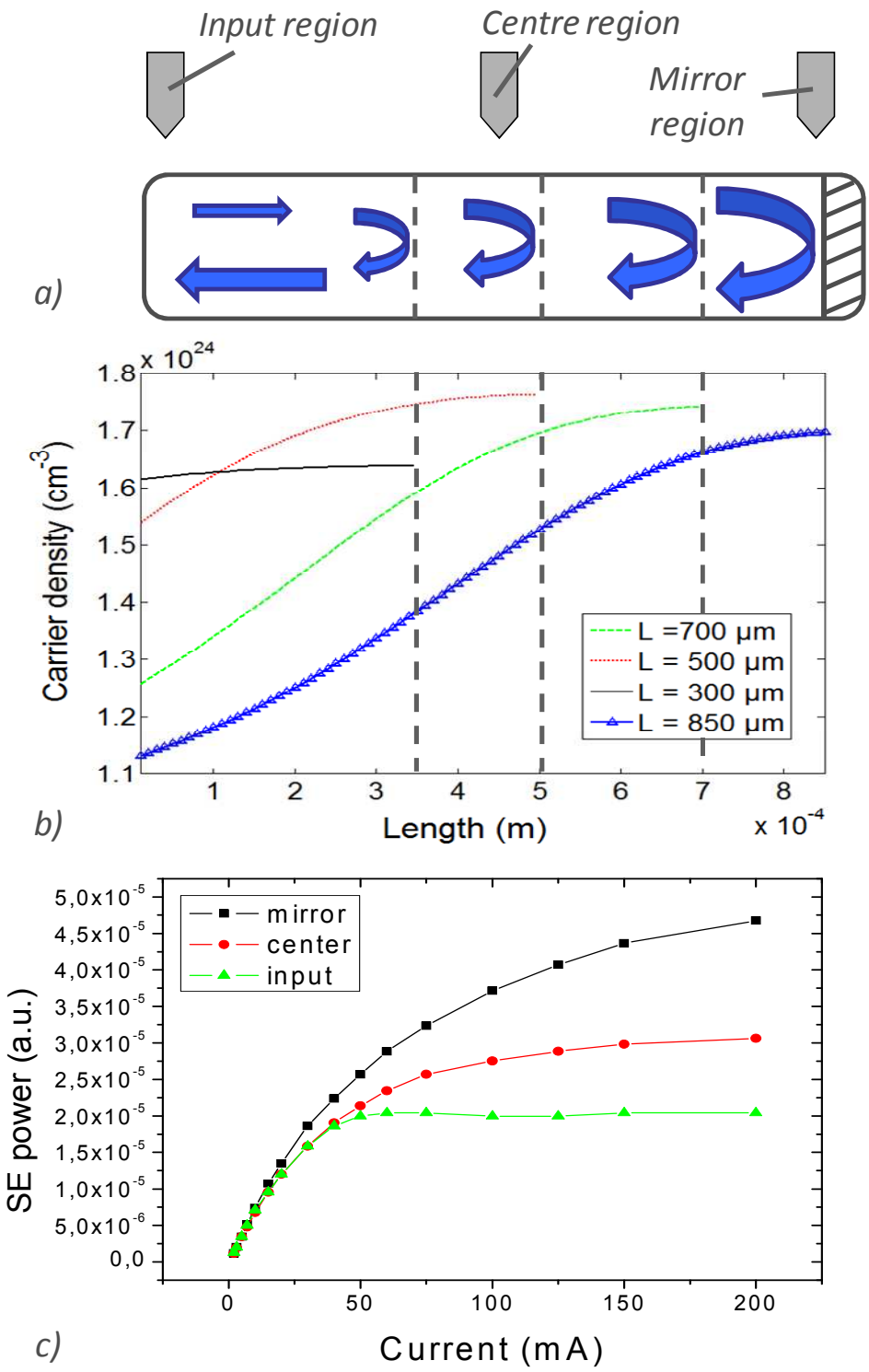

Figure 3-13 – (a) SE schematic measurement set-up; LSHB effect on (b)carrier density spatial distribution and (c) the optical gain in long RSOA device

When varying the length of the RSOA, those several effects account for the existence of an optimum length where the optical gain is maximised. The optical gain (extracted from Figure 3-11) versus the length of the device is plotted on Figure 3-14 for two current densities. The graph confirms the previous analysis and the maximum optical gain is obtained at L = 700 µm.

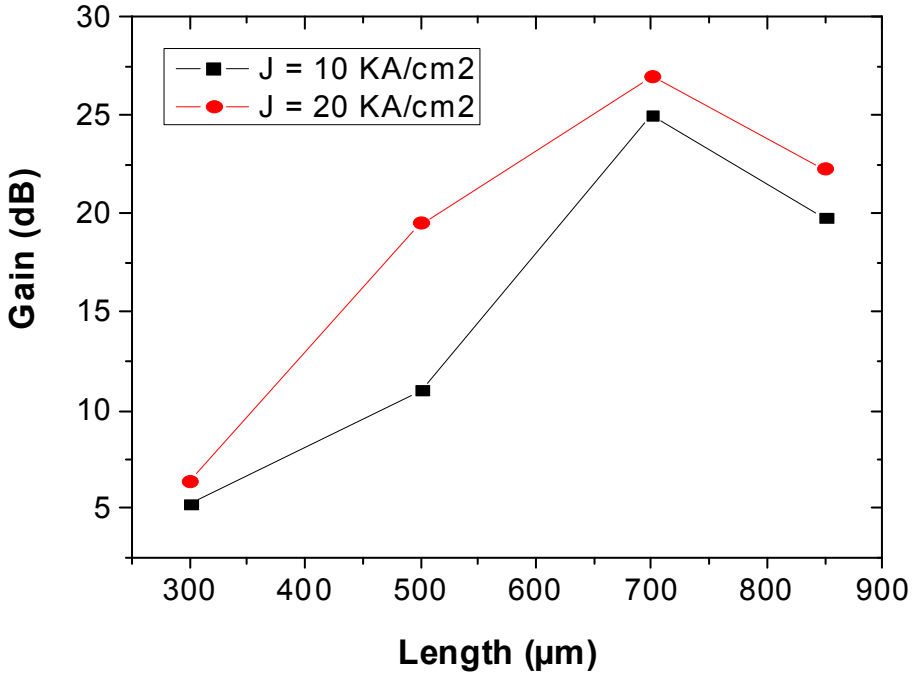

Figure 3-14 – Impact of the LSHB on the optical gain in long RSOA device

3.2.4 Impact of the facet Reflectivity

Reflectivity of facets is one of the key parameters in SOA and was recognized in the early work on SOA as in [17]. The reflectivity directly impacts on the device behaviour. As described in chapter 1, FP-SOA provides a resonant amplification between the facets due to high reflectivity. In contrast, TW-SOA requires negligible facet reflectivity. Therefore facet reflectivity control is of prime interest for these devices. Low facet reflectivity can be achieved using different techniques such as anti-reflection coating, tilted waveguide and window facet structure (chapter 2). The gain ripple depends on the single pass gain and the facet reflectivity (equation 2-4). It is essential to minimize the reflectivity in order to decrease the gain ripple. The goal of this section is to complete the theoretical approach done in Chapter 2 and study the impact of facet reflectivity on RSOA performances.

3.2.4.1 Threshold current and facet reflectivity in tilted waveguide

In order to study the impact of the tilted waveguides, SOA with various tilt angles have been processed. The SSC affects the reflectivity due to the optical mode expansion (Appendix I). In order to suppress this effect, we consider devices without the SSC by cleaving inside the AZ (Figure 3-15-(a)). Note that all devices are lasing, i.e. the reflectivity is high enough to induce low mirror losses (as described below). High reflectivity can be explained by a small optical mode inside the AZ. Furthermore large waveguide tilt angle induces large threshold current because of the low reflectivity. Their lasing threshold allows calculating their facets reflectivities as described below. The optical output power has been measured and is displayed in Figure 3-15-(b).

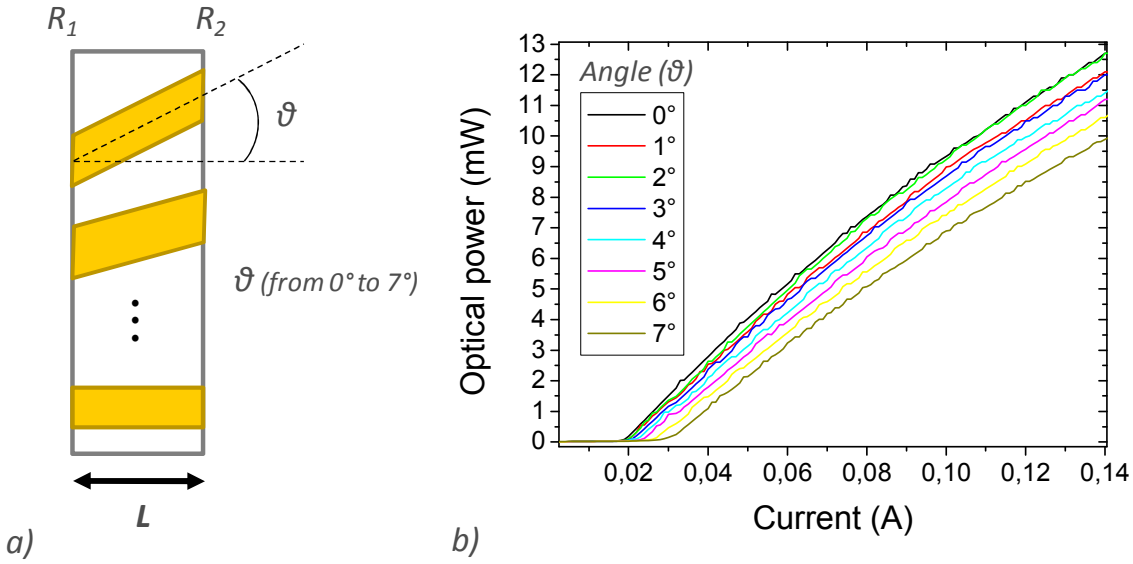

Figure 3-15 – Impact of tilted waveguide on output optical power with angle (θ) as parameter

FP lasers physics differ from the ones of SOA and more details can be found in [18].The oscillation conditions are derived from the small-signal gain analysis (section 1.3.2) and can be written as:

$$g_{net}(\lambda_M) = \frac{1}{2L}\ln\left(\frac{1}{R_1 R_2}\right)$$

$$\lambda_M = \frac{2n'(\lambda_M)L}{M}$$

3-25

It is common to characterize the term $\frac{1}{2L}\ln\left(\frac{1}{R_1R_2}\right)$ as the cavity mirror loss α_m. The cavity roundtrip gain g_c is defined as:

$$g_c = g_{net} - \alpha_m$$

3-26

Lasing takes place when the net modal gain is exactly equal to the mirror losses and this condition remains unchanged all the time at lasing. The net gain was derived from equation (1-35), we can then write:

$$\Gamma . g_m - \Gamma\alpha_a - (1-\Gamma)\alpha_c = \frac{1}{2L}\ln\left(\frac{1}{R_1R_2}\right)$$

3-27

We define n_{th} as the threshold current density and ${g_m}^{th} = a(n_{th} - n_0)$ is the material gain for $n = n_{th}$(from equation (1-31))

Note the carrier density is clamped at lasing and g_m remains constant. We demonstrated in section 3.1.1 that the rate-equation can be written as in equation (3-9). In order to find the

threshold current, we apply the rate-equation almost at the threshold when n ~ n_{th}, but the stimulated recombination is still small. At the steady state, we obtain:

$$0 = \frac{I_{th}}{e.V} - A.n_{th} + B.{n_{th}}^2 + C.{n_{th}}^3$$

3-28

Therefore the facet reflectivity of the devices represented in Figure 3-15-(a) can be extracted from the threshold current. Considering R_1 is equal to R_2 due to the symmetry of the device, equation (3-27) becomes:

$$\Gamma.a(n_{th} - n_0) - \Gamma\alpha_a - (1-\Gamma)\alpha_c = \frac{1}{L}\ln(\frac{1}{R})$$

3-29

The reflectivity and the threshold current for 700 µm long devices are represented in Figure 3-16. The simulation has been done considering the parameters presented in Table 3-1.

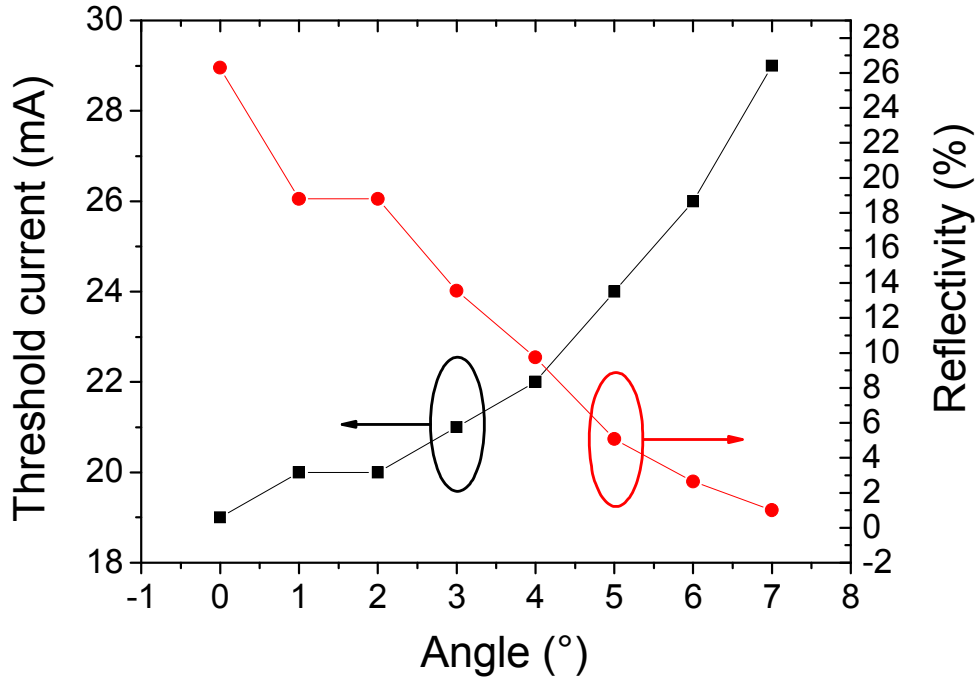

Figure 3-16 – Threshold current and reflectivity for various tilted waveguides

As expected, the reflectivity decreases when the angle increases. However the reflectivity at θ = 7° is much lower than the one calculated in section 2.2.3.3. Two different wafers have been used as well as different lengths and no direct comparison is possible. From this first analysis, we can extract the facet reflectivity of a cleaved waveguide depending on the waveguide angle. We can use it to study RSOA configurations when both facets reflectivities are different.

3.2.4.2 SSC and AR coating

In the same wafer, we cleave active waveguides (AW) with passive SSC in one end. AR coating were deposited. Four AW configurations are studied:

- Cleaved SSC-AW
- AR SSC AW
- Cleaved SSC with no tilted AW
- AR SSC with no tilted AW

The different configurations are represented in Figure 3-17. The idea is to calculate the different reflectivities as we already know R_2.

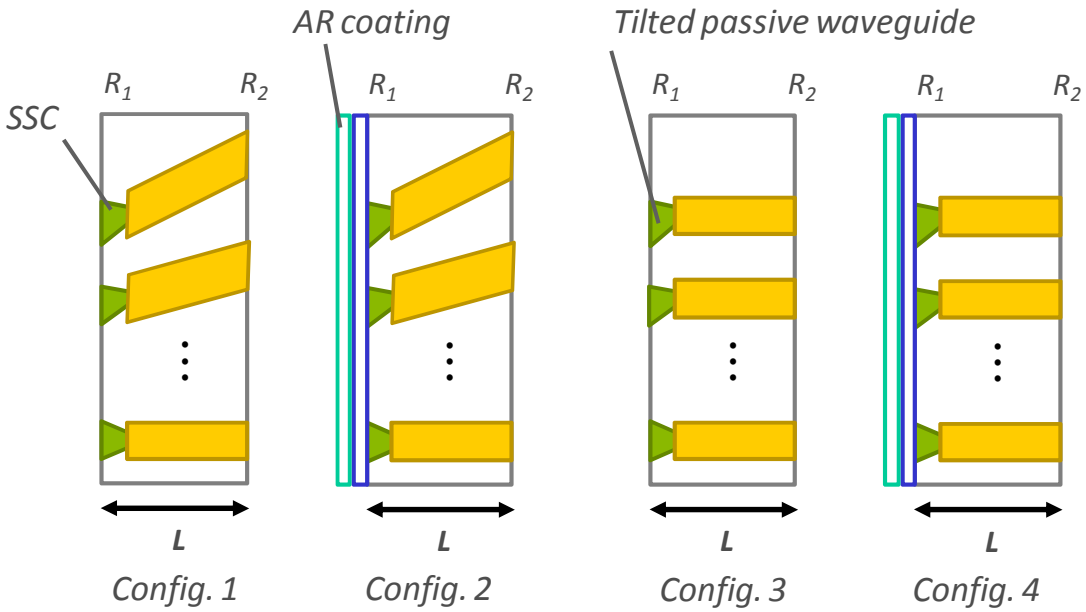

Figure 3-17 – Schematic representation of RSOA configurations

The idea was to measure reflectivity in the configurations described; however it didn't work out as expected, certainly because of fabrication issues. As explained in Chapter 2, an imperfect taper induces internal reflection at the interface between the active region and the InP material. We measure the optical power depending on the bias current and extract the threshold current. All results are reported in Figure 3-18. Tilted waveguides (configuration 1 and 2) clearly affect the threshold current however configuration 3 and 4 do not affect it. It means that when R_2 is constant, the facet reflectivity R_1 does not change with the angle variation. Reflections due to the internal active taper can explain this phenomenon (as explained in section 2.1.3.2). Therefore we cannot evaluate the reflectivity for these configurations due to the parasitic reflectivity. Optimized designs need to be done in order to overcome this effect as explained in chapter 2. The static and dynamic performances are measured on another wafer to evaluate our RSOAs. However Configuration 1, 2, 3 and 4 were not processed on this wafer. New wafers with optimized RSOA design and the several configurations need to be processed and measured.

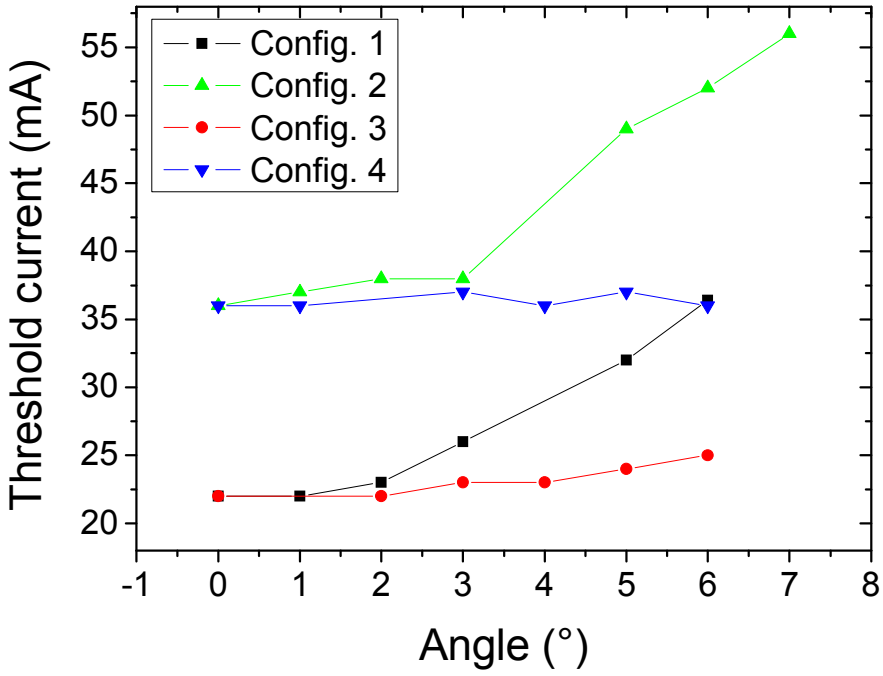

Figure 3-18 – Threshold current depending on the facet angle

3.3 Conclusions

In this chapter, the different physical mechanisms involved in the SOA/RSOA carrier density at the steady state were described and analyzed. It was shown that the applied current, the radiative and non-radiative recombination rates as well as the stimulated recombination process govern the carrier density variations. This approach has been completed considering forward and backward propagation. Therefore we developed a multi-section model including the forward and backward signal amplification, the gain compression factor and the impact of the ASE. Approximations are needed to keep the model as simple as possible with low computation time: for example the ASE is considered as a white noise. The model behaves as expected. The influence of the ASE is crucial in the determination of the steady state condition and becomes even greater at low optical power or high input bias current. We simulated the carrier density distribution inside SOA and RSOA devices. They appear to be completely different and the ASE strongly affects the RSOA carrier density due to the HR coating in one end.

Static experimental characterizations of various RSOA devices have been carried out in order to study the impact of tuneable physical parameters. The new fabricated devices (with an optical confinement of Γ = 20%) are compared to the previous generation (Γ = 80%). The new ones show an improvement of the optical gain as well as the saturation output power. The improvement can be explained by a reduction of the LSHB which has been described, simulated and measured. The reduction of the optical confinement leads to less guided ASE that does not deplete the carriers as much as in high optical confinement.

Based on these optimized devices, we studied the influence of the length. In this case, a length of 700 µm is found to be optimal. The forward and backward photon propagations (of the

ASE and the signal) deeply saturate the carrier density in long RSOAs. This saturation effect reduces the optical gain for long active zones.

Then we focused on the influence of the facet reflectivity in the static performances. Active waveguides with different angles were used to modify the facet reflectivity. The reflectivity has been calculated from the threshold current. A large angle induces a low reflectivity. Thus, as we need to prevent the device from lasing, tilted waveguide seems to be necessary. Furthermore high reflectivity induces more gain ripple which is not desirable for multi-wavelength amplification (colourless application). The evaluation of SSC and AR coating reflectivity was not possible due to a spurious fabrication problem (on the tapers) which induces strong internal reflectivity.

Finally, we found a trade-off between all these parameters in order to obtain the best static performances as high gain (30 dB) and reasonably high saturation power (7 dBm). This optimization has been done from a static point of view and the principal question remains:

Does RSOA for dynamic performances have the same optimized parameters as for static behaviour?

Chapter 4 aims to answer this question.

References

[1] J. L. Pleumeekers, M.-A.Dupertuis, T. Hessler, P. E. Selbmann, S. Haacke, and B. Deveaud, "Longitudinal Spatial Hole Burning and Associated Nonlinear Gain in Gain-Clamped Semiconductor Optical Amplifiers", J. Quantum Electron., Vol. 34, No. 5, May 1998, pp. 879-886
[2] R. Brenot et al., "Experimental study of the impact of optical confinement on saturation effects in SOA", in proc. OFC 2005, OME50, March 2005, Anaheim, CA, USA
[3] M. J. Connelly, "Wideband Semiconductor Optical Amplifier Steady-State Numerical Model," J. Quantum Electron., Vol. 37, No. 3, March 2001, pp. 439-447
[4] T. Durhuus, B. Mikkelsen, and K. E. Stubkjaer, "Detailed dynamic model for semiconductor optical amplifiers and their crosstalk and intermodulation distortion", J. Lightw. Technol., Vol. 10, No. 8, Aug. 1992, pp. 1056–1065
[5] M. J. Connelly, "Wide-Band Steady-State Numerical Model and Parameter Extraction of a Tensile-Strained Bulk Semiconductor Optical Amplifier", J. Quantum Electron., Vol. 43, No. 1, Jan. 2007, pp. 47-56
[6] G. P. Agrawal and N. A. Olsson, "Self phase modulation and spectral broadening of optical pulses in semiconductor laser amplifier", J. Quantum Electron., Vol. 25, No. 11, Nov. 1989, pp. 2297–2306
[7] P. P. Baveja et al, "Self-Phase Modulation in Semiconductor Optical Amplifiers: Impact of Amplified Spontaneous Emission", J. Quantum Electron., Vol. 46, No. 9, Sep. 2010, pp. 1396-1403
[8] R. Olshansky, C. A. Su, J. Manning and W. Powazinik, "Measurement of radiative and nonradiative recombination rates in InGaAsP and AlGaAs light sources", J. Quantum Electron., Vol. 20, No. 8, 1984, pp. 838-854
[9] N. Cheng and L. G. Kazovskym, "Implications of injection current and optical input power on the performance of reflective semiconductor optical amplifiers," in Proc. SPIE, 2007, Vol. 6468, San Jose, CA, USA
[10] M. J. Connelly, "Semiconductor Optical Amplifiers", Boston, MA: Kluwer Academic, Chap. 5, 2002, pp. 73-77
[11] Zhansheng Liu, MojtabaSadeghi, Guilhem de Valicourt and RomainBrenot, Manuel Violas, "Experimental Validation of a Reflective Semiconductor Optical Amplifier Model used as a Modulator in Radio over Fiber Systems", Photonics technology letters, Vol. 23, No. 9, May 1, 2011, pp. 576-578
[12] M. J. Connelly, "Semiconductor Optical Amplifiers", Boston, MA: Kluwer Academic, Chap. 5, 2002, pp. 69-84
[13] D. D'Alessandro, G. Giuliani and S. Donati, "Spectral gain and noise evaluation of SOA and SOA-based switch matrix", IEE Proc.-Optoelectron., Vol. 148, No. 3, June 2011, pp. 125-130
[14] M. J. Connelly, "Wideband dynamic model numerical model of a tapered buried ridge stripe semiconductor optical amplifier gate", IEE Proc.-Circuits Devices Syst., Vol. 149, No. 3. June 2002, pp. 173-178
[15] W. Mathlouthi, P. Lemieux, M. Salsi, A. Vannucci, A. Bononi, and L. A. Rusch "Fast and Efficient Dynamic WDM Semiconductor Optical Amplifier Model", J. Lightw. Technol, Vol. 24, No. 11, Nov. 2006, pp. 4353-4365
[16] S. Tanaka, S. Tomabechi, A. Uetake, M. Ekama, and K. Morito, "Recard high saturation output power (+20 dBm) and Low NF (6.0 dB) polarization-insensitive MQW-SOA module", IET Electronics Letters, Vol. 42, No. 18, August 2006, pp. 1050-1060
[17] J. W. Crowe and R. M. Craig, "GaAs Laser Linewidth Measurements by Heterodyne Detection", Appl. Phys. Lett. Vol. 5, No. 4, 1964, pp. 72-74
[18] T. Tamir et al., "Guided-wave optoelectronics", Springer-Verlag, Chap. 5, 1988, pp. 234-245

Chapter 4. Carrier dynamics study

In the previous chapter, we studied the static behaviour of RSOA devices. The performances can be optimized by adjusting physical parameters such as the optical confinement (Γ), the length of the active zone (L) and the facet reflectivity (R). We found out that carrier density is not clamped and strongly depends on these parameters.

As demonstrated in chapter 3, ASE governs the carrier density profile and should be taken into account for dynamic study. In 1989, the dynamic of the amplification process of short optical pulses was described by G. P. Agrawal and N. A. Olsson [1]. Self-phase modulation (SPM) was demonstrated as a dominant source of spectral broadening. In 2010, Agrawal's model was extended to include the impact of the ASE [2]. ASE was added phenomenologically at the output of the SOA and did not influence the gain dynamics, thereby limiting the application to very small saturation levels which are not compatible with our study.

The influence of the LSHB on the modulation characteristics is also an unsolved issue and has to be included in our study. Optical Pulse propagation has been simulated [3] but without considering data modulation for transmission measurements. The second point is the lasing effect which is not present in classic RSOA configuration. In lasers, the gain medium is clamped due to a limited carrier density and at the same time high photon density is produced by high facet reflectivity. The resonant cavity induces an electron to photon resonance increasing the available modulation bandwidth. The SOA modulation response has been simulated and it is heavily influenced by propagation effects. Even if waveguide internal losses can lead to the appearance of a resonance in the modulation response, the underlying physical behaviour completely differs from that of a laser [4].

Therefore, the modulation response of RSOA is more complex than in laser devices. Due to higher carrier density in RSOA devices than lasers, carrier lifetime is determined by Auger recombination rather than stimulated emission (at low photon density). The modulation speed mainly depends on the carrier lifetime which should be reduced as much as possible. Therefore high photon density in the active zone is needed to obtain fast modulated device. A preliminary analysis of the Auger recombination and stimulated emission rate needs to be done in order to understand the physical limitations of these devices.

In this chapter, the physical phenomena driving the carrier dynamic are studied. We analyze the behaviour of RSOA devices under modulated current and compare it to classic laser devices. Based on the proposed multi-section model approach, we obtain a first evaluation of the carrier lifetime along the active zone. This first approach allows us to understand the impact of the carrier lifetime on the modulation bandwidth when approximated as a low pass filter. The limitation of the electro-optic bandwidth is described through this first approximation. Carrier lifetime seems to be the main limiting factor and should be minimized.

Digital modulation is then modelled using a simple approach to focus on the influence of Auger and stimulated recombination rates. Some solutions to overcome this limit will be discussed.

4.1 Why RSOA bandwidth is limited?

4.1.1 Laser and RSOA comparison

RSOA devices have limited electro-optical (E/O) bandwidth (between 1 to 2 GHz [5]) compared to laser devices (usually between 8 to 10 GHz [6-7]). The difference can be explained by two effects that are not present in RSOA devices. The first effect is gain clamping. The carrier density stays low even at high electrical input current while the photon density is increasing. This produces a shorter carrier lifetime particularly advantageous for high speed modulation. The second effect is the electron to photon resonance due to the presence of a cavity. The resonance appears clearly in the modulation response (Figure 4-1) increasing the effective -3dB E/O bandwidth.

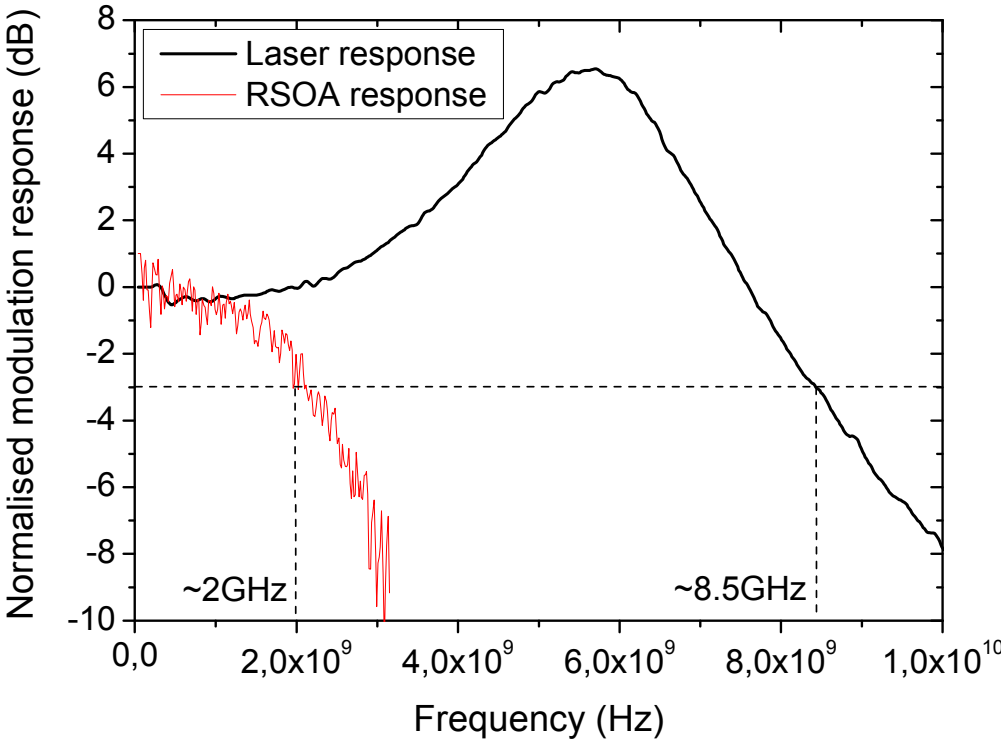

Figure 4-1 – Comparison of laser and RSOA modulation response

The absence of cavity in RSOAs limits the modulation speed of this device. The modulation response behaves as a low pass filter with a characteristic cut-off frequency (when the link gain drops by 3dB). Therefore a first approximation can be done considering a homogenous carrier lifetime along the AZ as detailed in section 4.1.2. Another limitation is due to carrier density spatial distribution. High carrier density combined with low photon density induces long carrier lifetime mainly controlled by the Auger recombination rate. Furthermore we saw in chapter 3 that the carrier and photon densities strongly depend on the position z along the device. Therefore a non-homogeneous carrier lifetime is obtained. So far, no detailed analysis has been completed and we do not know how it affects the modulation response. This section aims to answer these fundamental questions.

4.1.2 Approximation of the modulation bandwidth

The small modulation bandwidth in SOA and RSOA can be approximated as a low pass filter which cut-off frequency depends on the carrier lifetime. This model is proposed as a simple approach in order to determine the key parameters influencing the cut-off frequency. The problem is to calculate the time varying output power P(t) when the injected current is modulated. We made some assumptions in order to keep our demonstration as simple as possible: the carrier lifetime and the carrier density are considered as constant over the length of the AZ and the rate of carrier recombination R(n) is approximated by $\frac{n}{\tau_0}$, where τ_0 is the carrier lifetime. Therefore the rate-equation from equation (3-11) becomes:

$$\frac{dn}{dt} = \frac{I}{e.V} - \frac{n}{\tau_0} - g_{net}.S(z,t).v_g$$

4-1

At steady state condition, we demonstrate that carrier density and photon density converge to a final value therefore $S = S_f$ and $n = n_f$. We also make for this demonstration the linear approximation of the material gain and consider it as the net gain. Therefore we obtain:

$$0 = \frac{I_f}{e.V} - \frac{n_f}{\tau_0} - \Gamma a(n_f - n_0).S_f.v_g$$

4-2

In order to simplify the problem, we will use the small signal approximation.

$$I(t) = I_f + \Delta I(t)$$
$$n(t) = n_f + \Delta n(t)$$
$$S(t) = S_f + \Delta S(t)$$

4-3

Substitution of the n(t) and S(t) into equation (4-1) gives:

$$\frac{dn}{dt} = \frac{I_f + \Delta I(t)}{e.V} - \frac{n_f + \Delta n(t)}{\tau_0} - (\Gamma a v_g\left[(n_f - n_0) + \Delta n\right])(S_f + \Delta S(t))$$

4-4

Taking into account equation (4-2) and neglecting second-order small products $\sim \Delta n \times \Delta S$, we obtain:

$$\frac{dn(t)}{dt} = \frac{\Delta I}{e.V} - (\frac{1}{\tau_0} + \Gamma.a.S_f.v_g)\Delta n - \Delta S[\Gamma.a.v_g.\left(n_f - n_0\right)]$$

4-5

The first-order approximation might be equal to zero thus we neglect the photon modulation (ΔS). In fact, the modulation response is not limited by ΔS which can be modulated at very high speed. Considering the Fourier transform of this equation we obtain:

$$j \times \Omega \Delta\tilde{N} = \frac{\Delta\tilde{I}}{e.V} - \frac{1}{\tau_{eff}} \Delta\tilde{N}$$

4-6

The equation can be expressed as a first-order low-pass filter in Fourier notation as:

$$\frac{\Delta\tilde{N}}{\Delta\tilde{I}} = \frac{1}{e.V} \frac{1}{\left(j \times \Omega + \frac{1}{\tau_{eff}}\right)}$$

4-7

Where τ_{eff} is the effective carrier lifetime.

The modulation response can be simulated based on this approximation and an input carrier lifetime.

A similar expression can be found from the small–signal analysis based on the travelling-wave model [8]. Combining the TW-analysis by Adams et al. and precise recombination mode [9], the modulated current amplitude δI induces the modulation of the carrier density δN as [10]:

$$\delta N = \frac{\delta I}{e.V} \frac{\tau_{eff}}{\sqrt{1 + \left(\omega_m \tau_{eff}\right)^2}}$$

4-8

The magnitude of equations (4-7) reduces to equation (4-8) thus they exhibit the same behaviour. Based on equation (4-7), the modulation response of a classic SOA has been simulated in Figure 4-2-(a). The effective carrier lifetime has been measured in SOA and values between 200 and 800 ps have been obtained [11]. Based on this carrier lifetime value, the – 3dB E/O bandwidth is extracted from the simulation and plotted in Figure 4-2-(b). A modulation bandwidth below 1 GHz is obtained which corresponds to classic SOA E/O bandwidth [12].

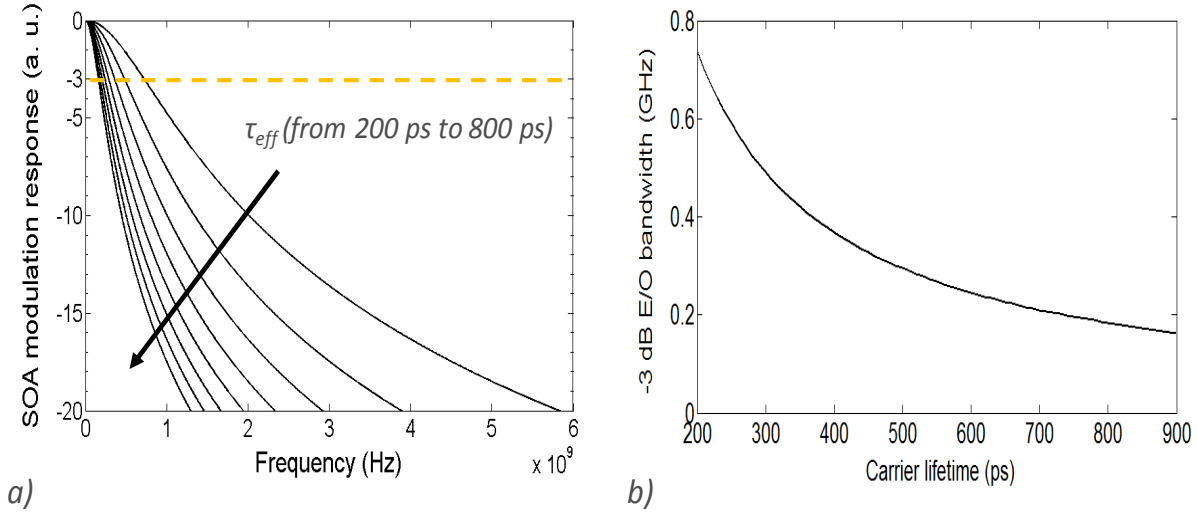

Figure 4-2 – Simulation of SOA direct modulation Bandwidth (a) and -3dB E/0 Bandwidth (b) with the effective carrier lifetime (τ_{eff}) as parameter

This preliminary analysis shows that the modulation bandwidth strongly depends on the effective carrier lifetime which should be reduced in order to obtain large 3 dB E/O bandwidth. A first approximation was done considering a constant carrier density and carrier lifetime along the AZ. However, some RSOA devices show larger modulation bandwidth between 1.5 and 2.5 GHz [13-14].

Based on the model developed in Chapter 3, we propose a second estimation of the effective carrier lifetime and its influence on the modulation bandwidth considering a non-homogenous spatial distribution of the carrier density.

4.1.3 Carrier lifetime analysis

The objective is to obtain a first approximation of the carrier lifetime for the steady state condition. From the first development order of equation (4-6), we obtain:

$$j \times \Omega \Delta\widetilde{N} = \frac{\Delta\tilde{I}}{e.V} - \left[(A + B.n + C.n^2) + \left(\frac{\partial g}{\partial N} \times S + \frac{\partial S}{\partial N} \times gm \times \Delta S\right) \times \Gamma \times v_g\right] \Delta\widetilde{N} \quad \text{4-9}$$

The term $\frac{\partial S}{\partial N} \times gm \times \Delta S$ can be neglected for the same reason as before. Therefore, by comparing equation (4-6) and (4-9), we can deduce a first approximation of the carrier lifetime.

$$\frac{1}{\tau_{eff}} = A + B.n + C.n^2 + \Gamma \times a \times S \times v_g \quad \text{4-10}$$

Where the differential gain is defined by $a = \frac{\partial g}{\partial N}$ and S is the total photon density including the signal and the ASE.

The carrier lifetime is inversely proportional to the recombination rate. The recombination rate can be described using two different terms: one directly proportional to the spontaneous emission and non-radiative recombination (due to the defect or Auger process as described in section 3.1.1) and the second one depending on the stimulated recombination.

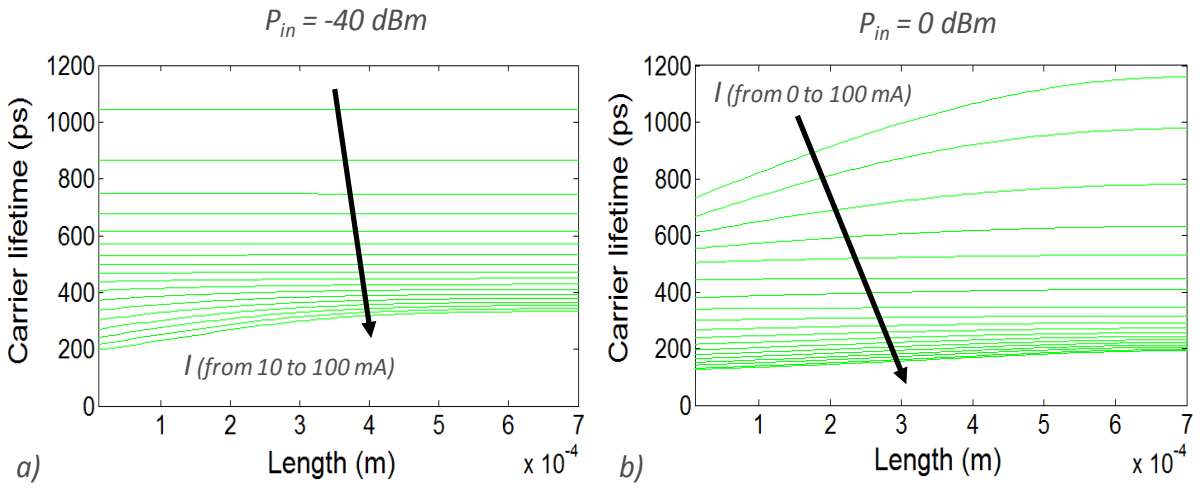

Figure 4-3 – Carrier lifetime simulation along 700 µm RSOA device at (a) low (P_{in} = -40 dBm) and (b) high (P_{in} = 0 dBm) optical injection

Simulations of the carrier lifetime have been carried out along the active region. Figure 4-3 represents the results with the bias current as parameter at P_{in} = -40 dBm (Figure 4-3-(a)) and P_{in} = 0 dBm (Figure 4-3-(b)). Obviously, in both cases, carrier lifetime decreases by increasing the input electrical current. It is mainly due to the increase in all recombination terms. The second important observation is the non-uniformity of the carrier lifetime along the device. At large optical input power (P_{in} = 0 dBm), the saturation effect described in section 3.2.3 is much stronger than with low input injection at low bias current. The average carrier lifetime is also smaller in this condition, due to a larger photon density. In order to understand the influence of the different recombination mechanisms on the carrier lifetime, it is important to follow the evolution of both terms ($A \times 2.B.n \times 3.C.n^2$ and $a \times S \times v_g$) depending on the bias current and the input optical power.

Figure 4-4 represents the spatial distribution of these two terms at various operation conditions. At low input optical power ((a) and (b)), the spontaneous and non-radiative recombination rates are dominant even at high bias current. Therefore the carrier lifetime depends on this recombination term. At high input optical power ((c) and (d)), the photon density is much higher than in the previous situation, thus the stimulated recombination rate tends to overcome the spontaneous and non-radiative recombination terms. This is also confirmed at high input bias current (d) when the signal and ASE are strongly amplified along the RSOA. However at low bias current (c), both phenomena balance each other and both are responsible for the carrier lifetime. They are more or less equal and do not vary that much over z. This analysis is crucial for digital modulation as the input conditions change over time, therefore the dynamic of the device will depend on which recombination rate is dominant at a precise time.

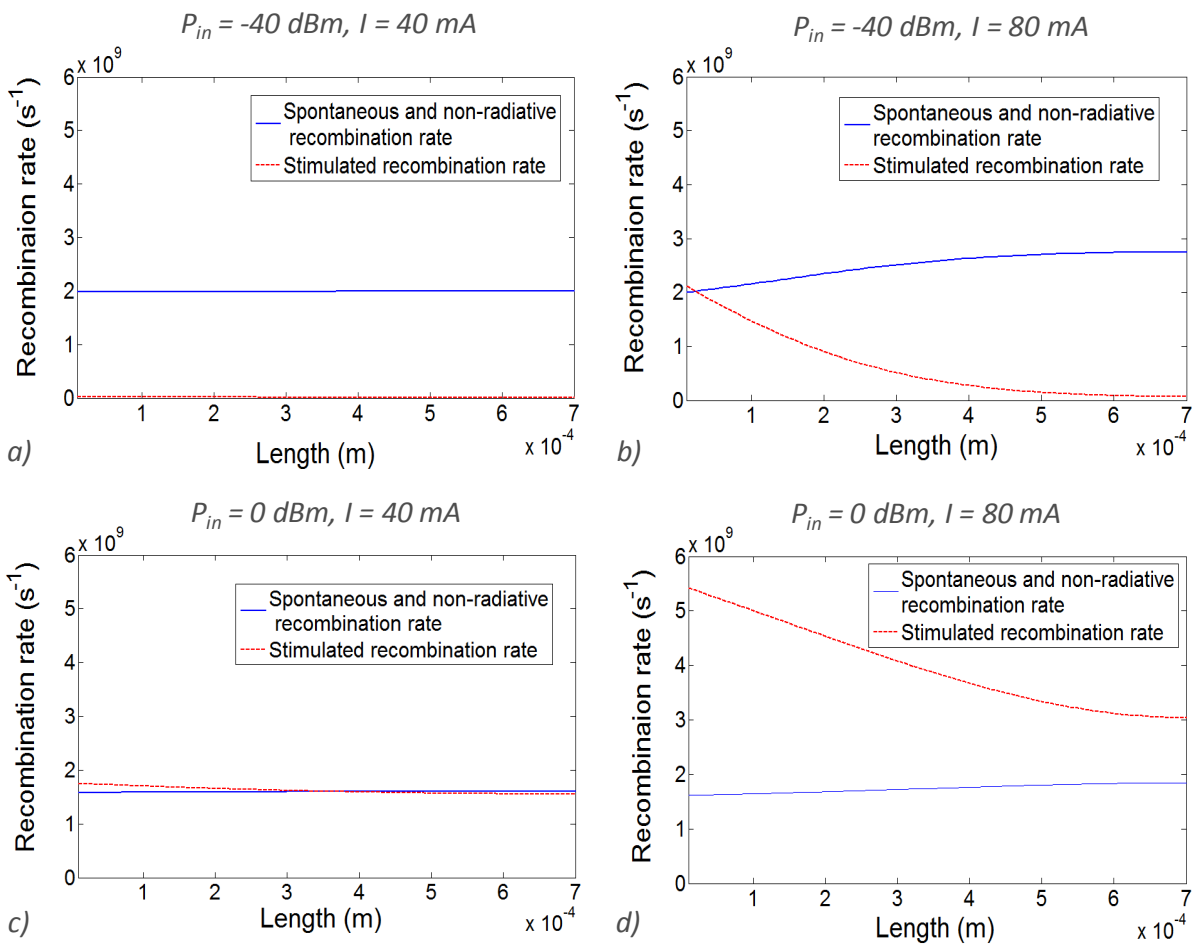

Figure 4-4 – Spatial distribution of spontaneous and non-radiative recombination rate compared to stimulated recombination rate in 700 µm long RSOA at different input conditions. (a) P_{in} = -40 dBm and I = 40 mA, (b) P_{in} = -40 dBm and I = 40 mA, (c) P_{in} = 0 dBm and I = 40 mA and (d) P_{in} = 0 dBm and I = 80 mA

In order to validate our simulation, a comparison with experimental measurements should be done. High-frequency characterization is then needed. The experimental set-up and results are described in the next section.

4.1.4 High-frequency experimental set-up and characterization

We realize a RSOA-based microwave fibre-optic link as depicted in Figure 4-5. All different devices of this experimental set up can be considered as two-port components and classified according to the type of signal present at the input and output ports. E/E, E/O, O/E or O/O are possible classifications where an electrical (E) signal or an optical (O) signal power are modulated at microwave frequencies [15].The RSOA is considered as an E/O two-port device which is characterized by the electro-optic conversion process, i.e. the conversion of microwave current to modulated optical power.

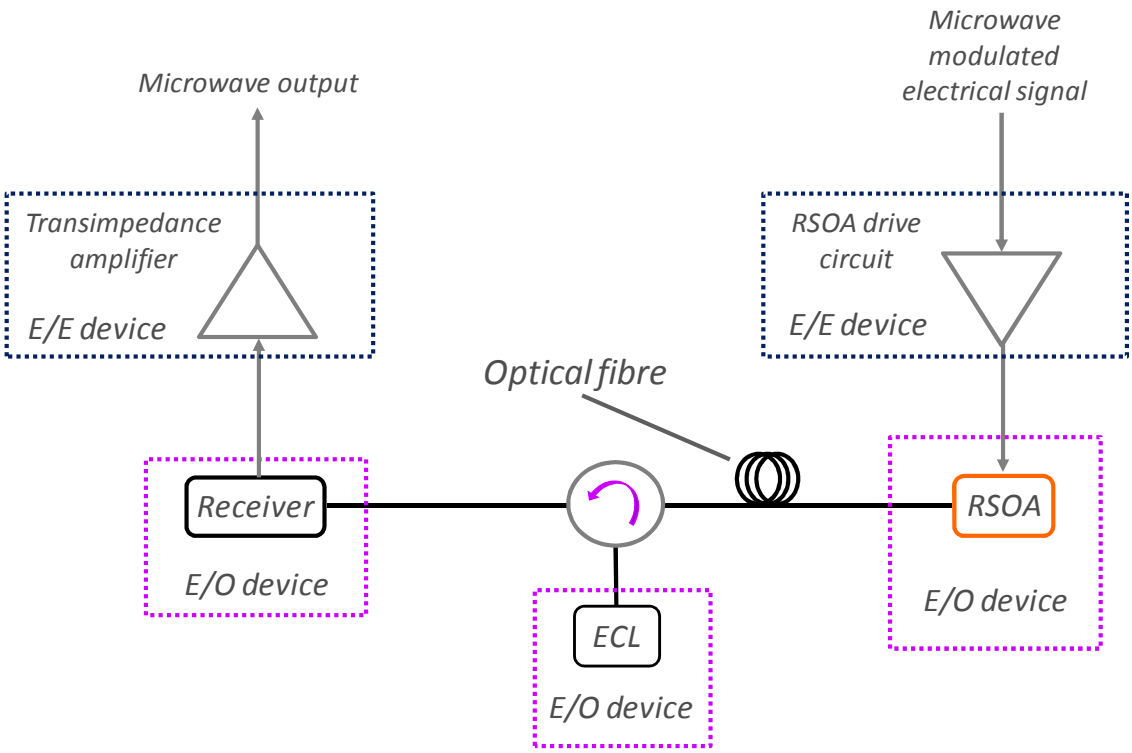

Figure 4-5 – high speed fibre-optic link

A full two-port optical characterisation of the complete set up is important to quantify the system performances. Dynamic characterization allows the measurement of the electrical response of the two-port network. The scattering parameters (S-parameters) can be defined for all four types of two-port lightwave component as well as for the two-port network. The reflection and the transmission of the microwave wave on the different connections of this two-port network are characterised by these S parameters. Figure 4-6 shows the signification of S parameters. Today, this technique is well known and in 1999, S. Iezekiel, B. Elamaran and R. D. Pollard were awarded the 1999 IEE Measurement Prize for their pioneering work on two-port lightwave network analysers and self-calibration techniques.

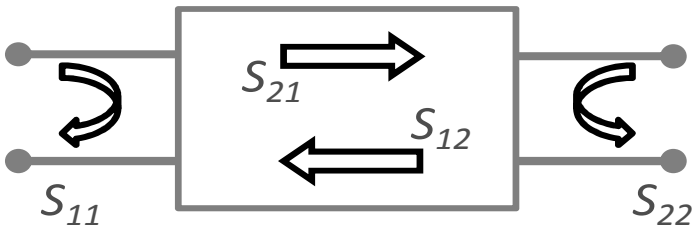

Figure 4-6 – S parameters scheme

A high-frequency signal is sent to the RSOA and the optical modulation is detected by a photodiode. The $|S_{21}|^2$ parameter (gain) is measured over a range of frequency from 0 to 10 GHz. Figure 4-7 shows the electrical response of a typical RSOA device.

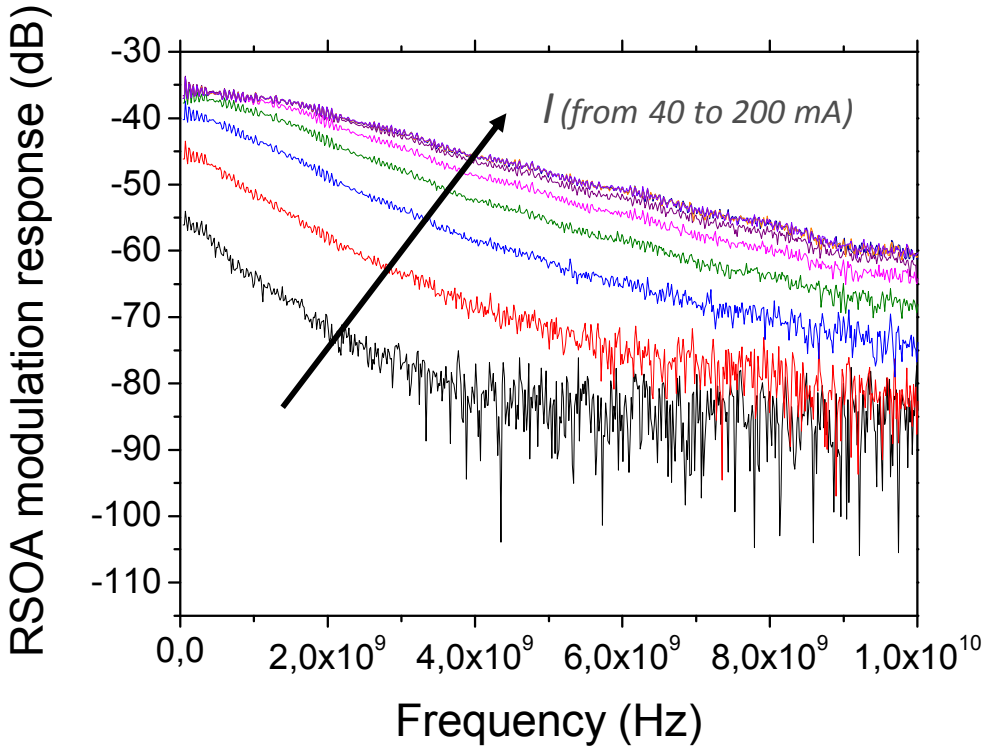

Figure 4-7 – Direct modulation measurements S_{21} in 700µm long RSOA device

From equation (4-7), we simulate the modulation bandwidth depending on the carrier lifetime. The carrier lifetime can be estimated along the RSOA but shows a non-homogenous spatial distribution. The first approach consists of considering an average carrier lifetime over the whole device. Simulation and experimental data are compared in Figure 4-8-(a) for a 700 µm long RSOA at 80 mA. The simulation results fit well with the measurements over a limited range (from 0 to 2GHz). The difference beyond can be explained by the addition of the buried ridge structure (BRS) limitation. As described in section 2.1.2, the BRS equivalent electrical circuit exhibits a cut-off frequency around 3 GHz.

The -3 dB E/O bandwidth has been extracted from Figure 4-7 and plotted in Figure 4-8-(b). A second approach is proposed by simulating the modulation bandwidth based on the carrier lifetime at z = 0 where the saturation effect is stronger. At low bias current, the first model fits better with the experimental values. However at high electrical current (I > 80mA), the second model is more adapted. Simulation results at larger bias current have not been compared due to the model's limitation. As explained in Chapter 3, high photon density induces convergence problems therefore high bias current or high input optical power conditions were not simulated.

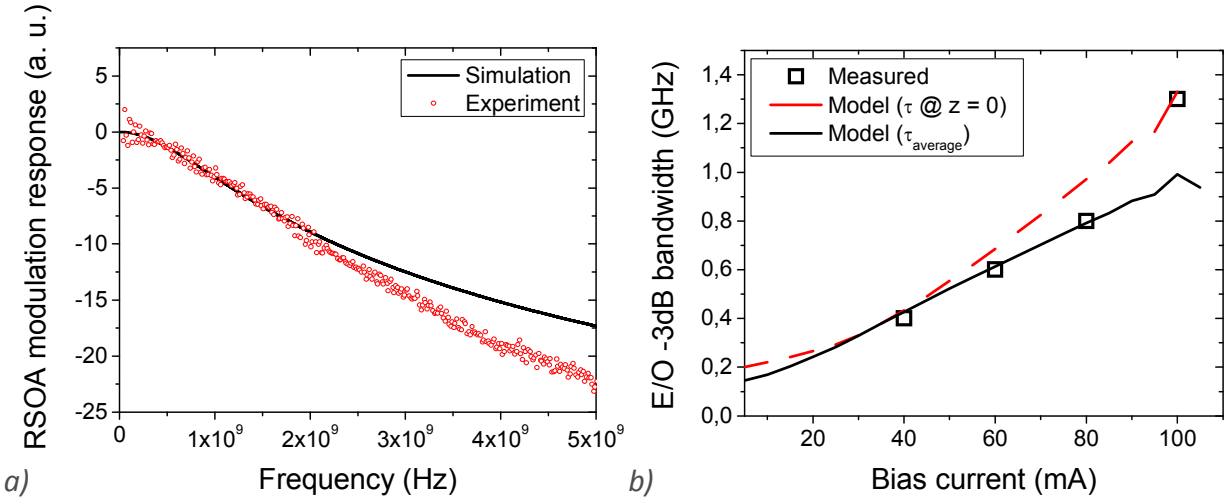

Figure 4-8 – RSOA (a) E/O modulation bandwidth versus frequency at I = 80 mA (b) -3 dB E/O modulation bandwidth versus bias current for 700µm of AZ

The simulations confirmed by the measurements describe why the modulation bandwidth is limited in RSOA devices. It is mainly due to a larger carrier lifetime than in laser which is caused by a smaller photon density. In fact, the cavity resonance in laser increases the photon density as well as the modulation bandwidth and reduces the effective carrier lifetime. This key parameter depends on several recombination rates and strongly on the operating conditions. The stimulated recombination rate can be increased at high input optical power and electrical current. These conditions induce high photon density inside the active zone reducing the carrier lifetime and increasing the -3 dB E/O bandwidth. However these conditions are not suitable for low power consumption networks. Therefore another solution for increasing the photon density seems to be a required condition to push back the RSOA frontiers.

4.2 How to overcome this limit?

As the saturation effect is the direct consequence of the photon density profile, it is of prime interest to analyze its impact on the dynamic RSOA performances. It has been demonstrated that its influence becomes dominant in specific conditions. In Chapter 3, long devices exhibit stronger saturation effects which strongly affect the optical gain. However this effect can be beneficial to the reduction of the carrier lifetime. This property is studied in the next section.

4.2.1 Carrier lifetime reduction

Simulation has been carried out along the active stripe (at low injection power and high current density) and shows an increase in the carrier depletion by increasing the length of the RSOA (section 3.2.3). For short devices, the carrier density is almost homogenous and strong carrier depletion at the output of the device appears for longer devices. Carrier depletion is caused by high photon density. In order to confirm our simulation, spontaneous emission from the active stripe was measured at the input/output, centre or mirror section (Figure 3-13). The

saturation effect becomes dominant at high input bias current. We will now study experimentally this saturation effect at various RSOA lengths. The saturation effect was already strong in 700 µm RSOA. Therefore we first decide to compare 500 µm and 850 µm long RSOA. The SE spectrum is measured in Figure 4-9 for both lengths.

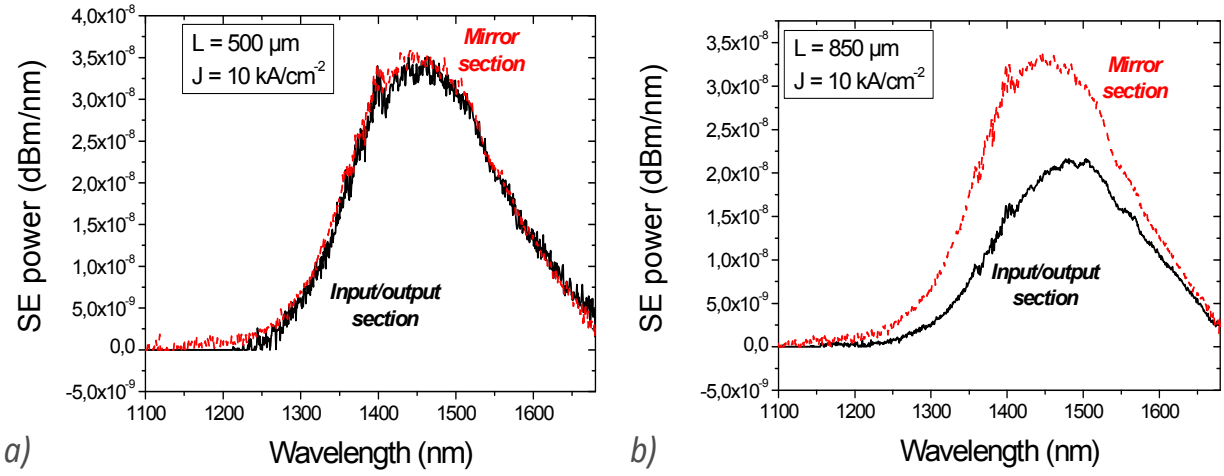

Figure 4-9 – SE spectra at both facets of (a) 500µm and (b) 850 µm long RSOA.

At the input/output facet, the shift of the SE spectrum confirms the variation of the carrier density for 850 µm RSOA. It is not the case for shorter devices as 500µm where the saturation effect is negligible. From the variation of the carrier density, it is possible to describe qualitatively the variation of the carrier life time.

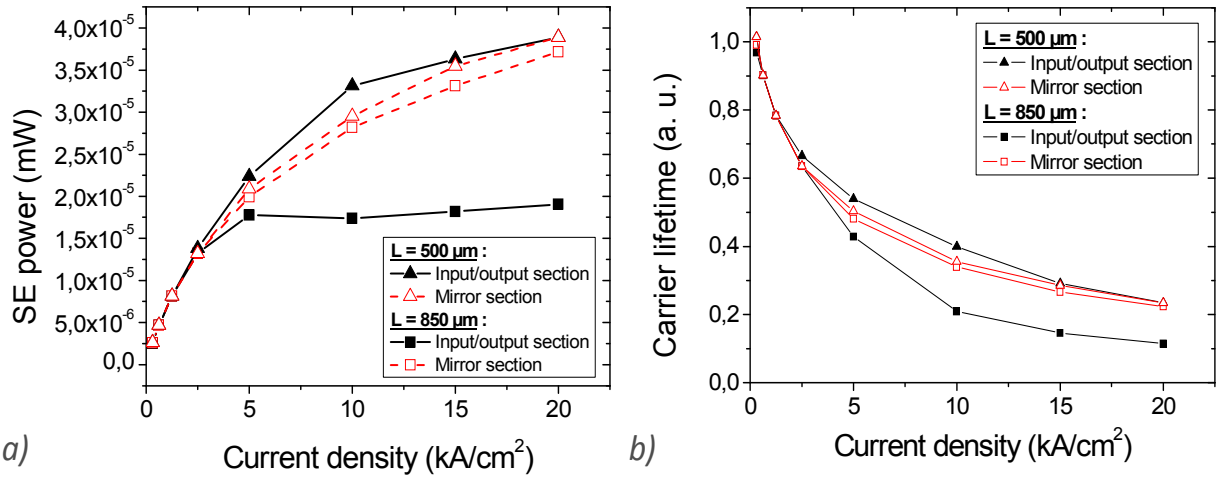

Figure 4-10 – (a) SE power and (b) effective carrier lifetime on both facets of 500µm and 850µm long RSOA as a function of the current density.

Measurements at both facets depending on the current density are realized and confirm the reduction of the carrier density at high current density and therefore the carrier lifetime. At the input/output facet of the longer RSOA, carrier lifetime is reduced by the high photon density when current density exceeds 5 kA/cm^2.

The 3dB E/O bandwidth depends on the carrier lifetime and has been measured for various RSOA lengths (from 300 µm to 850 µm). The chips have been mounted on a HF-submount, and we have measured the E/O modulation bandwidth in order to correlate the decay time with the injected current (as presented in Figure 4-8). The comparison of the 3dB modulation bandwidth for the different RSOA lengths is presented in Figure 4-11-(a). An improvement of 1 GHz is observed at high bias current for long devices (850 µm) compared to 700 µm device and an E/O modulation bandwidth of 3 GHz is obtained, which is well above state-of-the-art values [16-17]. This effect is even more pronounced considering the – 10 dB electro-optic bandwidth with an improvement of 2 GHz (Figure 4-11-(b)).

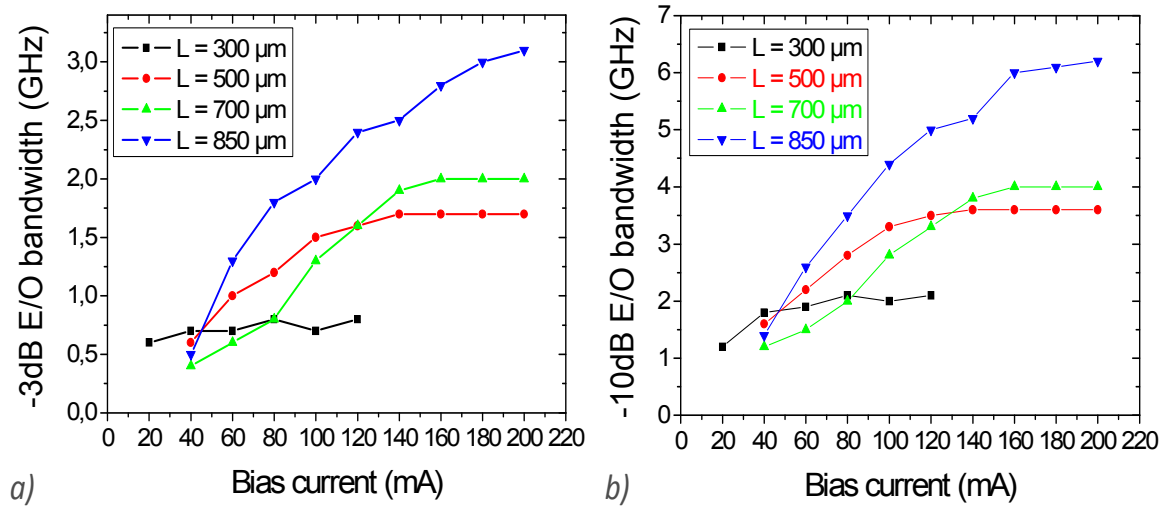

Figure 4-11 – (a) -3 dB and (b) -10 dB small-signal modulation bandwidth of various RSOA as a function of the injected current.

High bit rate transmission could be performed by taking advantage of the large modulation bandwidth in long RSOAs. The next section is dedicated to the RSOA behaviour under digital modulation and a 10 Gbit/s transmission is demonstrated in Chapter 6 (section 6.1.3) for optical access network.

4.2.2 Binary dynamic: rise and fall time

Since RSOAs have been firstly developed for access networks, we have assessed the performances of our new devices for this application. This is also in line with the envisioned convergence between wireless and optical access networks, where analog and digital modulation can be used. The RSOA current is modulated by a 2^{31}-1 pseudo-random bit sequence (PRBS), while a CW laser beam is injected. DC bias current is around 80 mA with ± 20 mA for the binary modulation. Different bit rates (from 1.25, 2.5, 5 and 10 Gbit/s) can be applied to the RSOA. The operation conditions for RSOA devices are detailed in Chapter 6.

Firstly, we simulate the steady state condition when the applied electrical signal is "0" (I = 60 mA) and "1" (I = 100 mA) at P_{in} = -10 dBm. At the "OFF" state, the spontaneous and non-radiative recombination terms mainly govern the carrier density and lifetime (Figure 4-12-(a)). Therefore long carrier lifetime is obtained between 260 and 370 ps (Figure 4-12-(d)). In the

"ON" state, the stimulated recombination rate and R(n) are balanced along the RSOA, therefore the carriers are more rapidly consumed and a shorter carrier lifetime is obtained (between 150 and 290 ps). The last case is presented in (Figure 4-12-(b)). The carrier density spatial distribution is presented in (Figure 4-12-(c)).

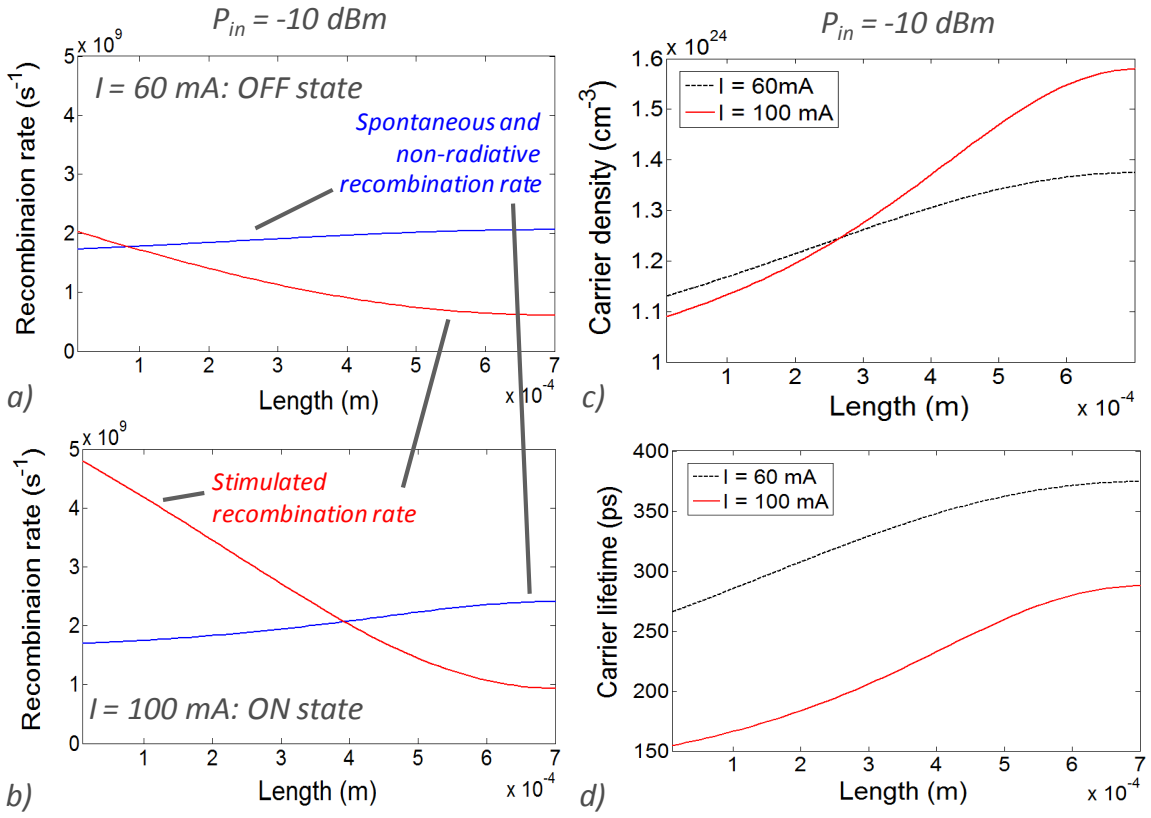

Figure 4-12 – RSOA dynamic mechanisms comparison (a) at "OFF" state (b) "ON" state and (c) carrier density profile, (d) carrier lifetime in both cases. The input optical power is -10 dBm

This preliminary analysis raises two main points. The first point is that at the "ON" and "OFF" states, the balance between the different recombination rates is completely different which leads to two different carrier lifetimes. Therefore the RSOA speed is not the same over time when the input bias current is modulated. The second point is to determine, during the transition between the two states, when one mechanism becomes dominant (as R(n)) and limits the modulation speed. This main interrogation can be formulated as follows: does the dominance occur in the same way for a sequence "0" to "1" and "1" to "0"?

However this analysis is very complex and an advanced model should be developed to take into account all the varying parameters. A complete study has been done in bulk SOA [18]. Here, we propose a simplified dynamic model based on the previous static analysis. A modulated electrical signal is applied to the RSOA. The electrical modulation is much slower than the RSOA transit time. The carrier lifetime is responsible for the transition and is a hundred of picoseconds long (as indicated by the calculation in section 4.1.3). The RSOA responses are simplified by approximating g_{net} by g_m, assuming a homogenous carrier density along the RSOA and an average photon density (considering the signal and the ASE) is extracted from the static model. The simplified final equation is given by:

$$\frac{dn(t)}{dt} = \frac{I(t)}{e.V} - (A.n(t) + B.n(t)^2 + C.n(t)^3) - v_g g_{max}.S(t)$$

4-11

The constants are the same as in the static model. Figure 4-13 presents the rise time from the "OFF" to the "ON" state. The simulations are realized for two different "OFF" states (Figure 4-13-(a)) from I = 40 mA or 60 mA to 100 mA and also two different input optical power (Figure 4-13-(b)). At high input optical power (P_{in} = 0 dBm), the rise time is faster than at low input optical power (P_{in} = -40 dBm). It can be explained by a higher photon density inside the device reducing the carrier lifetime. A similar observation can be done on a high "OFF" state bias current. As demonstrated in section 3.1.4, high bias current induces strong saturation effect (therefore a large photon density) inducing short carrier lifetime (section 4.2.1). Of course, the opposite is true by considering a low bias current, we obtain a low carrier density (therefore R(n) is small) and no-saturation effect (low photon density) producing a long carrier lifetime.

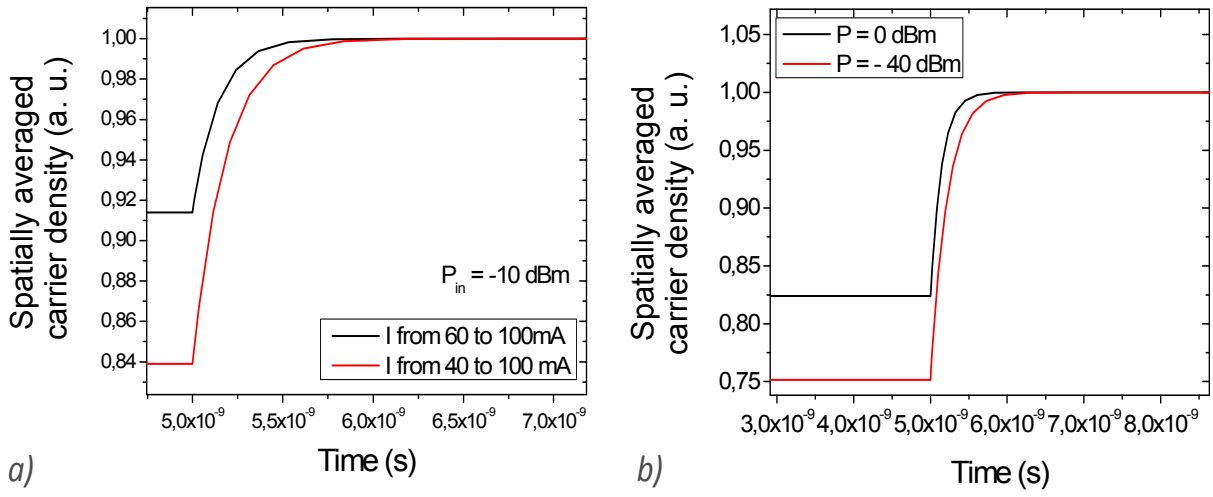

Figure 4-13 – Rise time of the carrier density dynamic in response to a rise in current (a) at different "OFF" bias level (b) at different input optical power

The rise time strongly depends on the photon density. It becomes faster at high photon density which means high bias current and high input optical power are needed. However these conditions also decrease the extinction ratio. A trade-off needs to be found to keep a low BER.

The fall time concerns the transition between "1" and "0". It usually limits the RSOA speed. Furthermore, it displays two different time constants. It is very fast at the beginning, and then a much slower decay appears. This slow decay is commonly observed on all RSOAs (Figure 4-14). This effect can be explained by considering the spatial distribution of the carrier density and photon density. When the carrier density is high, the spontaneous and non-radiative recombination processes are dominant (mainly due to the Auger recombination: n^3). However when the photon density reaches high values, the stimulated emission rate becomes more significant (at the input/output facet). Depending on the bias current (Figure 4-10), the dominant recombination mechanisms are different. At high bias current (I = 100 mA), Figure 4-10-(b) shows that the stimulated and spontaneous recombination rates mainly govern the speed

of the device. When reaching the "OFF" state, the photon density decreases and the Auger recombination becomes the dominant recombination mechanism and produces a longer carrier lifetime. Therefore the stimulated and Auger recombination rate evolve in opposite ways along the RSOA.

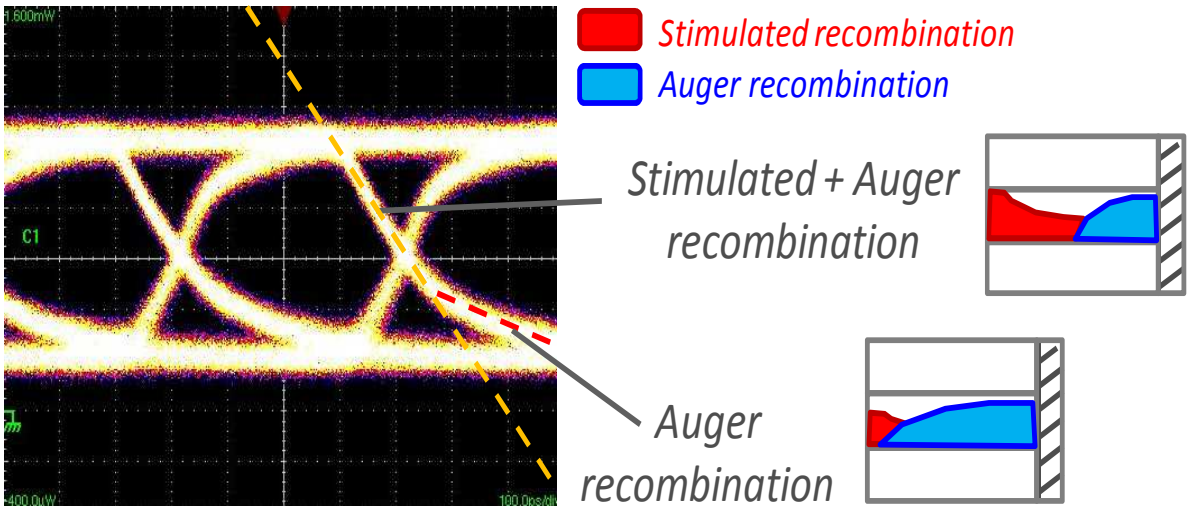

Figure 4-14 – Recombination mechanism analysis during the fall time along the RSOA devices.

As it is represented in Figure 4-14, we can deduce that at the beginning of the commutation from "1" to "0", neither dominates the other. The Auger recombination is dominant around z = L and the stimulated recombination becomes dominant once we are closer to the input/output facet. Over time, the Auger recombination becomes more and more dominant along the RSOA. Therefore at "0", it is the principal recombination rate responsible for the carrier lifetime. If the "OFF" state is at low bias current (for example I_{OFF} = 40 mA), the fall time is longer due to the increase in the carrier lifetime during the transition as the Auger process controls entirely the final carrier density stabilization. A comparison between two different "OFF" levels is presented in Figure 4-15-(a). In Figure 4-15-(b), the fall time is compared at two different input optical power (P_{in} = - 40 and 0 dBm). It is observed that the fall time at large input optical signal is shorter than the one at low input optical signal.

However Figure 4-15 is a rough approximation and does not include the two fall times as observed in the experimental eye diagram. The Auger process controls the consumption of carrier at the end of the commutation end and the fall time depends on its decrease rate. Therefore the fall time should mainly depend on this rate. However this dynamic cannot be taken into account using a model which considers homogeneous carrier density distribution. In fact, the influence of this mechanism is hidden by the average values of the carrier and photon density. More complex analysis (considering the non-homogeneous spatial distribution of the carrier and photon density) have been done and confirm the previous affirmations based on power and phase measurements [19]. A preliminary approximation can be done considering different photon densities and by consequence different carrier lifetimes during the commutation.

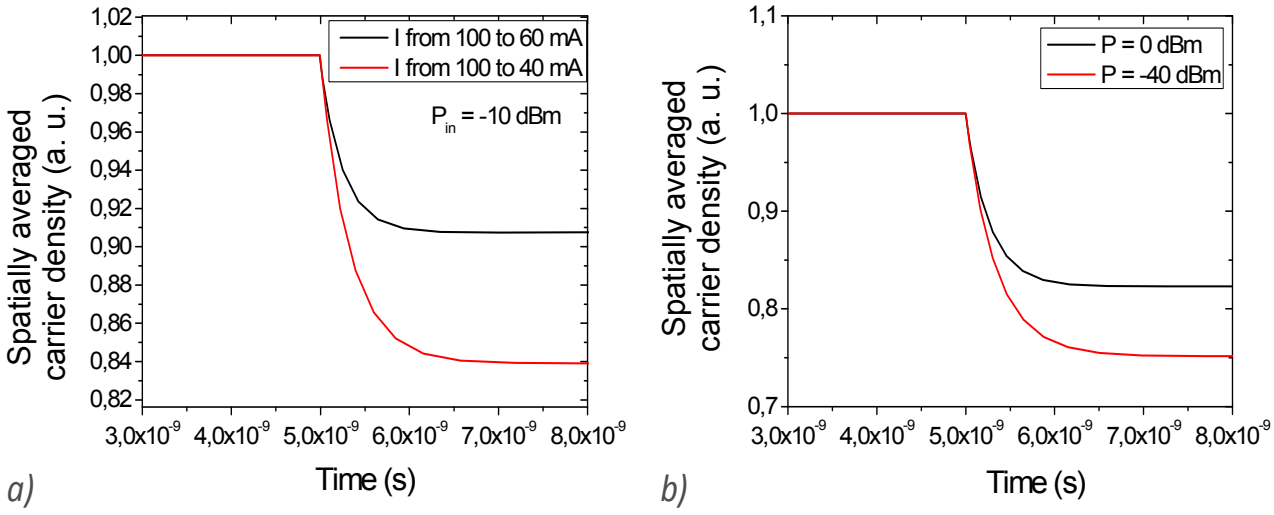

Figure 4-15 – Fall time of the carrier density dynamic in response to a fall in current (a) at different "OFF" bias level (b) at different input optical power

The idea is to consider two different simulations based on two photon densities and bias currents in order to obtain a qualitative representation of this phenomenon. Let's consider an electrical modulation from 100 mA to 40 mA. In the previous simulations the fall time was governed by the Auger recombination rate and the final photon density at I = 40 mA. In fact, when I is switched to the lower bias current value (I = 40 mA), the photon density is also switched to its steady-state value at I = 40 mA (the photon density is obtained using the multi-section model presented in chapter 3). Therefore just one regime, when the spontaneous and non-radiative recombination terms mainly govern the carrier density and lifetime, is considered.

We consider that the transition between the two regime occurs at 80 mA (It is an arbitrary value). Therefore a first simulation is performed based on the photon density at I = 80 mA (extracted from the multi-section model). Then we realize a second simulation from I = 80 mA to 40 mA based on the photon density at I = 40 mA. The comparison between both simulations is presented in Figure 4-16. The blue curve represents the addition of the two simulations. As in the Figure 4-14, two different time constants are observed. The levels of the involved recombination rates are also calculated.

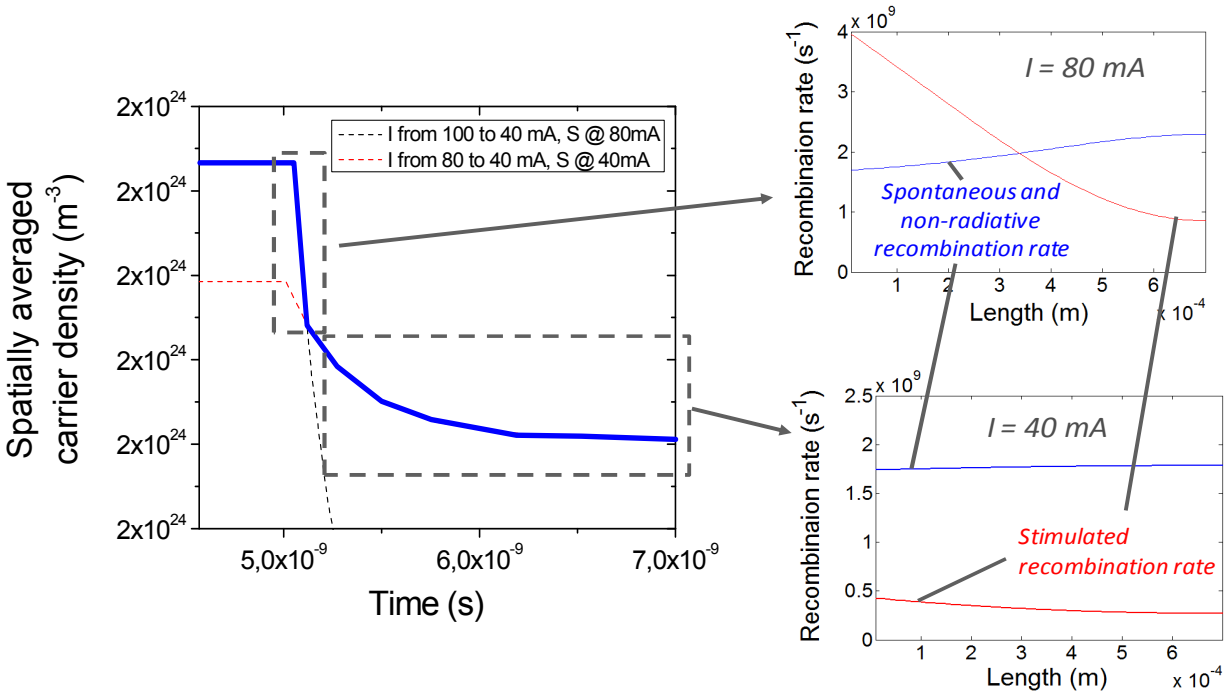

Figure 4-16 – Fall time of the carrier density dynamic considering a photon density variation over the time

In order to get closer to the experimental observations, the photon density needs to be re-calculated at each time. The influence of the photon density (or recombination rate dominance) is analyzed depending on when the transition between these two regimes would be. Figure 4-17 compares two simulated responses considering two different transitions between the stimulated recombination rate dominance and the Auger recombination rate.

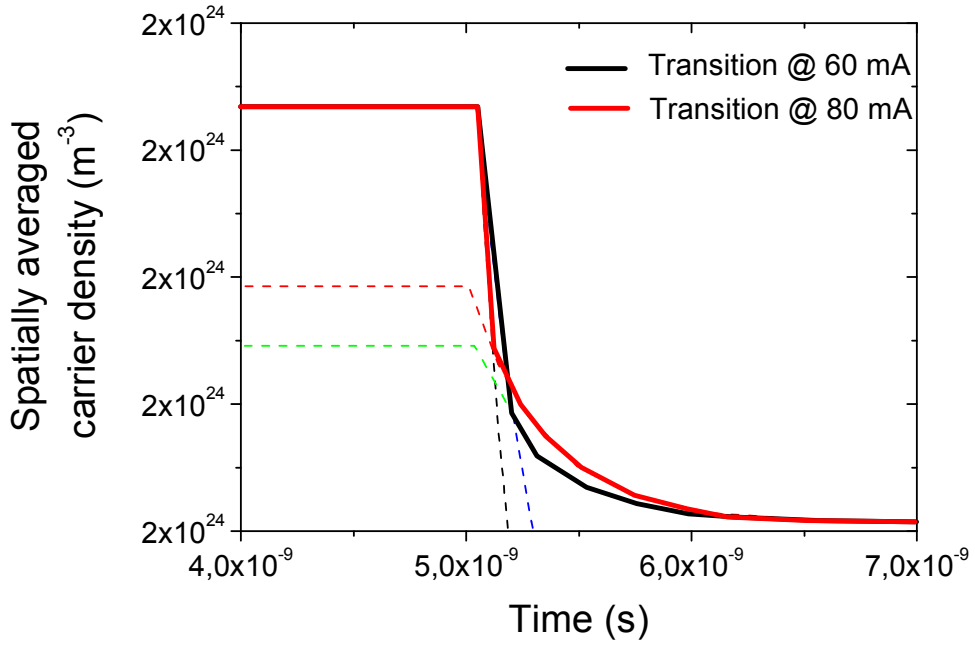

Figure 4-17 – Impact of the transition bias current on the fall time over the time

However these simulations represent a qualitative but not quantitative approach, therefore the rest of the study will be based on experimental data.

4.2.3 High speed RSOA for digital modulation

The experimental setup is the same as in Figure 3-8. A CW wavelength is injected into the RSOA through an OC. The optical power is modulated and reflected to an oscilloscope in order to perform eye diagram analysis. The eye diagram is an oscilloscope display of a digital signal, repetitively sampled to get a good representation of RSOA dynamic behaviour. It is a common indicator of performance in digital transmission systems. The reflective SOA is driven by a 2^{31}-1 pseudo-random bit sequence (PRBS) with a DC bias current of 80 mA and a binary modulation of ±20 mA. First, we compare 700 µm long RSOAs with different optical confinements (Figure 4-18). At 2.5 Gbps, both devices (Γ~80% and Γ~20%) present wide and clear eye openings. However the Γ~20% RSOA exhibits large extinction ratio. The Γ~80% RSOA is saturated by the ASE which explains a small extinction ration. As it also presents better static performances, we focus on the Γ~20% RSOA device for the rest of the analysis.

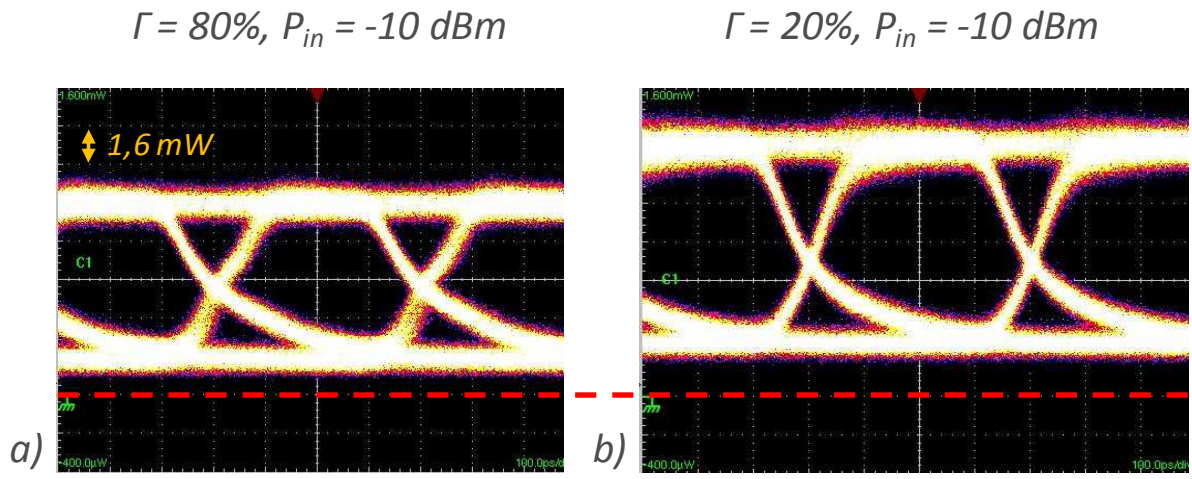

Figure 4-18 – 2.5 Gbit/s eye-diagram comparison at the output of the 700 µm long RSOA with (a) Γ~80% and (b) Γ~20%. Red line is the dark level.

The eye diagram is obtained at various input powers in order to highlight the consequence of saturation effects, as well as for different cavity lengths (L = 500 and 700µm). The measurements are presented in Figure 4-19. Increasing the length of a RSOA improves the modulation performances of the device. In fact, increasing the length up to 700 µm reduces carrier lifetime because of the large gain and ASE photon density as demonstrated previously.

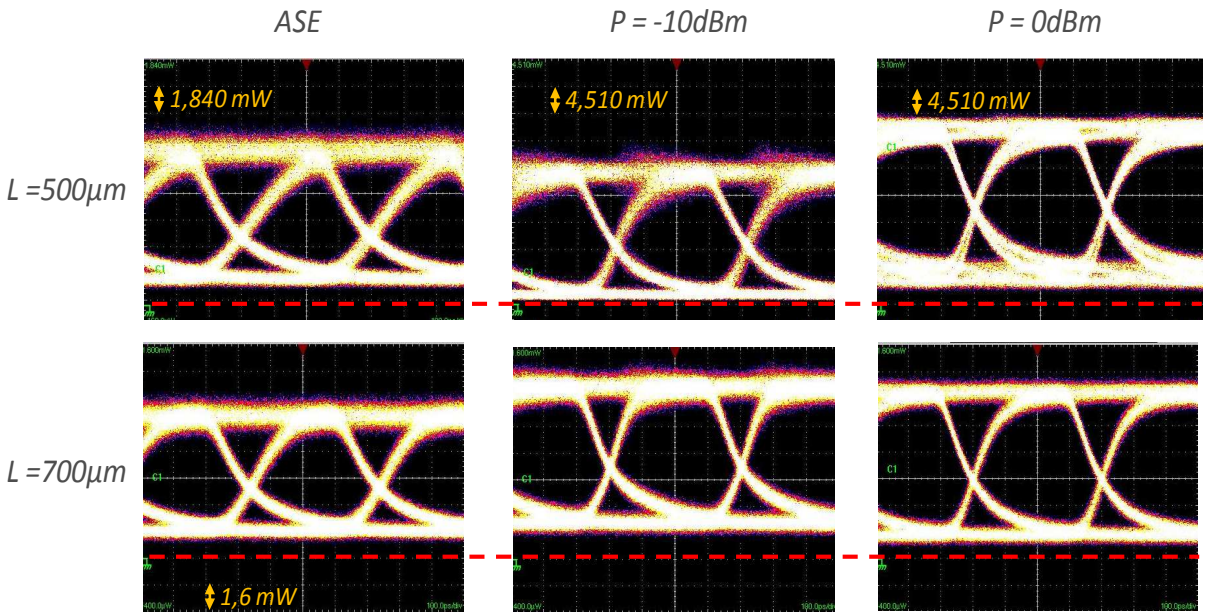

Figure 4-19 – 2.5 Gbit/s eye-diagram at the output of the RSOA with Γ~20%. Red lines are the dark levels.

Long RSOA devices lead to large E/O modulation bandwidth because of the carrier lifetime reduction. 3 GHz of E/O bandwidth has been obtained in 850 µm RSOA. The impact of the length is evaluated in Figure 4-20 with digital modulation for 500, 700 and 850 µm RSOA. Reasonably low timing jitter is obtained at 2.5 and 5 Gbit/s with Γ~20% RSOA (for all lengths), which confirms the high speed performances of these devices. We applied a digital modulation at 10 Gbit/s with a 2^{31}-1 PRBS sequence. One can observe from Figure 4-20, the two different time constants over the fall time. The slower decay leads to patterning effects at larger bit rates. It can be reduced either by increasing the length, or in very strong optical injection regimes (due to the high photon density). 500µm and 700µm long devices do not enable 10 Gbit/s modulation. However the first direct 10 Gbit/s modulation on RSOA devices is obtained with the 850 µm long RSOAs, well above state-of-the-art achievements. Double traces are visible because of patterning effects.

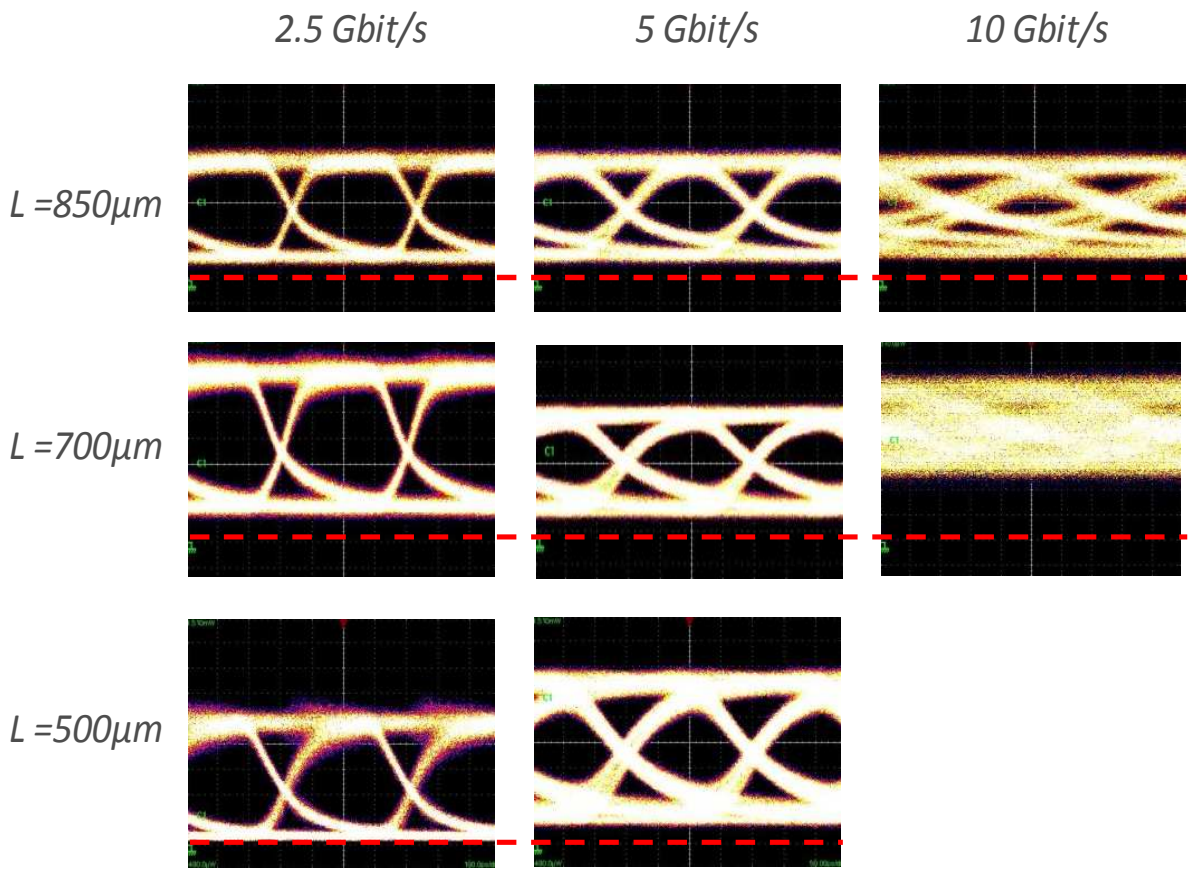

Figure 4-20 – Eye diagrams at various bit rates of RSOA whose length varies from 500 to 850 µm. The collected power is pure ASE. Red lines are the dark levels.

From the last results, a major trade-off seems to be unavoidable. Long devices lead to high photon density, which is confirmed by the presence of a strong saturation effect. This leads to a decrease in the static performances (lower optical gain that 700 µm RSOAs) but also enables high speed modulation up to 10 Gbit/s due to the carrier lifetime reduction. Therefore an optimized length needs to be found in order to obtain the best compromise between the optical budget and the bit rate. 10 Gbit/s transmission measurements are presented in Chapter 6.

4.3 Conclusions

The carrier dynamic in RSOA devices has been studied in this chapter. Compared to laser modulation response, SOA and RSOA devices show a limited bandwidth due to the absence of resonance. Therefore, it has been demonstrated that E/O modulation bandwidth of these devices behaves as a low pass filter and the cut-off frequency mainly depends on the effective carrier lifetime. Short carrier lifetime values induce large 3 dB modulation response and the reduction of this parameter becomes a major concern. The analysis of the carrier lifetime is complex and needs to be handled carefully. We propose in this chapter a first approximation of this characteristic time. It was found that the carrier lifetime depends on two main recombination mechanisms: R(n), the spontaneous and non-radiative recombination rates, and the stimulated emission rate (proportional to the photon density S). The carrier lifetime is non-homogenous along the RSOA and strongly depends on the operating conditions.

Simulations of the modulation response have been compared to experimental data and show a good fit over several GHz. The simulated 3 dB E/O bandwidth, which takes into account the average carrier lifetime along the device, fits the experimental values for bias currents up to 80 mA. Then the 3 dB E/O bandwidth starts to rise faster at high bias current and short carrier lifetime at the output of the device (where the saturation effect is stronger) looks more appropriate to simulate the 3 dB E/O bandwidth. However due to the model limitation, bias currents over 100 mA have not been modelled and more simulations need to confirm this preliminary analysis.

As the main limitation from the small signal analysis comes from the effective carrier lifetime, we propose to take advantage of the saturation effect in RSOA in order to decrease this characteristic time. Previous simulations in Chapter 3 show that high saturation effect is obtained in long RSOAs, we complete this approach by an experimental validation of this effect comparing short (500 μm) and long (850 μm) RSOAs. SE measurements are used to demonstrate the carrier density saturation as well as the carrier lifetime reduction. Finally, the E/O modulation bandwidth is measured and state-of-the-art -3 dB E/O bandwidth is obtained (3 GHz). However as the carrier lifetime strongly depends on the operating condition, the RSOA dynamic under digital modulation needs to be further understood.

From the steady-state solution, the dominant recombination mechanisms at the "ON" and "OFF" state have been identified. We propose a simplified dynamic model based on the carrier density rate-equation. The rise time is faster when the photon density increases. Therefore the best conditions in order to obtain a fast transition are a high bias current and high input optical power. However this induces a small extinction ratio.

The analysis of the fall time is more complicated since two decay times are observed. It is the result of the balance between the recombination mechanisms. This effect has not been modelled properly due to the approximation on our dynamic model. However it was analysed and described based on experimental measurements. The influence of various parameters such as the length, the optical input power and the modulation speed are described in section 4.2.3.

Finally, we found that 850 μm RSOAs are faster than shorter devices and enable a 10 Gbit/s modulation. The optimum length is then different from a static or dynamic point of view and this trade-off needs to be considered in system implementation. We push back the modulation limits of RSOA devices however the chirp is still an issue. Further works are presented to overcome this effect using multi-electrode devices in the next chapter.

References

[1] G. P. Agrawal and N. A. Olsson, "Self phase modulation and spectral broadening of optical pulses in semiconductor laser amplifiers", J. Quantum Electron., Vol. 25, No. 11, Nov. 1989, pp. 2297–2306
[2] P. P. Baveja et al, "Self-Phase Modulation in Semiconductor Optical Amplifiers: Impact of Amplified Spontaneous Emission", J. Quantum Electron., Vol. 46, No. 9, Sep. 2010, pp. 1396-1403
[3] M.J. Connelly and C. O'Riordan, "Simple Model for Optical Pulse Propagation in a Reflective Semiconductor Optical Amplifier", Proc. Of NUSOD, 2010, pp.37-38, Atlanta, USA
[4] Jesper Mørk, Antonio Mecozzi and Gadi Eisenstein, "The Modulation Response of a Semiconductor Laser Amplifier", J. of Selected Topics in Quantum Electron., Vol. 5, No. 3, June 1999, pp. 851-860
[5] M. Omella, V. Polo, J. Lazaro, B. Schrenk and J. Prat, "10 Gb/s RSOA Transmission by Direct Duobinary Modulation", in Proc. ECOC'08, Tu.3.E.4, Sept. 2008, Brussels, Belgium
[6] M. Faugeron, G. de Valicourt, J. Jacquet and F. Van Dijk, "High Power, Low RIN, 1.55µm DFB Laser For Analog Applications", International workshop on high speed semiconductor laser, Oct. 2010, Wroclaw, Poland
[7] G. de Valicourt, Anthony Nkansah, David Wake, Nathan Gomes, M. Faugeron, R. Brenot, C. Ware and Frederic Van Dijk, "High efficiency 1.5 µm DFB laser for uncooled 10 GHz bandwidth analog transmission", European Semiconductor Laser Workshop, Sept. 2010, Pavia, Italy
[8] M. J. Adams, J. V. Collins, and I. D. Henning, "Analysis of semiconductor laser optical amplifiers", in IEE Proc. Pt. J, Vol. 132, Feb. 1985, pp. 58-63
[9] J. Wang, H. Olesen, and K. E. Stubkjaer, "Recombination, gain, and bandwidth characteristics of 1.3-prn semiconductor laser amplifiers", J. Lightwave Technol., vol. LT-5, No. 1, Jan. 1987, pp. 184-189
[10] G. Grosskopf, R. Ludwig, R. Schnabel, and H. G. Weber, "Characteristics of semiconductor laser optical amplifier as phase modulator", Electron. Lett., Vol. 25, No. 17, Aug. 1989, pp. 1188-1189
[11] N. Storkfelt, B. Mikkelsen, D. S. Olesen, M. Yamaguchi, and K. E. Stubkjaer, "Measurement of Carrier Lifetime and Linewidth Enhancement Factor for 1.5-pm Ridge-Waveguide Laser Amplifier", Photonics technology letters, Vol. 3, No. 1, July 1991, pp. 632-634
[12] J. Yas, N. G. Valker, C. Hunter, C. R. Ualker, C. Sherlock, "5 Gbit/s Transmission System Using a MQW Semiconductor Optical Amplifier as an Amplitude Modulator ", IEE Colloquium on Very High Bit Rate Optical Systems, April 1992, London, UK
[13] K. Y. Cho, Y. Takushima, and Y. C. Chung, "10-Gb/s Operation of RSOA for WDM PON", Photonics technology letters, Vol. 20, No. 18, Sept. 2008, pp. 1533 - 1535
[14] Hoon Kim, "10-Gb/s Operation of RSOA Using a Delay Interferometer", Photonics technology letters, Vol. 22, No. 18, Sept. 2010, pp. 1379-1381
[15] S. Iezekiel, B. Elamaran and R.D. Pollard, "Recent developments in lightwave network analysis", Engineering Science and Education Journal, Vol. 09, No. 06, Dec. 2000, pp. 247-257
[16] G. Qi, A.V.Tran, C. Chang-Joon, "20 Gb/s WDM-PON system with 1 GHz RSOA using partial response equalization and optical filter detuning", in Proc. OFC'11, OThT2, 2011, Los Angeles, USA
[17] T. Duong, N. Genay, P. Chanclou, B. Charbonnier, A. Pizzinat, R. Brenot, "Experimental demonstration of 10 Gbit/s upstream transmission by remote modulation of 1 GHz RSOA using Adaptively Modulated Optical OFDM for WDM-PON single fiber architecture", in Proc. ECOC'08, Th.3.F.1, 2008, Brussels, Belgium
[18] Horacio Soto Ortiz, "Dynamique des amplificateurs optiques à semi-conducteurs massifs ", PhD Thesis, École Nationale Supérieure des Télécommunications, Chap. 2, 1996, pp. 51-65
[19] H. Soto, D. Erasme and P. Doussiere, "Experimental and theoretical study the switching response of semiconductor optical amplifiers", In Proc. ECIO, 1995, Delft, Netherlands

Chapter 5. Two-section RSOA improvements

Hybrid TDM/WDM PON needs to be compatible simultaneously with long reach or high optical budget network configuration. In previous chapters, we have shown the design and fabrication of high-performance RSOAs, focusing on device parameters: high gain (30 dB), large optical bandwidth (45 nm), relatively low noise factor (7-8 dB), and high E/O modulation bandwidth in long RSOAs (3 GHz). The high gain RSOAs we described already enable high optical budget. For instance, up to 36 dB and 45km transmission at 2.5 Gbit/s has been demonstrated (chapter 6).

However, if RSOAs are to work as colourless transmitters for converged low-deployment-cost networks, further challenges must be addressed. Specifically, the chirp and the uplink radio range remain the limiting factors, respectively in Access and R-o-F architectures. In order to reach long distances and high bit rate transmissions, the chirp should be as low as possible. Furthermore, high link gain is required to increase the uplink radio range.

To meet these challenges, we designed multi-electrode devices.
In section 5.1 of this chapter, we demonstrate that their use reduces the chirp factor and leads to error-free transmission improvements. A complete theoretical and experimental study is presented.

In section 5.2, we demonstrate that 2-section RSOAs, optimised for R-o-F [1], can be used in order to increase the internal efficiency of the device and as a consequence, the link gain in this application. Link gain measurements are performed and confirm the theoretical approach.

5.1 Chirp reduction in RSOA-based Access network

In this section, the chirp in RSOAs is discussed in detail. At high optical powers, SOAs are nonlinear, resulting in signal degradation notably by self-phase modulation (SPM) [2]. Upon current modulation, carrier density is modulated which introduces a variation of the refractive index. In RSOA devices, the modulation of the refractive index introduces a frequency change of the incoming continuous wave signal, commonly called chirp. We propose a theoretical comprehension based on gain and chirp measurements in order to confirm this effect. A dual electrode configuration is used to reduce this limiting factor. We could take advantage of the carrier density non-homogeneity and reduce the carrier density variation. In fact, 2-section SOAs, under particular operating condition, can be considered as the addition of two sections with opposite chirp factor. Therefore, the overall chirp can be reduced. Figure 5-1 represents a schematic idea of a 2-section SOA.

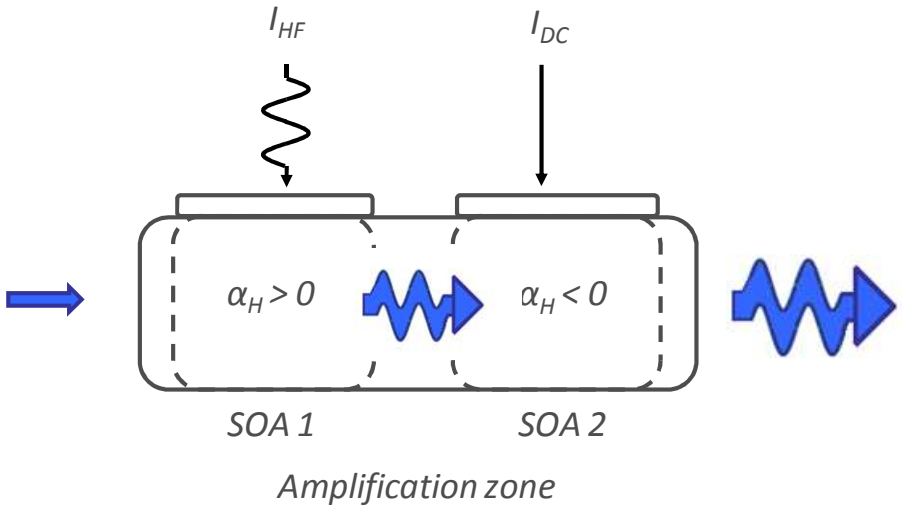

Figure 5-1 – Schematic representation of a 2-section SOA

A RSOA-based hybrid WDM/TDM architecture is implemented. Frequency chirp and Bit error rate measurements confirm the chirp reduction in 2-section RSOAs. Optimization of the system performances for long reach PON are presented in chapter 6.

5.1.1 Theoretical approach

As we described in chapter 1, the gain medium affects the propagation of the light. Maxwell's equations are used to describe the optical wave propagation in a gain medium (equation (1-43)). However RSOAs have a specific vertical structure as described in chapter 2. A rectangular waveguide is used to confine the light. The active zone presents a complex refractive index where the real part is responsible for the refraction of light and the imaginary part is responsible for the gain (see section 1.3.1). The refractive index presents a spatial variation due to the waveguide geometry. The gain modulation by applying a modulated electrical current can induce a temporal variation of the refractive index. As a first approximation, we assume that the electromagnetic wave is not affected by the gain medium. n_0, β_0 and ξ_0 are respectively the refractive index, the propagation constant and the transverse distribution considering a passive waveguide. Thus n_0 is a purely real number i.e without gain as well as $\beta_0 = k_0.n_0$ and ξ_0. Therefore the refractive index can be written as:

$$n(x,y) = n_0(x,y) + \delta n(x,y) \qquad 5\text{-}1$$

Where $|\delta n| << n_0$, δn is the refractive index variation along the RSOA structure.

Based on Helmholtz's equation (equation (1-36)), the solutions for a wave propagating forward and backward inside the AZ have been calculated in equation (1-43). Now considering that the transverse distribution $\xi_0(x,y)$ depends on $n_0(x,y)$, the solution for the forward wave propagation is given by:

$$E^+(z,t) = \xi_0(x,y).A^+.e^{i(\omega t-\beta_0 z)}$$

5-2

Where $E^+(z, t)$ is the electric field, which depends on the position z and time t. z, A^+ and ω are the propagation direction, a coefficient and the angular frequency respectively.

k_0, ξ_0 and n_0 can be calculated using the effective-index method [3]. Considering the waveguide as a gain medium, n becomes a complex number as well as β. The modifications of β modify the complex variation of the slowly varying envelope.

At z, the field can be expressed using the Fourier transform as:

$$A(z,t) = \int_{-\infty}^{+\infty} \tilde{A}(z,\Omega)\, e^{i\Omega t} d\Omega$$

Where $\Omega = \omega - \omega_0 = \Delta\omega$.

5-3

So we can demonstrate that:

$$\frac{\partial A(z,t)}{\partial z} = -i \int_{-\infty}^{+\infty} \tilde{A}(z,\Omega)\, e^{i\Omega t} \beta d\Omega$$

5-4

And,

$$\frac{\partial A(z,t)}{\partial t} = \int_{-\infty}^{+\infty} \tilde{A}(z,\Omega)\, e^{i\Omega t} i\Omega d\Omega$$

5-5

Therefore,

$$\boxed{\frac{\partial A(z,t)}{\partial z} + \beta' \frac{\partial A(z,t)}{\partial t} = -i\beta_0 A(z,t)}$$

5-6

Where β'= $1/v_g$, v_g is the group velocity and $\beta_0 = \frac{\omega}{c}(\Delta n)$. The last expression can be developed as:

$$\beta_0 = \frac{\omega}{c}(\Delta n) = \frac{\omega}{c}\left(\Delta n' + i\Delta n''\right) = \frac{\omega}{c}\left(\frac{\Delta n'}{\Delta n''} + i\right)\Delta n'' = \frac{\omega}{c}(-\alpha_H + i)\Delta n''$$

5-7

Where α_H is the Henry factor (chirp parameter).

In 1982, Henry found that the increased linewidth results from a coupling between intensity and phase noise. It was caused by refractive index dependence on the carrier density in semiconductor materials [4]. We know from section 1.2.1 that the imaginary part n" of the refractive index is responsible for the gain. It can be defined: $g = 2k_0\Delta n''$. From section 1.2.2, the net gain can be expressed as:

$$g_{net} = g_{mod} - \alpha_i = \Gamma.g_m - \alpha_i \quad \text{(equation (1-35))}$$

Therefore we obtain:

$$\boxed{\frac{\partial A(z,t)}{\partial z}+\frac{1}{v_g}\frac{\partial A(z,t)}{\partial t}=-i(-\alpha_H+i)\frac{g_{net}}{2}A(z,t)=\frac{g_{net}}{2}(1+i\alpha_H)A(z,t)}$$

5-8

The chirp behaviour in a classic SOA under current modulation (with constant optical power) and under optical modulation (constant current injection) has been analyzed.

From the previous equation, A(z,t) is the complex amplitude of signal electric field which propagates along the SOA. It can also be written as: $A(z,t)=\sqrt{P(z,t)}e^{i\Phi(z,t)}$
Under optical or electrical modulation, we introduce the reduced time as in [5]:

$$\tau=t-\frac{z}{v_g}$$

5-9

The amplitude of the propagating wave can be re-written in a moving frame which moves with the pulse along the trajectory. Thereby using the reduced variable, the amplitude of the variation can be expressed as:

$$\frac{1}{A}\frac{dA}{d\tau}=\frac{1}{2}v_g g_{net}(1+i\alpha_H)$$

5-10

The signal power and the phase are found to satisfy [2]:

$$\boxed{\begin{aligned}\frac{dP}{dz}&=g(z,\tau)P\\ \frac{d\Phi}{dz}&=\alpha_H\frac{g(z,\tau)}{2}\end{aligned}}$$

5-11

It can be demonstrated by combining both equations that:

$$\boxed{\alpha_H=2P\frac{\partial\Phi}{\partial P}}$$

5-12

Where $\frac{\partial\Phi}{\partial P}$ is the variation of the phase over the variation of the optical power.

5.1.1.1 Modulation of the input optical intensity

It has been shown that SOAs can be used in order to control the chirp of an input optical pulse [6]. The chirp parameter α_H is defined as in equation (5-12). N is the carrier density and ΔN is the carrier density variation. Assuming the ΔN is homogeneous along the SOA, the gain variation (from the single pass gain expression, section 1.3.2) can be written as:

$$G_{dB} = 10log_{10}\left(e^{\Gamma a(N-N_0)L}\right)$$

5-13

The net gain can be approximated by $\Gamma g_m = \Gamma a(N - N_0)$ (we neglect the internal losses α_i). So the gain change in dB units can be written as:

$$\Delta G_{dB} = 10log_{10}e\,.\Gamma a\Delta NL$$

5-14

And the phase variation as:

$$\Delta\Phi = -\frac{2\pi}{\lambda}\Delta nL = \frac{\alpha'}{2}\,\Gamma a\Delta NL$$

5-15

Where λ, n and L are wavelength, refractive index and SOA length. α' is the linewidth enhancement factor of the semiconductor material which is defined as:

$$\alpha' = -\frac{4\pi}{\lambda\Gamma a}\left(\frac{\partial n}{\partial N}\right)$$

5-16

The chirp parameter depends on the gain variation under modulated input optical power. It can be demonstrated as in [7]:

$$\boxed{\alpha_H = \alpha'\frac{dG/dP_{in}}{1 + dG/dP_{in}}}$$

5-17

where P_{in} is the SOA input power.

When the optical input power is low enough, equation (5-17) gives $\alpha_H = 0$ because the carrier density remains unchanged compared to the value at the equilibrium (ΔN = 0) and $dG/dP_{in} \sim 0$. However, as the optical input power increases, carrier depletion occurs in SOA (ΔN < 0) and induces gain saturation ($dG/dP_{in} < 0$). Since $\alpha' > 0$ in gain medium such as in SOA, the chirp parameter is negative ($\alpha_H < 0$) for the gain-saturated SOA.

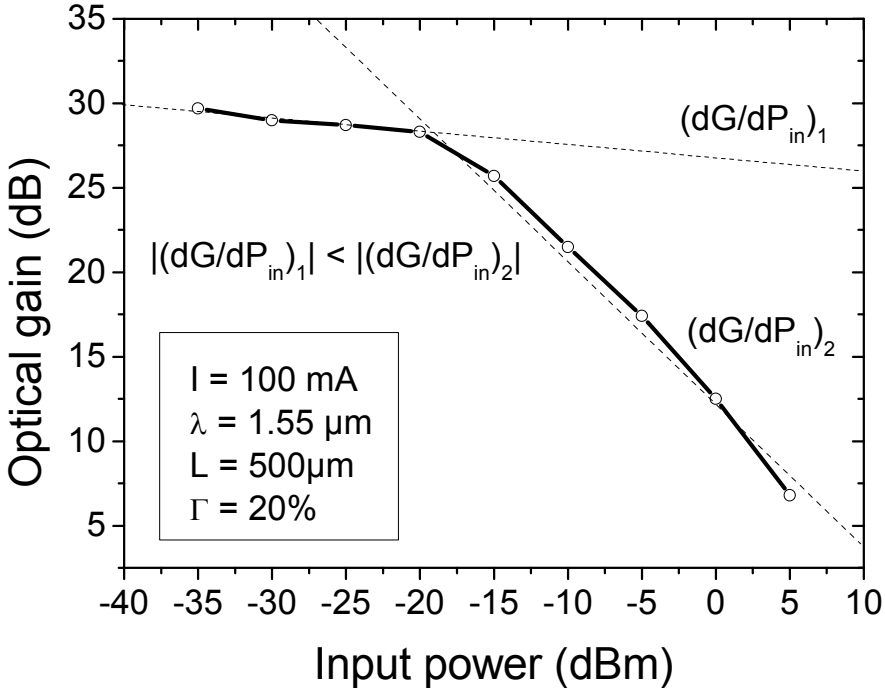

Figure 5-2 – Optical gain versus input optical power

Figure 5-2 represents the experimental optical gain depending on the input power. Assuming an optical variation at low input power, a small change of the gain is observed ($(dG/dP_{in})_1$ is close to zero). While the input power increases, the optical gain decreases due to gain saturation which leads to negative chirp parameter ($|(dG/dP_{in})_2| < 0$). The frequency components of the leading edge of the pulse are red-shifted and trailing edge blue-shifted when the chirp is negative ($\alpha_H < 0$) as explained in [6].

5.1.1.2 Modulation of the input electrical current

The SOA and RSOA gain also depends on the input electrical current as simulated in Chapter 3. The modulation of the electrical current induces a modulation of the gain. More efficient modulation is obtained at low direct current (DC). It can be explained by the gain saturation at high bias current. From equation (5-12), the chirp factor can be written as:

$$\alpha_H = 2P\frac{d\Phi}{dG} \times \frac{dG}{dN} \times \frac{dN}{dP} \qquad 5\text{-}18$$

Considering $P_{out} = P_{in}e^{\Gamma a \Delta N L}$ and $\frac{\partial P_{out}}{\partial N} = P_{in}e^{\Gamma a \Delta N L} \times \Gamma a \Delta N L$, therefore we can demonstrate that α_H can be expressed as:

$$\boxed{\alpha_H = \frac{\alpha'}{\Gamma a \Delta N L . 10 log_{10} . e}\left(\frac{\partial G}{\partial N}\right)} \qquad 5\text{-}19$$

The linewidth enhancement factor is positive α' > 0 in the SOA gain medium as well as $\frac{\partial G}{\partial N} > 0$ as represented in Figure 5-5-3. Then the chirp parameters (α_H) is positive too. The Figure 5-5-3 represents the optical gain variation depending on the input electrical current.

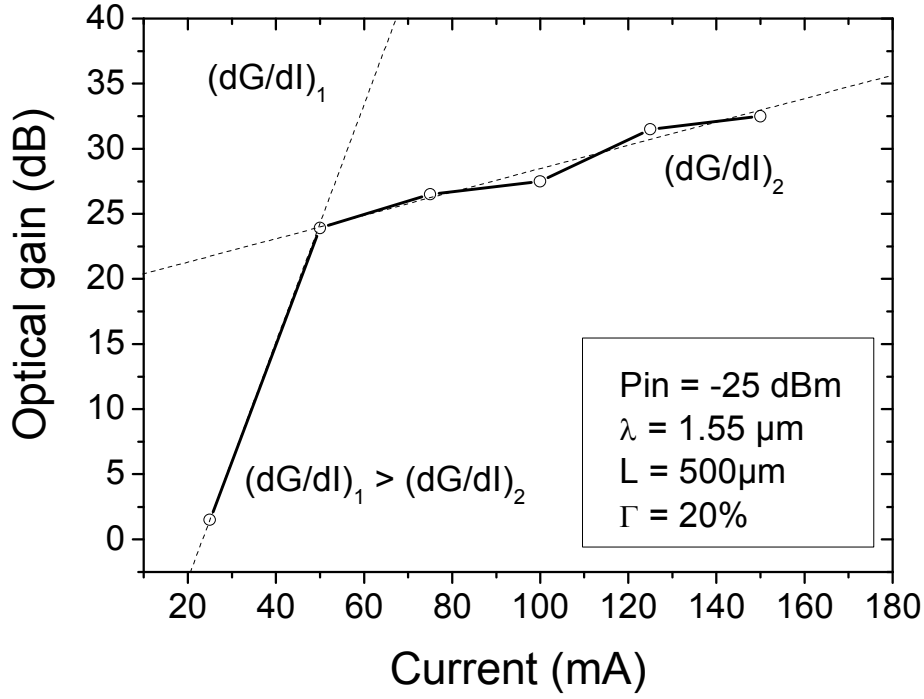

Figure 5-3 – Optical gain versus current injection

As the electrical input current increases, carrier density also increases in SOA (ΔN > 0). The optical gain is proportional to the injected carrier density (common approximation as detailed in equation (1-31)) therefore $dG/dN > 0$. Since $\alpha' > 0$ in a gain medium such as an SOA, the chirp parameter is also positive ($\alpha_H > 0$) below gain-saturated condition. At high bias current, the modulation efficiency becomes lower ($(dG/dI)_1 > (dG/dI)_2$). Under modulated electrical current, the frequency components of the leading edge of the pulse are blue-shifted and the trailing edge red-shifted because the chirp is positive.

In summary, we obtain a positive alpha parameter when the bias current is modulated and a negative alpha parameter when the optical power is modulated.

5.1.2 Chirp measurements

The chirp is measured as described in [8].A Pseudo-Random Binary Sequence (PRBS) generator is used to apply electrical impulsions to the RSOA device. We use an external cavity laser to launch a constant optical power via an optical circulator at 1550 nm.

A 1x3 switch controls the injected optical power and wavelength into a Mach Zehnder (MZ) interferometer. The MZ interferometer is used as an optical discriminator to measure the time-resolved frequency chirp of the RSOA. Then any frequency deviation due to chirp is converted into an amplitude variation because of the MZ interferometer transfer function. A 2x2

switch is used to connect the MZ interferometer. The experimental set up is represented in Figure 5-4.

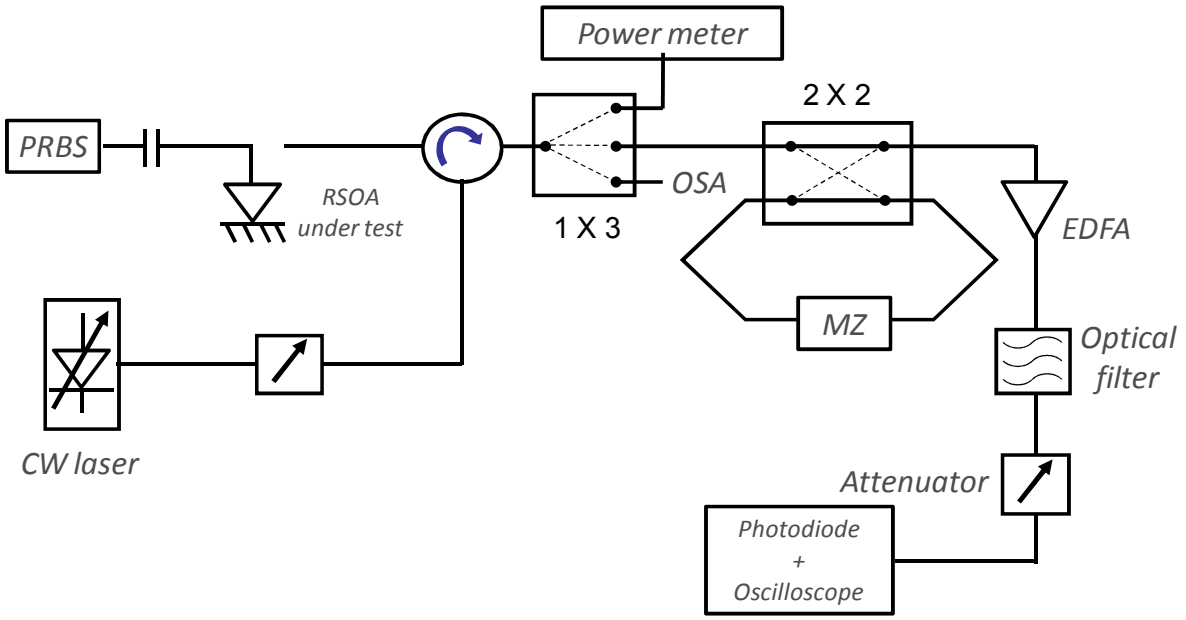

Figure 5-4 – Experimental setup used for the determination of amplitude and frequency responses of RSOA devices

When the chirp is positive, pulse broadening occurs. The penalties over long transmission distances increase due to the optical fibre dispersion. There is no adiabatic chirp in SOA or RSOA because the wavelength is fixed by the external cavity laser. We perform chirp measurements at different bias conditions and using low optical confinement RSOA structures which have been described in chapter 2. In Figure 5-5, frequency deviations of +6.5 GHz, +7.7 GHz, +8.6 GHz for leading edges are measured in single-section RSOA. At low bias current, the modulation efficiency is larger and leads to large frequency deviations. The width of the frequency peak increases at low bias current. It can be explained by a slower carrier dynamic behaviour compared to high bias currents. As demonstrated in Chapter 3, high photon density reduces the carrier lifetime and happens at high bias currents. However a low bias current leads to a large extinction ratio (Figure 5-5-(a). These results confirm the theoretical approach developed in section 5.1.1 and the impact of the bias current on the frequency variation.

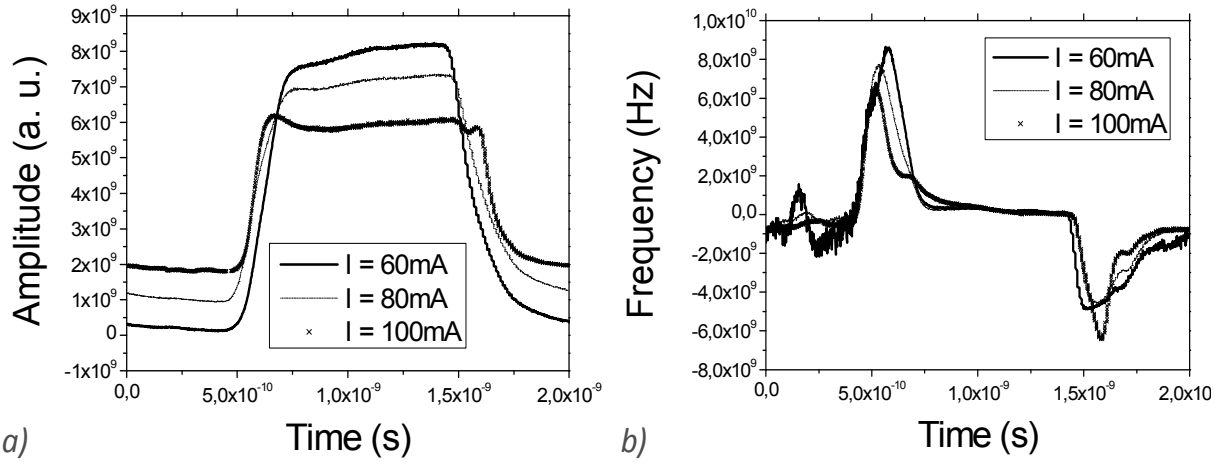

Figure 5-5 – Amplitude and frequency variation of RSOA optical output power under current modulation

As a consequence, small current injection is required in order to obtain high extinction ratio but it also induces a large frequency variation. Thus there is a trade-off between these two parameters in RSOAs.

Now, we consider a non chirped impulsion coming into the SOA then the frequency shift after the SOA can be calculated as in [7].

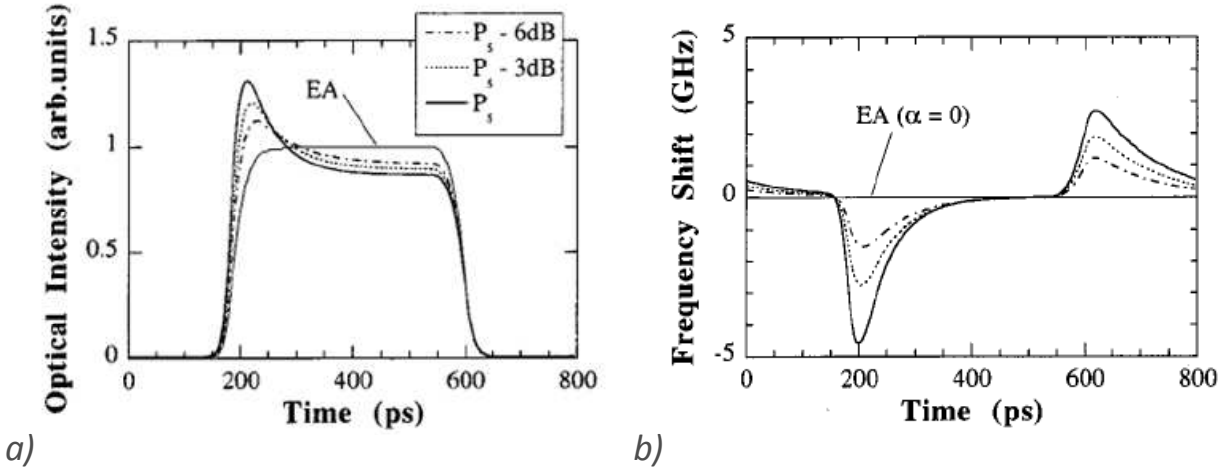

Figure 5-6 – Instantaneous amplitude and optical frequency change of an amplified optical pulse [7]

As the SOA input power increases, the optical frequency shifts more largely toward a lower frequency side. A large optical power induces more chirp as verified by equation (5-26).

2-section RSOAs can be used in order to take advantage of both effects. The main idea is to compensate for the positive chirp induced by one section by a negative chirp in the second section.

5.1.3 Multi-electrode design issue and analysis

In this section, three different RSOA configurations are studied (Figure 5-7). Single-electrode devices are compared to multi-electrode devices. The input/output section is defined as SOA1 and the mirror section is called SOA2. We apply a modulated current (AC) to one of the sections, synchronised with the data clock (In-phase). The AC current can be applied to:

- The input/output electrode (SOA1)
- The mirror electrode (SOA2)

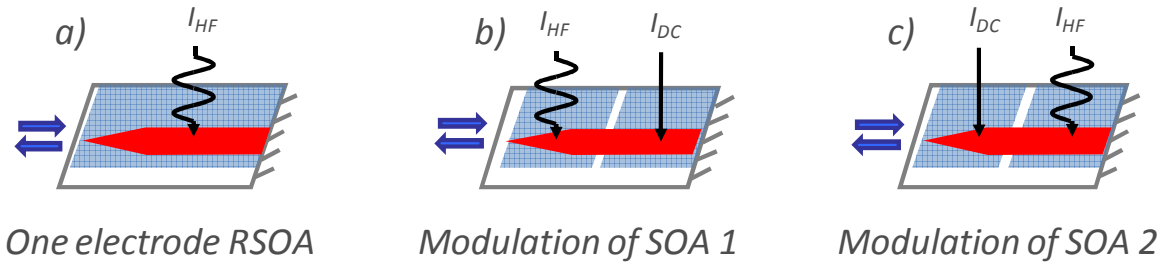

Figure 5-7 – Multi-section RSOA with one electrode (a), two electrodes modulating SOA 1 (b) and modulating SOA 2 (c)

A time domain model for RSOAs was developed by the Instituto de Telecomunicações (IT) and based on the carrier rate and wave propagation equations developed in Chapter 3. In this model, the non linear gain saturation effect and the influence of the amplified spontaneous emission on the carrier density have been included. It is to be noted that in a multi-electrode RSOA, the AC current can be either applied to the input/output electrode, or to the mirror electrode as described in Figure 5-7. We use a RSOA multi-section model, which allows simulating the carrier density distribution. These simulations will help us to define the optimized configuration in order to reduce the carrier density variation due to the electrical modulation. Figure 5-8 shows the carrier density distribution for one-section and two-section RSOAs (Γ = 80%) with a length of 500 µm at P_{in} = -25 dBm. On single-electrode devices, a DC current of 80mA is applied with ± 20 mA high frequency (HF) modulation. With two-electrode devices, the HF electrode is modulated with a current of 30 mA ± 20 mA. The other electrode is fed with a DC current of 35 mA in the input electrode when modulating the mirror electrode (SOA2) and a DC current of 100mA is used in the other case (modulation of the input section: SOA1). Both current values correspond to optimized conditions in order to minimize dispersion penalties (these parameters have been found experimentally).

In Figure 5-8-(a), one can observe strong carrier depletion at the input end, due to the high amplified spontaneous emission (ASE) power in the RSOA at ON state, and this effect is reduced at OFF state. Considering two-electrode configuration (Figure 5-8-(b) and Figure 5-8-(c)), it is to be noted that the carrier density levels in both sections are not independent and the modulation of one electrode could strongly affect the carrier density level of the other, due to carrier density saturation by the amplified input signal. However, we observe from Figure 5-8-(b) and Figure 5-8-(c) that modulating the mirror section introduces much larger carrier density variation than modulating the input section, due to the stronger carrier density saturation. The

difference of carrier density between ON/OFF state (ΔN in cm^{-3}) is depicted in Figure 5-8-(d), from which we have extracted the average value of this difference ($\Delta\overline{N}$) along the device. All values are reported in the respective figures. We can observe that $\Delta\overline{N}$ = 0.15x10^{18} cm^{-3} for modulation applied to the input electrode (SOA1), $\Delta\overline{N}$ = 0.37x10^{18} cm^{-3} for modulation applied to the mirror electrode (SOA2) and $\Delta\overline{N}$ = 0.27x10^{18} cm^{-3} for one-electrode device. It is to be noted that the chirp is directly proportional to $\Delta\overline{N}$ [9]. As we detailed in section 5.1.1, a positive ΔN induces $\alpha_H > 0$ and a negative ΔN produces $\alpha_H < 0$.

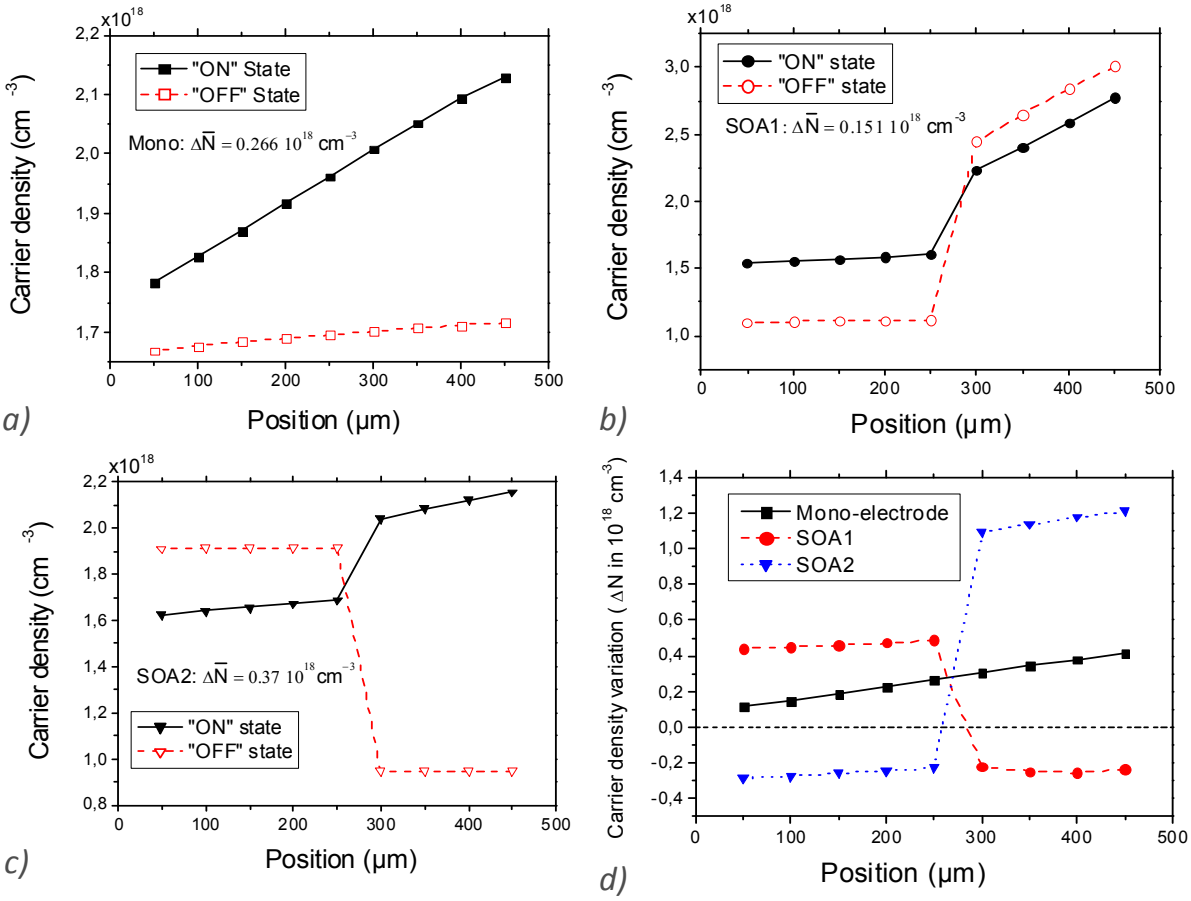

Figure 5-8 – Carrier density along mono-electrode (a) and bi-electrode RSOA with input (b) and (c) mirror electrode modulation for "ON" and "OFF" state. (d) Variation of the carrier density between ON/OFF state depending on different configuration

The first electrode is used to obtain a high extinction ratio (at low bias current) and the second section enables to compensate the frequency variation from the first section. AC current is applied to the first section and it receives a constant input optical power. As demonstrated above (section 5.1.1.2), these operating conditions induce a positive α_H factor. The second section receives a modulated optical signal and is biased with a constant current which produces a negative α_H factor (section 5.1.1.1). Thus, the two sections have opposite α_H factor.

We focus on the modulation of the input/output section (SOA1). The applied current in both sections directly impact the RSOA behaviour and further studies are presented.

5.1.3.1 *Influence of the input section*

The amplitude modulation (AM) response has been measured in Figure 5-9. The experimental set up is the same as described in Figure 5-4. It is clear that by decreasing the bias current of the input/output section (SOA 1: I_{HF}), the extinction ratio (ER) increases dramatically. However a low bias current also induces an increase of the frequency variation.

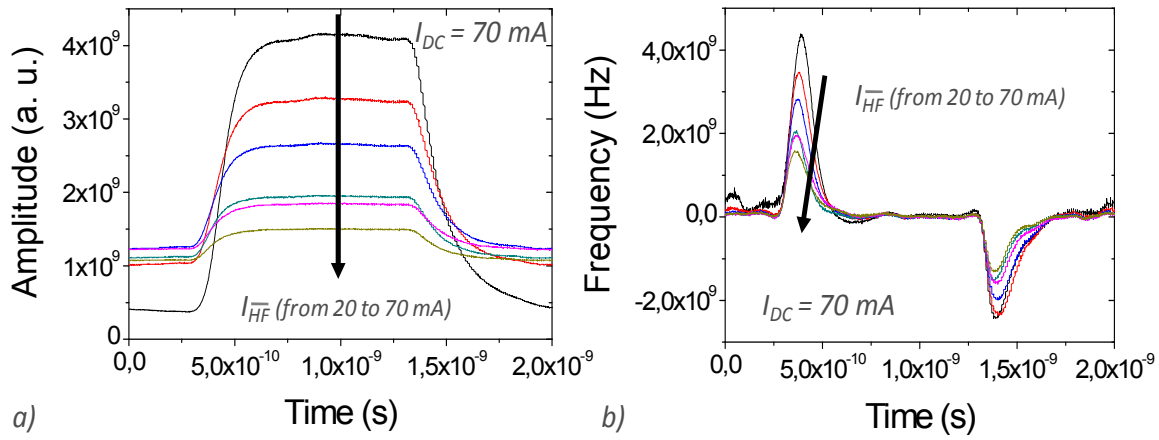

Figure 5-9 – Amplitude (a) and frequency (b) responses of 2-section RSOA with SOA1 bias current as input parameter

5.1.3.2 *Effect of the mirror electrode*

The second section allows compensating for the chirp created in the first section. High input optical power induces a lower gain than low input optical power (due to the gain saturation). Consequently, the second section (SOA2) produces a negative alpha factor as described in section 5.1.1. The ER is reduced as well as the frequency variation inside the second section. The ER decreases from 1.44 to 1.38 by increasing the SO2 bias current from 30 to 70 mA (Figure 5-10). The frequency deviation is also reduced from +1.75 GHz to +1.56 GHz for leading edges and -1.38 GHz to -1.31 GHz for trailing edges. SOA1 bias current is equal to I_{HF} = 70 mA. Larger attenuation is expected when higher extinction ratio is obtained in the first section (by using smaller SOA1 bias current).

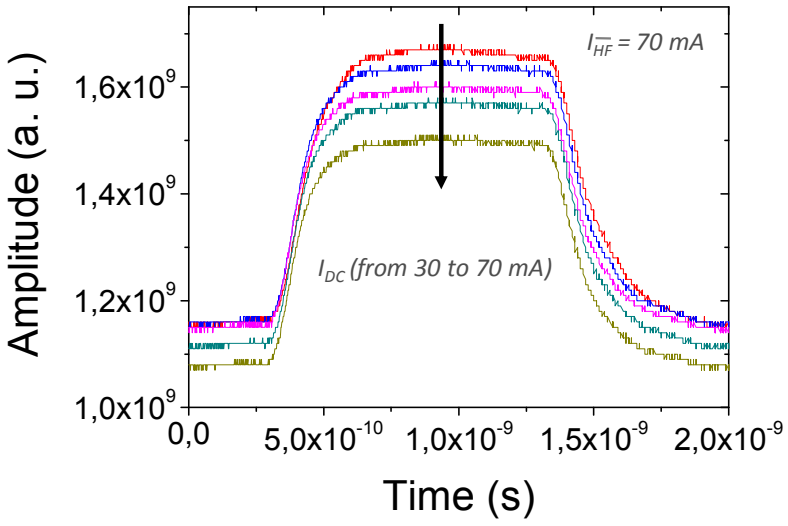

Figure 5-10 – Amplitude variation of 2-section RSOA with SOA 2 bias current as parameter

Another effect is observed: the reduction of the carrier lifetime. The second RSOA section (SOA2) amplifies the optical signal over 1000 µm of propagation (forward and backward amplification). High photon density is injected back to SOA1. Carrier life time reduction in long Reflective SOA due to an increase of the photon density has been demonstrated [10] and detailed in Chapter 4. The effect of the bias current (SOA2: I_{DC}) is presented in Figure 5-11. By increasing the SOA2 bias current, we obtain thinner frequency peak which can be explained by smaller decay times. Therefore carrier life time reduction contributes to the chirp reduction.

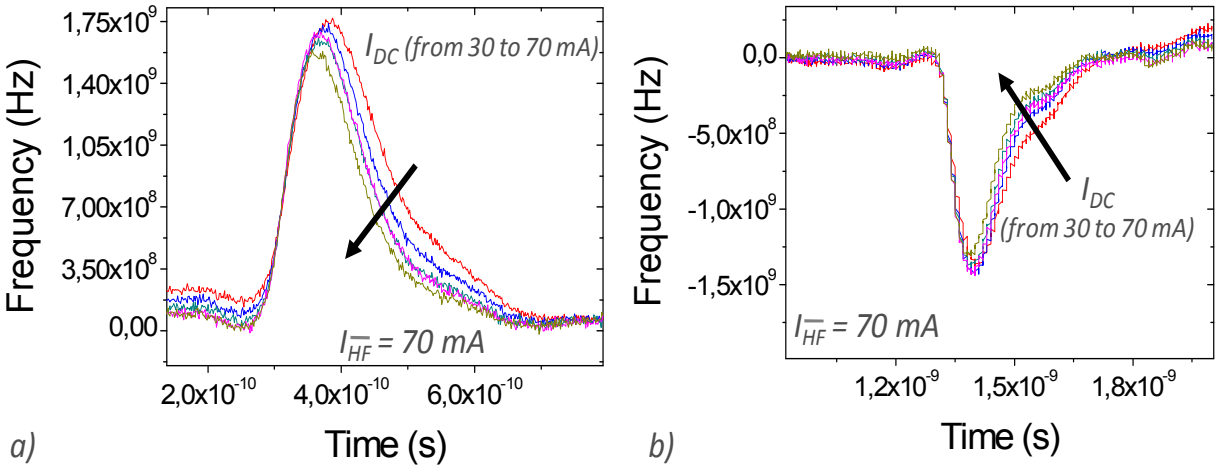

Figure 5-11 – Frequency variation of 2-section RSOA optical output power depending on the SOA2 bias current

5.1.3.3 Backward signal into the first section (SOA1)

The reflective behaviour of the RSOA induces to consider the signal coming back into the first section. If the signal propagates faster than the frequency modulation then the backward signal is under the same electrical modulation than the input signal. Considering 500µm long

RSOA, each section is about 250µm. The time to propagate forth and back along the second section is:

$$t = \frac{d}{c} = \frac{d}{c_0/n} = \frac{(2 \times 250).10^{-6}}{3.10^8/3.2} \approx 5{,}3.10^{-12}s$$

5-29

It is about 5 ps and corresponds to a frequency of 187.5 GHz. A modulation of 2.5 Gbit/s (at most 10 Gbit/s) is applied to the RSOA, therefore the backward signal is under the same modulation as the forward signal. The second modulation is added to the already modulated optical signal. We define I^+ and I^- as the "ON" and "OFF" current state respectively. The consequence of these two modulations is represented in Figure 5-12.

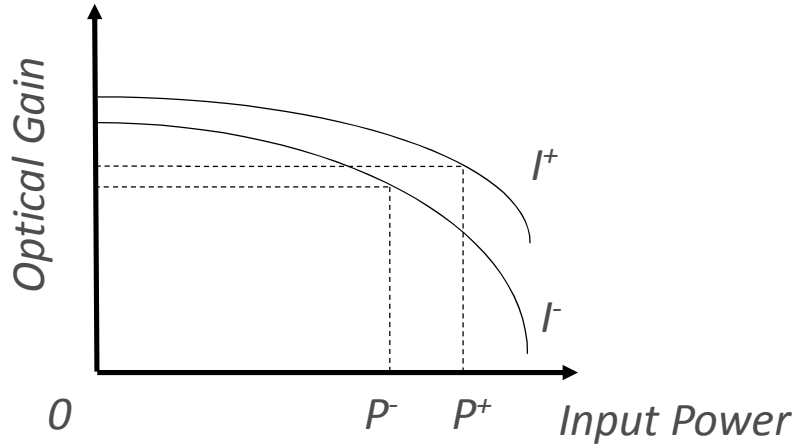

Figure 5-12 – Schematic representation of the optical gain versus input optical power under current and optical modulation in 2-section RSOA

The second electrical modulation is added to the first one because P^+ and I^+ produce higher optical gain than P^- and I^-. The ER increases because an extra gain is provided to the bit "1" (higher than the gain for the bit "0"). However it is difficult to quantify this effect and further study need to be done.

5.1.4 Transmission improvements

The previous analysis shows a clear reduction of the peak level and the width of the frequency variation when 2-section RSOAs are used. The trade-off between the extinction ratio and the frequency chirping is essential in order to reduce the transmission penalties. There is no adiabatic chirp in RSOA because the wavelength is fixed by the external cavity laser. Thus, in order to quantify the chirp, we consider the integral of the frequency variation from the leading and trailing edges (purely transient chirp). The total integral of the frequency deviation over the time needs to be reduced in order to minimize the chirp. We consider that the total frequency variation can be calculated as:

$$|\Delta f|_{total} = \frac{\left|\int_{t_A}^{t_B} f(t)\,dt\right|}{t_B - t_A} + \frac{\left|\int_{t_C}^{t_D} f(t)\,dt\right|}{t_D - t_C} \quad 5\text{-}30$$

Where t_A and t_B represent the time range of the leading edge, t_C and t_D represent the time range of the trailing edge (Δf is in Hz).

Figure 5-13 represents the method used to calculate this total variation ($|\Delta f|_{total}$).

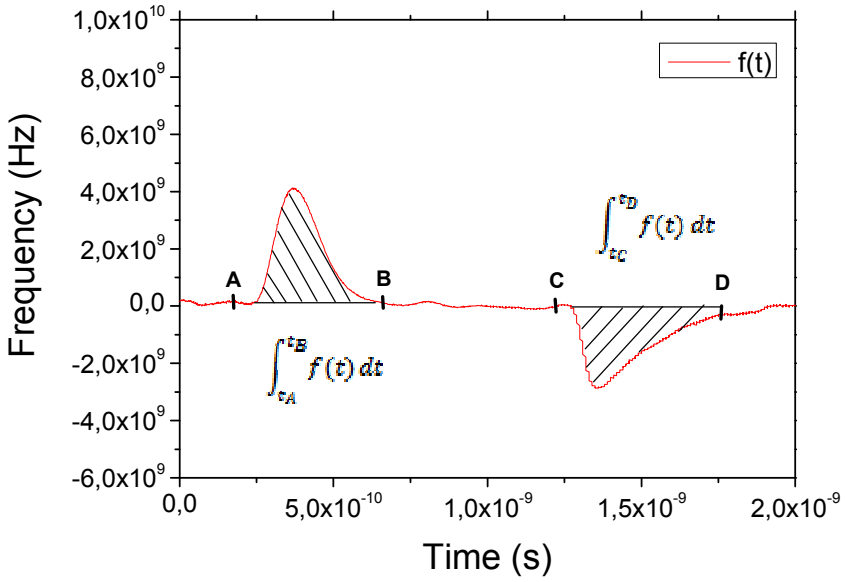

Figure 5-13 – Total frequency variation calculation method

The frequency deviation affects the systems performances due to spectral broadening of optical pulses. However a large ER enables open eye diagram. By increasing the ER, we also increase the total frequency deviation (Δf). Different amplitude modulation signals are applied to 1-section and 2-section RSOAs (modulation of SOA1). High AM electrical signals increase the ER. The ER is plotted against the total frequency variation $|\Delta f|_{total}$ in Figure 5-14. It is clear that 2-section RSOAs allow high extinction ratio while keeping a small total frequency deviation.

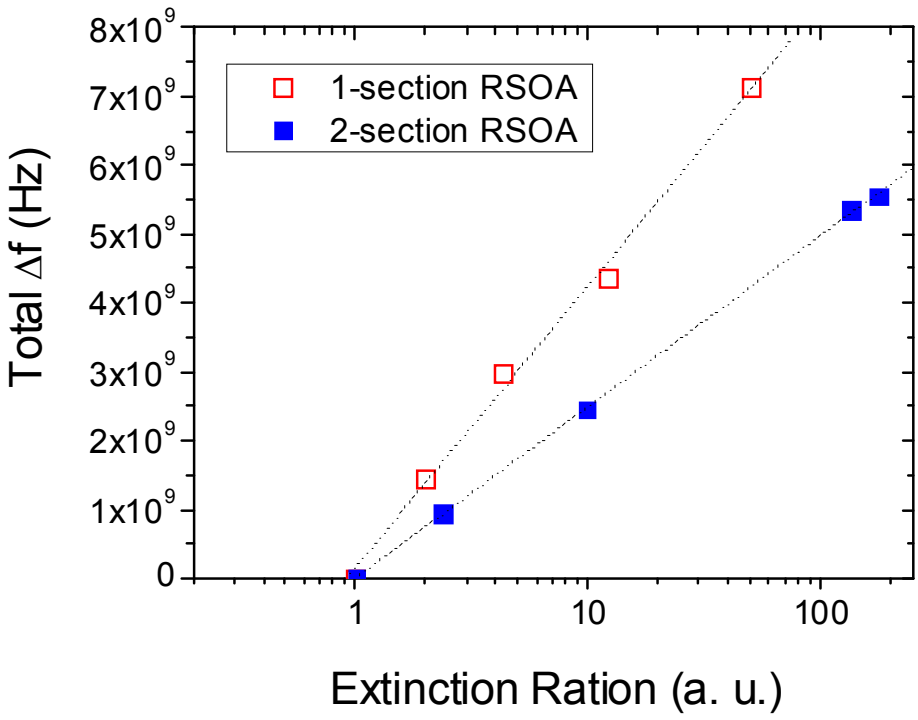

Figure 5-14 – Total frequency chirping depending on the ER

A back-to-back and transmission through 50 km SMF at 2.5 Gbit/s has been achieved using RSOA with one and two electrodes. We use RSOAs with 80 % of optical confinement where the frequency chirping is more important (compared to Γ = 20 %). Figure 5-15 displays BER measurements and unfiltered eye diagrams performed at 1540 nm and 2.5 Gbit/s as a function of the received power for one-section and two-section RSOA. The penalty due to the transmission with a single electrode device is equal to 6 dB.

With the 2-section device, penalties of 4.5 or 8 dB are obtained respectively for configurations SOA1 (Figure 5-15-(a)) and SOA2 (Figure 5-15-(b)). The minimum transmission penalty is achieved using an adequate two-electrode configuration (configuration SOA1) however the use of a non-adequate two-electrode configuration as configuration SOA2 increases transmission penalties up to 8 dB. These transmission results clearly show the correlation between the penalty and the chirp: the higher the RSOA chirp, the larger the transmission penalty.

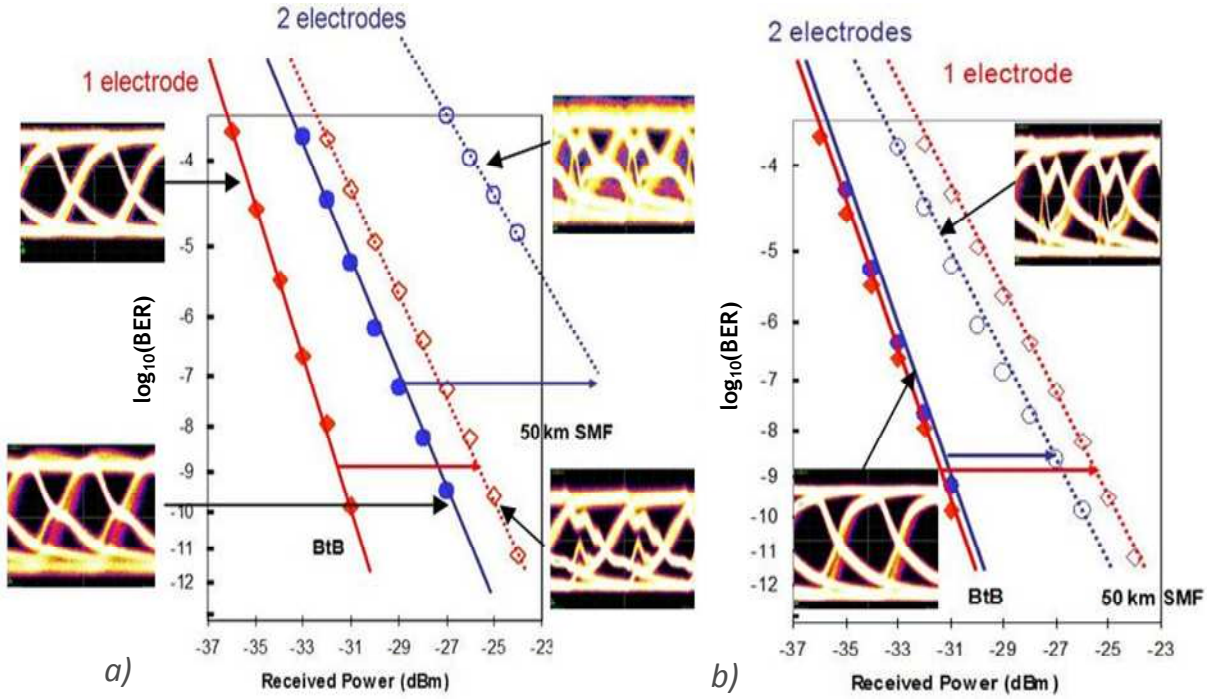

Figure 5-15 – BER curves as a function of the received power in Back-to-Back (solid lines) and after 50 Km transmission (dashed lines) for one (lozenges) and two electrodes configurations (circles). In bi-electrode configuration, the modulation IHF is applied to the mirror section and DC current I_{DC} to the input section (a) or inversely (b)

The configuration SOA1 corresponds to a moderate average current in the input section (30 mA), and leads to a degradation of the noise factor. This drawback can be overcome by using a tri-electrode device. A modulation applied on the middle section in this tri-electrode device enables penalty of 3 dB (Figure 5-16) which is half the penalties presented in classic configuration. The penalties due to the transmission over 50 km SMF at 2.5 Gbit/s are reduced from 6 dB to 3 dB using an optimized multi-electrode device. Tri-electrode devices turn out to be more efficient devices.

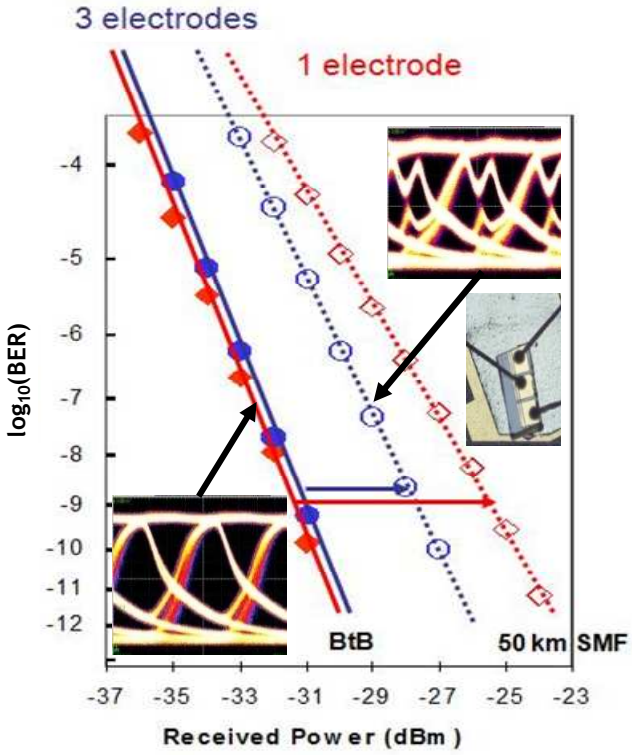

Figure 5-16 – BER curves as a function of the received power in Back-to-Back and after 50 Km transmission for tri-electrodes configurations.

Further works are underway to study more complex multi-electrode schemes in order to optimize the speed and the chirp at the same time. Also, the optimization of the length, shape and location of the electrodes could be done. Chirp limitation becomes even more important at higher bit rates (as described in chapter 6). In the same chapter, we use optimized RSOA (Γ = 20%) in order to demonstrate the feasibility of a long reach PON based on Reflective ONU.

5.2 Link gain improvement for R-o-F systems

Fibre-optics links have to be designed for analog signals from any number of sources. In most optical communication systems, the components used in the optical transmitter provide the most significant constraints on the capabilities of the system, and this is certainly the case for most analog, R-o-F systems. RSOA devices have been developed as remote modulators for optical access networks during the past few years and their large optical bandwidth has placed them in a leading position for the next generation of transmitters in WDM systems. The reduction of deployment costs with a universal device is one of the main drivers in RSOA research and development. Another driver is the recent demonstration of high performances RSOA devices having a high optical gain, a large output power and a reasonable E/O modulation bandwidth.

As studied in the FUTON project, RSOAs show a real potential for R-o-F network. The RSOAs would be electrically modulated by the RF signal coming from the sending antennas, as detailed in chapter 6. High linearity and low noise level are shown in chapter 6, which are essential in calculating the radio range. As noted earlier, another parameter RSOAs can help with

in a network is optical link gain, which is the main limiting factor in these devices. Two-section RSOA can be used to overcome this limitation. A comparison using various link types can be found in [11]. The next table shows a comparison between DML, RSOA and MZM R-o-F link parameters.

Parameter	DML	MZM	RSOA
gain, dB	-28	-42	-42
output noise power, dBm/Hz	-159	-167	-165

Table 5-1 – RoF link parameters (measured) [11]

A 10 dB of optical attenuation is used between the optical source and the photodiode. Link gain values are quoted that include this optical attenuation. The RSOA performances are limited due to the small link gain (-42 dB) compared to DML devices (-28dB). The link gain increases using two-section RSOA which enables a longer radio range. This effect is investigated theoretically and experimentally.

5.2.1 Link gain calculation

The first difficulty in designing optimized optical transmitters for R-o-F application is the impedance matching. It is usually done at the optical transmitter and receiver side. Photodiode (PD) has high impedance compared to low impedance for RSOA devices. This unmatched condition induces losses and reflection when transmitting an analog signal. The coefficient of reflection can be calculated as:

$$\Gamma_L = \frac{Z_{RSOA} - Z_{PD}}{Z_{RSOA} + Z_{PD}} \qquad 5\text{-}31$$

Where Z_{RSOA} is the RSOA impedance and Z_{PD} is the photodiode impedance.

The typical RSOA and PD impedances are respectively around 5 Ω and 50 Ω. Therefore the coefficient of reflection is equal to 0.82. This means 67 % ($= \Gamma_L^2$) of the input power is reflected by the RSOA so 4.8 dB of loss. This can be improved by adding a 50 Ω impedance in series, however it is not the case in our experiment. The link gain can be calculated considering all link parameters between the RSOA and the photodiode (see Figure 5-17) [12].

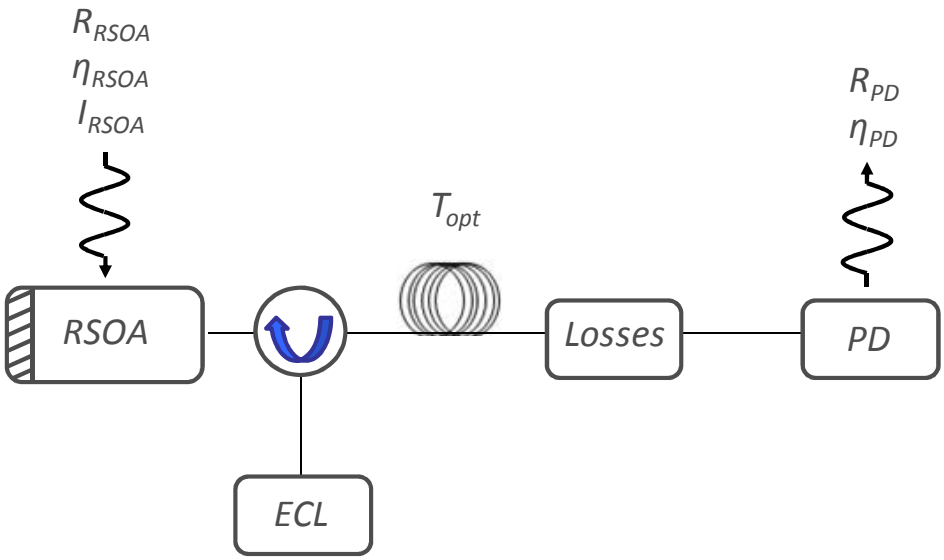

Figure 5-17 – Optical link scheme

The RSOA characteristics are defined by the resistance, the efficiency (optical watts per modulation ampere) and the bias current. The photodiode is characterized by the responsivity and the resistance. The link losses are called T_{opt}. The impedance mismatch induces a strong reflection and this should be considered in the link gain calculation. The losses due to the reflection in the RSOA can be quantified by the transmission coefficient T_{RF_RSOA} (= 1 - Γ_L^2). We also define T_{RF_PD} as the transmission coefficient at the output of the photodiode. Therefore the link gain can be expressed as [13]:

$$G_{hyp} = \frac{P_{PD}}{P_{signal}} = \left(\frac{R_{PD} . \eta_{PD}{}^2}{R_{RSOA}} \times T_{RF\_RSOA} \times T_{RF\_PD} \times T_{opt}^2 \right) \times \eta_{RSOA}{}^2 \quad \text{5-32}$$

The link gain is calculated using the next numerical values presented in Table 5-4.

Symbol	Parameter	value	unit
R_{RSOA}	RSOA impedance	5	Ω
R_{PD}	Photodiode impedance	50	Ω
η_{RSOA}	RSOA efficiency	0.1	W/A
η_{PD}	Photodiode efficiency	0.8	A/W
T_{opt}	Link losses (3 dB of losses due to the connectors and 3 dB of losses due to the optical circulator, the optical fibre losses are negligible due to the very small distance)	-6	dB
T_{RF_RSOA}	RSOA transmission coefficient	-4.4	dB
T_{RF_PD}	PD transmission coefficient	-3	dB

Table 5-2 – Main parameters of optical link RSOA based

Therefore, we obtain:

$$G_{hyp\_RSOA} = -31.4 \text{ dB}$$

5.2.2 Internal efficiency improvement

RSOA devices have already been optimized for low noise level and high linearity using low optical confinement (Γ=20%) as demonstrated in Chapter 6. In this section, we demonstrate that the link gain can be further improved by using 2-section RSOAs. First, the internal efficiency is evaluated considering only the amplified spontaneous emission (ASE). The RSOA is used as a modulated optical source without any input optical power. Direct modulation consists of the superposition of a constant bias current (DC) with the modulated signal (AC). The direct modulation strongly depends on the internal efficiency as represented in Figure 5-18. Link gain measurements with and without laser injection are performed in this section in order to validate the ASE configuration.

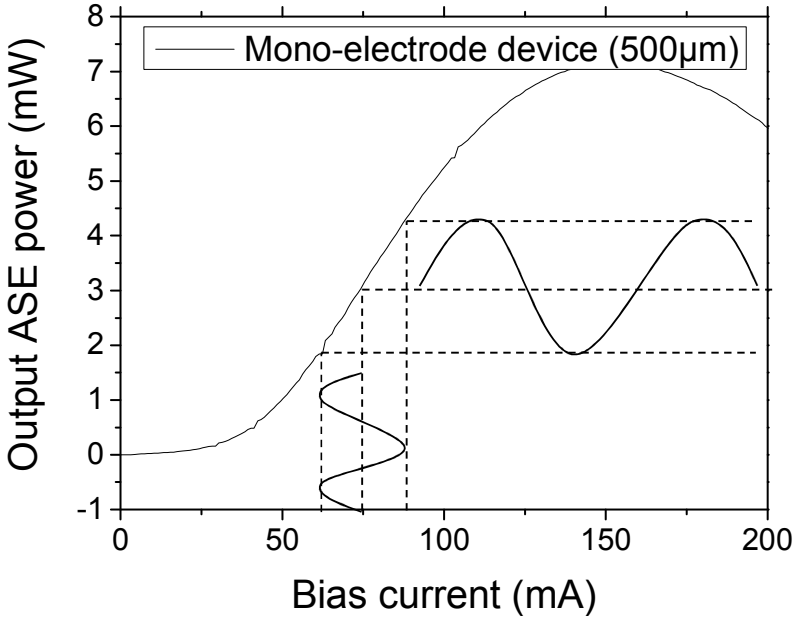

Figure 5-18 – Output ASE power depending on the bias current

The link gain directly depends on the efficiency of the device (equation 5-31). The 1-section and 2-section RSOAs efficiencies are measured in Figure 5-19. The maximum efficiency for 1-section RSOA is around 0.09 W/A, however values up to 0.21 and 0.22 W/A are obtained using 2-section RSOAs respectively for a modulation of SOA1 and SOA2. Using equation (5-32), link gain of -32.34 dB, -24.98 and – 24,58 dB can be calculated respectively for 1-section and 2-section RSOAs (SOA1 and SOA2 configurations).

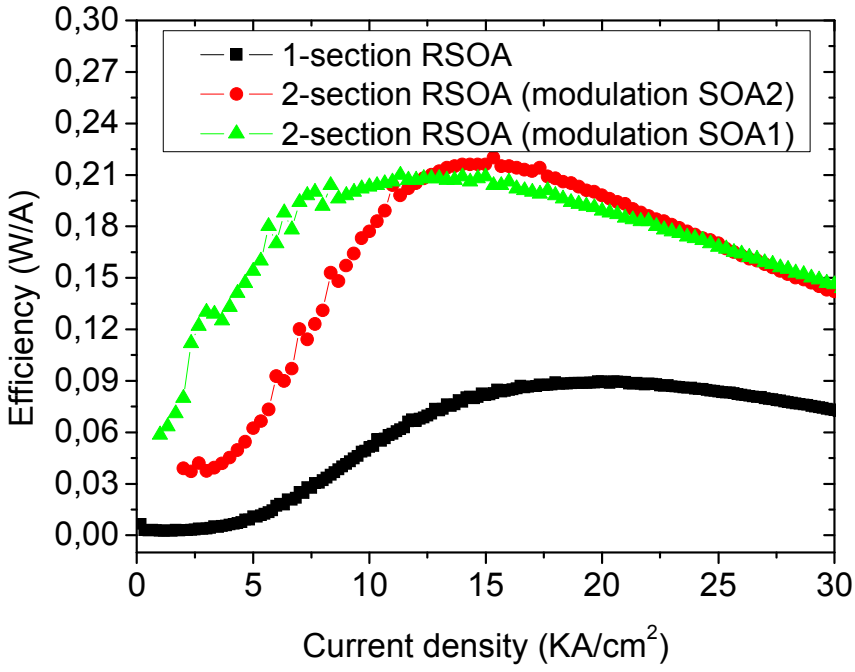

Figure 5-19 – RSOA efficiency for 1-section and 2-section devices

In order to validate the ASE configuration, link gain measurements are performed with and without laser injection using 1-section RSOA (Figure 5-20). Without any optical injection, the link gain is closed to previous calculated value: -33.2 dB. It increases by 3 dB when an optical power is launched into the RSOA. Therefore, high optical power injection induces a higher efficiency than no input optical power.

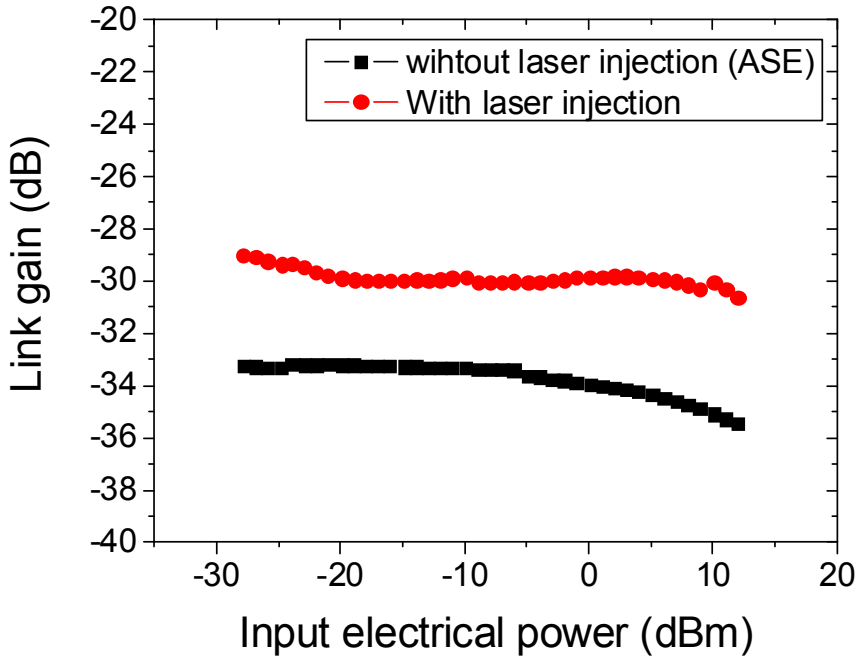

Figure 5-20 – Link gain measurements for 1-section RSOA at Pin = -6.5 dBm and without laser injection

In 2-section RSOAs, the microwave modulation is biased at 20 mA and a bias current of 70 mA is applied to the non-modulated section. In mono-electrode configuration, the bias current is 70mA. We realize a RSOA-based microwave fibre-optic link as described in section 4.1.4 and evaluate the effect of 2-section RSOAs (modulation on SOA1 and SOA2) under optical injection (P = - 10 dBm). The measured frequency responses of both devices are depicted in Figure 5-21.

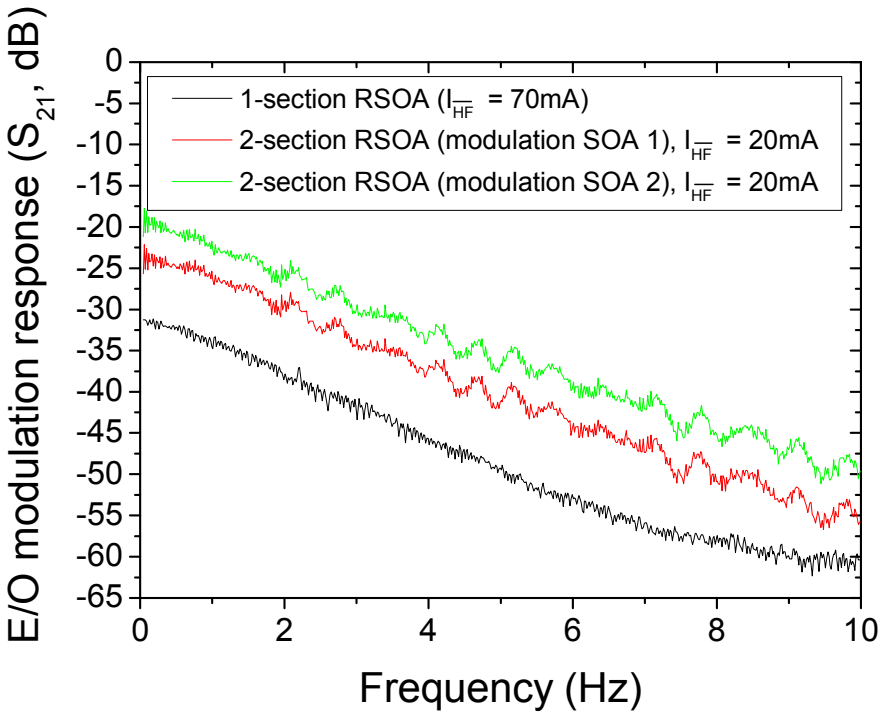

Figure 5-21 – RSOA frequency response on mono and bi-electrode configuration

The scattering parameters (S-parameters) are defined as in section 4.1.4. S_{21} values (at f = 0 GHz) of -20, -24 and -31.3 dB are measured using respectively 2-section RSOAs (modulation on SOA2 and SOA1) and one-section RSOA. An improvement of 11.3 and 7.3dB is observed respectively for SOA2 and SOA1 modulation compared to the single-section RSOA. As defined in chapter 4, the $|S_{21}|^2$ parameter is the link gain (dimensionless) of the 2-port network.

The improvement on the link gain is higher when modulating SOA2 than SOA1, however the efficiency is close to be the same (Figure 5-19). Link gain increases at high input optical power. When modulating SOA2, the optical signal is first launched into SOA1 which behaves as a pre-amplifier. The second section receives more optical power and the link gain increases. Therefore under optical injection, SOA2 configuration enables higher link gain compared to SOA1configuration. The link gain depends on the bias current of the modulated electrode. The next figure represents the E/O response of the 2-section devices with the bias current as parameter. A small variation of 30 mA induces a 10 dB and 3.5 dB reduction depending on the modulated electrode (SOA2 and SOA1).

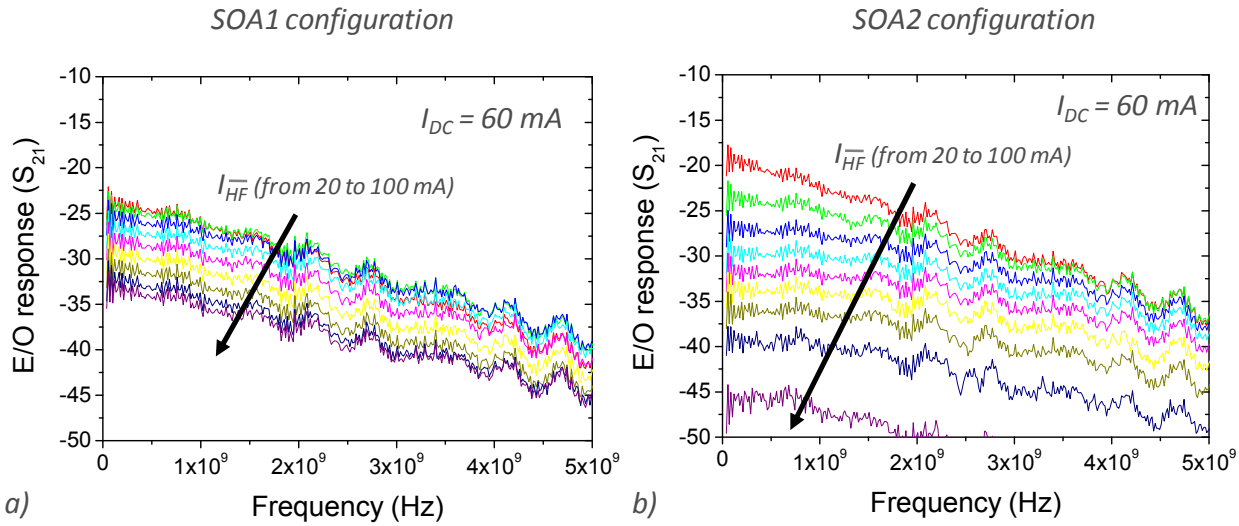

Figure 5-22 – multi-electrode RSOA frequency response for increasing bias currents

As observed in Figure 5-22, the link gain varies much more by modulating the second section (SOA2). In fact, Figure 5-19 shows that SOA1configuration has a broader efficiency peak than SOA2 configuration. Then the link gain from the SOA2 configuration strongly depends on I_{HF} bias current. Error Vector Magnitude (EVM) measurements and radio range calculation are compared in chapter 6 for R-o-F systems. The link gain improvement leads to a high radio range similar to laser devices.

5.3 Conclusions

In this chapter, we investigated the use of multi-section RSOAs. The chirp was a major issue in classic RSOA devices and we demonstrate that 2-section RSOAs leads to chirp reduction. A theoretical analysis is presented and confirmed by chirp measurements. The impact of each section on the ER and the frequency deviation is studied. Then the trade-off between the ER and the frequency chirping is overcome based on 2-section RSOAs. High ER is obtained while keeping a low total frequency deviation. Transmission through 50 km SMF at 2.5 Gbit/s is achieved using RSOA devices. Multi-section RSOAs reduce by 3 dB the penalties compared to classic RSOA.

In R-o-F network, RSOAs show smaller performances compared to DML due to the limited link gain. 2-section devices are used to overcome this drawback. The internal efficiency increases by using two-electrode RSOAs and leads to a link gain improvement. The theory behind the link gain is detailed and compared to experimental data. SOA2 configuration provides better improvement than SOA1 configuration. However it mainly depends on the operating conditions which have to be carefully controlled. Multi-section RSOAs are high potential candidates for colourless ONU and RAU as they solve part of the problems raised by access and R-o-F networks.

The main interrogation is: how far can they really improve the system performances? Chapter 6 evaluates these new devices in both networks and answers the previous question.

References

[1] G. de Valicourt, M. A. Violas, D. Wake, F. van Dijk, C. Ware, A. Enard, D. Maké, Zhansheng Liu, M. Lamponi, G. H. Duan and R. Brenot, "Radio over Fibre Access Network Architecture based on new optimized RSOA Devices with large modulation bandwidth and high linearity", Microwave Theory and Techniques, Vol. 58, No. 11, October 2010, pp 3248-3258

[2] G. P. Agrawal and N. A. Olsson, "Self phase modulation and spectral broadening of optical pulses in semiconductor laser amplifier", J. Quantum Electron., Vol. 25, No. 11, Nov. 1989, pp. 2297–2306

[3] G. H. Duan, "COM 341: FON Physique des Lasers", lecture notes, Ecole National Supérieure des Télécommunications, Chap.?, 2006-2007, pp ??- ??

[4] C. H. Henry, "Theory of the linewidth of semiconductor lasers", J. Quantum Electron., Vol. 18, No. 2, 1982, pp. 259-264

[5] P. P. Baveja et al, "Self-Phase Modulation in Semiconductor Optical Amplifiers: Impact of Amplified Spontaneous Emission", J. Quantum Electron., Vol. 46, No. 9, Sep. 2010, pp. 1396-1403

[6] F. Koyama and K. Iga, "Frequency chirping in external modulators", J. Lightwave Technol., Vol. 6, No. 1, Jan. 1988, pp. 87-93,

[7] T. Watanabe et al., "Transmission Performance of chirp-Controlled Signal by using Semiconductor Optical Amplifier", J. Lightwave Technol., Vol. 18, No. 8, Aug. 2000, pp. 1069-1077

[8] R.A. Saunders, J.P. King and I. Hardcastle, "Wideband chirp measurement technique for high bit rate sources", Electronics Letters, Vol. 30, No. 76, Aug. 1994, pp. 1336-1338

[9] G. P. Agrawal, "Fiber-optic communication systems", Third Edition, John Wiley & Sons Inc., Chap. 6, 2002, pp. 237-241

[10] G. de Valicourt, D. Maké, C. Fortin, A. Enard, F. Van Dijk and R. Brenot, "10Gbit/s modulation of Reflective SOA without any electronic processing", in Proc. OFC'11, OThT2, 2011, Los Angeles, USA

[11] David Wake, Anthony Nkansah, Nathan J. Gomes, Guilhem de Valicourt, Romain Brenot, Manuel Violas, Zhansheng Liu, Filipe Ferreira and Silvia Pato, "A Comparison of Radio over Fiber Link Types for the Support of Wideband Radio Channels", J. Lightwave Technol., Vol. 28, No. 16, March 2010, pp. 2416-2422

[12] Reynald Boula-Picard, "Contribution a l'étude des amplificateurs optiques à semi-conducteur pour applications analogiques", PhD thesis, Université de Rennes 1, Chap. 2, july 2004, pp. 99-101

[13] H. Zmuda and E. N. Toughlian, "Photonics aspect of Modern Radar", Artech House, Boston 1994

Chapter 6. Telecommunication Network

Higher capacity networks are needed to satisfy the continuous penetration of internet and to support applications such as high definition television, video-on-demand, on-line gaming. Fibre-to-the-premises (FTTP) is considered as the main solution to satisfy the demand. Today the Time-Division Multiplexing (TDM) technique, employing two wavelength channels to serve multiple users for up- and downstream traffics, is being widely used in Passive Optical Networks (PON). For next-generation access networks, upgradeability and high capacity could be obtained using Wavelength-Division Multiplexing in PON (WDM-PON) [1]. For uplink transmission systems using WDM, each ONU requires an optical source, such as a directly modulated laser (DML) [2]. If wavelengths are to be dynamically allocated, one to each ONU, colourless devices are needed in order to minimize the deployment cost. Reflective Semiconductor Optical Amplifier (RSOA) devices can be used as a low-cost solution due to their wide optical bandwidth [3]. The same type of RSOA can be used at different ONUs where they perform modulation and amplification functions. However, cost and compatibility with existing TDM-PONs is still an issue.

In the first section of this chapter, we introduce the envisaged architectures of access networks based on RSOA. The development of new high performances RSOAs as described in Chapter 2 leads to efficient colourless ONU and we demonstrate an extended reach hybrid PON, based on RSOA devices. In section 6.1.2, it is shown that 2-section RSOAs improve the transmission quality over long distance and this demonstrates the possibility of long reach PON. High speed RSOAs show the feasibility of a 10 Gbit/s modulation without any electronic processing as detailed in section 6.1.3.

At the same time users increasingly shift towards mobile devices and on-the-road connectivity. Consequently, there is a demand for higher-capacity wireless networks, since customers want to enjoy the same quality for mobile multimedia services as for fixed networks. In this context, WLAN hot-spots or third-generation (3G) wireless networks are already able to establish wide-area wireless connectivity for services such as voice telephone, video calls, and wireless data, all in a mobile environment. Radio over fibre (R-o-F) technology enables different types of services to be combined into a homogenous infrastructure using distributed antenna systems (DAS), which is very attractive for next generation wireless networks [4]. DAS consists of a large number of remote antenna units (RAU) over the coverage area and a central unit (CU). In order to obtain a wide service coverage area, many RAUs should be connected to a Central Unit (CU) via an optical fibre network. Efficient architectures have been proposed using WDM techniques, allowing a reconfigurable radio over fibre network (RoFnet) [5]. The issues raised by WDM techniques are similar to the ones for access network and colourless devices are needed. In this chapter, we investigate the critical parameters of RSOAs for a R-o-F link and we use the fabricated RSOA structures for a colourless R-o-F Access Network architecture. This study was part of the FUTON project. The radio range is improved by taking advantage of the link gain increase detailed in chapter 5.

6.1 Next generation of Access Network

One potential solution for next generation of optical access networks is to use Wavelength-Division Multiplexing (WDM) in order to offer network flexibility and also increase data bit rate. However, cost and compatibility with existing TDM-PON (Time Division Multiplexing Passive Optical Network) networks are still important issues to be considered. As a consequence, hybrid (TDM+WDM) architecture is being investigated for next generation access network [6,7], as a transition from TDM to WDM PONs where some optical splitters could be re-used. In order to optimize the operation and management deployment cost of a colorized access network, the ONU (Optical Network Unit) must be colourless. ONU transmitters using RSOA are potential candidates for low cost deployment and colourless devices. However, reflective modulation schemes suffer from Rayleigh Back-Scattering (RBS) when using a single fibre [8].Conventional RSOAs display saturation powers well below 10 dBm, which limits the optical budget (OB) of RSOA-based links.

The interest for these devices increased rapidly in the last five years. However another concern about Hybrid PON is its property to be compatible with long reach or high optical budget network configuration. Thus high gain and low chirp devices are needed and were demonstrated in chapter 3 and 5 respectively.

Recently, the first commercial hybrid PON based on reflective semiconductor optical amplifiers (RSOA) has been announced [9]. Such a network allows serving 1024 subscribers at 1.25 Gbit/s over 20 km. In this work, we are aiming at an extension of the link and the bit rate based on high performances RSOA and new network design.

6.1.1 RSOA devices as colourless ONU

In RSOA devices, the wavelength is externally fixed. Various options have been studied such as using multi-wavelength sources (such as tuneable lasers, External cavity laser (ECL) , Photonic Integrated Circuits (PIC) or a set of Directly Modulated Laser (DML) at selected wavelengths), creating a cavity with the active medium of the RSOA, or using filtered white source. Therefore, RSOA devices as colourless transmitters can be used in different configurations:

- Laser seeding
- Spectrum-sliced EDFA seeding
- Wavelength re-use
- Self-seeding

In the laser seeding approach, the multi-wavelength external laser source can be located at the CO [10] or at the remote node [11]. From the CO, the optical budget is limited to 25 dB and strong RBS impairments appear. These limits are overcome by locating the laser at the remote node. One laser per remote node is needed, thus raising deployment cost, control management and power consumption issues.

Another possible architecture is using spectrum-sliced EDFA seeding [12].An erbium-doped fibre amplifier (EDFA) is used as a broadband source of un-polarised amplified

spontaneous emission and this broad spectrum is then sliced by the Arrayed Waveguide Grating (AWG) for each ONU.

Wavelength re-use has been developed by Korean and Japanese companies [13, 14]. The downstream source from the CO is re-modulated as an upstream signal at the ONU using RSOA. Simple efficient ONU is obtained as no additional optical source is needed.

The final approach is using a RSOA-based self-seeding architecture. This recent concept has been proposed by Elaine Wong in 2007. This novel scheme uses at the remote node (RN) a reflective path to send back the ASE (sliced by the AWG) into the active medium. The self-seeding of the RSOA creates a several km long cavity between ONU and RN. The wavelength is determined by the connection at the RN. This technique is attractive because a self-seeded source is functionally equivalent to a tuneable laser. Recent progresses show 1.25 Gbit/s [15] and 2.5 Gbit/s [16] operation based on stable self-seeding of RSOA. Another way to obtain self-seeding configuration is using an external cavity laser based on a RSOA and Fiber-Bragg Grating (FBG). BER measurements show that the device can be used for upstream bit rates of 1.25 Gbit/s and 2.5 Gbit/s [17].

In this thesis, we focus on the laser seeding approach. We present the scheme of a laser seeding architecture based on RSOA on Figure 6-1. Actually, Figure 6-1 shows the up-stream part of the link using an RSOA, i.e. the information sent from the subscriber to operator/network. At the central office, a transmitter is used to send light (containing no information) to the subscriber through an optical circulator. Light propagates through several kilometres of optical fibre. The signal is then amplified and modulated by the RSOA in order to transmit the subscriber data for uplink transmission.

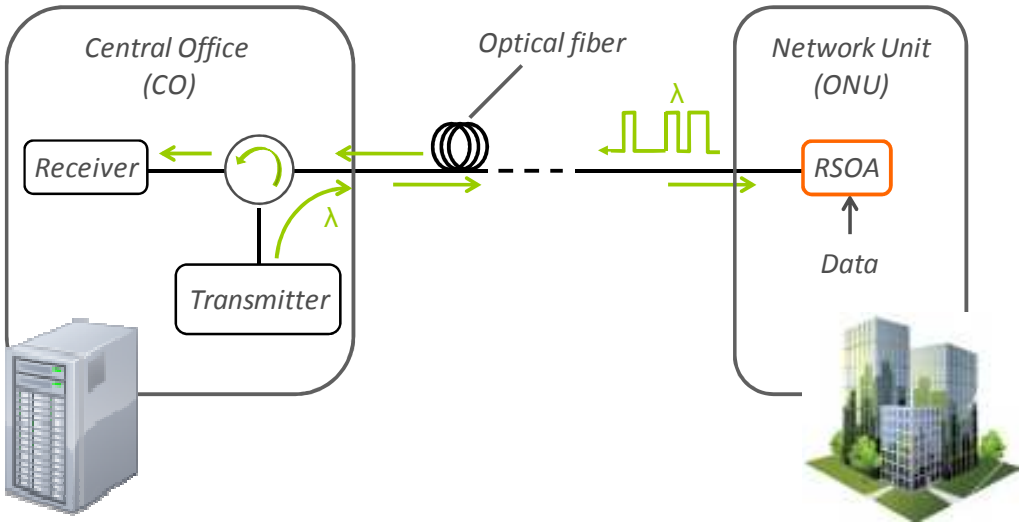

Figure 6-1 – Laser seeding Network architecture based on RSOA

In this section, we demonstrate an extended reach hybrid PON, based on a very high gain RSOA operating at 2.5 Gbit/s with a saturation power in excess of 10 dBm. To reduce RBS impairments, we locate the continuous wave (CW) feeding light source in the remote node, and the large gain of the RSOA allows using moderate CW powers. Alternative devices such as remotely pumped erbium doped fiber amplifier (EDFA) can be used in order to avoid the

deployment of active devices in a remote node; this approach could also reduce the RBS level owing to a lower seed power and the management cost of the system [18], [19].

Figure 6-2 shows the up-stream part of the proposed link. At the remote node, an external cavity laser (ECL) is used to launch an 8 dBm CW signal into the system through an optical circulator (OC). A wavelength demultiplexer is used to break a potential multi-wavelength signal back into individual signals. A given wavelength represents one of up to 8 sub-PON on a 100 GHz grid (from λ_1 = 1553.3 nm to λ_8 = 1558.9 nm). The output of the wavelength demultiplexer is coupled into a 20 km long Single Mode Fibre (SMF) followed by a 12 dB optical attenuator used to simulate a passive splitter for 16 subscribers. The CW signal is then modulated by the RSOA, generating the upstream signal. The RSOA is driven by a 2^{31}-1 pseudo-random bit sequence (PRBS) at 2.5 Gbit/s, with a DC bias of 90 mA. From the remote node, the upstream signal propagates on another 25 km long SMF which simulates the reach extension provided by the proposed network design. A variable optical attenuator is placed in front of the receiver in order to analyze the performance of the system as a function of the optical budget. This attenuator also accounts for the insertion-loss of the multiplexer at the CO (between 3 to 5 dB). Bit-error-rate (BER) measurements are done using an Avalanche Photo-Diode (APD) receiver and an error analyzer.

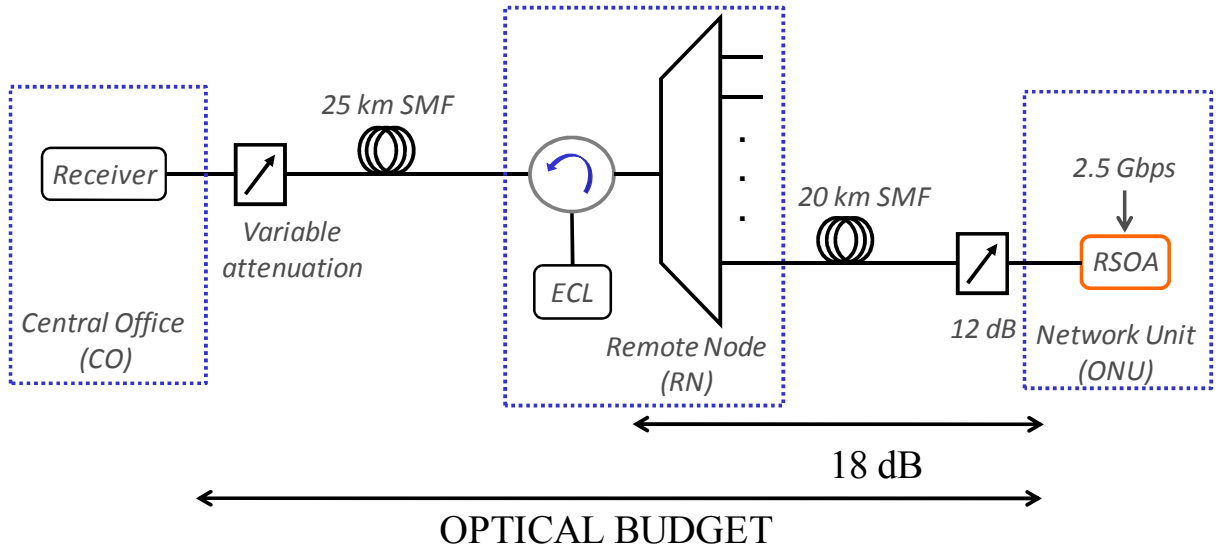

Figure 6-2 – Experimental setup of WDM/TDM architecture using RSOA

At low bit rate, the best trade-off between gain, modulation bandwidth and saturation power is obtained for a 700 µm long cavity RSOA, therefore we chose this device in the experimental setup. The RSOA is driven at 90 mA with a -10 dBm input power. Figure 6-3 displays BER measurements performed at 1554.1 nm and 2.5 Gbit/s as a function of the optical budget between the CO and the extended optical network unit (ONU). The inset shows the open eye diagram measured at the output of the RSOA. Sensitivities at 10^{-9} in back-to-back (BtB) configuration and after transmission are -32 dBm and -27 dBm respectively. These performances are mainly due to the large output power of the RSOA, which allows for an increased optical budget compared to standard RSOAs: a BER of 10^{-9} is thus measured with an optical budget of more than 36 dB. Whatever the OB, the input power in the RSOA is -10dBm, which ensures that the device operates in the saturated regime, with a reflection gain of 20 dB. Gain saturation leads

to a low sensitivity of the RSOA to back-reflections, since the output power only slightly depends on the input power.

In Figure 6-3-(b), the BER of 8 WDM channels (100GHz spacing), is shown, for a 40 dB optical budget ; in this case, the BER is 10^{-7}, well below the forward error correction (FEC) limit. No penalty is observed due to the large bandwidth of the RSOA. Besides, this OB corresponds to two 12 dB (16*16 subscribers) power splitters, taking into account mux/demux, propagation and circulator losses. A compromise between split ratio and range needs to be considered. Thus, one of the two 12 dB budget increase can also allow for a reach extension between the CO and the remote node (including the 25 km reach extension). However, propagation effects such as RBS and dispersion in the fibre would limit this extension. A reduction in RBS level is also needed to improve the performance of this configuration. Different solutions have been studied to reduce the RBS level: low frequency modulation of the laser source [20], applying bias dithering at the RSOA [21]. Power penalty can then be improved by more than 3dB.

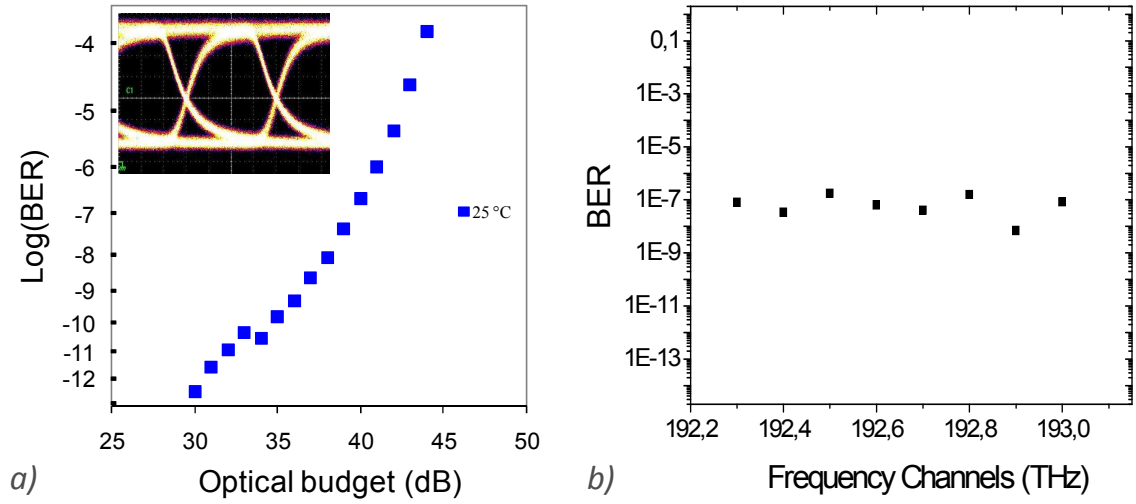

Figure 6-3 – (a) BER as a function of the optical budget. Inset: 2.5 Gbit/s eye-diagram at the output of the RSOA driven at 90 mA and with an input power of -10 dBm (b) BER values for different λ-channels for an optical budget of 40 dB, or a Rx input power of -30 dBm

A cost effective hybrid WDM/TDM-PON which can potentially feed 2048 subscribers (16×16×8 = 2048 subscribers) at a data rate of 2.5 Gbit/s is presented in this section. The large gain and high output power of the RSOA have also allowed extending the link reach up to 45 km instead of the standard 20 km. However, these achievements are obtained at the expense of an increase in deployment and operation costs. We believe this solution is economically viable since these costs are shared between many users, and multi-wavelength sources are becoming cheaper with the advent of Photonic Integrated Circuits (PIC). This 2.5 Gbit/s upstream colourless result allows investigating this solution to achieve in the trunk line a wavelength multiplex of several next generation access solutions (10 Gbit/s down- and 2.5 Gbit/s up-stream).

6.1.2 Long Reach PON using low chirp RSOA

Another question about Hybrid PON is its property to be compatible with long reach network configuration. It was shown in the previous section that high gain RSOAs enable high

optical budget, for instance, up to 36 dB and 45km transmission at 2.5 Gbit/s. A high optical budget is necessary to obtain a long reach PON (compensation of the fibre attenuation). The limitation imposed on the bit rate and distance by the fibre dispersion can dramatically increase depending on the spectral width of the source. The input pulses broaden more rapidly when they are chirped Gaussian pulses (or super-Gaussian pulses). The bit-rate limitation has been studied using a super-Gaussian model for a NRZ-format bit stream [22]. This problem can be overcome by reducing the chirp produced by the RSOA device.

In Chapter 5, we have demonstrated chirp reduction using a 2-section RSOA and how it can be used to reduce the transmission penalties. We now propose an extended reach hybrid PON, taking advantages of a very high gain Reflective Semiconductor Optical Amplifier (RSOA) and the two-electrode configuration operating at 2.5 Gbit/s.

A transmission on SMF over 100km is demonstrated below the FEC limit. We have located the CW feeding light source on the remote node for the same reasons as previously. The frequency deviations have been measured as described in section 5.1.2. In Figure 6-4, frequency deviations of +4.1GHz for leading edges and -2.9GHz for trailing edges were measured for single-section RSOA. In the case of a dual-electrode RSOA, the frequency deviations are changed to +4.3GHz for leading edges and -2.3GHz for trailing edges. Also the width of the frequency peak is reduced which means a faster dynamic behaviour. It also reduces the penalties during long reach transmissions. The full width at half maximum (FWHM) at the leading edge has been measured and is reduced from 1.67×10^{-10} to 1.15×10^{-10} s for the one- and two-section RSOA respectively. We notice that the pulse amplitude is also higher (Figure 6-4-(b)) which leads to a better extinction ratio. The 2-section RSOA results in a good balance and achieves a high extension ratio and a low chirp. The measurement conditions are the same and are the optimized conditions to obtain low transmission penalties. For the same chirp level, we obtain a higher extension ratio for a 2-section RSOA which is strongly desirable in long reach PON.

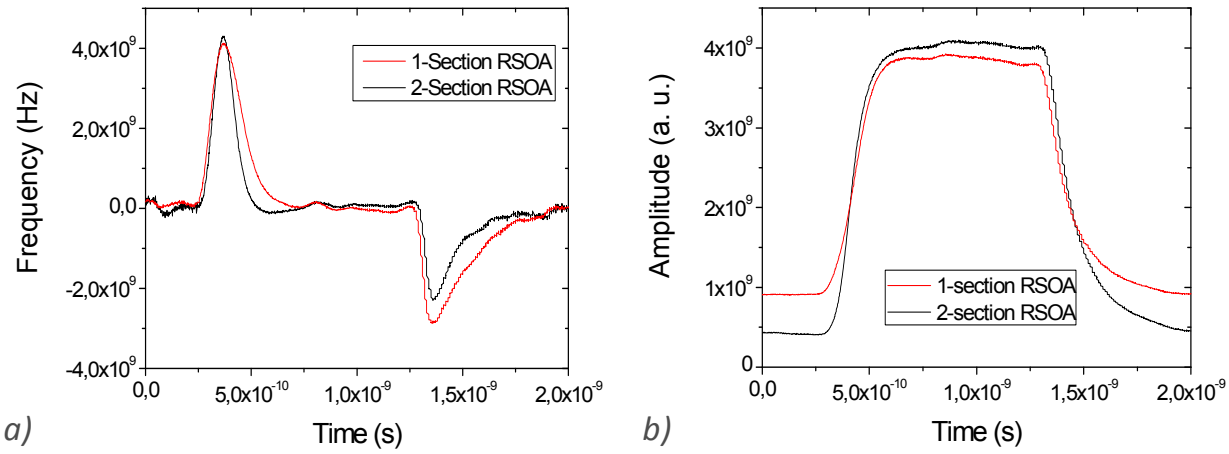

Figure 6-4 – Frequency a) and amplitude b) responses of single and dual-electrode RSOAs

The performances of a long reach PON making use of single- or dual-electrode RSOA are assessed to demonstrate the reduction of the chirp. The experimental set-up is similar to the one described in Figure 6-2. A Wavelength Division Multiplexer selects the required wavelength and is coupled to a 50 km long SMF. The upstream signal propagates after the RN on another 0, 25 or 50 km long SMF. The 6 dB optical attenuator is used to simulate a passive splitter for four

subscribers. RSOA with a 500 μm long cavity are used in the experimental setup, one with single and the other with dual-electrode configuration. The single electrode RSOA was driven at 60 mA and the bi-electrode at 20 mA on the input electrode (SOA1) and 115 mA at the mirror electrode (SOA2). Both current values correspond to conditions optimized for low transmission penalties. In both cases, the CW optical input power was –8.5 dBm. Figure 6-5 displays BER measurements performed at 1554 nm and 2.5 Gbit/s as a function of the received power for one- and two-section RSOA. The penalties due to 100 km transmission with a single-electrode RSOA do not enable to reach the FEC limit. From 25 km to 50 km (100 km), we obtain penalties of 1.2 (3.4) dB. One can see that a BER of 10^{-4} (FEC limit) has thus been measured with dual-electrode RSOA at a received optical power of -35 dBm over 100 km SMF. The penalties due to extended 25 and 50 km SMF are much lower than with one-electrode RSOA (respectively 0.5 and 1.3 dB). These transmission results clearly show the correlation between the penalty and the chirp. The latter has more pronounced effects over long SMF.

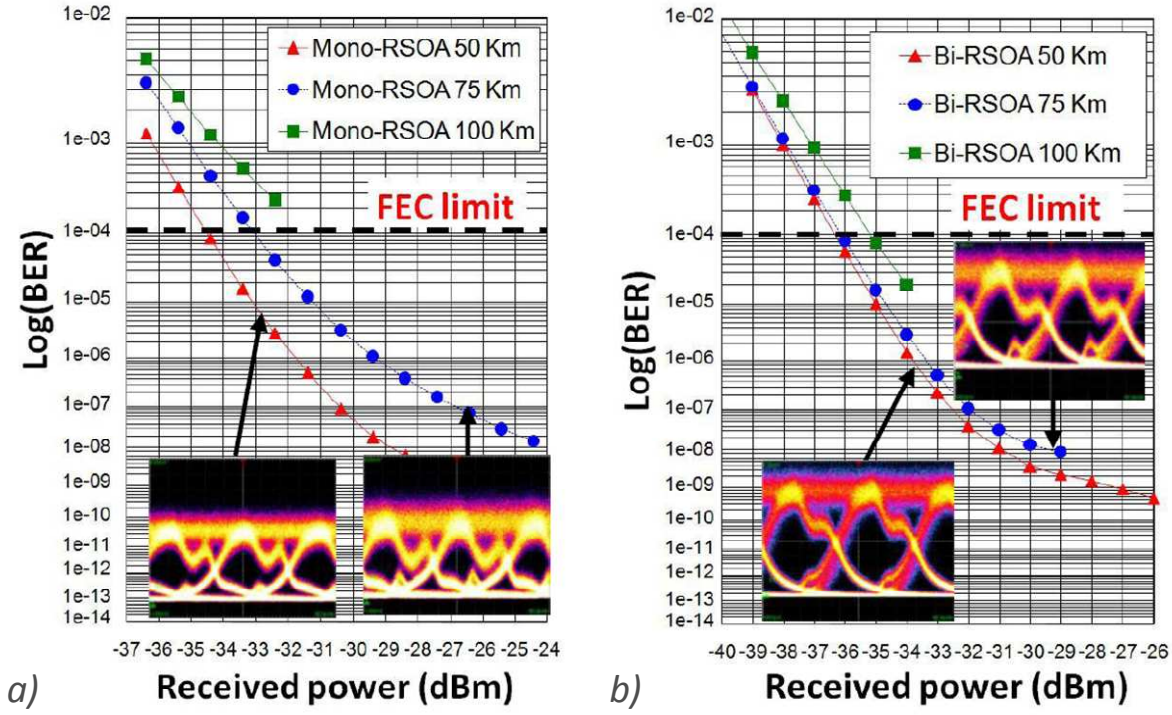

Figure 6-5 – Comparison of BER value as a function of the received power (a) for mono-electrode and (b) for bi-electrode RSOA over 50, 75 and 100 km at 2.5 Gbit/s

In Figure 6-6, a comparison between single and dual-electrode RSOA over 100 km transmission is shown and a difference of 4 dB is obtained at the FEC limit. After propagation on a long distance, the eye diagram is clearly less open for one-electrode devices due to the chirp. This effect is reduced to a great extent when using dual-electrode RSOAs which confirms BER measurements. The proposed network design allows the use of Dense-WDM (DWDM), which means 62 wavelengths considering the 50 nm optical bandwidth of the RSOA. By considering the 6 dB optical attenuator (passive splitter for four clients), 248 potential subscribers can be fed. At the FEC level, a variable attenuation of 4 dB is obtained which can be used as a splitter in order to design two parallels WDM PONs (2*248=496 customers) over 100Km.

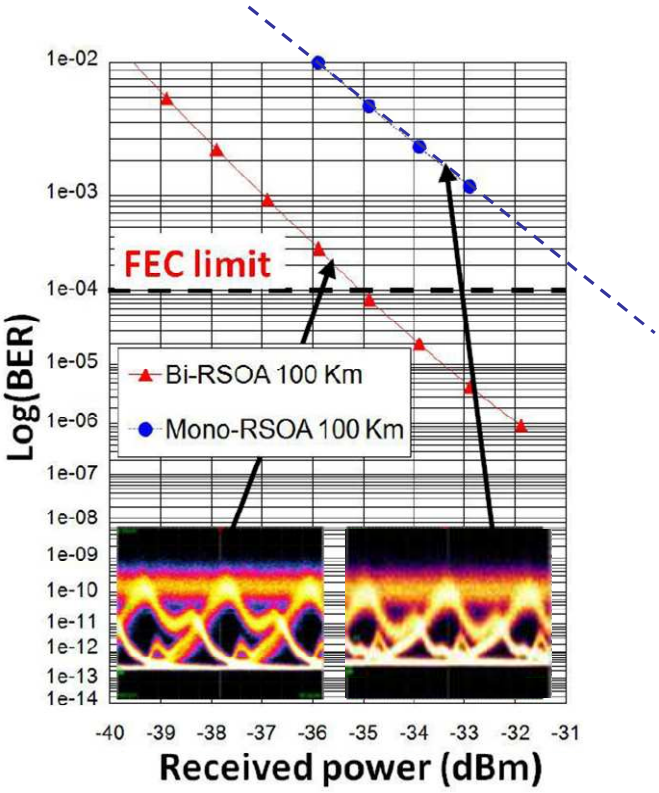

Figure 6-6 – Comparison of BER value as a function of the received power for mono-electrode and bi-electrode RSOA over 100 km at 2.5 Gbit/s

A long reach Hybrid WDM/TDM PON which can potentially feed 496 subscribers was presented. It was shown that the large gain of the RSOA and also the low chirp allows a reach extension of the link from standard 20km to 100 km. We demonstrated that penalties due to the transmission over 100 km SMF at 2.5 Gbit/s are reduced using an optimized multi-electrode device and a BER below the FEC limit was achieved. We also believe this effect will be even more pronounced when 10 Gbit/s RSOA will be used.

6.1.3 10 Gbit/s modulation without any electronic processing

Active research on high bit rate RSOA has led to 10 Gbit/s operation with EDC [23], OFDM [24] or electronic filtering [25]. Bandwidth improvement to 7 GHz small-signal bandwidth with dual-electrode devices [26-27] have been obtained but no large signal operation. However the modulation bandwidth of one-section RSOA is limited to 2 GHz [28] and increasing the modulation bandwidth of RSOA is still a challenge. Since carrier lifetime is mainly governed by stimulated emission rate, we have decided to increase the length of our RSOA to increase photon density, hence reducing carrier lifetime. The Chapter 4 presents the impact of length increase on the modulation bandwidth, either in small-signal or large-signal operation conditions. The RSOA structure has been designed to achieve a small optical confinement (Γ~20%) and has a cavity length of 850 μm. This device was chosen because an open eye diagram was obtained (Chapter 4) when the RSOA was driven by a 2^7-1 PRBS at 10 Gbit/s. The experimental set-up used for the 10 Gbit/s modulation is represented in Figure 6-7.

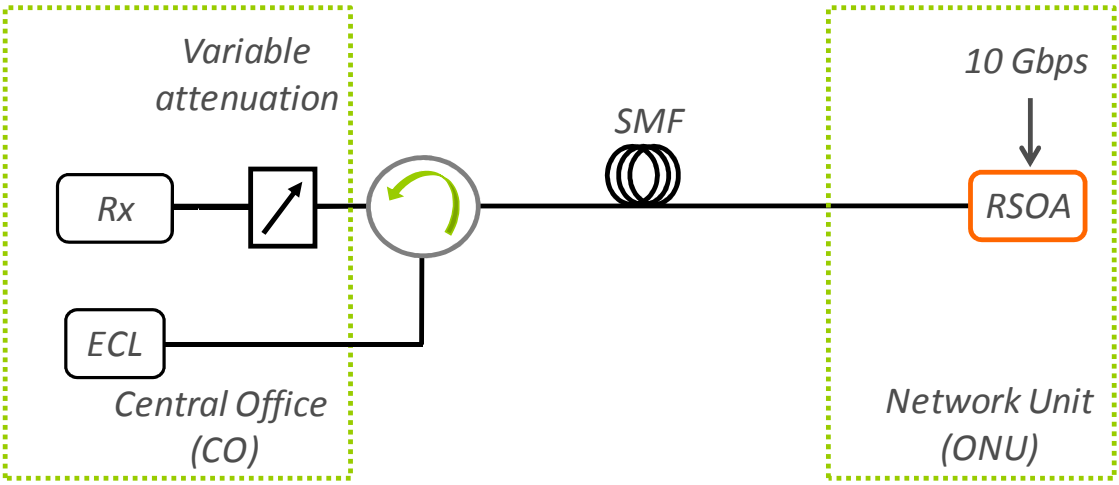

Figure 6-7 – Experimental setup of a simplified PON architecture using RSOA at 10 Gbit/s

An ECL is used to launch a 4.5 dBm CW signal into the system through an optical circulator (OC). The signal is coupled into the RSOA which is modulated and generates the upstream signal. The RSOA is driven by a 2^7-1 PRBS at 10 Gbit/s, with a DC bias of 160 mA. The upstream signal propagates on various SMF lengths. A variable optical attenuator is placed in front of the receiver in order to analyze the performance of the system as a function of the received power. BER measurements are done using an APD receiver and an error analyzer. BER measurements without ECL have led to a BER floor of 10^{-6} (ASE regime).

With optical injection, BER values below the FEC limit in BtB and after 2km transmission are obtained (Figure 6-8). Error-free operation can either be obtained with FEC codes, or under certain optical injection regimes. However we can clearly see that the eye diagram tends to be closed due to the chirp over long distances. Multi-electrode devices can be used in order to compensate for this effect as demonstrated in Chapter 5.

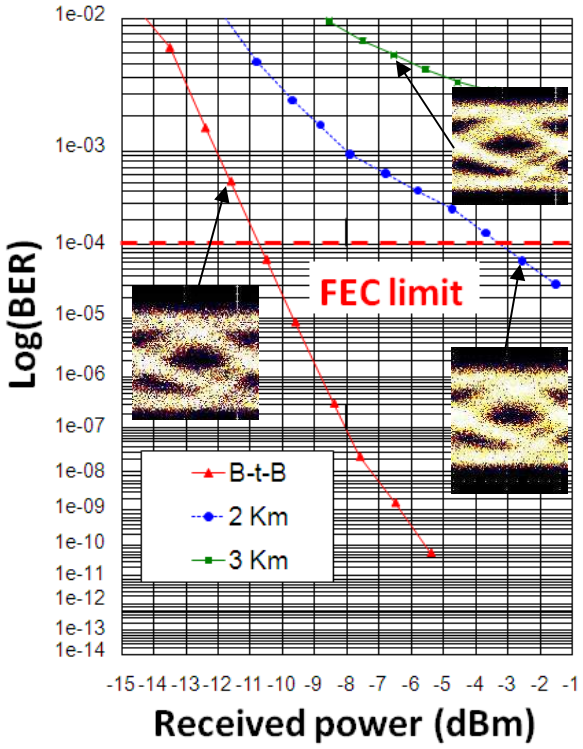

Figure 6-8 – BER value as a function of the received power for 850 µm long RSOA modulated at 10 Gbit/s

As described in Chapter 4, the modulation speed of RSOA is limited by the carrier lifetime. In the large signal regime, the slow decay is probably governed by the Auger recombination process, which increases the carrier lifetime. A 3 GHz modulation bandwidth can be obtained with 850 µm long RSOA, which has led to the first eye-opening of a RSOA at 10 Gbit/s without electrical equalization or passive electronic filtering. Limitation due to the chirp is observed and further works are underway to overcome this effect using multi-electrodes devices. Longer devices and dual-electrode devices will be studied to improve the modulation and transmission properties.

6.2 Radio-over-Fibre Network

The high bit rates envisaged for 4th generation wireless networks (4G) can be provided by a hybrid optical-radio infrastructure which has been tentatively developed in the FUTON (fibre optic networks for distributed, extendible heterogeneous radio architectures and service provisioning) project [29]. Recently, compact wireless access nodes for WDM bidirectional radio-over-fiber networks based on RSOA have been demonstrated [30], however RSOAs for analog transmissions are still an issue and no complete studies of these devices as remote modulator have been done for R-o-F applications [31]. In [30, 31, 32], the electrical modulation bandwidth of the RSOA has limited the wireless system performance. In this section, we investigate the critical parameters of RSOAs for a R-o-F link and compare low and high optical confinement RSOA structures developed in Chapter 2. The devices are driven by a standard Wi-Fi 802.11g signal which is easily generated using existing lab equipment and can be used to demonstrate the RSOA capability in a R-o-F link. In particular, we demonstrate an uplink configuration which

exploits high-performance RSOAs (electrical bandwidth up to 3 GHz) in order to perform modulation and amplification for OFDM modulated signals. A 64-QAM modulation format is applied via electrical injection to a RSOA. A similar experiment has been reported on SOA [32] but for the first time, to the best of our knowledge, the signal is applied to a Reflective-SOA and the device responds as expected. Optimized RSOAs allow the integration of the wireless and optical technologies, and demonstrate the feasibility of a distributed broadband wireless system (DBWS) which uses a DAS architecture in combination with a high throughput radio interface. This study is the result of a strong collaboration between III-V lab, the University of Kent and Instituto de Telecomunicações of Aveiro, Portugal.

6.2.1 R-o-F Network architecture RSOA based (The FUTON project)

The global architecture of the R-o-F DAS network concept is represented in Figure 6-9. This specific architecture is developed in the framework of the FUTON project and more details can be found in [33]. A large number of Remote Antenna Units (RAU) are used to provide wireless connections with mobile users and each RAU covers a geographical range of approximately 500m.

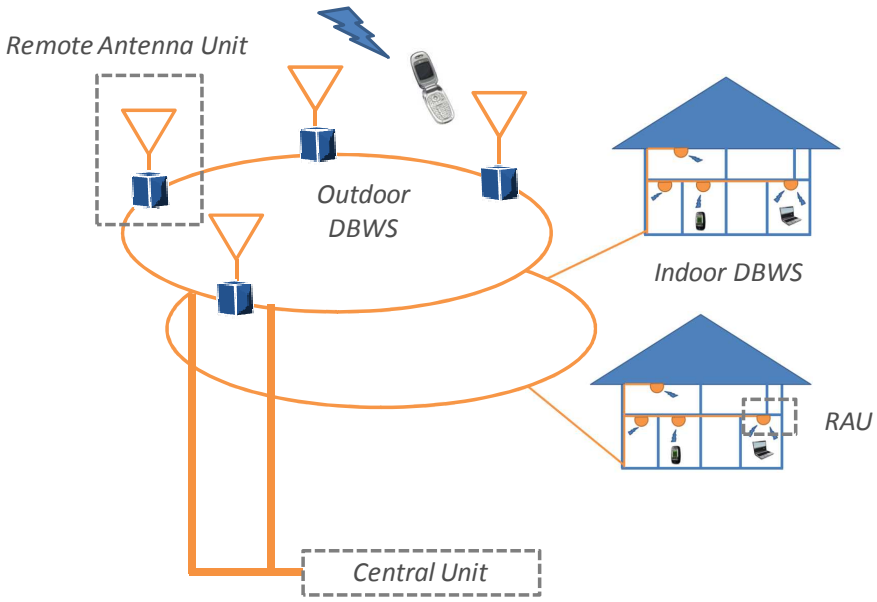

Figure 6-9 – Architecture and solution for next generation indoor and outdoor Distributed Broadband Wireless Systems

The RAUs are linked to a Central Unit (CU), using a transparent optical fibre system, and are able to send/receive signals from various wireless systems. WDM is used in order to provide a high network capacity with relatively low cost by allocating one wavelength per RAU. RSOAs are ideal devices for low-cost uplink configurations. They replace potentially WDM sources at the RAUs such as directly modulated lasers (DML) and high-speed external modulators with CW lasers. Due to their broad-bandwidth characteristics, the same devices can be used over a wide range of wavelengths, therefore they allow the realization of a colourless R-o-F network with the possibility of a dynamic wavelength allocation, which will reduce the deployment cost. The radio channels can be carried using subcarrier multiplexing (SCM), where the channels are frequency

translated to intermediate frequencies (IF). This limits the transmission requirements to lower frequencies. This architecture enables the high bit rates targeted in the broadband component of future wireless systems and provides a framework for the integration of heterogeneous wireless systems. In order to study the behaviour of a RAU based on a RSOA, an experimental setup represented in Figure 6-10 is implemented. This experimental set-up was realized with the collaboration of IT (Instituto de Telecomunicações) in Aveiro.

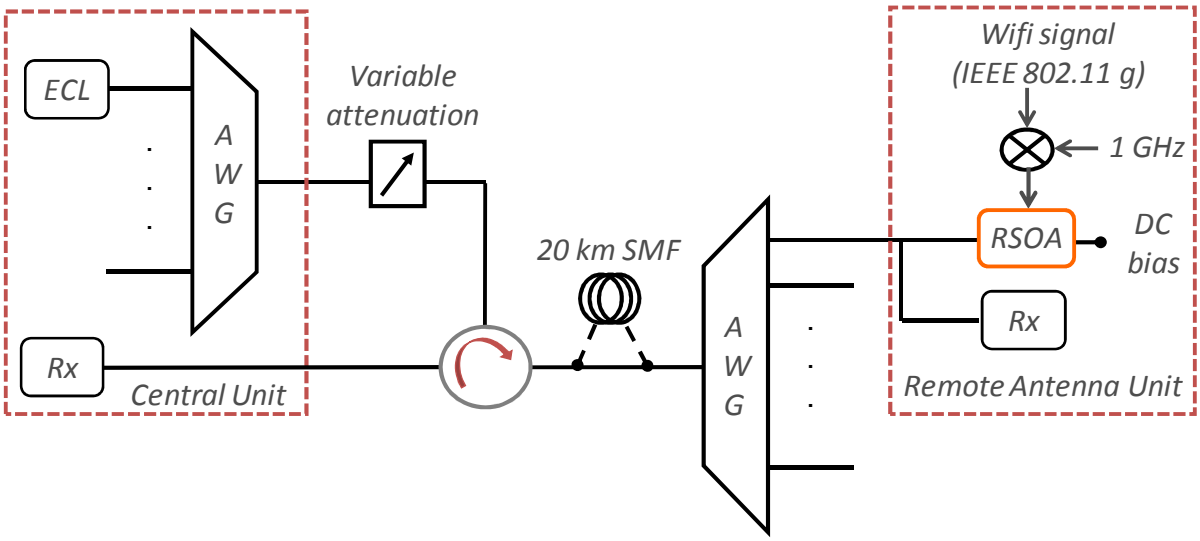

Figure 6-10 – Set-up for uplink signal based on RSOA device

It consists of an optical network which uses an AWG to separate the wavelengths assigned to particular RAUs. A vector signal generator (SMU 200A) provides the standard Wi-Fi signal (IEEE 802.11g) with a 64-QAM modulation format at an IF frequency of 1 GHz, which modulates the RSOA through a linear radio frequency (RF) power amplifier. An ECL is used to launch the required wavelength into the system and an optical attenuator is used to set the CW output power. The CW signal passes through an OC and can be coupled into a 20 km long SMF. It reaches a wavelength demultiplexer which selects the required wavelength. This wavelength is sent to the RAUs. The receiver is composed of a photodiode and a low-noise Mini-circuits amplifier connected to the vector signal analyzer.

6.2.2 RIN, Spur-free dynamic range and EVM measurements (RSOA characteristics for R-o-F link)

Within the bandwidth of the link, the contribution of noise from the various components must also be considered. Low noise levels should be obtained at the transmitter. A low optical confinement improves the noise factor by reducing carrier depletion due to the ASE compared to large optical confinement. However, the noise level also depends on the input power. The Relative Intensity Noise (RIN) is given by [34]:

$$[RIN_{RSOA}]_{dB} = -156 + \left(\frac{1}{G_{opt}} + 2 \times \left(\frac{\gamma_{ASE}}{(G_{opt} - 1) \times h\nu}\right)\right) - P_{in\ opt}$$

6-1

Where G_{opt} is the fibre-to-fibre gain, γ_{ASE} the noise spectral density, h the Planck constant, ν the photon frequency and $P_{in.opt}$ the input optical power.

Figure 6-11-(a) shows the RIN level of an optimized RSOA at different input powers. The noise level is reduced at high input optical power. In fact, at high input power, most of the carriers are consumed by the stimulated emission at the signal wavelength which means less ASE is produced and the noise level decreases. Because the noise properties are mainly governed by the ASE, it is important to reduce its influence. Optimized optical confinement reduces the influence of the ASE inside the device. A comparison of Relative Intensity Noise of two RSOA devices with 80% and 20% of optical confinement is presented in Figure 6-11-(b). As we can see, the RIN level is reduced at low optical confinement, which seems consistent with equation (6-1) (RIN is proportional to the amount of ASE and to the inverse of the gain). As we demonstrated in chapter 3, higher gain values are obtained with 20% optical confinement RSOAs compared to 80 % optical confinement RSOAs (10 dB higher). Low RIN levels are obtained, as low as -145 dB/Hz, which can be compared with high-performance DFB lasers. Due to the relatively low gain of high optical confinement RSOAs, noisier measurements are obtained.

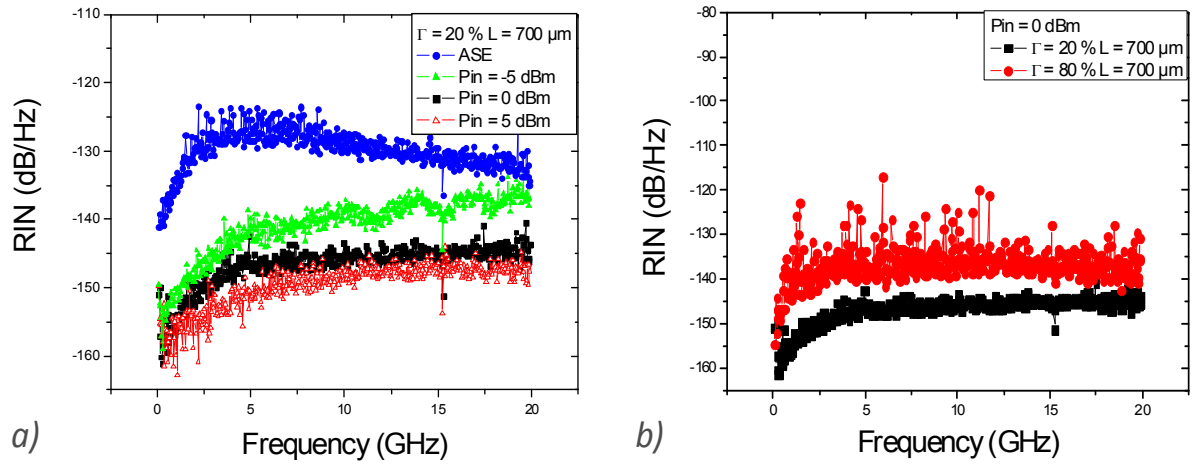

Figure 6-11 – RIN level (a) on optimized RSOA at different input power and (b) comparison of high and low optical confinement RSOA at an input power of 0dBm

While the noise floor (NF) determines the minimum RF signal detectable for a given link, non-linearities in lasers and amplifiers tend to limit the maximum RF signal that can be transmitted. The most straightforward limitation on the power of the input signal is the 1dB compression point, P1dB. For links transmitting a large number of signals, the third-order intercept point is frequently used to determine spur-free dynamic range (SFDR) [35]. Non-linearities distort the output and cause higher-order inter-modulation signals. In this section, we investigate how optimized RSOAs can fulfil the requirements of R-o-F systems. The linearity of the RSOAs has been measured using a two-tone inter-modulation setup (Figure 6-12).

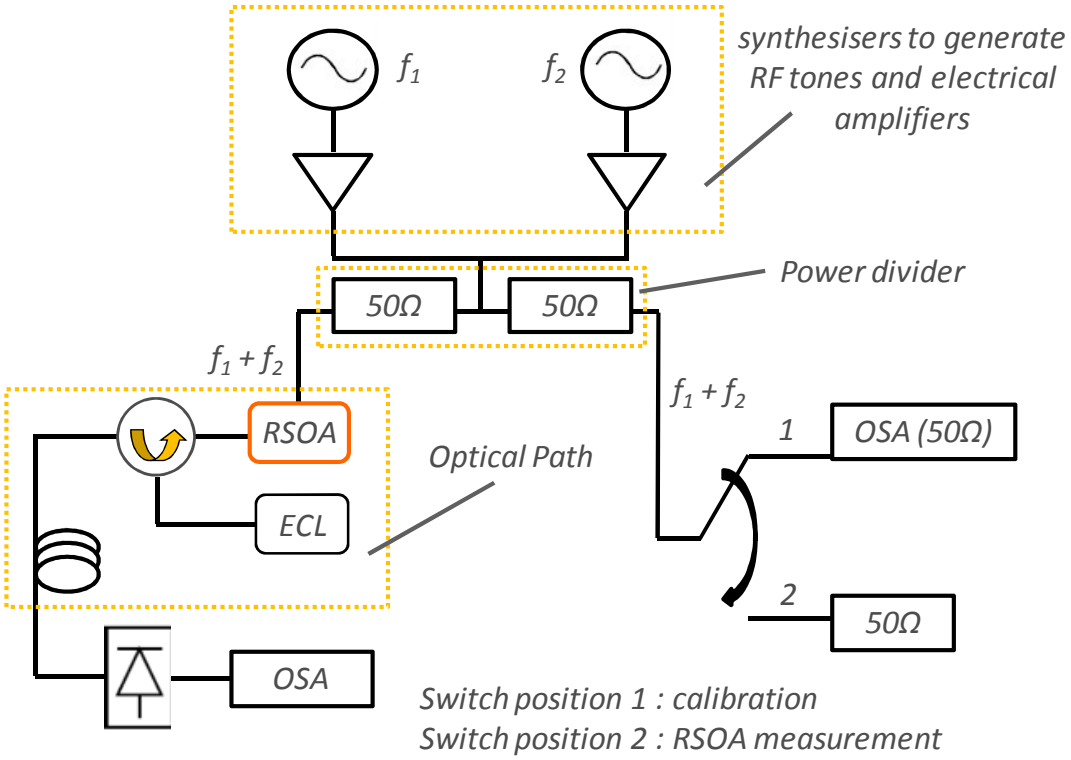

Figure 6-12 – Experimental set-up for two RF tones measurements on RSOA devices

Linearity measurements are performed on a 700 μm RSOA with low optical confinement. The optical input power is set to be –7 dBm with a DC bias current of 80 mA. We use two synthesisers to generate two RF tones separated by 100 MHz. Both frequencies are combined using a power divider and sent to the RSOA device. An ECL is used to launch the optical signal into the RSOA via an OC. The output power is measured both for the fundamental tones (at frequencies F_1 and F_2) and for the third-order products (at frequencies $2F_1$-F_2 and $2F_2$-F_1) by increasing the amplitude of the total input power. F_1 is 0.95 GHz and F_2 is 1.05 GHz. The measured output power includes insertion losses associated with the photodiode. An intermodulation distortion point (IMD3) from the third harmonic of 23 dBm can thus be measured (Figure 6-13-(a)). The RSOA input compression point was measured to be 14 dBm. This system can provide both a higher SFDR (92dB) and a lower NF (8 dB) than a conventional RSOA link (SFDR ~76 dB) [36]. The SFDR depends on the non-linearities and the noise floor of the devices. A low optical confinement reduces the interaction between photons and electrons which also reduces the non-linearity. As a consequence of the noise floor and non-linearity reduction, optimized RSOAs have higher SFDR.

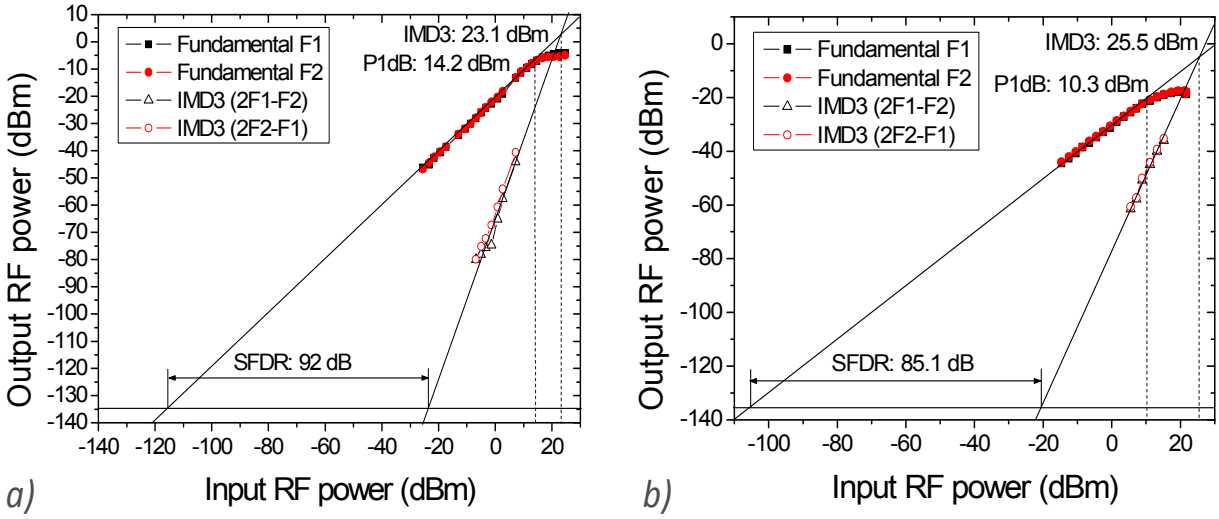

Figure 6-13 – Compression point (P1dB) and third order interception point measurement (IMD3) of low optical confinement RSOA at 1 GHz and at 2 GHz

The architecture should be based on the FUTON design as well as the frequencies values. RSOAs are located at the remote antenna unit (RAU) and the higher frequency which can be used is 0.9 GHz. However in order to evaluate the impact of higher frequency, two-tone inter-modulation measurements are performed at 2 GHz. Figure 6-13-(b) shows the linearity performances of the optimized RSOA at –7 dBm with a DC bias current of 80 mA. The SFDR dependence on input optical power and bias current has been evaluated at 2 GHz. The first set of measurements is realized at various bias currents (80, 100, 150 and 200 mA) without any optical injection. The second evaluation is done using 80 mA of bias current and different input optical powers (-10, -7 and 0 dBm). All results are summarized in the following tables:

Bias current (mA)	P1dB (dBm)	IMD3 (dBm)	SFDR (dB)
80	7.8	23.1	82.2
100	10.2	24.4	80.6
150	15.1	28.7	79.8
200	17.4	33	80.7

Table 6-1 – R-o-F RSOA parameters at several bias currents

The compression point and the third order interception point increase by increasing the bias current. However due to the augmentation of the noise floor (due to an increase of the RIN level), the SFDR remains constant.

Input optical power (dBm)	P1dB (dBm)	IMD3 (dBm)	SFDR (dB)
-10	10.1	20.3	81.9
-7	10.3	25.5	85.1
0	11	26.3	91

Table 6-2 – R-o-F RSOA parameters at various input optical power

By injecting more optical power, we can reduce the NF (due to the RIN reduction). We also increase the IMD3 point. The combination of these two factors leads to a better SFDR at high input optical power. Because of the FUTON requirements, the system evaluation through the Error-Vector Magnitude (EVM) measurements is performed at 1 GHz. The same RSOA is used in the experimental setup shown in Figure 6-10. The RSOA is driven at 80 mA DC current and standard IEEE 802.11Wi-Fi signal with a 64-QAM modulation format at a bit rate of 54 Mbit/s. CW input optical powers of –14 dBm and –7 dBm are used. In Figure 6-14, EVM measurements are presented at 1530 nm and a subcarrier frequency of 1 GHz as a function of the input electrical power in a Back-to-Back configuration. EVM measurements show the feasibility of this configuration using RSOAs and confirm the linearity measurements that were shown previously. Due to a large compression point value and a low noise level for the RSOA with 20% optical confinement, a wide range of input RF powers (from –23.8 dBm to 13.2 dBm) is compatible with EVM values lower than 5% for an input optical power of 0 dBm. This range is much larger for the 20% RSOA (37dB) than the 80% RSOA (from –17.2 dBm to 8.4 dBm: 25.6 dB).

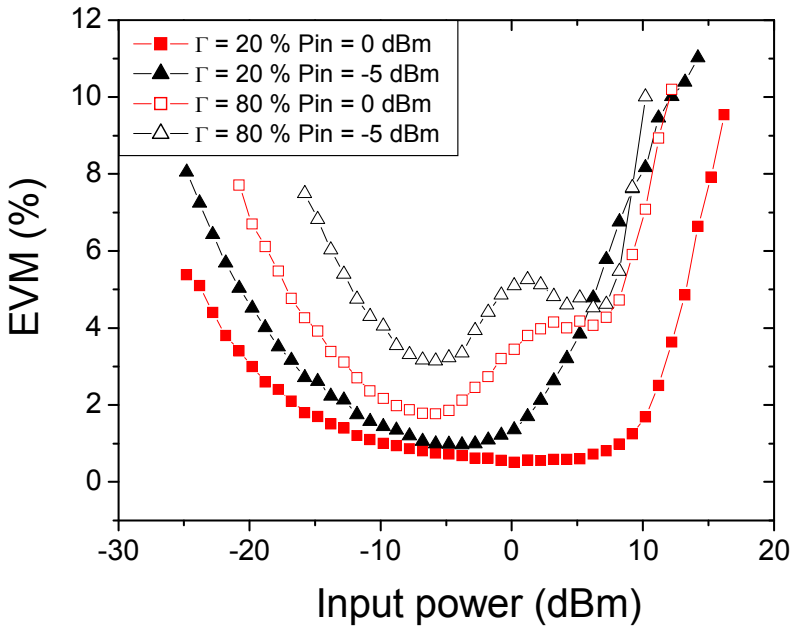

Figure 6-14 – EVM values as a function of electrical input RF power in b-t-b configuration

As it is pictured in Figure 6-10, the upstream signal propagates from the RAU into an AWG where all wavelengths can be multiplexed and launched to a 20 km long SMF. The same RSOA device with an optical confinement of 20% is used in the previous experimental conditions. EVM measurements after propagation on 20 km of SMF are presented in Figure 6-15 at an input optical power P_{in} = -10dBm (a) and -5 dBm (b). For an optical input power of – 5 dBm and a DC current of 90 mA, the insertion of SMF affects the minimum EVM values, which increase from 1% to 2.5%. Besides, the range of input powers which leads to EVM values lower than 4 % (we cannot consider 5% here due to the limited measurements) is reduced from 31 dB to 27 dB respectively for a current of 90 mA to 120mA. However at 60 mA, the input power dynamic range is smaller. In fact, a high current will induce larger noise but decreased non-linearity. A trade-off has to be considered in order to find an optimum point. The input optical power also strongly affects the EVM measurements. In either the b-t-b configuration or after 20 km of SMF, low EVM values are obtained over a large range of electrical input power when a high optical input power is launched to the device. When the RSOA becomes saturated, the ASE is strongly reduced, which leads to a reduction of EVM values. Thereby the input power range becomes larger. As for the bias current, an optimum value needs to be found depending on the trade off between noise and gain.

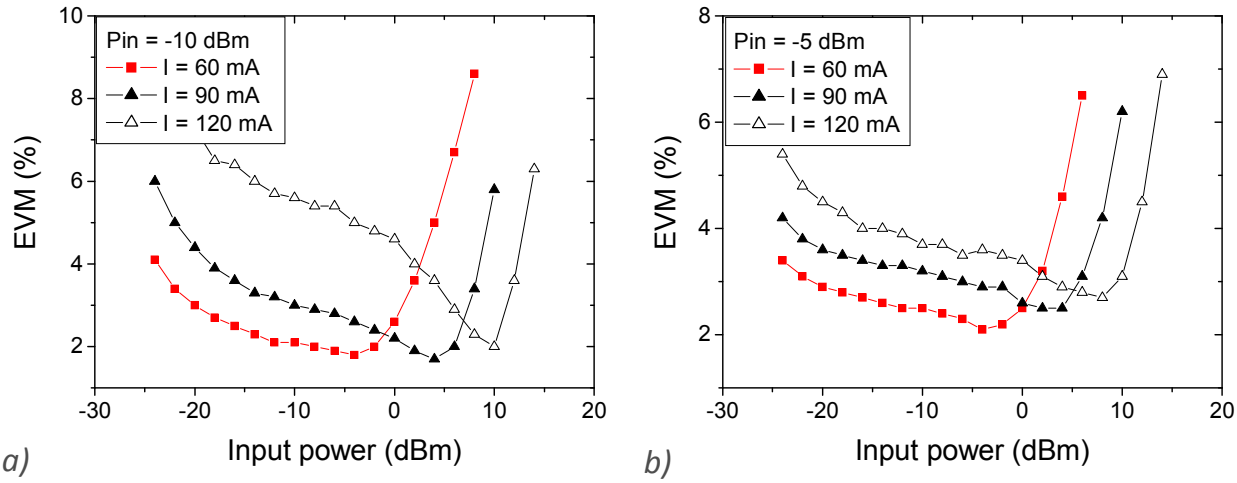

Figure 6-15 – EVM values as a function of electrical input RF power over a 20 km SMF using Γ = 20% RSOA at an input optical power of -10dBm (a) and -5dBm (b)

RSOA devices have been analyzed as remote modulators in R-o-F links. Simulations have been carried out in order to find the best internal RSOA parameters such as the length and optical confinement, which lead to some design rules. This analysis is confirmed experimentally by low RIN values and high linearity performance of the devices. New devices with lower confinement (20%) have been fabricated and compared to previous devices with higher optical confinement (80%). From a practical point of view, optimized RSOAs operating under saturation conditions (between -10 dBm and 0 dBm) give minimal degradation (compared to previous generation) when inserted into a radio over fibre link. The wireless range is typically limited by the uplink direction and can be evaluated depending of the link type [37].

Parameters @I=90MA and Pin = -5dBm	Classic RSOA	Optimized RSOA
RF gain, dB	-40.8	-40.8
Output noise power, dBm/Hz	-161	-168
Radio range, m	379.2	445.5

Table 6-3 – R-o-F link parameters and estimated wireless range

For the case where we consider radio signals with a channel width of 100 MHz, a modulation complexity of 256-QAM and free space propagation, the baseline wireless range (no optical link) is approximately 480m. By calculating the sensitivity and the path loss from Table 6-3, the wireless range can be estimated to approximately 379 m for the old RSOA generation and 446 m for the new generation. All details and a comparison using various link types can be found in [38]. It is clear that the new RSOA device has a limited impact on the wireless range for this type of wireless system. We have demonstrated that the use of an optimized RSOA device in a radio link drastically improves the performance compared to previous RSOA generations. According to the device characteristics, the RSOA can be used in a cost-effective R-o-Fibre network that can be extended to a WDM architecture which takes advantage of the large optical bandwidth of this device. The large electro-optic bandwidth of the RSOA as well as its high linearity has permitted high performance RF transmission over a fibre span of 20 km, which is confirmed by EVM measurements. Given the high 1dB compression point and the low noise level, the RSOA is a promising candidate compared to "coloured" devices. This upstream colourless result shows important advantages in the generation and management of wavelength allocation for the next generation of R-o-F Networks.

6.2.3 Radio range extension based on 2-section RSOA

We demonstrated low noise and high linearity devices using optimized RSOA structures. However it has been demonstrated that DMLs show higher radio range [38] than RSOAs. It is partially due to the high link gain of the laser then RSOA link gain need to be optimized.

6.2.3.1 Experimental set-up

The experiment setup for characterizing the RSOA devices is shown Figure 6-16. In partnership with the University of Kent, this set-up was realized in Kent in the frame of the FUTON project.

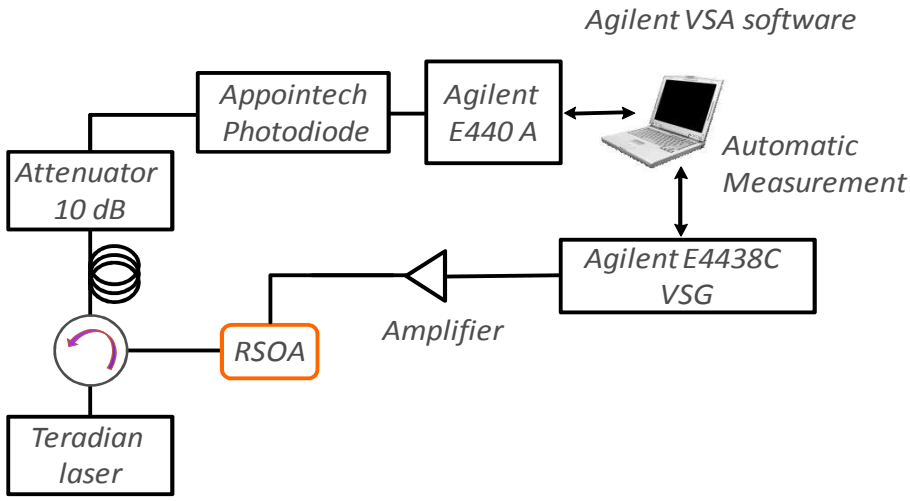

Figure 6-16 – experimental set up for R-o-F transmission using RSOA device

An optical power of -6.5 dBm is launched into the device through an optical circulator (OC). The RSOA (1-section) device is biased at various input currents (70, 90 and 120 mA). A 10dB optical attenuator was included in the optical link to reproduce losses such as wavelength multiplexing in radio over fibre systems.

6.2.3.2 Optical link gain and EVM measurements

The link gain is measured at the different bias currents and it is represented in

Figure 6-17. Frequencies of 0.3 GHz and 0.9 GHz are used in order to investigate the lower and upper limits of the RAU transmission frequencies (defined in the FUTON project). The effect of the transmission frequency can be neglected; therefore we will focus on 0.3 GHz. The link gain is around -41 dB which confirms the theoretical analysis presented in section 5.2.1 (G_{hyp} = -40.36 dB when considering an efficiency η_{RSOA} = 0.08 W/A). At the end of the optical link, an Appointech photodiode is placed for optical to electrical conversion. It can be noticed that the link gain remains constant when varying the bias current and the frequency. In fact, the efficiency peak (as explained in Chapter 5) is wide and small changes of the efficiency do not affect the link gain.

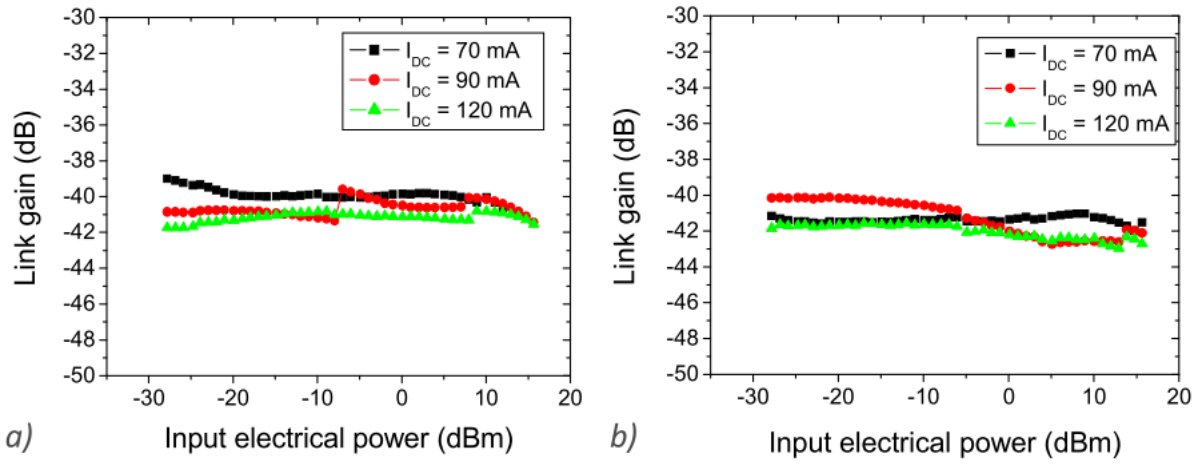

Figure 6-17 – Link gain measurements for 1-section RSOA at 0.3GHz (a) and at 0.9GHz (b)

Link gain measurements have been performed using 2-section RSOA and they confirm the strong dependence on the bias current.

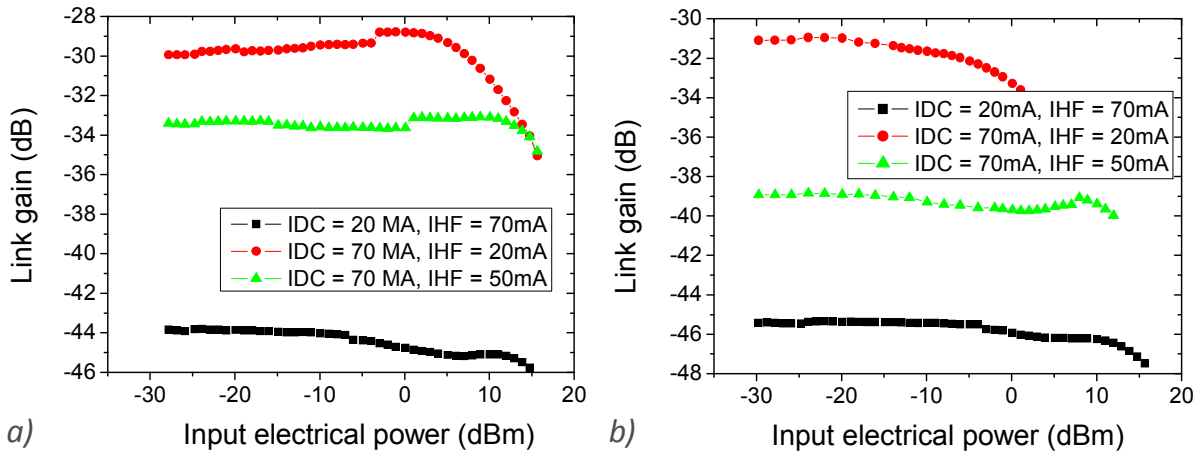

Figure 6-18 – Link gain measurements for 2-section RSOA by modulating SOA1 (a) and SOA2 (b) at 0.3GHz

An Agilent VSA (spectrum analyzer with a VSA software) measured the EVM of the 802.11n Wi-Fi signal exciting the Appointech photodiode. An automatic measurement software was used to vary the RF power launched into the RSOA and to measure the EVM at the photodiode. Every tested RSOA was receiving light from the same laser source at a wavelength of 1550nm with an optical power of -6.5dBm. EVM measurements show the feasibility of this configuration using 1-section and 2-section RSOAs. EVM values lower than 4% (IEEE 802.11n EVM transmitter limit) were obtained using 1-section RSOA and presented in Figure 6-19.

Different bias currents were studied at 70mA, 90mA and 120mA. Figure 6-19 shows that the linearity of 1-section RSOA increases by increasing the I_{DC} current. The powers at the 4% EVM limit are 7dBm, 10.15dBm and 12.4dBm for I_{DC} currents of 70mA, 90mA and 120mA respectively. Figure 6-19 also shows that, at the lower power levels (-30dBm to -10dBm), the EVM performance is degraded by increasing I_{DC} currents. Thus, the 1-section RSOA noise worsens with increasing I_{DC} currents. As ASE is usually predominant in an SOA, it is necessary to consider broadband photons and not only those at the amplified signal wavelength. At high input bias current, the ASE becomes even more dominant which increases the RIN. More details can be found in [39]. Therefore an optimum bias current is found and a trade-off between large noise values and high non-linearity needs to be considered.

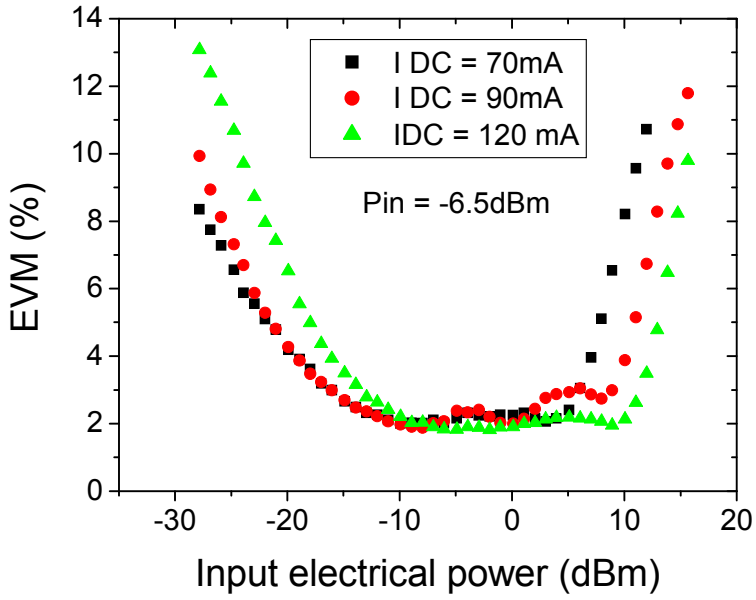

Figure 6-19 – EVM measurements for 1-section RSOA at 0.3GHz

2-section RSOAs are used in the same experimental conditions as previously. The two different modulation conditions (modulation of SOA1 and SOA2) are described in Chapter 5 and investigated under various current injections.

When modulating SOA1 (Figure 6-20-(a)) under high bias current (I_{HF} = 70mA) and low DC current injection (I_{DC} = 20mA), non-linearities are reduced. This setup results in a maximum input electrical power (for EVM < 4%) of 11 dBm. However, in this configuration, the noise level is very high (-11.1 dBm for EVM < 4%) and limits the range of input power to 22.1 dB. This high noise level limitation can be overcome by applying a high input DC current (70mA). The bias current of the modulated electrode also needs to be increased (from I_{HF}= 20mA to 50mA) in order to maintain a linearity as close as possible to the configuration with the high bias current (I_{HF} = 70mA). The input electrical power range for EVM below 4% is improved from 24.6 dB (-22.9 dBm to 1.7 dBm) to 30.2 dB (-20.6 dBm to 9.7 dBm).

Under optimal operating conditions, the device should achieve low noise level (high DC current), high non-linearity (high I_{HF} current) while keeping high link gain. Control rules to operate the device under its best performances can be derived from the optimal configuration found.

The same approach is studied when modulating the mirror electrode (SOA2: Figure 6-20-(b)). The same conclusions are verified; however non-linearity is more crucial in this configuration. This leads to smaller input electrical power range below 4 % EVM (21.7 dB, 21.7 dB and 24.8 dB for I_{DC} = 70mA/I_{HF} = 20mA, I_{DC} = 70mA/I_{HF} = 50mA and I_{DC} = 20mA/I_{HF} = 70mA, respectively). In spite of the low RF power range of the SOA configuration, it is still suitable for R-o-F links where the mobile equipment has transmit power control.

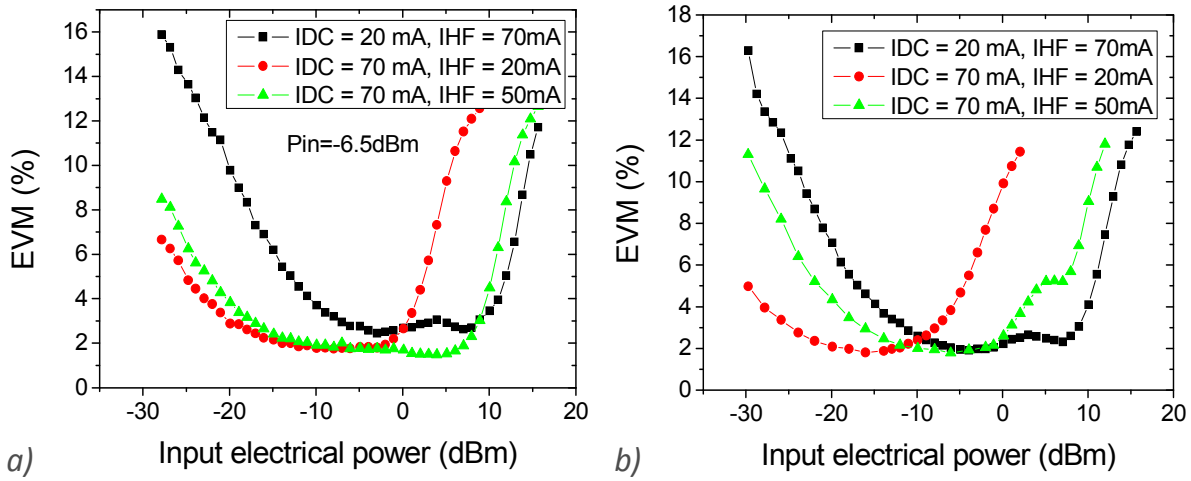

Figure 6-20 – EVM measurements for 2-section RSOA (a) by modulating SOA1 and (b) by modulating SOA2 at 0.3GHz

Using a 2-section RSOA with proper bias current configuration, an improvement of 1.2 dB on the input power range can be obtained compared to 1-section RSOA (Figure 6-19). These new devices allow obtaining low noise level and high link gain while keeping a good linearity.

6.2.3.3 Radio range calculation

These parameters are essential to the radio range calculation. The uplink direction usually limits the distance between the RAU and the mobile terminal. Therefore it is important to determine the maximum possible distance (radio range) based on the R-o-F link type. This colourless source allows a flexible architecture and a simple RAU which is an important aim for all R-o-F links. We measured different R-o-F parameters as the link gain and EVM values. In this section, we extracted from the previous measurements, the maximum input electrical power at EVM = 4% and the average link gain for 1-section and 2-section RSOA. The radio range can be calculated from the maximum path loss using a path loss exponent of 2.0 (FUTON open space approach). The noise factor can be calculated from the RIN measurements, then the overall noise figure is obtained [40]. The receiver sensitivity can be evaluated and determine the radio range as well as the maximum path loss. All calculation details can be found in [38]. The main parameters for the radio range calculation are summarized in Table 6-4 and Table 6-5.

1-section RSOA	I = 70 mA	I = 90 mA	I = 120 mA
Output noise power per Hz, dBm/Hz	**-167.2**	**-163.4**	**-160.1**
Max. i/p power (at 4% EVM), dBm	**7**	**10.1**	**12.5**
RF gain (no amp), dB	**-39.9**	**-40.7**	**-41.2**
Maximum radio range, m	**440.4**	**435,3**	**425.4**

Table 6-4 – Radio range and intermediate parameters for 1-Section RSOA

2-section RSOA, Conf. SOA 1	I_{DC}=20mA, I_{HF}=70mA	I_{DC}=70mA, I_{HF}=20mA	I_{DC}=70mA, I_{HF}=50mA
Output noise power per Hz, dBm/Hz	-169.6	-168.2	-169.1
Max. i/p power (at 4% EVM), dBm	11	1.9	9.7
RF gain (no amp), dB	-44	-29.6	-33.4
Maximum radio range, m	450.7	471.9	477.4

a)

2-section RSOA, Conf. SOA 2	I_{DC}=20mA, I_{HF}=70mA	I_{DC}=70mA, I_{HF}=20mA	I_{DC}=70mA, I_{HF}=50mA
Output noise power per Hz, dBm/Hz	-166.3	-164.7	-166
Max. i/p power (at 4% EVM), dBm	10	-5.8	3.6
RF gain (no amp), dB	-45.6	-31.4	-39.3
Maximum radio range, m	401.6	358	401.6

b)

Table 6-5 – Radio range and intermediate parameters for 2-Section RSOA (a) configuration 1 (b) configuration 2

It is common to plot the radio range depending on the link noise in order to compare R-o-F link performances as in Figure 6-21. In the FUTON project, RAUs are spaced around 500 m apart, therefore the target radio range is around 300 m. Some coverage overlap at the cell edges is obtained assuming the Manhattan-style grid. RSOA devices meet this requirement in all configurations. However a higher radio range cuts the deployment cost by reducing the number of RAU. It has been demonstrated that the radio range of a Directly Modulated laser is around 460 m [38]. One-electrode RSOA device shows lower performances with a maximum radio range of 440 m. This drawback can be overcome by using 2-section devices in the SOA1 configuration. The combination of a high link gain, high input electrical power and a low noise level from 2-section RSOAs gives a radio range of 477.4 m which is well above state-of-this-art values [41].

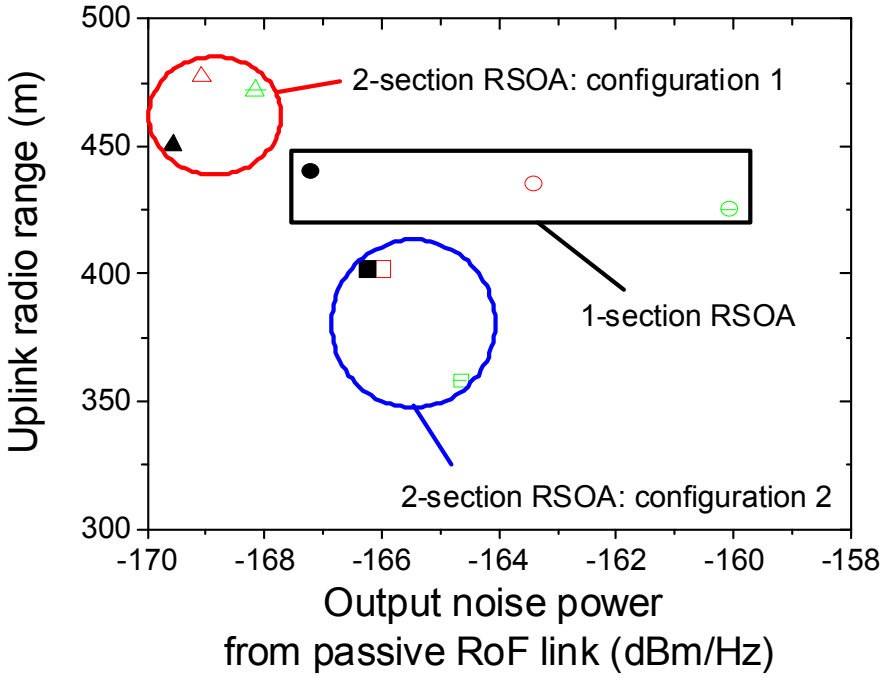

Figure 6-21 – Radio range depending on the RSOA configurations as a function of link output noise

Nonetheless this 2-section RSOA needs to be used in specific conditions. 2-section RSOAs in configuration SOA2 exhibit a maximum radio range around 402 m. We demonstrated that a 2-section RSOA can be used in order to increase the link gain in R-o-F link. As demonstrated in Chapter 5, it is caused by an increase of the internal efficiency due to higher photon density into the device. The second section is used as an extra amplifier to boost the optical power signal. An optimum configuration is found to be a modulation of the input electrode (SOA1) with specific bias current. EVM measurements confirm the good behaviour of the devices. The 2-section RSOA shows an improvement on the input electrical power range due to the high linearity and low RIN level. These suited features combined with the link gain improvement provide a wireless range estimated to 472 m. The radio range is improved from 1-section RSOA by 30 m and is higher than typical DML wireless range (460 m). This result places the RSOA as a favourite candidate for Re-configurable R-o-F system based on WDM technology allowing flexibility, performance and low cost deployment.

6.3 Conclusions

Earlier chapters have provided an overview of RSOA device from a theoretical and experimental point of view. Recent advances in RSOAs have been described including structure design, dynamic optimization and multi-section approach. This chapter was dedicated to describing some major applications of RSOA. Fibre amplifiers have become a key device of almost all fibre-optic communication systems, whereas SOA are still searching for a possible application. Modern WDM lightwave systems use a large number of channels (different wavelengths). The next generation of optical networks want to use the advantage of WDM technology all the way to the enterprises and homes. New potential use of RSOA as colourless transmitter boosts the interest and research into these devices. Different configurations exploit the reflective behaviour and large optical bandwidth of these components as detailed in section 6.1.1.

We focused on the laser seeding approach and we demonstrated a 36 dB of optical budget over 8 WDM channels at 2.5 Gbit/s. The high optical budget allows the insertion of a power splitter (12 dB = 16 clients) for TDM connections. FEC is included in the standard for the next generation of optical access network, therefore considering BER = 10^{-4} long distance transmission over 100 Km have been obtained using low-chirp RSOA. The chirp is reduced as described in Chapter 5. The main challenge for RSOAs is to reach the 10 Gbit/s modulation without expensive solution (as with EDC) or increase of the power consumption (using passive filtering). The carrier lifetime reduction operated in Chapter 4 has been used to obtain BER below the FEC limit. However the transmission distance is still an issue.

Colourless transmitters are also considered for R-o-F systems as proposed in the FUTON project. In the section 6.2.1, the global architecture was explained as well as the experimental set-up to test the RSOA in this original configuration. High gain and low noise RSOA were demonstrated as ideal candidates for R-o-F applications and have shown large SFDR. An optical link of 20 km was demonstrated and EVM values below 4 % were obtained. All results lead to a large radio range around 440 m even if the radio range was still limited by the link gain of the device. Chapter 5 demonstrates an increase of the link gain using a 2-section RSOAs. Therefore the radio range limit was overcome based on the previous analysis and leads to performances similar to DML.

In this chapter, RSOA is considered as a low cost solution for upstream signal production in converged network architecture and could lead to the next generation of transmitter.

References

[1] F. T. An, D. Gutierrez, K. S. Kim, J. W. Lee, and L. G. Kazovsky, "SUCCESS-HPON: A next generation optical access architecture for smooth migration from TDM-PON to WDM-PON," IEEE Commun. Mag., Vol. 43, No. 11, Nov. 2005, pp. S40–S47

[2] F. Lelarge, N. Chimot, B. Rousseau, F. Martin, R. Brenot and A. Accard, "Chirp Optimization Of 1550 nm InAs/InP Quantum Dash Based Directly Modulated Lasers For 10Gb/s SMF Transmission Up To 65Km" in proc. IPRM, May-June, 2010, pp. 1-3, Kagawa, Japan

[3] G. de Valicourt, D. Make, M. Lamponi, G. Duan, P. Chanclou and R. Brenot, "High Gain (30 dB) and High Saturation Power (11dBm) RSOA Devices as Colourless ONU Sources in Long Reach Hybrid WDM/TDM -PON Architecture", Photonics technology letters, Vol. 22, No. 3, Feb. 2010, pp. 191-193

[4] J. Campany, D. Novak, "Microwave photonics combine two worlds", Nature Photonics, Vol. 1, June 2007, pp. 319-330

[5] M. C. R. Medeiros et al., "Radio over fiber access network architecture employing reflective semiconductor optical amplifiers", in proc. ICTON-MW, Sa2.1, 2007, pp. 1-5, Sousse, Tunisia

[6] F.T An, K. Soo Kim, D. Gutierrez, S. Yam, E. Hu, K. Shrikhande and L.G. Kazovsky,"SUCCESS: A Next-Generation Hybrid WDM/TDM Optical Access Network Architecture", J. Lightwave Technol., Vol. 22, No. 11, November 2004

[7] D. Shin, D. Jung, H. Shin, J. Kwon, S. Hwang, Y. Oh, and C. Shim, "Hybrid WDM/TDM-PON for 128 subscribers using λ-selection-free transmitters", in Proc. OFC, PDP4, 2004, Los Angeles, USA

[8] S-K. Liaw, S-L. Tzeng and Y-J. Hung, "Power penalty induced by Rayleigh backscattering in a bidirectionalwavelength-reuse lightwave system", in Proc. CLEO, 2001, pp.475-476, Baltimore, USA

[9] H-H. Lee, S-H. Cho, J-H. Lee, E-S. Jung, J-H. Yu, B-W. Kim, S-S. Lee, S-H. Lee, J-S. Koh, B-H Sung, S-J. Kang, J-H. Kim, and K-T. Jeong, "First Commercial Service of a Colorless Gigabit WDM/TDM Hybrid PON System", in Proc. OFC, PDPD9, 2009, San Diego, USA

[10] P. Chanclou, F. Payoux, T. Soret, N. Genay, R. Brenot, F. Blache, M. Goix, J. Landreau, O. Legouezigou, F. Mallécot, "Demonstration of RSOA-based remote modulation at 2.5 and 5 Gbit/s for WDM PON", in Proc. OFC, OWD1, 2007, Anaheim, USA

[11] G. De Valicourt, D. Maké, J. Landreau, M. Lamponi, G.H. Duan, P. Chanclou and R. Brenot, "New RSOA Devices for Extended Reach and High Capacity Hybrid TDM/WDM -PON Networks", in Proc. ECOC'09, P9.5.2, 2009, Vienna, Austria

[12] P. Healey, P. Townsend, C. Ford, L. Johnston, P. Townley, I. Lealman, L. Rivers, S. Perrin and R. Moore, "Spectral slicing WDM-PON using wavelength-seeded reflective SOAs", Electron. Lett., Vol. 37, No. 19, Sept. 2001, pp. 1181 - 1182

[13] T-Y. Kim and S-K. Han, "Reflective SOA-Based Bidirectional WDM-PON Sharing Optical Source for Up/Downlink Data and Broadcasting Transmission", Photonics technology letters, Vol. 18, No. 22, Nov. 2006, pp. 2350-2352

[14] W. R. Lee, M. Y. Park, S. H. Cho, J. H. Lee, C. Y. Kim, G. Jeong, and B. W. Kim, "Bidirectional WDM-PON based on gain-saturated reflective semiconductor optical amplifiers", Photonics technology letters, Vol. 17, No. 11, Nov. 2005, pp. 2460–2462

[15] M. Presi and E. Ciaramella, "Stable self-seeding of R-SOAs for WDM-PONs", in proc. OFC, OMP4, March 2011, Los Angeles, USA

[16] L. Marazzi, P. Parolari, G. de Valicourt and M. Martinelli**,** "Network-Embedded Self-Tuning Cavity for WDM-PON Transmitter", in proc. ECOC, Mo.2.C.3, Sept. 2011, Geneva, Switzerland

[17] Quang Trung Le, Qian Deniel, Fabienne Saliou, guilhem de Valicourt, Romain Brenot and Philippe Chanclou, RSOA-based External Cavity Laser as Cost-effective Upstream Transmitter for WDM Passive Optical Network, CLEO 2011, JWA9, May 1-6, 2011, Baltimore, USA

[18] J. Oh, S. G. Koo, D. Lee and S-J. Park, "Enhanced System Performance of an RSOA Based Hybrid WDM/TDM-PON System Using a remotely Pumped Erbium-Doped Fiber Amplifier", in Proc. OFC, PDP9, 2007, Anaheim, USA

[19] J. Oh, S. G. Koo, D. Lee and S-J. Park, "Enhancement of the Performance of an Reflective SOA-Based Hybrid WDM/TDM PON System With a remotely Pumped Erbium-Doped Fiber Amplifier", J. Lightwave Technol., Vol. 26, No. 1, Jan. 2008, pp. 144-149

[20] E. Berglind, "Linewidth of an externally modulated laser subjected to Rayleighbackscattering from a fiber", Photonics Technology Letters, Vol. 2, No. 4, Apr 1990, pp. 239-241

[21] P. J. Urban, A. M. J. Koonen, G. D. Khoe, H. de Waardt, "Rayleigh Backscatterring-suppression in WDM Access Network employing a Reflective Semiconductor Optical Amplifier", in Proc. Symp. LEOS, S7, 2007, p147, Orlando, USA

[22] G. P. Agrawal, "Fiber-optic communication systems", Third Edition, John Wiley & Sons Inc., Chap. 2, 2002, pp. 50-53

[23] D. Torrientes et al, "RSOA-Based 10.3 Gbit/s WDM-PON with Pre-Amplification and Electronic Equalization", in proc. OFC, JThA28, 2010, San Diego, USA
[24] T. Duong, N. Genay, P. Chanclou, B. Charbonnier, A. Pizzinat, and R. Brenot, "Experimental demonstration of 10 Gbit/s upstream transmission by remote modulation of 1 GHz RSOA using adaptively modulated optical OFDM for WDM-PON single fiber architecture," in Proc. ECOC, Th.3.F, Sep. 2008, Brussels, Belgium
[25] B. Schrenk et al, "Direct 10-Gb/s Modulation of a Single-Section RSOA in PONs With High Optical Budget", Photon. Technol. Letters, Vol. 22, No. 6, Mar. 2010, pp. 392-394
[26] R. Brenot et al, "High modulation bandwidth reflective SOA for optical access networks", in Proc. ECOC, 2007, pp. 1-2, Berlin, Germany
[27] H.S. Kim et al, "Improvement of modulation bandwidth in multisection RSOA for colorless WDM-PON", Optics Express, Vol. 17, No. 19, Aug. 2009, pp. 16372-16378
[28] K.Y. Cho et al, "10-Gb/s Operation of RSOA for WDM PON", Photon. Technol. Letters, Vol. 20, No. 18, Sept. 15, 2008, pp. 1533-1535
[29] European project ICT-FP7-FUTON description available online at http://www.ict-futon.eu
[30] X. Yu, T. B. Gibbon, I. T. Monroy, "Compact wireless access nodes for WDM bidirectional radio-over-fiber system based on RSOA", in Proc. OFC, OWP1, 2009, San Diego, USA
[31] R. Boula-Picard, M. Alouini, J. Lopez, N. Vodjdani and J-C. Simon, "Impact of the Gain Saturation Dynamics in Semiconductor Optical Amplifiers on the Characteristics of an Analog Optical Link", J. Lightwave Technol., Vol. 23, No.8, 2005, pp. 2420- 2426
[32] F. Vacondio, M.M. Sisto, W. Mathlouthi, L. A. Rusch, S. LaRochelle, "Electrical-to-optical conversion of OFDM 802.11g/a signals by direct current modulation of semiconductor optical amplifiers", in proc. MWP, F1.5, 2006, Grenoble, France
[33] G. Heliotis, I.P. Chochliouros, G. Agapiou, "Fibre Optic Networks for Distributed, Extendible Heterogeneous Radio Architectures and Service Provisioning: The Case of the FUTON programme", The Journal of The Institute of Telecommunications Professionals, Vol. 2, Part 3, 2008, pp.113-118
[34] R. Boula-picard, "Contribution à l'étude des amplificateurs optiques a semiconducteur pour les applications analogiques", PhD Thesis, Université de Rennes 1, Chap. 2, 2004, pp 126-130
[35] J. H. Seo, Y. K. Seo, and W. Y. Choi, "Spurious-Free Dynamic Range Characteristics of the Photonic Up-Converter Based on a Semiconductor Optical Amplifier", Photon. Technol. Letters, Vol. 15, No. 2003, pp. 1591-1593
[36] Y-Y. Won, H-C. Kwon and S-K. Han., "1.25-Gb/s Wavelength-Division Multiplexed single-wavelength colorless radio-on-fiber systems using reflective semiconductor optical amplifier", J. Lightwave Technol., Vol. 25, No. 11, 2007, pp. 3472-3478
[37] D. Wake, A. Nkansah, P. Assimakopolous, N. J. Gomes, M. Violas, Z. Liu, S. Pato, F. Ferreira, G. de Valicourt, R. Brenot and F. Van Dijk , "Design and Performance of Radio over Fibre Links for Next Generation Wireless Systems using Distributed Antennas", Future Network and Mobile Summit, 2010, pp. 1-9, Florence, Italy
[38] D. Wake, A. Nkansah, N. J. Gomes, G. de Valicourt, R. Brenot, M. Violas, Z. Liu, F. Ferreira and S. Pato, "A Comparison of Radio over Fiber Link Types for the Support of Wideband Radio Channels", J. Lightwave Technol., Vol. 28, No. 16, March 2010, pp. 2416-2422
[39] M. Le Ligne and S. Motter, "Theory of signal degradation in semiconductor lasers amplifiers in direct detection systems", J. Lightwave Technol., Vol. 10, No. 8, 1992, pp. 1071-1077
[40] H. Friis, "Noise figure of radio receivers ", in proc. IRE, Vol. 32, Jul. 1944, pp. 419-422
[41] G. de Valicourt, M. A. Violas, D. Wake, F. van Dijk, C. Ware, A. Enard, D. Maké, Zhansheng Liu, M. Lamponi, G. H. Duan and R. Brenot, "Radio over Fibre Access Network Architecture based on new optimized RSOA Devices with large modulation bandwidth and high linearity", Microwave Theory and Techniques, Vol. 58, No. 11, October 2010, pp 3248-3258

Conclusion

Nowadays, research in the telecom area is partly focused on converged network architecture. Mobile and fixed services drive the fusion of both networks as users need more and more bandwidth on the road and at home. WDM-PON seems to be a promising approach allowing high data bit rate and flexibility. WDM techniques used in long-haul systems are now mature, however the shift to local access networks is more challenging. New requirements appear such as cost reduction, the need for new key devices at the ONU and compatibility with the existing network. Colourless ONU are necessary to obtain cost effective architecture and RSOA is one potential solution. In this manuscript, we focused on these devices.

General conclusion

The SOA theory has been discussed and applied to Reflective SOA devices. The fundamental theory of SOA is described and explained. The theoretical analysis of the material gain leads to a good understanding of the optical amplification process. The net gain is calculated considering the RSOA structure (including cladding and active zone losses) and an approximation of the material gain. Gain medium inside an optical cavity is then described. This first approach allows us to identify the key parameters affecting the optical gain. However RSOAs exhibit a non-homogeneous carrier density profile which strongly affects the overall gain. Therefore the net gain needs to be carefully integrated along the device taking in account this non-homogeneity. All these results confirm the presence of key parameters such as the length, the optical confinement and the facet reflectivity which should lead to design rules.

The design of high performances RSOAs is then presented. The material composition, thickness and strain have to be carefully controlled in order to achieve polarization insensitive devices for a specific optical confinement. Buried ridge structure is used to provide efficient current injection and a good thermal dissipation. Spot-Size Converter based on a double core structure is used to enlarge the output optical mode thereby reducing the divergence and the reflectivity. The optical mode propagation is modelled along the structure. Far-field measurements confirm the increase of the optical mode size inside the passive region. Fabrication issues and their impacts on the coupling ratio in the tapered structure are discussed. RSOA processing steps are explained as well as the cleaving, bonding and mounting of the final chips. The RSOA fabrication method includes straightforward instructions from the wafer growth to the final chip. In order to suppress the resonant cavity to obtain low gain ripple, AR facet coating is needed. We discussed in details the different approaches to reduce the reflectivity such as facet coating, tilted waveguide and window facet structure. HR coating is also explained and modelled. RSOA optical feedback is crucial in these devices and needs to be completely understood. We developed an original theoretical approach (Appendix I) in order to calculate the facet reflectivity depending on the optical mode size. The model fits with the experimental values and shows the importance of a large optical mode in order to reduce the facet reflectivity in tilted waveguides.

After processing RSOA devices, their steady state behaviour is studied. We underline several physical mechanisms that are responsible for the carrier density stabilization. The stimulated, radiative and non-radiative recombination rates are described. Assuming an average contribution of the spontaneous emission, the rate-equation is explained. Forward and backward signal propagations are also considered. A model has been developed, taking into account several longitudinal sub-sections of the active guide. The carrier density is then computed in each section and this calculus enables us to plot the carrier density spatial distribution, which is non-homogenous along the device. The reflective behaviour of the RSOA strongly affects the carrier density spatial distribution due to the LSHB. At the input/output of the device, a strong saturation effect is observed. The good match between the simulated and measured values confirms the relevance of the model but it is limited to some operating conditions. As we understand the underlying physics of this device, we tackle the impact of the design on the static performance. Two optical confinements are evaluated.

A reasonably low optical confinement ($\Gamma \sim 20\%$) leads to higher gain than high optical confinement ($\Gamma \sim 80\%$) due to the reduction of the LSHB. Various RSOA lengths are evaluated and a length of 700 μm is found to be the optimum. An optical gain of 30 dB was measured however the gain is reduced when using longer devices. A method was proposed in order to evaluate the impact of the facet reflectivity. The reflectivity was measured depending on the waveguide tilt. The SSC and AR coating reflectivity were not measured due to spurious fabrication problems (internal reflectivity). Complementary investigations need to be done to complete our study.

To assess the RSOA dynamics, the carrier lifetime is estimated. The E/O modulation bandwidth mainly depends on this parameter, for instance shorter carrier lifetime induces larger 3 dB E/O modulation bandwidth. The reduction of the carrier lifetime is required to obtain high speed RSOAs. The preliminary approximation was proposed and we observed that the carrier lifetime is not homogenous along the device. We identified the two main mechanisms controlling these key characteristics: R(n), including the spontaneous and non-radiative recombination rates, and the stimulated recombination rate. Based on the model developed in Chapter 3, we first calculated the carrier lifetime and extracted the 3 dB modulation bandwidth. The simulations fit with the measurements results between 0 to 100 mA. An average carrier lifetime over the AZ length or the carrier lifetime at the input/output of the devices (where the saturation effect is stronger) has to be considered. As we demonstrated in chapter 3, a long RSOA induces high saturation effect therefore the carrier lifetime is reduced. As we take advantage of this effect, 850 μm long RSOA enables 3 GHz of E/O modulation bandwidth. Under large signal modulation (binary modulation), the analysis is more complex. The Auger recombination process is more or less dominant depending on the bias condition and strongly modifies the speed of the device. Decay times are observed and confirm the theoretical analysis. A simple dynamic model was proposed to explain this phenomenon. Faster transition between the "ON" and "OFF" state is obtained under high bias current and high input optical injection. In fact, this induces a balance between the two recombination mechanisms producing shorter carrier lifetime. However at low bias current, the Auger recombination process mainly controls the decay time and leads to a slower dynamic. Thus two different time constants are observed over the fall time. Finally, long RSOA allows performing the first direct 10 Gbit/s direct modulation with open eye diagram.

The theoretical understanding, the model, the design optimization and the characterization of several parameters enable us to obtain high static and dynamic performances RSOAs. However a trade-off between the static and dynamic performances needs to be considered. All results are summarized in the next table:

	2007 (Γ = 20%)	**2009** (Γ = 20%)	**2011** (Γ = 20%)
Gain (dB)	20	30	25
Saturation Power (dBm)	4	10	5
Optical Bandwidth (nm)	27	49	45
3-dB ASE bandwidth (GHz)	1.1	2	3
Polarization dependence (dB)	0.5	0.8	0.8
Noise Figure (dB)	10	8	8

Table 1 – Technical characteristics and evolution of RSOA during this work

Potential cost effective solutions for next generation of access network could be based on RSOA devices. Therefore, research on RSOA devices is driven by WDM-PON applications. It is of prime interest to solve issues related to this application. The chirp remains one major limiting factor as well as the modulation speed. 2-section RSOAs were used to overcome the first drawback. Theoretical analysis was performed and confirmed by chirp measurement. Based on 2-section RSOAs, high extinction ratio was obtained while keeping low total frequency variation. The recent convergence between radio-over-fibre and access network sparked our interest. RSOA as an universal device could be used in ONU as well as in RAU. However in R-o-F network, the radio range was limited by the RSOA link gain. 2-section RSOAs were used to increase the link gain by more than 10 dB. Therefore one- and two-section RSOAs show a great potential for converged network architecture.

RSOAs as colourless ONU have been investigated for both access and R-o-F network. New RSOAs developed during this work enable an upstream transmission of 8 WDM channel at 2.5 Gbit/s over 45 km. A high optical budget (36 dB) was demonstrated. The use of 2-section RSOAs allows a 100 km transmission below the FEC limit at 2.5 Gbit/s. Finally, 10 Gbit/s direct modulation over a few kilometres was obtained thanks to the modulation bandwidth increase. As part of the FUTON project, RSOA at the RAU is established as a potential solution. The device

behaves as expected and shows a good linearity and large SFDR. Error free transmission over 20 km was demonstrated (EVM below 4%) and large radio range was calculated around 440 m and 477 m respectively for one- and two-section devices.

Therefore, as a general conclusion, RSOAs show a great potential as a next generation of optical transmitter. It is an universal device which can be used in access and R-o-F networks. However the modulation speed is still limited and 10 Gbit/s modulation needs to be realised over a minimum of ten kilometres. The systems performances (distance and bit rate) are compared to state-of-the-art values in the Figure 6-1.

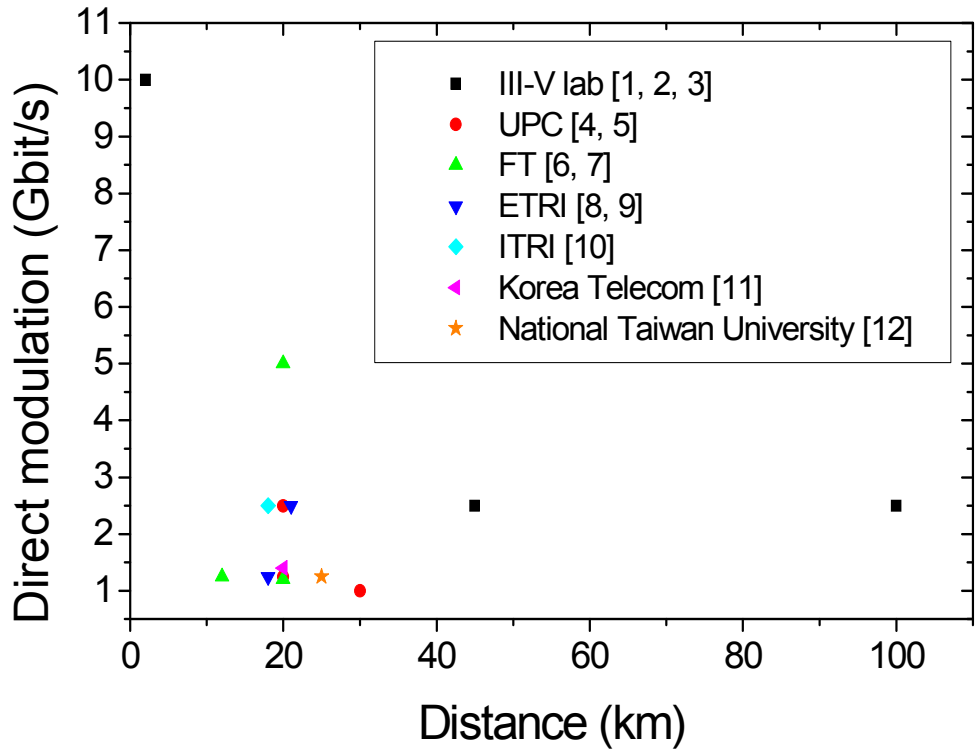

Figure 1 – RSOA systems performances comparison

Further work

In the future, several paths need to be deeply studied:

- The RSOA theory can be further understood. The optical mode size should strongly affect the noise factor (optical mode size effects on the β factor). This assumption needs to be verified and experimentally validated
- Another investigation should be carried out on the facet reflectivity impact. AR and HR (as well as the SSC) effects should be analyzed on static and dynamic performances
- New RSOA design needs to be done with complete passive tapers in order to reduce the leakage current and to obtain low consumption devices.

- In order to propose cost-effective devices, some studies on the fabrication cost should be undertaken. Other research groups use HR reflectivity closed to one hundred per cent. However as we demonstrated that the optical feedback in our RSOA is not one hundred per cent because of the tilted waveguide. One possibility should be to have a no-titled AZ and a tilted passive zone. Then no HR coating is needed in the mirror end in order to obtain the same reflectivity. As HR coating is an expensive processing step, cost reduction occurs
- Error free transmission at 10 Gbit/s should be extended to longer distances. The idea is to use long RSOA with 2 sections (may be with asymmetric electrodes). The second section could act as a booster and the carrier lifetime should be more reduced. The chirp reduction of the 2-section devices should improve the transmission quality
- The self-seeding approach is very interesting as no extra sources are needed. The theory should be completely understood and the systems performances evaluated
- Finally, the temperature remains the main issue. Uncooled devices should be obtained and should work in the range of -45 to 85 degrees

Improvements on the device itself reach a physical limit and trade-off between the different parameters is now needed. However higher performances could be obtained thanks to new modulation formats and/or electrical solutions. OFDM, coherent transmission, passive electrical filtering and EDC are potential solutions to reach 10 Gbit/s modulation over long distances. Nevertheless could they fit with local access requirements (low cost and low power consumption)? This is still an issue.

Last remarks

FTTH is now deployed based on the GPON technology. 55% of the French population should be connected by 2015. However no standardization of the NGPON2 has been done yet. Discussions started at FSAN/ITU for the next generation of optical access systems.

RSOA shows a great potential for colourless optical transmitter but will it be the chosen technology?

Tech-eco analysis has to be performed in order to evaluate the different technologies for WDM-PON and a trade-off between performances and cost will determine the future of optical access network. RSOA are still limited in terms of performances and architecture but new approach such as self-seeding could overcome these main issues. The SARDANA project proposes a ring-based WDM-PON solution by connecting metro and access networks with RSOA-based ONU. The great potential of this solution has been recognized and the project won the Global Telecoms Business Innovation Award 2011.

"*Convergence is what SARDANA is all about. By merging the metro and access parts of the networks, carriers can reduce capital costs*", says Dan Kelly, executive vice president, Tellabs global products

In 2011, Google announced its 1 Gbit/s project in Kansas city and Cisco prediction is 1 Gbit/s to the home by 2016. In Korea, the first commercial RSOA-based network has been deployed and enables a 1.25 GBit/s connection.

However the principal question about the compatibility with existing network remains.

Will operators have to change the current infrastructure or could RSOA-based WDM-PON be compatible with the evolution of NGPON1?

This answer should be known in the next years as operators and Telecom companies are focusing on this issue.

References

[1] G. de Valicourt, D. Make, M. Lamponi, G. Duan, P. Chanclou and R. Brenot, "High Gain (30 dB) and High Saturation Power (11dBm) RSOA Devices as Colourless ONU Sources in Long Reach Hybrid WDM/TDM -PON Architecture", Photonics technology letters, Vol. 22, No. 3, Feb. 1, 2010, pp. 191-193
[2] G. de Valicourt, M. Lamponi, G.H. Duan, F. Poingt, M. Faugeron, P. Chanclou and R. Brenot, " First 100 km uplink transmission at 2.5 Gbit/s for hybrid WDM/TDM PON based on optimized bi-electrode RSOA", in Proc. ECOC'10, Tu.5.B.6, 2010, Torino, Italy
[3] G. de Valicourt, D. Maké, C. Fortin, A. Enard, F. Van Dijk and R. Brenot, "10Gbit/s modulation of Reflective SOA without any electronic processing", in Proc. OFC, OThT2, 2011, Los Angeles, USA
[4] J. Prat, V. Polo, C. Bock, C. Arellano and J. J. Vegas Olmos, "Full-Duplex Single Fiber Transmission Using FSK Downstream and IM remote Upstream modulations for Fiber-to-the-Home", Photonics technology letters, Vol.17, No.3, March 2005, pp.702-704
[3] J. M. Fabrega, A. El Mardini, V. Polo, J. A. Lázaro, E. T. Lopez, R. Soila and J. Prat, "Deployment analysis of TDM/WDM Single Fiber PON with Colourless ONU Operating at 2.5 Gbps Subcarrier Multiplexed Downstream and 1.25 Gbps Upstream", in Proc. OFC, NWB5, 2010, San Diego, USA
[6] F. Payoux, P. Chanclou, T. Soret, N. Genay and R. Brenot, "Demonstration of a RSOA-based Wavelength Remodulation Scheme in 1.25 Gbit/s Bidirectional Hybrid WDM-TDM PON", in Proc. OFC, OTuC4, 2006, Anaheim, USA
[7] P. Chanclou, F. Payoux, T. Soret, N. Genay, R. Brenot, F. Blache, M. Goix, J. Landreau, O. Legouezigou, F. Mallécot, "Demonstration of RSOA-based remote modulation at 2.5 and 5 Gbit/s for WDM PON", in Proc. OFC, OWD1, 2007, Anaheim, USA
[8] H-H. Lee, S-H. Cho, J-H. Lee, E-S. Jung, J-H. Yu, B-W. Kim, S-S. Lee, S-H. Lee, J-S. Koh, B-H Sung, S-J. Kang, J-H. Kim, and K-T. Jeong, "First Commercial Service of a Colorless Gigabit WDM/TDM Hybrid PON System", in Proc. OFC, PDPD9, 2009, San Diego, USA
[9] D. C. Kim, B-S. Choi, H-S. Kim, K. S. Kim, O-K. Kwon, and D-K. Oh, "2.5 Gbps Operation of RSOA for Low Cost WDM-PON Sources", in Proc. ECOC, P2.14, 2009, Vienna, Austria
[10] C-H. Yeh, H-C. Chien and S. Chi, "Cost-Effective Colorless RSOA-Based WDM-PON with 2.5 Gbit/s Uplink Signal", in Proc. OFC, JWA95, 2008, San Diego, USA
[11] D-H. Kim, P. Y. Xing, Y-Y. Won, S-J. Park and S-K. Han, "Bidirectional 1.25Gb/s colorless RSOA based WDM-PON using Suppressed Optical Carrier and Polarization Beam Splitter", in Proc. OFC, JThA97, 2008, San Diego, USA
[12] T-K. Cheng, G-C. Lin, H-L. Wang, and G-R. Lin, "Chirp of color-free injection-locked reflective semiconductor optical amplifier based transmitter in 200GHz AWG based WDM-PON after 25km metropolitan transmission", in Proc. CLEO, JWA101, 2008, San Jose, USA

Biography

Guilhem de Valicourt received the BSc degree in applied physics from the National Institute of applied Sciences (INSA), Toulouse, France, in 2008. From 2007 to 2008, he followed and passed the Master of Science in Photonics Devices at Essex University, U.K, through a European exchange. From 2006 to 2008, he realized different work placements at University of South Australia (UNISA), CESR (France), IMEC (Belgium) and QinetiQ (U.K). In 2008, he joined Alcatel-Thales III-V lab where he was working on design, fabrication, and characterization of photonic sources toward the Ph.D. He was involved in the EU FP7 Integrated Project FUTON – "Fibre Optic Networks for Distributed and ANR AROME project. His main research interests were focused on Reflective SOA and directly modulated DFB lasers for microwave photonic systems and next generation of optical access networks.

Research Publications

Patents

1. Romain Brenot and **Guilhem de Valicourt**, "Integrated selectable filter", 806825-EP-EPA, 29 sept. 2010

2. **Guilhem de Valicourt**, Romain Brenot and Marco Lamponi, "High radio range RSOAs", 809072-EP-EPA, 14 March 2011

3. Romain Brenot and **Guilhem de Valicourt**, "High speed reflective SOA", 809196-EP-EPA, 8 March 2011

4. Guang-Hua Duan, Marco LAMPONI, **Guilhem de Valicourt**, Francis Poingt, Gunter Roelkens, Dries Van Thourhout, "Hybrid III-V-silicon laser sources including transition from shallow ridge waveguide to deep ridge waveguide", 806822-EP-EPA, July 2011

5. **Guilhem de Valicourt**, Romain Brenot, Philippe Chanclou, Alban Le liepvre, "Separated Input/Output RSOA", 808297, Nov. 2010

6. Alban Le Liepvre, Marco Lamponi, Guang-Hua Duan, **Guilhem de Valicourt**, Badhise Ben Bakir, Antoine Descos "Séparateur d'états de polarisation et/ou de longueurs d'onde pour les circuits intégrés photoniques", 810921, Dec. 2011

Book Chapters

1. **G. de Valicourt**, G. H. Duan, R. Brenot and F. Van Dijk, "Next generation wireless communications using radio over fiber (The FUTON project)", Chapter 7, John Wiley & Sons, Ltd., accepted for publication, 2012
2. **G. de Valicourt**, "Next generation of Optical Access Network based on Reflective-SOA", (**invited**) , InTech, accepted for publication, 2012

Journal Publications

As first author:

1. **G. de Valicourt**, D. Make, M. Lamponi, G. Duan, P. Chanclou and R. Brenot, "High Gain (30 dB) and High Saturation Power (11dBm) RSOA Devices as Colourless ONU Sources in

Long Reach Hybrid WDM/TDM -PON Architecture", Photonics technology letters, Vol. 22, No. 3, Feb. 1, 2010, pp. 191-193

2. **G. de Valicourt**, F. Pommereau, F. Poingt, M. Lamponi, G.H. Duan, P. Chanclou, M. A. Violas and R. Brenot, "Chirp Reduction in Directly Modulated Multielectrode RSOA Devices in Passive Optical Networks", Photonics technology letters, Vol. 22, No. 19, Oct. 1, 2010, pp. 1425-1427

3. **G. de Valicourt**, M. A. Violas, D. Wake, F. van Dijk, C. Ware, A. Enard, D. Maké, Zhansheng Liu, M. Lamponi, G. H. Duan and R. Brenot, "Radio over Fibre Access Network Architecture based on new optimized RSOA Devices with large modulation bandwidth and high linearity", Microwave Theory and Techniques, Vol. 58, No. 11, October 2010, pp 3248-3258

4. **G. de Valicourt**, G. H. Duan, C. Ware, M. Lamponi and R. Brenot, "Experimental and theoretical investigation of Mode Size Effects on Tilted Facet Reflectivity", IET optoelectronics, Vol. 5, No. 4, 2011, pp. 175-180

As secondary author:

5. B. Schrenk, **G. de Valicourt**, M. Omella, J. Lazaro, R. Brenot and J. Prat, "Direct 10 Gb/s Modulation of a Single-Section RSOA in PONs with High Optical Budget", Photonics technology letters, Vol. 22, No. 6, March 15, 2010, pp. 392-394

6. David Wake, Anthony Nkansah, Nathan J. Gomes, **Guilhem de Valicourt**, Romain Brenot, Manuel Violas, Zhansheng Liu, Filipe Ferreira and Silvia Pato, "A Comparison of Radio over Fiber Link Types for the Support of Wideband Radio Channels", Journal of Lightwave technology, Vol. 28, No. 16, March 2010, pp. 2416-2422

7. H. Carrère, V. G. Truong, X. Marie, R. Brenot, **G. De Valicourt**, F. Lelarge, T. Amand, "Large optical bandwidth and polarization insensitive semiconductor optical amplifiers using strained InGaAsP quantum wells", Appl. Phys. Lett. 97, 121101 (2010)

8. B. Schrenk, **G. de Valicourt**, J.A. Lazaro, R. Brenot, and J. Prat, "Rayleigh Scattering Tolerant PON Assisted by Four-Wave Mixing in SOA-based ONUs," IEEE/OSA J. Lightwave Technol., vol. 28, pp. 3364-3371, Dec. 2010

9. Zhansheng Liu, Mojtaba Sadeghi, **Guilhem de Valicourt** and Romain Brenot, Manuel Violas, "Experimental Validation of a Reflective Semiconductor Optical Amplifier Model used as a Modulator in Radio over Fiber Systems", Photonics technology letters, Vol. 23, No. 9, May 1, 2011, pp. 576-578

10. Bernhard Schrenk, Jose A. Lazaro, Dimitrios Klonidis, Francesc Bonada, Fabienne Saliou, Victor Polo, Eduardo Lopez, Quang T. Le, Philippe Chanclou, Liliana Costa, Antonio Teixeira, Sotiria Chatzi, Ioannis Tomkos, Giorgio M. Tosi Beleffi, Dmitri Leino, Risto Soila,

Spiros Spirou, **Guilhem de Valicourt**, Romain Brenot, Christophe Kazmierski, and Josep Prat, "Demonstration of a Remotely Dual-Pumped Long-Reach PON for Flexible Deployment", IEEE/OSA J. Lightwave Technol., Accepted 2012

11. L. Marazzi, P. Parolari, R. Brenot, **G. de Valicourt** and M. Martinelli, "Network-Embedded Self-Tuning Cavity for WDM-PON Transmitter", Optic Express, Accepted 2012

12. M. Lamponi, S. Keyvaninia, C. Jany, F. Poingt, F. Lelarge, **G. de Valicourt**, G. Roelkens, D. Van Thourhout, S. Messaoudene, J.-M. Fedeli, G.H. Duan, "Low-threshold heterogeneously integrated InP/SOI laser with a double adiabatic taper coupler", Photonics technology letters, Vol. 24, No. 1, Jan 1, 2012, pp. 76-78

International Conference and workshop publications

As first author:

1. **G. de Valicourt**, D. Maké, C. Fortin, A. Enard, F. Van Dijk and R. Brenot, "10Gbit/s modulation of Reflective SOA without any electronic processing", in Proc. OFC'11, OThT2, 2011, Los Angeles, USA

2. **G. de Valicourt**, M. Lamponi, G.H. Duan, F. Poingt, M. Faugeron, P. Chanclou and R. Brenot, " First 100 km uplink transmission at 2.5 Gbit/s for hybrid WDM/TDM PON based on optimized bi-electrode RSOA", in Proc. ECOC'10, Tu.5.B.6, 2010, Torino, Italy

3. **G. de Valicourt**, F. Pommereau, F. Poingt, M. Lamponi, G.H. Duan, P. Chanclou, M. A. Violas and R. Brenot, " Low chirp RSOA using multi-sections devices for optical access networks", in Proc. ECIO'10, FrC2, 2010, Cambridge, UK

4. **G. De Valicourt**, D. Maké, J. Landreau, M. Lamponi, G.H. Duan, P. Chanclou and R. Brenot, « New RSOA Devices for Extended Reach and High Capacity Hybrid TDM/WDM - PON Networks », in Proc. ECOC'09, P9.5.2, 2009, Vienna, Austria

5. **G. de Valicourt**, M. A. Violas, F. van Dijk, D. Maké and R. Brenot, « Colourless Radio over Fibre Access Network architecture using New RSOA devices for high performances », EU-Workshop on photonic solution for wireless, access, and in-house networks, 2009, Duisburg, Germany

6. **G. de Valicourt**, Anthony Nkansah, David Wake, Nathan Gomes, M. Faugeron, R. Brenot, C. Ware and Frederic Van Dijk, "Uncooled operation of 1.55 μm DFB laser for Converged Wireless over Fiber Access Networks", International workshop on high speed semiconductor laser 2010, October 7-8, 2010, Wroclaw, Poland

7. **G. de Valicourt**, Anthony Nkansah, David Wake, Nathan Gomes, M. Faugeron, R. Brenot, C. Ware and Frederic Van Dijk, "High efficiency 1.5 μm DFB laser for uncooled 10 GHz bandwidth analog transmission", European Semiconductor Laser Workshop 2010, September 24 – 25, 2010 Pavia, Italy

As secondary author:

8. F. Raharimanitra, P. Chanclou, T. N. Duong, B. Charbonnier, M. Ouzzif, N. Genay, A. Gharba, F. Saliou, J. Le masson, R. Brenot, **G. De valicourt**, «Sources tranchées spectralement et modulées en format AMOOFDM pour le WDM et TDM PON », Journées Nationnal d'Optique Guidée (JNOG), 2009

9. A.F. Raharimanitra, P. Chanclou , T. N. Duong , J. Le Masson , B. Charbonnier, M. Ouzzif, N. Genay , Gharba, F. Saliou, R. Brenot, **G. Devalicourt**, "Spectrum Sliced Sources MOOFDM Modulated for WDM&TDM PON", in Proc. ECOC'09, P.6.5.3, 2009, Vienna, Austria

10. H. Carrère, X. Marie, A. Kunold, V. G. Truong, T. Amand, **G. De Valicourt**, R. Brenot, F. Lelarge, "Band structure engineering of InGaAsP quantum wells for wide optical band SOAs", ICO - Emerging Trends and Novel Materials in Photonics, October 7-9, 2009, Delphi, Greece

11. David Wake, Anthony Nkansah, Philipos Assimakopolous, Nathan Gomes, Manuel Violas, Zhansheng Liu, Silvia Pato, Filipe Ferreira, **Guilhem de Valicourt**, Romain Brenot and Frédéric Van Dijk, "Design and Performance of Radio over Fibre Links for Next Generation Wireless Systems using Distributed Antennas", Future Network and Mobile Summit, June 16-18, 2010, pp. 1-9, Florence, Italy

12. B. Schrenk, **G. de Valicourt**, F. Bonada, J.A. Lazaro, R. Brenot, J. Prat, " Self-Pumped Dense (40λ×32 split) PON with Extended 30 dB Loss Budget and ONUs Comprising a Single 10 Gb/s RSOA", in Proc. ECOC'10, Tu.3.B.3,2010, Torino, Italy

13. R. Brenot, **G. De Valicourt**, F. Poingt, F. Lelarge and F. Pommereau, "Potential benefits and limitations of SOA in Access Networks", ANIC 2010 (invited), June 21, AThC1, Karlsruhe, Germany

14. Zhansheng Liu, Manuel Violas, Motjaba Sadeghi and **Guilhem de Valicourt**, "4 channels subcarrier multiplexing optical link using an RSOA modulator", MWP 2010, Oct. 5-9, pp. 201-209, Montreal, Canada

15. B. Schrenk, Christos Stamatiadis, Ioannis Lazarou, Alexandros Maziotis, **Guilhem de Valicourt**, Jose A. Lazaro, Josep Prat, and Hercules Avramopoulos, "On an ONU for Full-Duplex 10.5 Gbps with Shared Delay Interferometer for Format Conversion and Chirp Filtering", in Proc. OFC'11, OThB7, 2011, Los Angeles, USA

16. B. Schrenk, **Guilhem de Valicourt**, Jose A. Lazaro, and Josep Prat, "FSK+ASK/ASK Operation for Optical 20/10 Gbps Access Networks with Simple Reflective User Terminals", in Proc. OFC'11, JWA79, 2011, Los Angeles, USA

17. Quang Trung Le, Qian Deniel, Fabienne Saliou, **guilhem de Valicourt**, Romain Brenot and Philippe Chanclou, RSOA-based External Cavity Laser as Cost-effective Upstream Transmitter for WDM Passive Optical Network, CLEO 2011, JWA9, May 1-6, 2011, Baltimore, USA

18. J. A. Lazaro, V. Polo, B. Schrenk, F. Bonada, I. Cano, E. T. Lopez, C. Kazmierski, **G. de Valicourt**, R. Brenot, J. Bauwelinck, X.-Z. Qiu, P. Ossieur, M. Forzati, P.-J. Rigole, I. T. Monroy, E. Tangdiongga, M. Morant, L. Nicolau, A. L. Teixeira, D. Erasme, D. Klonidis, I. Tomkos, J. Prat, C. Kouloumentas, H. Avramopoulos , "Optical Subsystems for Next Generation Access Networks", ANIC 2011 (invited), Toronto, Canada

19. L. Marazzi, P. Parolari, **G. de Valicourt** and M. Martinelli, "Network-Embedded Self-Tuning Cavity for WDM-PON Transmitter", in proc. ECOC, Mo.2.C.3, Sept. 2011, Geneva, Switzerland

20. B. Schrenk, J. Lazaro, D. Klonidis, F. Bonada, F. Saliou, V. Polo, E. Lopez, Q. Le, P. Chanclou, L. Costa, A. Teixeira, S. Chatzi, I. Tomkos, G. Tosi Beleffi, D. Leino, R. Soila, S. Spirou, **G. de Valicourt**, R. Brenot, C. Kazmierski, J. Prat, "Demonstration of a Remotely Pumped Long-Reach WDM/TDM 10 Gb/s PON with Reflective User Terminals", in proc. ECOC, Th.12.C.3, Sept. 2011, Geneva, Switzerland

21. Frédéric van Dijk, Alain Enard, Guang-Hua Duan, Alain Accard, François Lelarge, Olivier Parillaud, Akram Akrout, **Guilhem de Valicourt**, Stephane Ginestar, Abderrahim Ramdane, "Laser diodes for microwave and millimeter wave photonics", Mediterranean Microwaves Symposium MMS'2009, , November 15-17, 2009 (invited), Tangiers, Morocco

22. M. Lamponi, S. Keyvaninia, F. Pommereau, R. Brenot, **G. de Valicourt**, F. Lelarge, G. Roelkens, D. Van Thourhout, S. Messaoudene, J.-M. Fedeli, G.-H. Duan, "Heterogeneously integrated InP/SOI laser using double tapered single-mode waveguides through adhesive die to wafer bonding", Group IV Photonics (GFP), Sept. 1-3, 2010, pp. 22 – 24, Beijing, China

23. M. Faugeron, **G. de Valicourt**, J. Jacquet and F. Van Dijk, "High Power, Low RIN, 1.55µm DFB Laser For Analog Applications", International workshop on high speed semiconductor laser 2010, October 7-8, 2010, Wroclaw, Poland

Appendix I

Experimental and theoretical investigation of Mode Size Effects on Tilted Facet Reflectivity

Reflectivity of cleaved facets is one of the key parameters in integrated optical circuits. Components such as semiconductor optical amplifiers (SOAs) need a careful control on reflection from its end mirrors. In Fabry-Perot lasers, it can be desirable to minimize or maximize losses due to the facet reflectivity which play a significant role in mode selection [1]. Therefore facet reflectivity characterization is of prime interest for these different applications. In the case of reflective semiconductor optical amplifiers (RSOAs), low reflectivity and high reflectivity (for different end mirrors) are key to their performance. The reflection control can be done through several ways. First, facet coating is used to achieve low facet reflectivity [2, 3]. However to achieve reproducible values of different facet reflectivity, we need in-situ monitoring (control of the thickness and refractive index of the various layers). A second efficient way is by tilting the waveguide [4] or a combination of coating and tilting [5, 6]. In order to predict facet reflectivity, different models are used to facilitate devices design. Complex models have been proposed taking into account the 2-D [7] or 3-D nature of the waveguide [8]. SOA integrated with spot-size-converter (SSC) are extensively studied for the improvement of coupling efficiency with single-mode fibre (SMF) and for cost reduction in packaging. The facet reflectivity of a spot-size-converter integrated SOA has been calculated, but no direct studies of the reflectivity dependence on the optical mode size were realized.

In this appendix, we propose a very simple analytical model, which allows rapid calculation of the modal reflectivity of a tilted facet. An optimization can be done in order to obtain the lowest reflectivity with optimum mode size using tilted angle facets. The experimental observation is described in section I. In section II, the analysis of the reflectivity mode size dependence is presented and facet reflectivity is calculated based on guided optical mode equations and Fresnel reflectivity. All results are discussed in chapter 2 and conclusions are presented in section II.

I. Experimental observation

The integration of a taper increases the optical mode size as demonstrated in [9]. In order to evaluate the effect of optical mode size on the facet reflectivity, two types of a 7° tilted SOA with a 500 μm long cavity are used. The first one is an SOA device with the taper and the second one an SOA without the taper. As a consequence, the mode size is larger in the first one than in the second one. A typical spot-size-converter semiconductor optical amplifier (SSC-SOA) structure and the simulated optical modes are represented in figure 2-12 (a) and 2-12 (b). The optical mode before and after the taper have been calculated using Beam Prop software. Optical mode simulations give horizontal mode width values of 4.5μm and 1.7μm with and without SSC. The optical spectrum emitted by SOA structures with spot-size converter is measured in figure I-1. From these measurements, the reflectivity can be evaluated depending on the linear gain and the ripple. The reflectivity is given by equation (2-5):

$$R = \frac{1}{G_{linear}} \times \left(\frac{G_{max}}{G_{min}}\right)_{dB} \times \frac{\ln(10)}{40} \qquad \text{I-1}$$

A ripple of 0.25 dB has been measured on the spot-size converter SOA which gives a low reflectivity of 1.4 x 10^{-4} for a single pass gain around 20 dB. This dependence of the gain ripple on the facet reflectivity is represented in Figure 2-31.

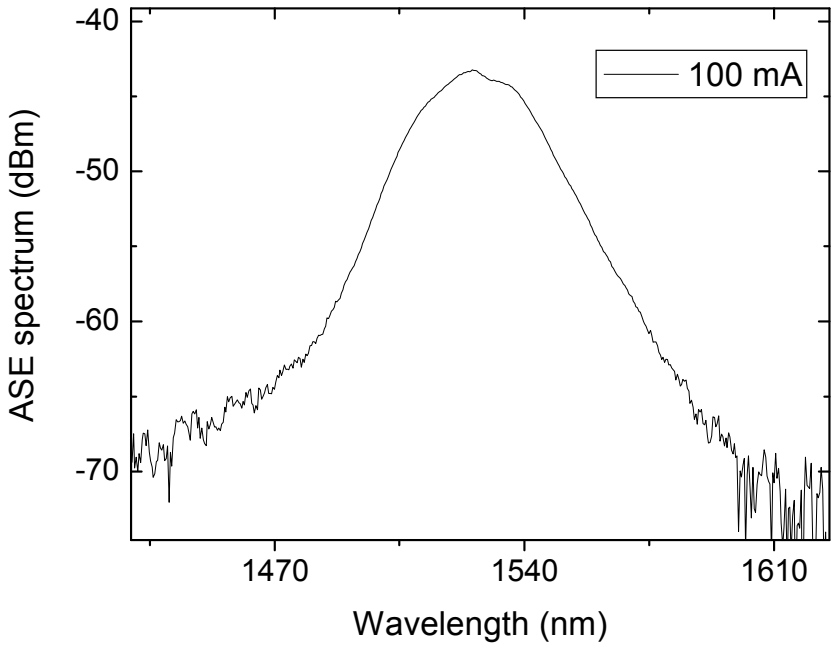

Figure I-1 - Optical spectrum of ASE generated by SOA structure with spot-size converter (resolution: 0.1 nm)

When the SOAs are cleaved without the taper, they start lasing with a threshold current of 37 mA. This indicates either a higher facet reflectivity or smaller internal cavity losses induced by the lack of the tapers. We assume that the integrated spot size converter introduces no losses. Therefore the lasing conditions are obtained only due to the higher reflectivity. From the laser gain condition of a Fabry-Perot (FP) cavity, the reflectivity can be extracted using the oscillation condition [10]. A reflectivity of 6.25 % is evaluated by measuring an optical gain of 16 dB and assuming that both facets have the same reflectivity. The optical spectrum has been measured on Figure I-2 and P-I measurements are shown in the inset. The reflectivity is much higher than in the SOA structure that includes an output taper. We have performed the far field measurement of the SOAs, as shown in Figure 2-13 (a) with SSC and in Figure 2-13 (b) without SSC. We observe small divergence values with SSC due to a large optical mode and high divergence in the case of a small optical mode without SSC.

The 3-dB divergence angles ($\Delta\alpha_{3dB}$) in both horizontal and vertical directions are shown in table 2-2. The values of the mode size Δx and those of the wave variation vector (Δk_x), expressed as a function of the full width at half maximum (FWHM) of the divergence as demonstrated in part II.B, are also shown in this Table. Depending on the vertical ($\varphi = 90°$) or horizontal axis ($\varphi = 180°$), minor differences occur. All results are summarized in table 2-2.

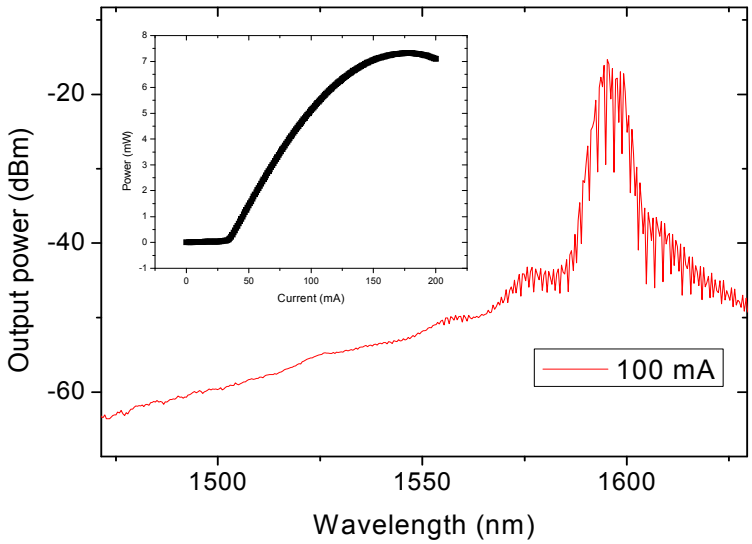

Figure I- 2 - Optical spectrum of SOA structure without spot-size converter (resolution: 0.1 nm)

II. Theoretical approach and numerical analysis

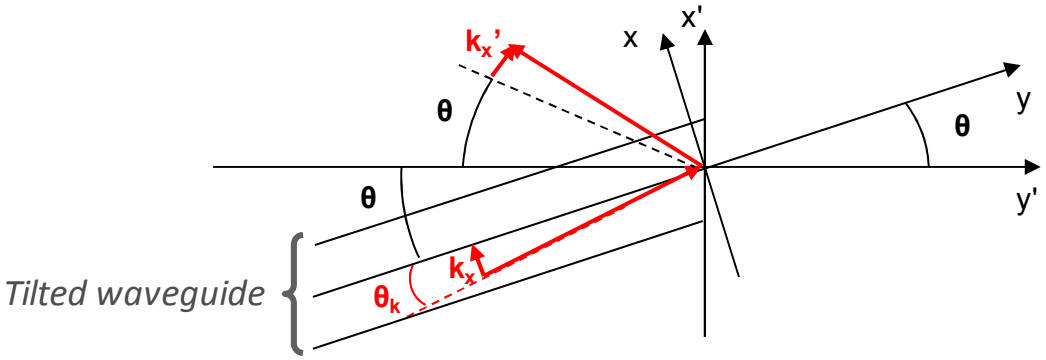

Figure I- 3 - Schema of tilted waveguide with wave vectors representation

Let us consider the tilted waveguide as represented in figure I-3. The waveguide is tilted by θ degrees, compared to the normal direction of the facet. The incoming field ($E_{in}(x)$) can be decomposed by an infinite sum of plane waves using the Fourier transformation. k is the wave vector of each incoming plane wave and k_x its component on the x axis. The incoming guided optical mode and the reflected field can be given respectively by:

$$E_{in}(x) = \int_{-\infty}^{+\infty} \widetilde{E_{in}}(k_x)\, e^{-jk_x x} dk_x \qquad \text{I-2}$$

$$E_r(x) = e^{-j2k\theta x} \int_{-\infty}^{+\infty} E_{in}(k_x) R(k_x)\, e^{-jk_x' x} dk_x \qquad \text{I-3}$$

Where R(k_x) is the amplitude reflectivity of the input wave with a wave vector of k_x.

According to Fresnel's law, k_x' can be expressed as $k_x' = k_x + 2k\sin(\theta) \approx k_x + 2k\theta$ where θ is assumed to be small. The coupled reflected field to the guided mode is assumed to be the coupled fundamental guided mode and the high order optical modes. The incoming mode should satisfy the fundamental mode determined by the waveguide in order to be guided therefore the reflected field back to the waveguide is expressed as:

$$E_r = C.E_{in} + E_{superior\ order} \quad \text{I-4}$$

Where C is the coupling coefficient.

Given that modes are orthogonal, the coupling coefficient can be extracted by projecting equation (I-4) over E_{in}. The resulting expression of C is:

$$C = \frac{\int_{-\infty}^{+\infty} E_r E_{in}^* dx}{\int_{-\infty}^{+\infty} E_{in} E_{in}^* dx} \quad \text{I-5}$$

Substituting equation (I-2) and (I-3) into equation (I-4), we obtain:

$$C = \frac{\int_{-\infty}^{+\infty} \Gamma(k_x + k.sin\theta) E_{in}(k_x) E_{in}^*(k_x + 2k\theta) dk_x}{\int_{-\infty}^{+\infty} |E_{in}(k_x)|^2 dk_x} \quad \text{I-6}$$

The coupling coefficient C gives directly the reflectivity of the input guided mode.

A. Reflectivity dependence on the wave vector

The input field is assumed to be a Gaussian distribution (equation (I-7)); the reflected coefficient ($\Gamma(k_x)$), depending on the polarization mode, is expressed in equations (I-8) and (I-9), for the classical case of planar reflection at incident and transmitted angles θ_i and θ_t.

$$|E_{in}(k_x)| = e^{-\frac{{k_x}^2}{\Delta {k_x}^2}} \quad \text{I-7}$$

For TM mode,

$$\Gamma_{TM} = \frac{n_1 - n_2 \frac{cos\ (\theta_t)}{cos\ (\theta_i)}}{n_1 + n_2 \frac{cos\ (\theta_t)}{cos\ (\theta_i)}} \quad \text{I-8}$$

For TE mode,

$$\Gamma_{TE} = \frac{n_1 - n_2 \dfrac{cos\ (\theta_i)}{cos\ (\theta_t)}}{n_1 + n_2 \dfrac{cos\ (\theta_i)}{cos\ (\theta_t)}}$$

I-9

The transmitted beam angle is given by the following equation:

$$cos\ (\theta_t) = \sqrt{1 - \left(\frac{n_1}{n_2}\right)^2 sin^2\ (\theta_i)}$$

I-10

Considering equation (I-8) and (I-10), we obtain for the TM mode:

$$\Gamma_{TM}(k_x) = \frac{n_1 - n_2 \left(\dfrac{\sqrt{1 - \left(\frac{n_1}{n_2}\right)^2 \left(\frac{k_x}{k}\right)^2}}{\sqrt{k^2 - k_x^2}/k} \right)}{n_1 + n_2 \left(\dfrac{\sqrt{1 - \left(\frac{n_1}{n_2}\right)^2 \left(\frac{k_x}{k}\right)^2}}{\sqrt{k^2 - k_x^2}/k} \right)}$$

I-11

Using the same approach for the TE mode, the coupling coefficient can be expressed as a function of the wave variation vector in the x direction (Δk_x) for both polarizations:

For the TM mode,

$$C_{TM} = \frac{\int_{-\infty}^{+\infty} \left(\dfrac{n_1 - n_2 \left(\dfrac{\sqrt{1 - \left(\frac{n_1}{n_2}\right)^2 \left(\frac{k_x + k.sin\theta}{k}\right)^2}}{\sqrt{k^2 - (k_x + k.sin\theta)^2}/k} \right)}{n_1 + n_2 \left(\dfrac{\sqrt{1 - \left(\frac{n_1}{n_2}\right)^2 \left(\frac{k_x + k.sin\theta}{k}\right)^2}}{\sqrt{k^2 - (k_x + k.sin\theta)^2}/k} \right)} \times e^{-\frac{{k_x}^2}{{\Delta k_x}^2}} \times e^{-\frac{(k_x + 2k\theta)^2}{{\Delta k_x}^2}} \right) dk_x}{\int_{-\infty}^{+\infty} e^{-\frac{{k_x}^2}{{\Delta k_x}^2}} dk_x}$$

I-12

For the TE mode,

$$C_{TE} = \frac{\int_{-\infty}^{+\infty} \left(\frac{n_1 - n_2 \left(\frac{\sqrt{k^2 - (k_x + k.sin\theta)^2}/k}{\sqrt{1 - \left(\frac{n_1}{n_2}\right)^2 \left(\frac{k_x + k.sin\theta}{k}\right)^2}} \right)}{n_1 + n_2 \left(\frac{\sqrt{k^2 - (k_x + k.sin\theta)^2}/k}{\sqrt{1 - \left(\frac{n_1}{n_2}\right)^2 \left(\frac{k_x + k.sin\theta}{k}\right)^2}} \right)} \times e^{-\frac{{k_x}^2}{\Delta {k_x}^2}} \times e^{-\frac{(k_x + 2k\theta)^2}{\Delta {k_x}^2}} \right) dk_x}{\int_{-\infty}^{+\infty} e^{-\frac{{k_x}^2}{\Delta {k_x}^2}} dk_x}$$

I-13

Therefore, the coupling function depends on the differential Δk_x and θ angle. A numerical integration is performed using Simpson's rule. The interval is limited from k to –k for both integrals. Calculations are performed at λ =1.55 μm, the effective refractive index n_1 = 3.3 and n_2 = 1. Furthermore, to compare simulations with experimental values, the reflectivity needs to be expressed in intensity and not amplitude, so as R = C^2. The result is plotted in figure I-4 as a function of Δk_x for various waveguide angles and polarizations. From equation (I-12) and (I-13), if we consider plane waves approximation ($\Delta k_x = 0$), Fresnel's law is obtained, which verifies our model. Also, considering normal incidence (θ = 0) and for effective refractive index n_1 = 3.3 and n_2 = 1, a reflectivity of 0.286 is computed, which corresponds to the Fresnel's reflection coefficient of this interface. For an untilted waveguide, the two polarizations exhibit a different behaviour. It can be explained by considering the reflected coefficient ($\Gamma(k_x)$) defined above. In fact, for the TM mode, $\Gamma(k_x)$ decreases in the range $0 < k_x < 4$ and then it increases again. For the TE mode, an increase is observed up to $k_x \sim 4$ and then it decreases. Therefore the reflectivity for both polarizations at delta k_x = 10 is almost equal.

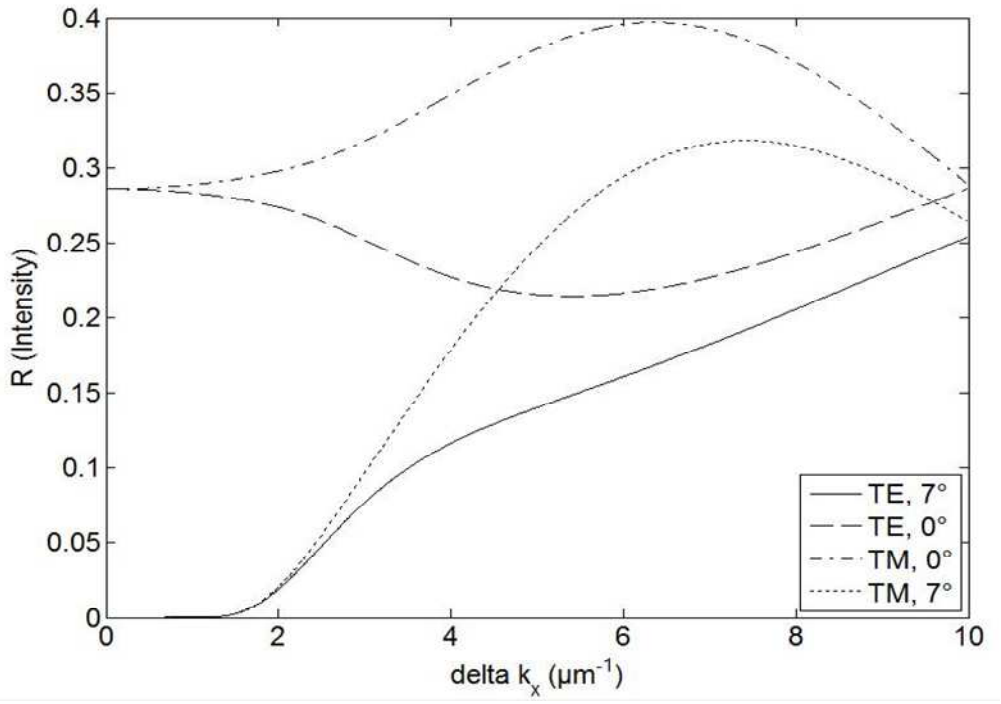

Figure I- 4 - Reflectivity depending on the variation $\Delta \mathbf{k_x}$

B. *Optical mode approximation and beam divergence in tilted waveguide*

Considering figure I-3, the relation between the fundamental waveguide optical mode and the optical mode at the facet is calculated as follows. The transformation between primed and unprimed coordinate systems is given by:

$$\begin{pmatrix} x \\ y \end{pmatrix} = \begin{pmatrix} cos\theta & sin\theta \\ -sin\theta & cos\theta \end{pmatrix} \begin{pmatrix} x' \\ y' \end{pmatrix}$$

I-14

Let us consider the two-dimensional distribution of the incident electric field on the (x) and (y) axes.

$$E_{in}(x,y) = AE_{in}(x)e^{-jk_y y} = Ae^{-\frac{x^2}{W^2}}e^{-jk_y y}$$

I-15

Where A is a constant and $E_{in}(x)$ is approximated by a Gaussian distribution.

In the primed coordinate system, we obtain:

$$E_{in}(x',y') = Ae^{-\frac{(x'.cos\theta + y'.sin\theta)^2}{W^2}}e^{-jk_y(-x'.sin\theta + y'.cos\theta)}$$

I-16

At the facet (y'=0), the previous equation becomes:

$$E_{in}(x', y' = 0) = Ae^{-\frac{(x'.cos\theta)^2}{W^2}} e^{jk_y(x'.sin\theta)}$$
$$= A' \int_{-\infty}^{+\infty} e^{-(k_x' - k_y.sin\theta)^2 \left(\frac{W^2}{cos\theta}\right)^2} e^{-jk_x' x'} dk_x'$$

I-17

Considering equation (I-7), the Fourier transform of incident electric field is also expressed as:

$$\left|E_{in}(k_x')\right| = e^{-\frac{(k_x' - k_y.sin\theta)^2}{\Delta k_x'^2}} = e^{-(k_x' - k_y.sin\theta)^2 \left(\frac{W}{cos\theta}\right)^2}$$

I-18

Therefore,

$$\Delta k_x = \frac{cos\theta}{W} = \Delta k_x cos\theta$$
$$\Delta k_x = \frac{\Delta k_x'}{cos\theta}$$

I-19

The difference between the internal (Δk_x) and external ($\Delta k_x'$) wave vector variation is due to a factor 1/cosθ. At the facet interface the optical mode size will also increase by this factor. This increase needs to be considered on the perpendicular axis of the propagation. We use a 7° tilted waveguide which gives factor values around one (~0.99) and can be neglected. So in the first part, all calculations have been done on unprimed coordinate system. Δk_x can be directly related to the optical mode diameter and the full width at half maximum (FWHM) of the divergence ($\Delta\alpha_{3db}$). $\Delta\alpha_{3db}$ is given by the difference between the two extreme values of the independent variable (α: angle of divergence) at which the dependent variable (output power) is equal to half of its maximum value. $\Delta\alpha_{3dB}$ is defined by equation (I-20) in the x coordinate system :

$$\Delta\alpha_{3dB} = 2\sqrt{\log(2)} \times \Delta\alpha$$

I-20

It can be demonstrated that

$$\Delta k_x = \sqrt{2} \times k_0 \times \Delta\alpha = k_0\sqrt{2} \times \frac{\Delta\alpha_{3dB}}{2\sqrt{ln2}}$$

I-21

Where $k_0 = \frac{2\pi}{\lambda}$.

If we assume an $\Delta\alpha_{3dB}$ = 50°, Δk_x = 3 μm^{-1} which gives a reflectivity around 7.7 % and 9.7 % respectively for TE and TM mode in a 7° tilted waveguide.
In tilted waveguide, this effect has been experimentally confirmed in Chapter 2: The smaller the divergence, the lower the reflectivity.

We have investigated the reflectivity of a waveguide and propose an analytical simulation model. The effective facet reflectivity of SOA depending on the optical mode size has been studied both theoretically and experimentally. 1-D analysis has been made based on electric field theory and compares with experimental measurements in figure 2-38. The optical mode size clearly affects the facet reflectivity according to plane-wave decomposition techniques and

Fresnel's law. The effect of a tilted waveguide is also investigated. Low reflectivity SOA can be obtained using spot size converter and tilted waveguide.

References

[1] Eugene I. Gordon, "Mode Selection in GaAs Injection Lasers Resulting from Fresnel Reflection", IEEE journal of quantum electronics, Vol. QE-9, No. 7, July 1973

[2] T. Saitoh, T. Mukai, and O. Mikami, "Theoretical analysis and fabrication of antireflection coatings for laser-diode facets", IEEE Journal of Ligthwave technology, Vol. LT-3, pp. 288-293, 1985

[3] G. P. Agrawal, N. A. Olson, and N. K. Dutta, "Effect of fiber-far-end reflections on intensity and phase noise in InGaAsP semiconductor laser," Appl. Phys. Lett., Vol. 45, No. 6, pp. 597-599, Sept. 1984

[4] C. E. Zah, J. S. Oinski, C. Caneau, S. G. Menocal, L. A. Reith, J. Salzman, F. K. Shokoohi, and T. P. Lee, "Fabrication and performance of 1.5 μm GaInAsP travelling-wave laser amplifiers with angled facets," Electron. Lett., vol.23, pp. 990-992, 1987.

[5] G. De Valicourt, D. Maké, J. Landreau, M. Lamponi, G.H. Duan, P. Chanclou and R. Brenot, « New RSOA Devices for Extended Reach and High Capacity Hybrid TDM/WDM -PON Networks », in Proc. ECOC'09, P9.5.2, 2009

[6] C. E. Zah, C. Caneau, F. K. Shokoohi, S. G. Menocal, F. Favire, L. A. Reith, and T. P. Lee, "1.3 μm GaInAsP near-travelling-wave laser amplifiers made by combination of angled facets and antireflection coatings," Electron. Lett., vol. 24, pp. 1275-1276, 1988.

[7] S. T. Lau and J. M. Ballantyne, "Two-Dimensional Analysis of a Dielectric Waveguide Mirro", IEEE Journal of Ligthwave technology, Vol. 15, No. 3, pp. 551-558, March 1997.

[8] J. Shim, J. Kim, D. Jang, Y. Eo and S. Arai, "Facet reflectivity of a spot-size-converter integrated semiconductor optical amplifier", IEEE journal of quantum electronics, Vol. 38, No 6, 2002

[9] J. R. Kim, J. S. Lee, S. Park, M. W. Park, J. S. Yu, S. D. Lee, A. G. Choo, T. I. Kim, and Y. H. Lee, "Spot-Size Converter Integrated Polarization Insensitive Semiconductor Optical Amplifiers", IEEE Photonics technology letters, Vol. 11, No. 8, Aug. 1999, pp. 967-969

[10] L. A. Coldren and S. W. Corsine, "Diode Laser and Photonic Integrated Circuits", John Wiley & Sons Inc. (1995)

Appendix II

Processing Techniques

In this appendix, we detail the different processing techniques used to realize our final RSOA device.

I. Photolithography

Photolithography is used to transfer a pattern from a mask to the wafer. The masks are designed using the layout editor: L-Edit [1]. A photoresist material is used which is a light-sensitive material. Using this technique, we can define the different regions where the material has to be deposited or removed. The basic procedure consists in the following steps:

- Preparation of the wafer and photoresist application (by spin coating)
- Contact between the mask and the wafer
- The photoresist is exposed in the regions where the mask is transparent using UV light
- The wafer is then immersed in the developer, which dissolves the exposed photoresist
- Deposition or etching can be performed
- We remove the rest of the photoresist by using acetone

Therefore the process allows printing the exact replica of the mask pattern defined in the photoresist on the substrate. The maximum resolution is around 0.8 μm which is not suitable for precise spot-size converter. Then E-beam lithography can be used.

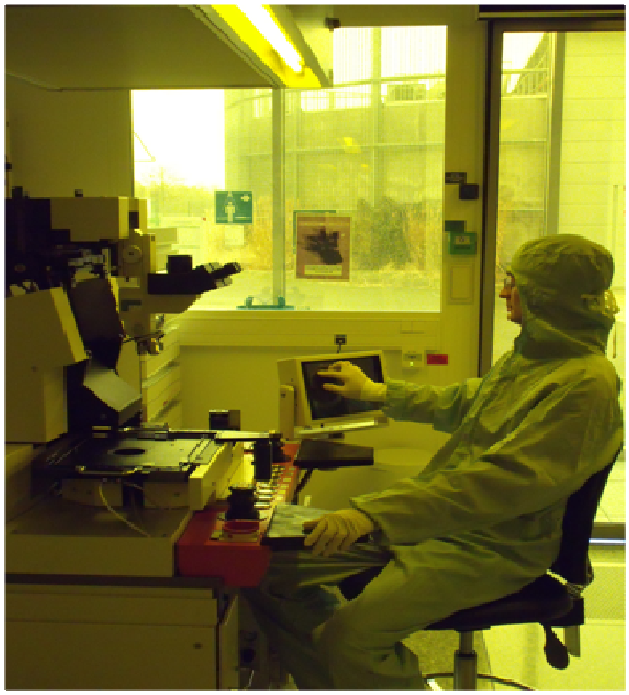

Figure II- 1 – Lithography equipment in III-V lab Clean room

II. Electron beam lithography

Electron beam lithography (E-beam lithography) is a particular technique of lithography. Instead of using a mask with UV radiation, a beam of electrons is used to pattern the photoresist material. Compared to classic techniques, E-beam lithography allows a resolution of a few hundred nanometers. The main drawback is the processing time. In this work, E-beam lithography was used to pattern the active waveguide including the active taper part.

III. Metal and Dielectric Deposition

Various techniques are employed for metal deposition, such as evaporation, sputtering and electroplating. This RSOA process is based on the sputtering technique. The target material to be deposed (metal) is placed in the vacuum chamber as well as the substrate. Atoms are ejected from the target material due to bombardment of the target by accelerated ions. It is called Ion Beam Sputter Deposition (IBSD).

Evaporation can also be used in III-V lab for directional deposition. The principle is similar to the sputtering technique. The material source is evaporated in a vacuum using a hot source. Then the evaporated particles can travel directly to the deposition target where they condense on the substrate. The latter process has not being used but it works on the principle of electrolysis.

Dielectric deposition is based on Plasma Enhanced Chemical Vapour Deposition (PECVD). This technique consists in depositing dielectric material from a gas state to solid state. A plasma of the reacting gases is created by using a strong electromagnetic field applied with a microwave generator then chemical reaction occurs and enables the deposition of the dielectric.

IV. Wet and Dry Etching

Etching techniques are used to remove materials. Specific geometric patterns can be etched using lithography techniques as described above. Then dry or wet etching can be applied to the wafer. The technique and chemicals used depend on the material to be etched, the etch rate required and the directionality.

Dry etching is based on plasma generation as described previously. A difference of potentials is applied between the two electrodes and pulls the nucleus toward the cathode. Then the bombardment by ions etches the exposed surface.

In wet etching techniques, an etchant (chemical solution) is used. The wafer needs to be deep in the etchant which dissolves the material.

Reactive Ion Etching (RIE) is a form of dry etching where ion bombardment occurs as well as wet etching by reaction of the ion with the wafer surface. We usually used dry etching in our process as it is more directional. The compositions of the reactive gases are described in Chapter 2.

V. Etching and Lift-Off Techniques

When the pattern is defined by lithography, material can be added or removed. Two techniques are commonly used:

- Etching to remove materials in specific regions
- Deposition to add materials and then a lift-off process

Lift-off process is a method to pattern a specific material using a sacrificial material such as the photoresist material.

The etching process has been detailed above; however, to etch specific patterns, several processing steps are needed, including material deposition, patterning using photolithography, and then etching to remove the deposited material in the regions where it is not required. All different steps are represented in Figure II-27-a).

Another solution to deposit material in specific regions is by lift-off techniques which consist of patterning using photolithography, deposition and then lifting-off the regions of material with the photoresist underneath (Figure II-27-b)).

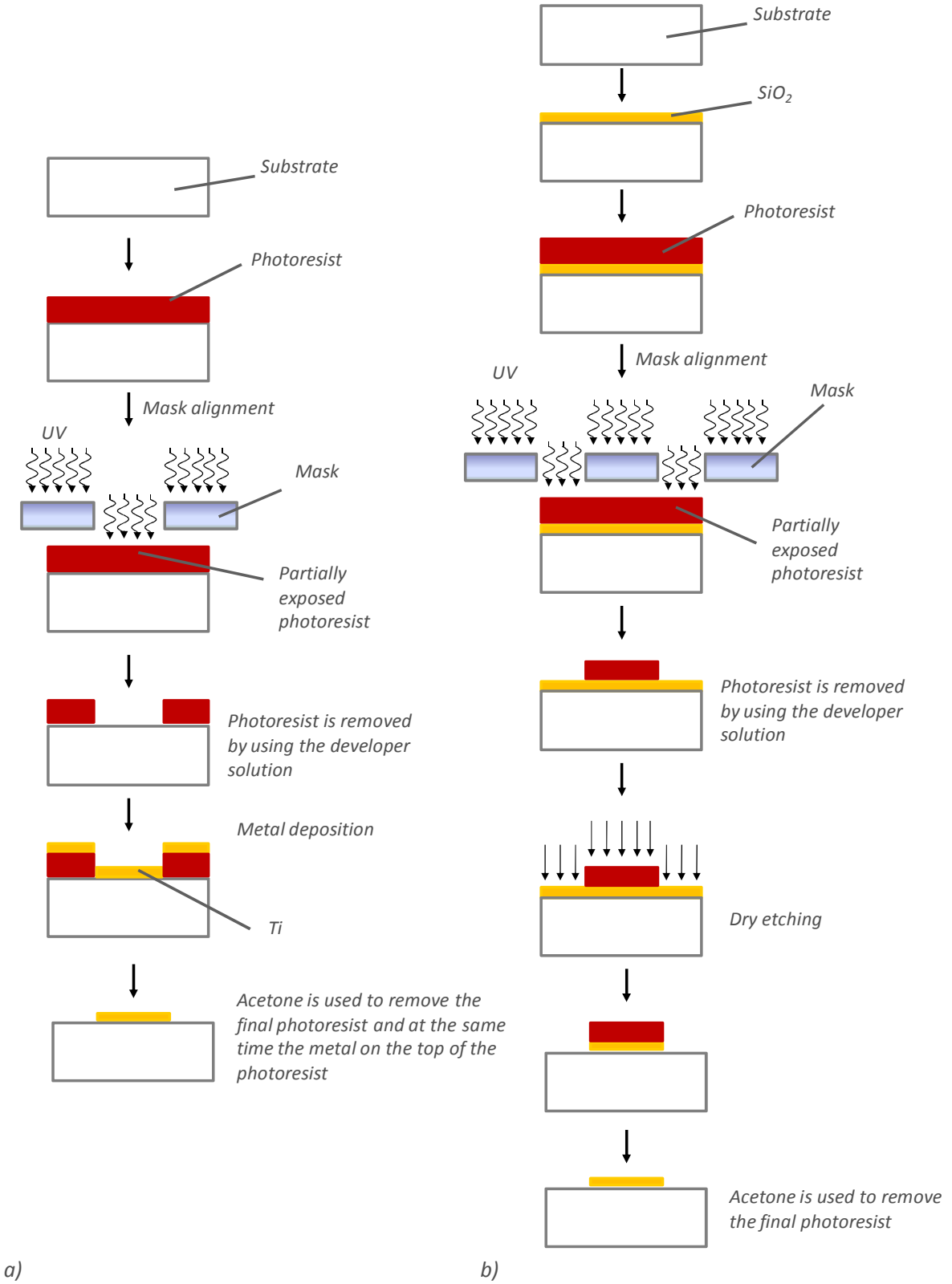

Figure II- 2 – Comparison between (a) lift-off and (b) etching technique to define specific pattern

VI. Reflectometry

Laser probes techniques are extensively used in order to characterize a plasma etching process. In situ measurements are performed to control the changes in the surface and real-time analysis become possible. Reflectometry is a simple laser probe technique based on the laser interferometry concept [2]. A real time interferometric Process Monitor is used to control the depth of the etching process [3]. This technique is performed during the etch of the active and passive zone. The materials under the etching process need to be at least partially transparent. Therefore a wavelength with higher energy than the bandgap of the active zone material is used (if not there is absorption). Besides, the incident light must be partially reflected. The reflectance varies during the etching process. It is the consequence of the interferences between the reflected light at the surface with the reflected light from the interfaces between the different layers.

Sinusoidal optical signal amplitude is obtained for the reflected beam due to constructive and destructive interferences. The period Δ can be calculated as:

$$\Delta = \frac{\lambda}{2\sqrt{n_R^2 - sin^2\theta}} \qquad \text{II-1}$$

Where n_R is the refractive index of the material, λ is the wavelength and θ is the angle of incidence.

This technique can be used to detect the several layers during the etching process as well as to determine the etch rates. Figure II-28 shows an example of the signals obtained during the etching of the passive zone (See also Figure 2-22). Oscillations with a specific period correspond to a specific layer and by counting the interference periods in time it is possible to find the etch rate.

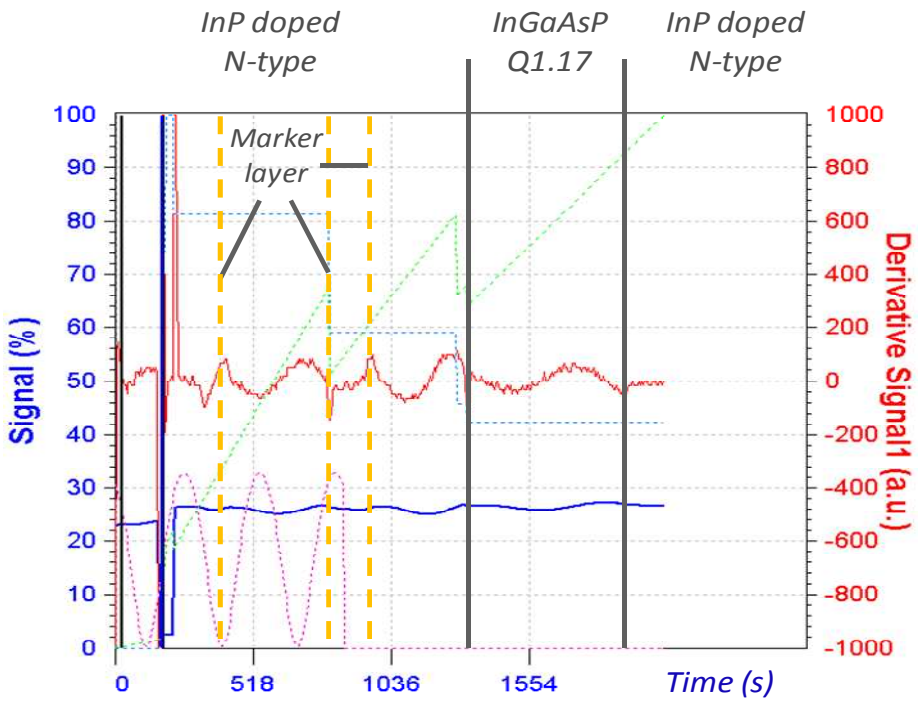

Figure II- 3 – Reflectometry control of the passive zone etching

It can be used for endpoint detection. An extra marker layer is usually grown to control the stop of the etching (See the reflectometry control of the AZ etching in Figure 2-22).

References

[1] http://www.artwork.com/
[2] A. J. Van Roosmalen, J. A. G. Baggerman and S. J. H. Brader, "Dry Etching for VLSI", Plemum Press, 1991, New York, USA, pp. 147-149
[3] http://www.horiba.com/fr/semiconductor/products/product-lines/semiconductor-manufacturing-process-monitor/details/real-time-interferometric-process-monitor-lem-ct-670-g50-2887/

Appendix III

Evaluation of Process and Design tolerance

The purpose of this appendix is to evaluate the coupling ratio tolerance depending on some key parameters as the alignment between the active and passive layers or the taper tip width. Several simulations have been realized using Beam prop software. The optical mode propagation and how it is affected by the taper tip width or the misalignment are respectively represented in Figure III-29 and Figure III-30.

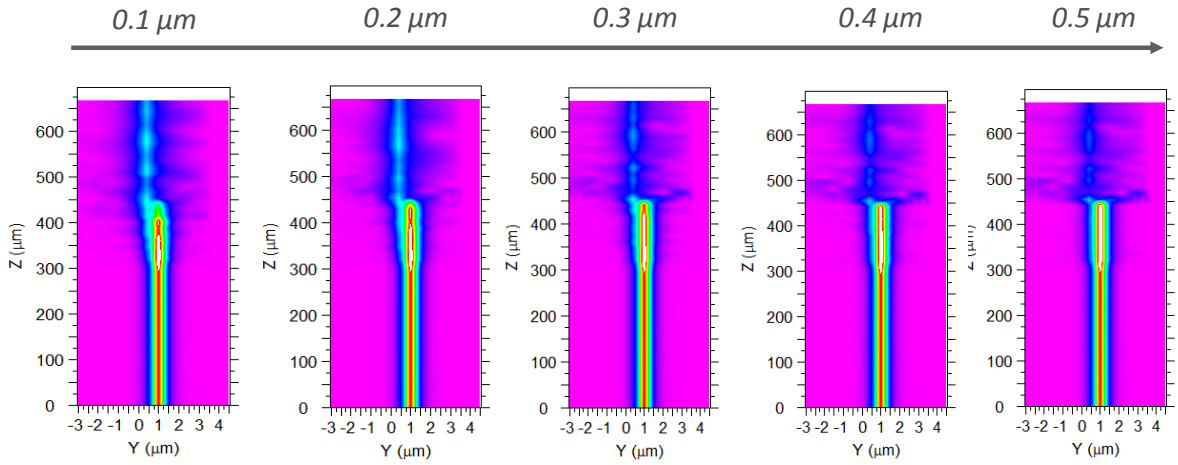

Figure III- 1 – Simulations of optical beam propagation depending on the taper tip width

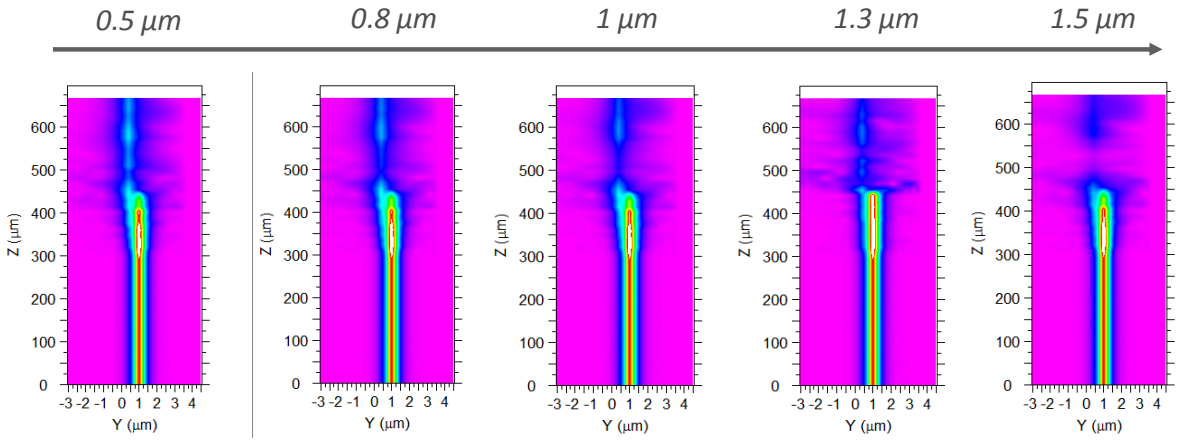

Figure III- 2 – Simulations of optical beam propagation depending on the misalignment between the active and passive layer

The coupling ratio is extracted from the previous simulations. All results are summarized in Figure III-31. The RSOA design is more tolerant to a large misalignment than a large taper tip. The impact of the taper tip width is a key parameter for the coupling efficiency. Small variation of the width strongly affects the coupling ratio. A variation of 0.4 µm induces a decrease of 50% of the coupling ratio. Therefore taper tip need to be carefully control in order to obtain high efficiency for the coupling.

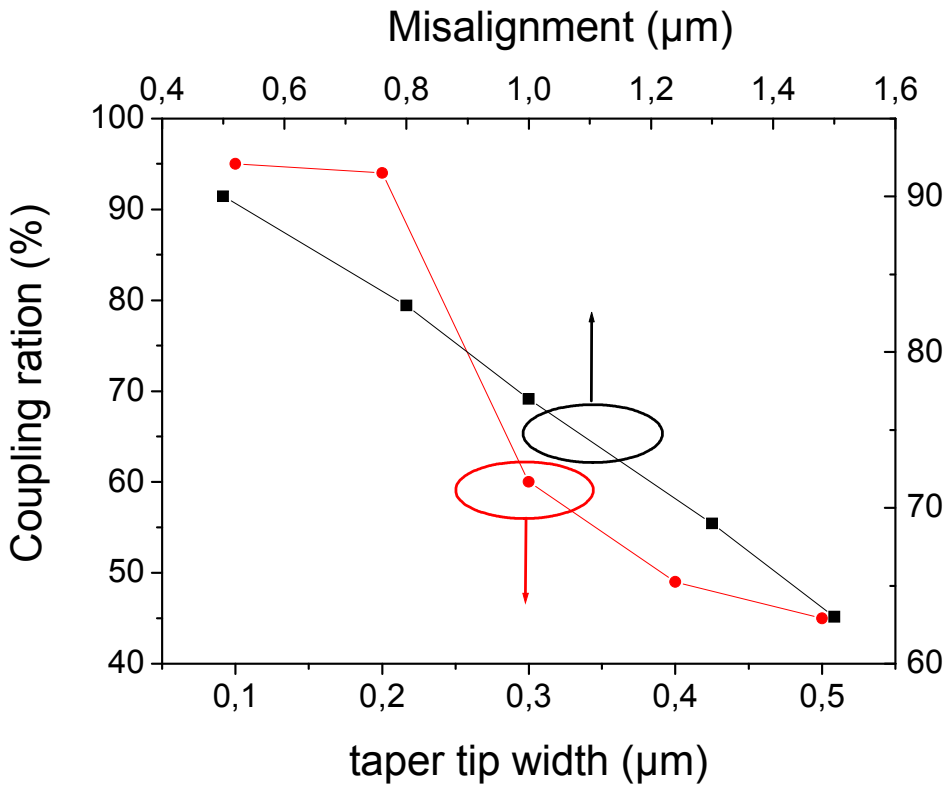

Figure III- 3 – Coupling ration depending on the width of the taper tip and the misalignment

Télécom ParisTech
Grande école de l'Institut Télécom – membre fondateur de ParisTech
46, rue Barrault – 75634 Paris Cedex 13 – Tél. + 33 (0)1 45 81 77 77 – www.telecom-paristech.fr

Conception, fabrication et évaluation de modulateurs déportés pour les réseaux d'accès et radio sur fibre

RESUME : L'évolution des outils télécommunicationnels répond à une révolution des usages. Les réseaux d'accès et de type radio-sur-fibre doivent répondre à cette demande de l'utilisateur final et le déploiement massif de la fibre optique confirme cette évolution. Dans cette perspective, l'utilisation du multiplexage en longueur d'onde (largement utilisé dans les réseaux cœurs) est maintenant considérée dans le cas d'une augmentation du débit chez l'utilisateur. Néanmoins de nouvelles problématiques, propres à ces réseaux, émergent, telles que le coût pour l'abonné. De nouveaux composants indépendants de la longueur d'onde sont donc nécessaires pour réduire les coûts de déploiement tout en apportant flexibilité et facilité de gestion de ce type de réseaux. Les modulateurs déportés (ou RSOA) sont une solution répondant à ces exigences mais ils doivent se plier à celles, nouvelles, des réseaux d'accès et des réseaux radio-sur-fibre.

Cette thèse propose une étude détaillée des propriétés physiques de ces composants ainsi que de ces applications en tant qu'émetteur indépendant de la longueur d'onde dans plusieurs configurations réseaux. Les notions fondamentales nécessaires à la compréhension de ces travaux seront abordées ainsi que la conception et la fabrication de ces composants en salle blanche. Une analyse des performances statiques et dynamiques des composants en fonction de certains paramètres clefs tels que le confinement optique, la longueur de la zone active et la réflectivité des facettes est détaillée. La théorie, une modélisation et des mesures expérimentales seront utilisées pour la création de composants optimisés ayant des performances conformes à l'état de l'art. De nouvelles configurations de RSOA à deux électrodes seront proposées pour diverses utilisations originales de ces composants. Finalement, une étude système viendra compléter notre analyse pour des applications concernant les réseaux d'accès et les réseaux de type radio-sur-fibre.

Mots clés : Modulateur déporté, Communication optique, Amplificateur optique à base de semi-conducteur, Amplificateur optique en réflexion, Multiplexage temporelle, Multiplexage en longueur d'onde, réseaux d'accès, radio sur fibre, transmission de signaux radio.

Design, fabrication and evaluation of Reflective Semiconductor Optical Amplifier for access and RoF Network

ABSTRACT : Fibre-to-the premises (FTTP) is considered as the main solution in order to satisfy the demand for higher capacity networks. For next-generation access networks, upgradeability and high capacity could be obtained using Wavelength-Division Multiplexing in PON (WDM-PON). However, cost and compatibility with existing TDM-PON networks is still an important issue. If wavelengths are to be dynamically allocated, one to each RAU, colorless devices are needed in order to minimize the deployment cost. Reflective Semiconductor Optical Amplifier (RSOA) devices can be used as a low-cost solution due to their wide optical bandwidth.

In this study, RSOAs are optimized for WDM PON and R-o-F access technology. The design, fabrication and system evaluation are presented. This study oscillates between a theoretical approach, a modeling of the physical mechanisms as well as experimental measurements. 2-section RSOAs are also investigated. Finally, the envisaged architectures of access and RoF networks based on optimized RSOA are evaluated.

Keywords : Modulation, Optical fiber communication, Semiconductor optical amplifiers, Reflective Semiconductor Optical Amplifier, Time division multiplexing, Wavelength division multiplexing, Access Network, radio over fibre.

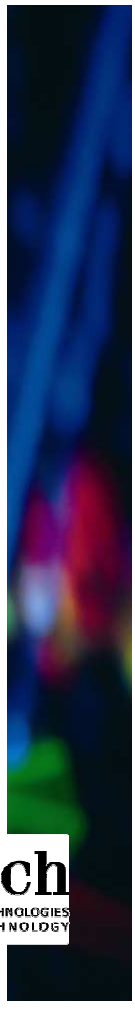

TELECOM ParisTech

EDITE

ParisTech
INSTITUT DES SCIENCES ET TECHNOLOGIES
PARIS INSTITUTE OF TECHNOLOGY